Flux Pumping for No-Insulation High Temperature Superconducting REBCO Magnets

JUN MA

Department of Engineering, University of Cambridge

Churchill College

This dissertation is submitted for the degree of

Doctor of Philosophy

May 2020

I would like to dedicate this thesis to my loving parents.

Especially my dear mother

Mrs. Shuiqing Chen

Declaration

This thesis is the result of my own work and includes nothing which is the outcome of work done in collaboration except as declared in the Preface and specified in the text. It is not substantially the same as any that I have submitted, or, is being concurrently submitted for a degree or diploma or other qualification at the University of Cambridge or any other University or similar institution except as declared in the Preface and specified in the text. I further state that no substantial part of my thesis has already been submitted, or, is being concurrently submitted for any such degree, diploma or other qualification at the University of Cambridge or any other University or similar institution except as declared in the Preface and specified in the text. It does not exceed the prescribed word limit for the relevant Degree Committee.

Jun Ma

May 2020

Flux Pumping for No-Insulation High Temperature Superconducting REBCO Magnets

Jun Ma

Abstract

The high temperature superconducting (HTS) REBCO magnet has many advantages compared to the low temperature superconducting (LTS) magnet, including high operating temperature, high critical current under high magnetic fields, and strong mechanical properties. Due to these excellent properties, HTS REBCO magnets have huge potential in high-field high-current applications, such as accelerator magnets, tokamak fusion magnets, magnetic resonance imaging (MRI) systems, ultra-high-field magnets. It can pave the way for a more compact and economical superconducting magnet system, including. Currently, a novel no-insulation (NI) type HTS REBCO magnet has a self-protection ability, which has solved a long-lasting “thermal quench” problem. The self-protection ability has significantly improved the reliability of HTS REBCO magnets and makes the NI HTS REBCO magnet very advantageous in practical use.

However, lossless superconducting joints for HTS REBCO coated conductors are not available. To maintain a stable magnetic field for the HTS REBCO magnet, an external power supply is required via a bulky no-superconducting copper current leads. The copper current leads consume a huge amount of electricity and increase the size of the magnet system. In order to reduce energy loss and the size of the magnet system, flux pumping technology was invented, which is a contactless charging technology and removes the no-superconducting resistive current leads. Up to now, however, flux pumping technology only focuses on conventional insulated type HTS REBCO magnets. The novel NI HTS REBCO magnet has different characteristics from the conventional insulated HTS REBCO magnet, such as bypass current and characteristic resistance (R_c).

This thesis studies the flux pumping technology for the no-insulation type HTS REBCO magnet, figures out the technical challenges, and improves the flux pumping performance for NI HTS REBCO magnet with a very low R_c. Chapter 2 introduces the basic theory of superconductivity, the development of superconductors, and various superconducting applications. Chapter 3 reviews the flux pumping technology, including LTS and HTS flux pumps. Chapter 4 presents an active-switching HTS transformer rectifier flux pump (TRFP), including the fundamental physics, key components, and overall system. Chapter 5 presents the design and fabrication of the NI HTS REBCO magnet and proposed a novel solder impregnated NI HTS REBCO magnet. The characteristics of this novel NI HTS magnet are discussed. Chapter 6 studies the flux pumping performance of the HTS TRFP for different NI HTS REBCO magnets, analyses the unique flux pumping characteristics, and improves the flux pumping performance for NI REBCO magnet with a very low R_c. Chapter 7 designs high-performance switches for active-switching HTS TRFP via a multi-physics FEM COMSOL model.

This thesis will help promote the use of the flux pumping technology for the NI HTS REBCO magnets systems, and it will be of interest to physicists and engineers who want to build an energy-efficient, compact, and reliable superconducting magnet system.

Acknowledgement

I would like to thank the Cambridge Trust and China Scholarship Council for funding my Ph.D. at the University of Cambridge. I would also like to thanks Churchill College for supporting me during my Ph.D. study. I would also like to thank Vest Scholar Program and North Carolina State University for providing a research opportunity in the USA.

I would like to thank my Ph.D. supervisor Dr. Tim Coombs for his advice and support throughout my Ph.D. study. He led my way to independent research, allowed me the freedom to explore my ideas, and provided strong support for my PhD study. I would also like to thank the members of EPEC Superconductivity Group, especially Dr. Jianzhao Geng. It is a happy time to finish my Ph.D. with all of you. I also want to thank Prof. Justin Schwartz and Dr. Wan Kan Chan for hosting and supervising me at North Carolina State University.

I would like to thank IEEE Council on Superconductivity for awarding me the IEEE CSC Graduate Study Fellowship (Class of 2020). It is a huge honour and encouragement for me and I will keep making contributions to our field of applied superconductivity.

I would like to thank Prof. Zhijian Jin, Prof. Zhiyong Hong, and all the group members for supporting me at Shanghai Jiao Tong University. Without you, I won't be able to study at the University of Cambridge. I would also like to thank Zhejiang University for the undergraduate education, which had built a solid foundation for my later studies.

I would like to thank all my dear friends in Cambridge. My Ph.D. study in becomes delightful because of you and it will be an unforgettable experience in my whole life.

Finally, I want to thank my parents. You are always encouraging me and providing strong support during my entire life. Thank you for raising me up and teaching me to be a good man.

List of Publications

[1] **Jun Ma**, *et al*, "A temperature-dependent multilayer model for direct current carrying HTS coated-conductors under perpendicular AC magnetic fields", *Superconductor Science and Technology*, vol. *33, no.* 4, Art. ID 045007, 2020.

[2] **Jun Ma**, *et al*, "Impact of Stabilizer Layers on the Thermal-Electromagnetic Characteristics of Direct Current Carrying HTS Coated Conductors under Perpendicular AC Magnetic Fields", *IEEE Transactions on Applied Superconductivity,* vol. 30, no. 4, Art. ID 6600906, 2020.

[3] **Jun Ma**, *et al*, "High-temperature superconducting (HTS) transformer-rectifier flux pump for powering no-insulation superconducting magnet with low characteristic resistance". *Physica C: Superconductivity and its Applications*, vol. 560, May, 2019.

[4] **Jun Ma**, *et al*, "Rotating Permanent Magnets Based Flux Pump for HTS No-Insulation Coil". *IEEE Transactions on Applied Superconductivity*, vol. 29, no. 5, Art. ID 5202106, 2019.

[5] **Jun Ma**, *et al*, "Flux pumping for non-insulated and metal-insulated HTS coils". *Superconductor Science and Technology***,** vol. 31, no. 1, Art. ID 015018, 2017.

[6] **Jun Ma**, *et al*, "Numerical Study of HTS Power Switch based on Dynamic Resistance Effect". Submitted to *IEEE Transactions on Applied Superconductivity*, 2020.

Contents

List of Figures

List of Tables

Chapter 1
Introduction

1.1. Background

The superconducting magnet is used as a key component in many applications because of its zero-resistance and high current carrying capabilities, such as magnetic resonance imaging (MRI) devices, tokamak fusion energy devices, particle accelerators, and high power superconducting electrical machines. Currently, commercial superconducting applications use low temperature superconducting (LTS) conductors due to the low price and mature manufactures technologies. However, the fast-developing high temperature superconducting (HTS) rare-earth barium copper oxide (REBCO) conductors are demonstrating huge potentials due to the significant advantages over LTS counterpart, such as high operating temperature, high critical current under high magnetic fields, strong mechanical properties, and the reducing price.

With the fast progress of commercial REBCO coated conductors, the HTS magnets technology has been developing very quickly in recent years. HTS REBCO magnets have already become a key enabling technology for high field applications. The HTS magnets are co-wound with insulation layers, but it exists with a long-lasting thermal-quench problem for this conventional magnet design. In 2011, Hahn firstly proposed a novel no-insulation (NI) type HTS REBCO coil magnet [1], which removed the turn-to-turn insulation layers. The NI REBCO magnets have a self-protection ability, which successfully solved the long-lasting thermal-quench problem. NI REBCO magnets can survive from large overcurrent and are free from the detrimental impact of small defect spots in the HTS conductors. These unique advantages make the NI REBCO magnets super reliable and especially suitable for high-field high-current applications. The NI REBCO magnet has proven its significant advantages by enabling a new world record of the strongest magnetic field at 45.5 T in 2019 [2]. The NI

REBCO magnet is also on its way to enabling compact and economical tokamak fusion energy devices [3], which can provide limitless clean energy from fusion reactions and remove the environmental damage caused by traditional fossil fuels.

However, lossless HTS REBCO joints are unavailable and HTS REBCO magnets can only be charged by external power supplies via bulky and energy-inefficient current leads. These technical obstacles place limits on the achievable current capacity and energy density of the magnets and also makes the superconducting magnets less thermally-stable and less reliable, which has significantly impeded the widespread uptake of HTS magnet technology. However, these problems can be effectively solved by the HTS flux pumping technology. HTS flux pumps enable HTS REBCO magnets to operate in a persistent current mode in a closed-loop mode within a closed cryogenic environment.

Up to now, HTS flux pump technology only focuses on conventional HTS REBCO magnets wounded with turn-to-turn insulation. Very limited research work can be found for powering the novel no-insulation type HTS REBCO magnets. It is an important research gap between the HTS flux pumping technology and this novel type of HTS magnets. The flux pumped NI HTS REBCO magnets have huge potential in building energy-efficient, compact, and reliable superconducting magnet systems, which could be used in portable MRI devices, compact tokamak fusion devices, particle accelerators, and high-power-density electrical machines.

1.2. Research aim and outline

This thesis aims to promote the use of the contactless flux pumping technology for the novel no-insulation type HTS REBCO magnets. It is hoped to help researchers understand the unique characteristics and performance of flux pumping technology for NI REBCO magnets. It figures out the technical challenges and improves the flux pumping performance for NI REBCO magnets. This thesis answers two major driving questions: (1) Is HTS flux pumping technology suitable for the novel no-insulation type REBCO HTS magnets? (2) How to improve the performance of HTS flux pump for powering NI REBCO magnets? This thesis will help promote the use of the contactless flux pumping technology for a variety type of HTS REBCO magnets, including the NI REBCO magnets. This thesis will be of interest to physicists and engineers who want to build an energy-efficient, compact, and reliable superconducting magnet system.

To support reading the thesis, its outline is presented graphically in Fig. 1.1.

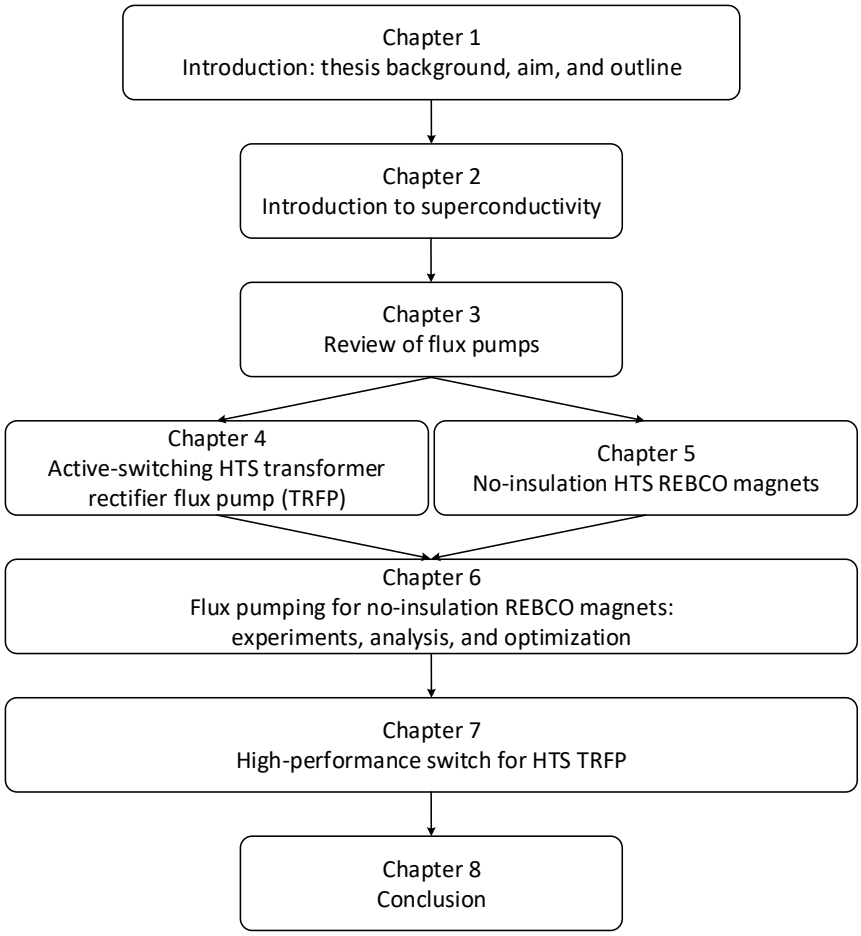

Fig. 1.1. Thesis outline and flow of information.

Chapter 2 introduces the basic theory of superconductivity, including its definition, characteristics, and classification of superconductors. The development of superconductors and their applications are reviewed. Important aspects of superconducting magnet technology are reviewed and discussed.

Chapter 3 reviews the progress of flux pumping technology, including the LTS flux pumps and LTS flux pumps.

Chapter 4 presents the design and fabrication of an active-switching HTS transformer reciter flux pump (TRFP). It presents the fundamental physics: "dynamic resistance effect", the key component: "AC field controlled switch", and the overall system of the HTS TRFP. An operational test is also presented to evaluate the performance of the HTS TRFP.

Chapter 5 presents a conventional NI REBCO HTS coil magnet and a novel NI REBCO HTS coil magnet using solder as turn-to-turn impregnation. Solder impregnated no-insulation HTS magnets are significantly mechanically strengthened by solder impregnation. The

manufacturing process is different and so is its properties. This chapter details their manufacturing processes and properties.

In *Chapter 6*, two different NI HTS REBCO magnets, together with a traditional insulated HTS REBCO magnet, were pumped by the HTS TRFP. The flux pumping characteristics for three different HTS magnets are compared and analyzed. Based on the unique characteristics of the flux pumping performance for the low-R_c NI HTS magnet, an optimization on the circuit design of the HTS TRFP is proposed. This optimization improves the flux pumping performance for NI HTS magnets with a very low R_c.

Chapter 7 studies the high-performance switch for HTS TRFP. The AC-field-controlled HTS switch is a key component in the active-switching HTS TRFP, and determines the performance and reliability of TRFP. The study is based on numerical simulation via a multi-physics model for REBCO coated conductor tape, which has successfully coupled thermal physics and electromagnetic physics. Different designs for high-performanc HTS switches have been discussed and analyzed.

Chapter 8 summarizes this thesis and proposes the future work.

This thesis shows that the flux pumping technology is suitable for NI REBCO magnets. The flux pumped NI REBCO magnets have huge potential in making an energy-efficient, compact, and reliable superconducting magnet system. It could be used in a variety of superconducting applications.

Chapter 2
Introduction to Superconductivity

This chapter gives a brief introduction to the basic theory of superconductivity, including its definition, characteristics, and classification. The development of superconductors, their major applications, and important aspects of the superconducting magnets technology are reviewed.

2.1. Discovery and definition of superconductivity

2.1.1. Discovery of zero resistivity

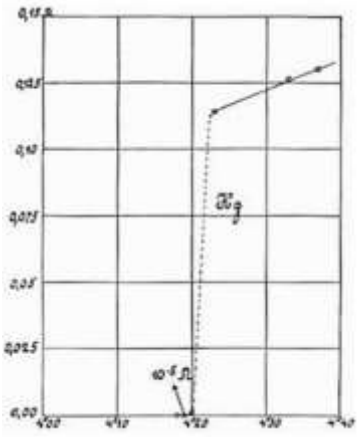

Fig. 2.1. Resistance (y-axis) vs temperature in degrees Kelvin (x-axis) of pure Mercury from Onnes's experiments [4].

In 1911, Dutch scientist Heike Kamerlingh Onnes firstly discovered the "superconductivity" [4]. At the time, Onnes was working with liquid helium, and several theories were predicting on how material resistivity would behave at temperature approaching absolute zero. Onnes discovered that the resistance of mercury dropped to zero when it was cooled below 4.2 K, as

shown in Figure 2.1. In the following years, many other materials also found be exhibit a superconductivity below a certain critical temperature (*Tc*).

2.1.2. Ideal diamagnetism

In 1933, 22 years later, W. Meissner and R. Ochsenfeld renewed and deepened the understanding of "superconductivity" via the discovery of the "Meissner Effect" [5]: the superconductor acts as a perfect diamagnet under field cooling condition, which is different from the "ideal conductor" that people thought the superconductors should be.

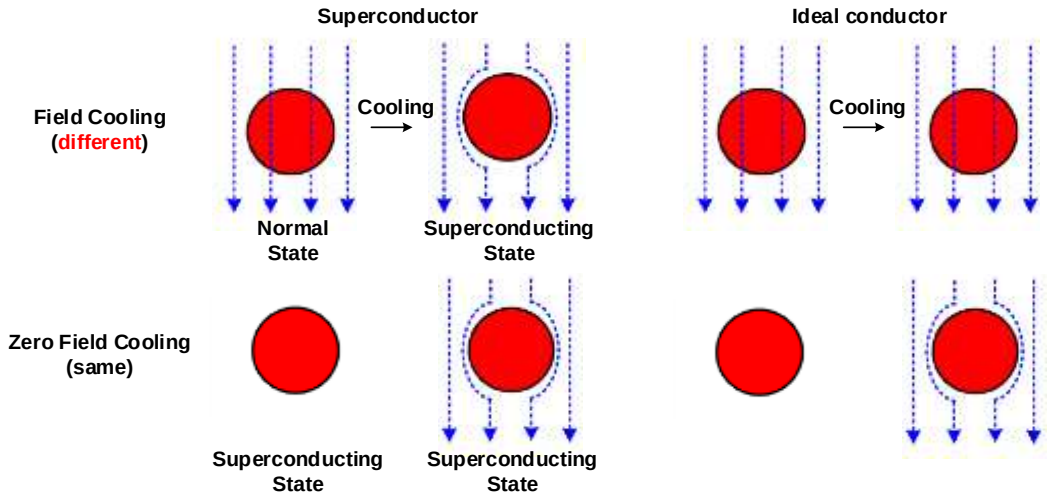

Fig. 2.2. A comparison between a "superconductor" and an "ideal conductor" under fielding cooling process and zero-field cooling process [5]. Under the field cooling condition, the superconductor expels the magnetic flux from the interior, which is defined as the "Meissner Effect", while the ideal conductor holds the magnetic flux in the conductor. During the zero-field cooling, the behaviors of the "superconductor" and the "ideal conductor" are the same.

Fig. 2.2 shows a comparison between a superconductor and an ideal conductor under the fielding cooling process and zero-field cooling process. During the field cooling process (the superconductor and ideal conductor are placed in an external magnetic field before being cooled below the critical temperature), the superconductor shows "perfect diamagnetism", which means expelling all the magnetic flux from its interior ($B = 0$ inside the superconductor), while in contrast, the ideal conductor keeps the magnetic flux inside ($B \neq 0$). However, during the zero-field cooling process (the superconductor and ideal conductor are both placed in an external magnetic field after being cooled below the critical temperature), the behaviors of the superconductor and the ideal conductor are identical. Both two conductors will induce screening currents to expel the external field from the interior of the conductors. The

"Meissner effect" indicates that any magnetic field will be expelled out from the interior of a superconductor, as long as the material is in superconducting state.

To be a superconductor, the material must satisfy two conditions: (i) ideal conductivity or zero resistance ($\rho = 0$) and (ii) the ideal diamagnetism.

2.1.3. Three conditions for superconductivity: T_c, B_c, and J_c

To guarantee the superconducting state, three conditions should be met: (1) below the critical temperature (T_c), (2) below the critical magnetic density (B_c), and (3) below the critical transport current density (J_c). As shown in Fig. 3.3, the red space represents the effective zone where the superconductors remain a superconducting state.

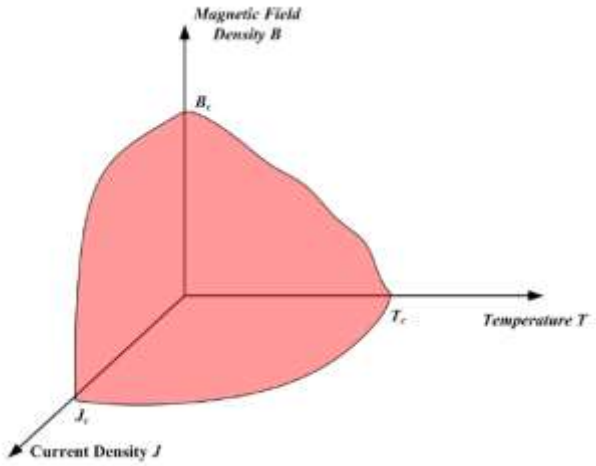

Fig. 2.3. Three boundary limits for the superconducting state: (1) magnetic field (B), (2) temperature (T), and current density (J), taken from [6, 7].

2.2. Classification of superconductors: Type-I & Type-II

According to the definition of "superconductivity", all superconductors enters the Meissner State in a certain magnetic field. However, if the external field increases, the Meissner effect will breakdown. However, different superconductors behave differently. Some superconductors return to a normal state directly, while others enter a "mix state" first and then return to a normal sate. Superconductors can be classified according to the magnetization behaviors responding to an externally applied magnetic field. Type-I superconductors refer to those who only have the superconducting and the normal state. Type-II superconductors refer

to those who have three states: the superconducting state, the "mixed state", and the normal state. This criterion considers intrinsic and microscopic differences.

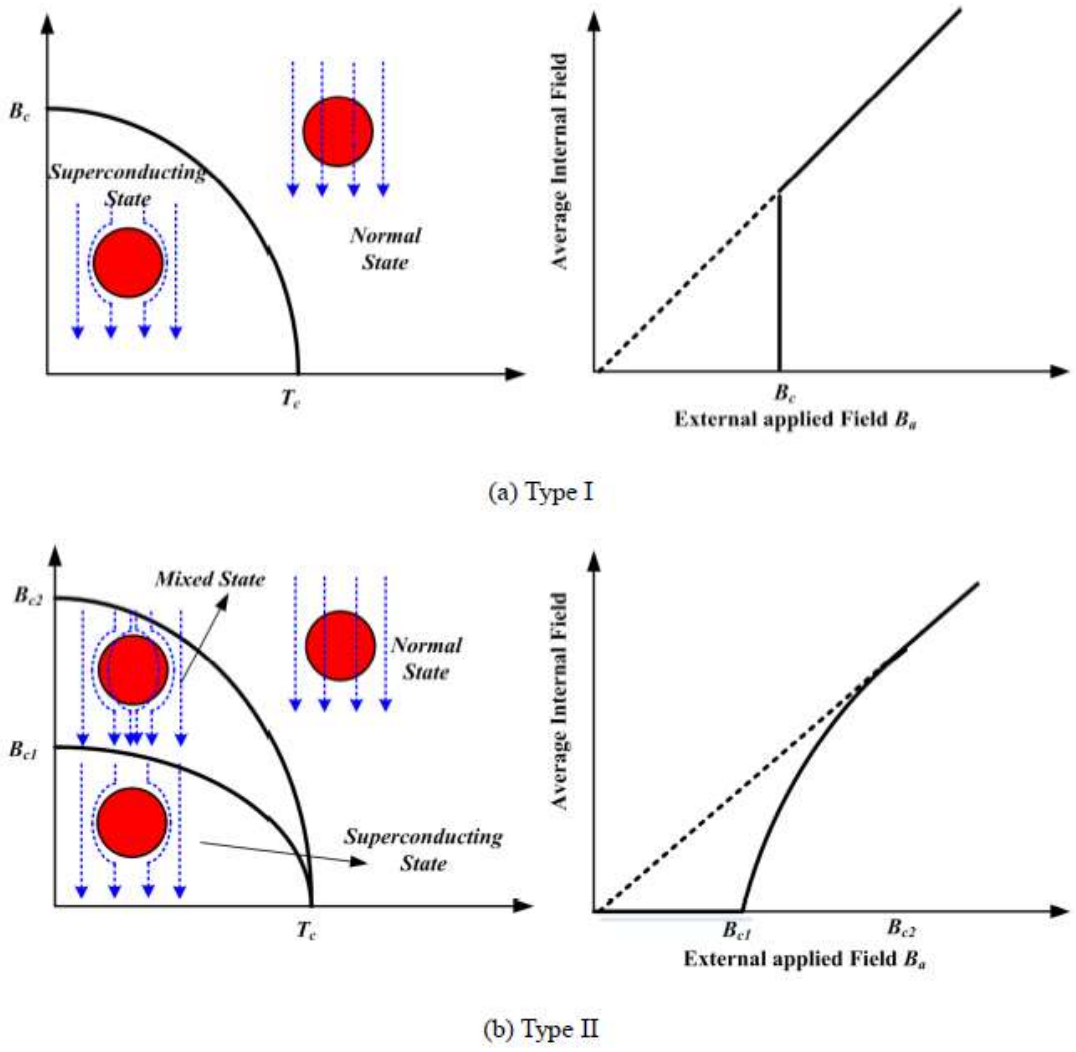

Fig. 2.4. Magnetization and internal magnetic field of Type-I and Type-II superconductors as the external magnetic field increases, taken from [8].

Fig. 2.4 shows the magnetization and internal magnetic field of Type-I and Type-II superconductors as the external magnetic field increases. Type-I superconductors remain perfectly diamagnetic until the external field exceeds the field B_c, after which the external field fully penetrates the superconductors and the superconductors suddenly enter a normal state. In contrast, the Type-II superconductors will turn from Meissner state to the "mixed state" (or critical state) if the external field exceeds the lower critical field B_{c1}. With the increases in the external field from B_{c1}, the superconductors will be gradually penetrated from the outer to the inner. If the external field exceeds a certain value called upper critical field B_{c2}, the superconductors will be fully penetrated and finally reach the normal state.

The "mixed state" of the type-II superconductors is crucial for many superconducting devices working in a background magnetic field. The understanding and modeling of this "mixed state" are quite important to help design and develop many superconducting devices. The "mixed state' is also called "critical state".

2.3. Characteristics and models of Type-II superconductors

2.3.1. Critical state and flux pinning

The "mixed state" or "critical state" is a unique characteristic of Type-II superconductors. There is an important physics in the critical state of Type-II superconductors called "flux pinning". The "mixed state" is mainly caused by "Flux pinning". Thanks to the flux pinning, type-II superconductors can transport high density current with little power loss. This advantage makes the type-II superconductors very promising in practical applications.

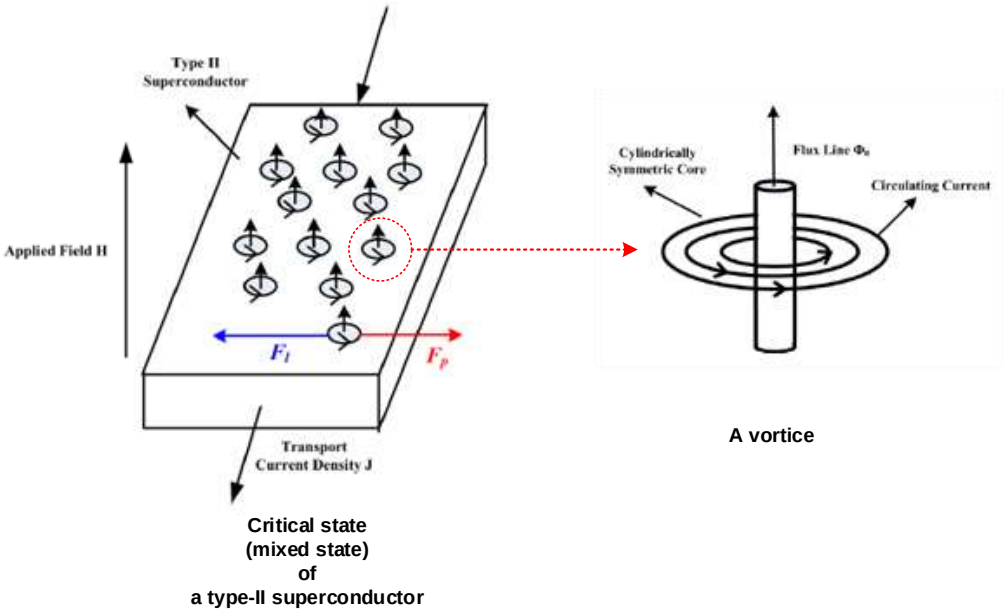

Fig. 2.5. A diagram (in the left) of the "flux pinning" phenomenon in the critical state of a type-II superconductor, and a plot (in the right) of a vortice.

If a type-II superconductor enters the mixed state (critical state), it means the superconductor has already been partly penetrated by the external magnetic field. The magnetic flux penetrates the type-II superconductor in the form of individual flux quanta, called vortices [9]. Each vortex consists of a cylindrical core through which the flux lines pass

and around which circular screen current flows. The vortices can be trapped by the impurities or crystalline defects in the type-II superconductors. This phenomenon is called "flux pinning" [10], and the impurities or crystalline defects points is called "pinning centers" [10]. The pining centers can hold the vortices with a force known as pining force (F_p). If the pinning force is strong, it is defined as a hard superconductor, otherwise, it is defined as a soft superconductor. Fig. 2.5 shows a diagram of the "flux pinning" phenomenon in the critical state of a type-II superconductor and a plot of a vortice.

2.3.2. *E-J* power law and flux flow

If a transport current is flowing through a type II superconductor, the vortices will be driven by the Lorentz force (F_L), which is shown in the equation (1.1). If the transport current increases, the Lorentz force will increase as well. The magnetic field density (B) can be either from an external magnetic field or a self-field generated by the transport current. The current density (J) can be either from a transport current or a screening current caused by magnetization process.

$$F_L = J \times B \tag{2.1}$$

The motion and distribution of the magnetic vortices in type-II superconductors are mainly determined by the interaction between the Lorentz force (F_L) and the pinning force (F_p), also as shown in Fig. 2.5. An electrical field (E) will be induced by the moving vortices (at a speed of v) across the superconductor, as shown in equation (1.2).

$$E = B \times v \tag{2.2}$$

When the pinning force (F_p) dominates, the vortices remain stationary and no electrical field (or DC voltage along the transport current direction) is generated. If the Lorentz force (F_p) increases to a level higher than the pining force (F_p), due to the increase of current density (J) or magnetic field (B), the vortices (or flux) will move from one side of the type-II superconductor to the other side, and therefore an electrical field (DC voltage) will develop along the conductor accordingly. This phenomenon is called "flux flow" [11].

To describe the electrical properties of Type-II superconductors, an *E-J* power law [12] was proposed. The *E-J* power law was obtained through experimental methods by researchers. *E-J* power law is frequently adopted in the numerical modeling and calculation.

$$E = E_c(\frac{J}{J_c})^n \qquad (2.3)$$

In equation (1.3), E_c is a constant, usually set as 10^{-4} V/m; J_c is the critical current density of the superconductor. Fig. 2.6 shows the *E-J* characteristics for superconductors with different n values. Note the limiting cases of n=1 corresponds to Ohms law or normal resistance and n = ∞ corresponds to the critical state model (Bean Model). Typical values of n for HTS are between 5 (for a superconductor with high flux creep) and 50 (which is typical of the limit for the transition between HTS and LTS). In most FEM models for superconductors, the *n*-value is set according to the specific material. For the HTS REBCO coated conductors, n generally is set between 21 and 31.

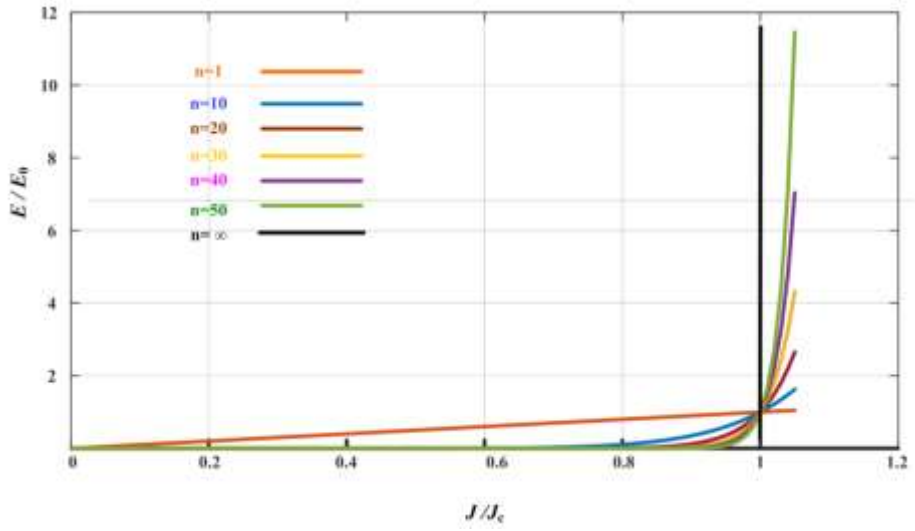

Fig. 2.6. The E-J curve with different values of n according to the E-J power law. The black curve describes Beans model; the orange curve represents the Ohm's law, which illustrates non-superconducting materials such as copper, taken from [8].

2.3.3. Critical state model

To explain the magnetization behaviors of type-II superconductors during the mixed state (or critical state), scientists proposed a useful model called “critical state model”. The critical state model describes the current-field distribution inside the type-II superconductors. These models are important tools to understand magnetization in Type-II superconductors and are also commonly used in numerical modeling for Type-II superconductors.

The critical state model was firstly proposed by Bean in 1962 [13]. It is a very useful model to describe the magnetization profile in a type-II superconductor. There are two assumptions in the Bean model: (1) the critical current density J_c is independent of the external magnetic field; (2) the current density in the type-II superconductor is either its critical current density J_c or zero, which means there are only three possible values for current density: 0 or $\pm J_c$.

The field and current in the superconductor can be expressed as diagrams of H field vs current density in a slab of superconductor, as shown in Figure 2.7. H^* in this figure is the threshold penetration field of the slab when currents flow through the entire slab. When a low external magnetic field (H) is applied to the type-II superconductor, a screening current with the critical current density (J_c) will be induced and flow along the outer part of the superconductor, wherever the external magnetic flux penetrates the type-II superconductor. No current flows along the inner part. This induced screening current will shield the inner part of the type-II superconductor and therefore the magnetic field (B) is zero.

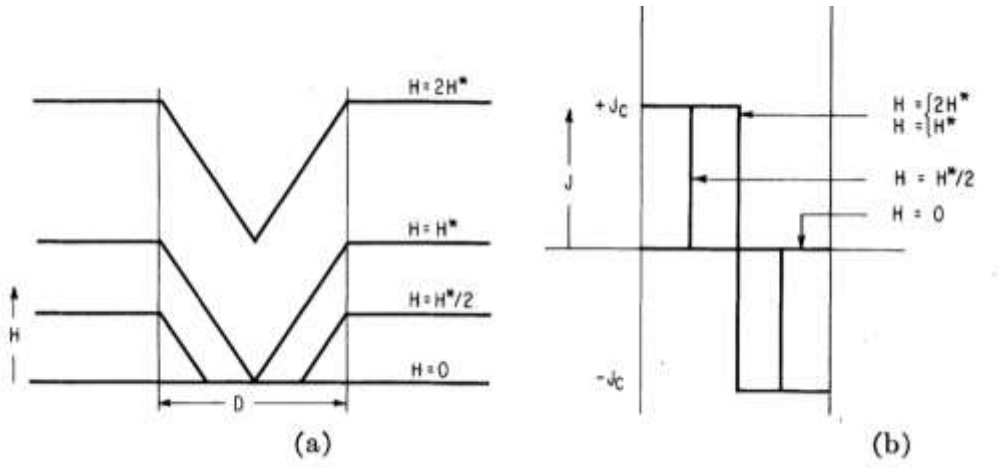

Fig. 2.7. The Bean critical state model showing (a) the applied field in a slab of superconductor and (b) the current density in the slab, taken from [13].

Bean model assumes that the current density in the type-II superconductor is either its critical current density J_c or zero, which means there are only three possible values for current density: 0 or $\pm J_c$. However, in fact, it is not the case. The critical current densities inside the superconductors are different and will be determined by external factors such as mechanical strain, temperature, and the background magnetic field.

2.3.4. Magnetic field dependency: $J_c(B)$

An empirical model accounting for the magnetic field dependency of J_c was proposed by Kim and Anderson [14-16] and can be expressed as equation (1.4). This Kim-Anderson model assumes that the critical current density depends on the local field intensity, is different from the Bean model. In equation 1.4, J_{c0} is the critical current density with no applied field, and B_0 is a constant. B is the magnetic field applied to the superconductor.

$$J_c(B) = \frac{J_{c0}}{1 + B / B_0} \tag{2.4}$$

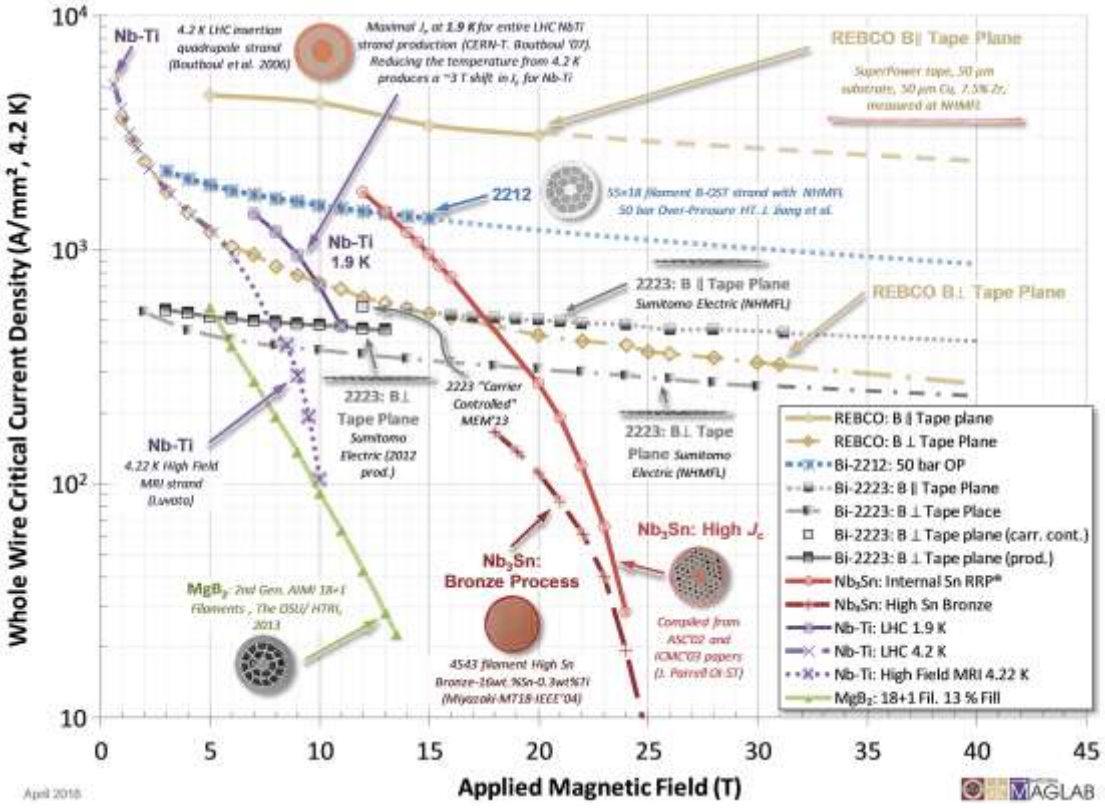

Fig. 2.8. Engineering Critical Current Density vs. Applied Field for Superconductors Available in Long Lengths, data is updated on April 11, 2018, taken from [17].

Fig. 2.8 shows the up-to-date engineering critical current density of different superconductors under an applied magnetic fields. As the applied magnetic field increases, the critical current density of all superconductors decreases.

Among current superconductors available in long length, the REBCO tape has an excellent critical current density under high background field. However, the REBCO tape has an

anisotropic critical current density in terms of the parallel and perpendicular field. The critical current density drops more quickly under the perpendicular field than under the parallel field. The anisotropic critical current density accounting for parallel and perpendicular fields can be expressed in equation (1.5). This anisotropic model has been frequently used by researchers [18-21].

$$J_c(B) = \frac{1}{(1+\frac{\sqrt{(kB_{para})^2 + B_{perp}{}^2}}{B_c})^b} \tag{2.5}$$

B_{para} and B_{perp} represent the magnetic field density parallel and perpendicular to the wide tape surface, respectively. k, B_c, and b are three parameters controlling the $J_c(B)$ curve. These three parameters are obtained by curve-fitting on experimental measured critical current data for a specific REBCO coated conductor wire from the manufacturers.

2.3.5. Temperature dependency: $J_c(T)$

Several empirical models accounting for the temperature dependency of J_c was proposed by H. Fujishiro and T. Naito in reference [22] and W.K. Chan and Justin Schwartz in reference [23, 24]. Equation (1.6) shows a simplified expression for the temperature dependency of J_c, proposed by W.K. Chan in [20, 21].

$$J_c(T) = \begin{cases} 1, T \le T_0 \\ \dfrac{T_c - T}{T_c - T_0}, T_0 < T < T_c \\ 0, T \ge T_c \end{cases} \tag{2.6}$$

T is the temperature for each element in the superconducting (YBCO) layer, which is calculated through the thermal module. T_0 = 77 K is the starting temperature of the 2G HTS CC in the model, which is the same with the temperature of the surrounding liquid nitrogen, T_c = 92 K is the critical temperature, above which the HTS element totally losses its superconductivity. As the temperature increases, the critical current density drops. In real cases, the critical current density won't drop linearly with the temperature.

2.3.6. Mechanical strain dependency: $J_c(\varepsilon)$

The critical current densities will also be impacted by the internal mechanical strain due to external mechanical stress. The mechanical strain dependency of critical current density should be paid special attention in high field high magnet. For the high field superconducting magnet carrying high DC (direct current), the superconductors will bear a considerable Lorentz Force. This Lorentz Force sometimes causes huge mechanical strain, which will lead to a decrease of critical current density. Fig. 2.9 shows an example of a critical current density decrease of REBCO coated conductor caused by applied tensile strain. As the applied tensile strain increases, the critical current increases, and it reaches an irreversible mechanical breakdown when the strain increases up to around 0.74 %, seen in point G below [25].

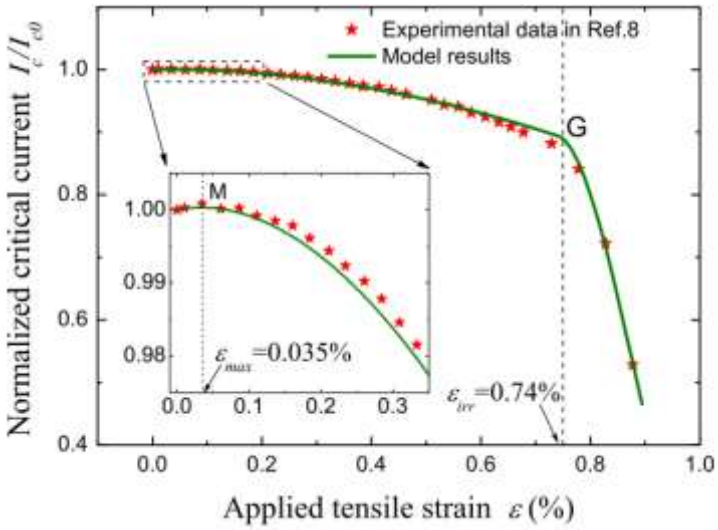

Fig. 2.9. Simulation results and experimental data for the strain dependence of normalized critical current for REBCO coated conductor wire [25].

2.3.7. AC loss

Most superconductors commonly work in DC applications to generate a persistent DC magnetic field. In the DC working mode, the zero-resistance characteristic of the superconductors is well utilized. However, in some real applications, the superconductors are inevitably subjected to an AC external background magnetic field, for example, HTS motors and generators. The superconductor will be no-longer a zero resistance conductor, and a dissipative loss will be generated, which we call “AC loss”. The AC loss in the superconductors consists of two main categories: magnetization loss and transport loss [26].

Magnetization loss is due to an applied AC magnetic field, which can be split into three subcategories: hysteresis loss, eddy current loss, and coupling loss. Hysteresis loss arises from the irreversibility of the flux pinning process and can be described by an M-H curve in Fig. 2.10. The energy loss per cycle is equal to the area enclosed by the loop and Fig. 2. 10 shows that loss per cycle is relatively constant with varying frequency. Eddy current loss arises in a similar way to normal conductors in that a changing magnetic field will produce an eddy current inside a conductor, which causes an eddy loss in the metal layers of the superconductors. Coupling loss arises from the interaction of multiple filaments of superconductors magnetically coupled together, which is also in a similar way to normal conductors.

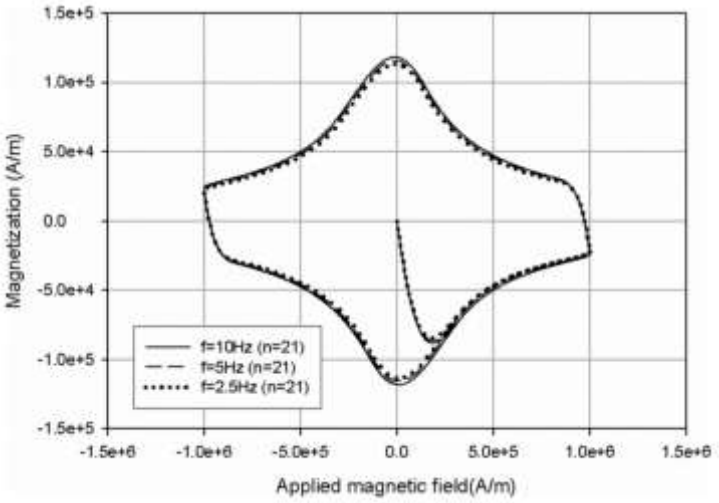

Fig. 2.10. M-H curve for a full cycle for a superconductor accounting for an E-J power law and field dependent Jc. Different field frequencies are applied, taken from [27].

Transport loss is due to the current flow in the superconductor, which can be split into two components: hysteresis loss and flux flow loss. Hysteresis loss is similar to magnetization loss, but the field is the self-field produced by the transport current rather than an external source. Flux flow loss arises from the motion of flux vortices caused by the Lorentz Force in the superconductors, which is already be presented in *E-J* power law in section 2.3.2.

There are several models for AC loss calculation. Norris [28] developed an analytical model for AC loss due to AC transport current under self-field. This model assumes that current density is independent of the magnetic field- which however is not correct, but makes the model simpler. Another form of AC loss arises from the interaction of a DC transport current and an applied AC field, which is known as “dynamic resistance” loss [29-35]. This dynamic resistance is very important in most superconducting application scenarios where the

superconductors carry a DC current and sometimes inevitably subjected to a large or small background field. Research on the field of AC loss will help understand and develop better conductors with low loss and heat dissipation. This dynamic resistance loss is very important in this thesis: The flux pumps and power switches are developed on this fundamental physics.

2.4. Development of superconductors

Fig. 2.11 shows a timeline showing the development of different superconducting materials and their critical transition temperature [36]. Each color and symbol represent a different family of superconductors. With the current development of the superconducting materials, researchers all over the world are still working on several important challenges and aspects: including developing a microscopic theory for high temperature superconductivity, studying the topological states of the matter [37] for the superconductors, developing and discovering new materials with a higher transition temperature higher than 200 K at high pressure [38], developing new superconductors with a good combination of practical physical properties such as MgB_2 [39] and iron-based superconductors [40], which as promising for future applications.

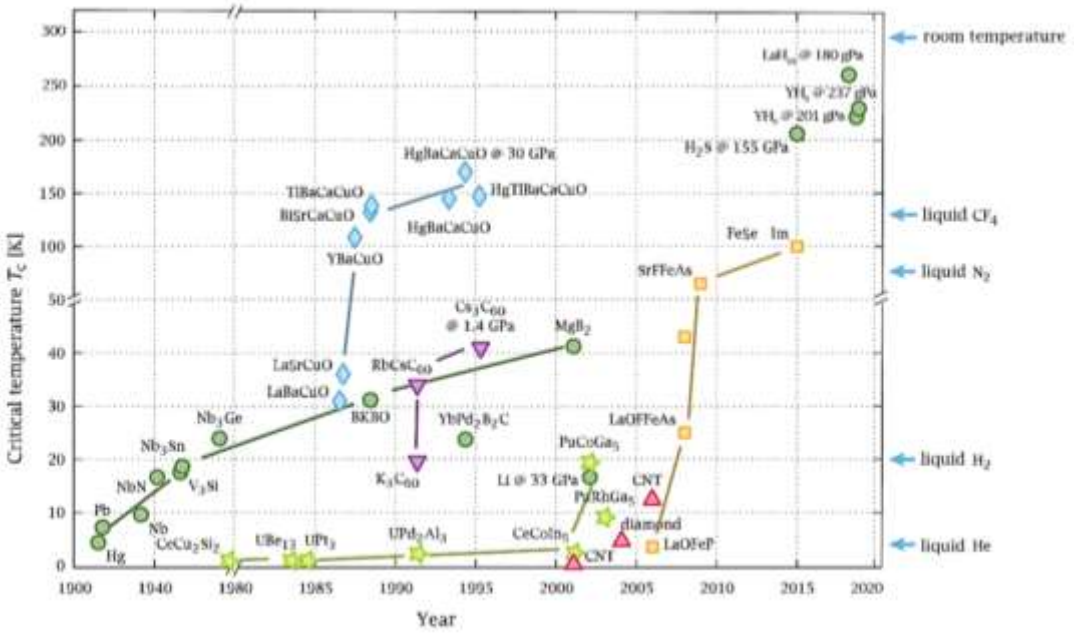

Fig. 2.11. Timeline showing the development of different superconducting materials and their critical transition temperature. Each color and symbol represent a different family of superconductors. Take from [36].

There is a wide and growing range of superconducting materials as shown in Fig. 2.11, and this means that there are many options for making practical commercial superconductors. The high temperature superconductors (HTS) were first discovered in 1986, and have proven to be

a promising potential replacement for their low temperature counterparts, the low temperature superconductors (LTS). The HTS material exhibit superconductivity at a practically realizable much higher temperature. This section gives an overview of the major superconductors currently in use and under fast development.

2.4.1. LTS conductors

According to the critical temperature (T_c), superconductors can be categorized into low temperature superconductors (LTS) and high temperature superconductors (HTS). A superconductor is defined as a low temperature superconductor if its Tc is below 30K, otherwise, it is defined as a high temperature superconductor. NbTi and Nb_3Sn are two main LTS conductors.

NbTi is by far the most widely used superconductor in the commercial superconducting applications, for example, MRI magnets [41], particle accelerator magnets [42, 43], and magnetically confined nuclear fusion reactors [44]. It has a critical temperature of around 10 K, an upper critical field of around 15 T, and a good critical current density. It is also affordable and can be manufactured into long length conductor wire, making it appropriate for most applications. Around 80% of NbTi is used in MRI systems with other significant applications in particle accelerators and fusion reactors.

Nb_3Sn has a critical temperature of around 18K and an upper critical field of around 30 T. This makes it suitable for high field applications, such as high field NMR magnets [45, 46]. Nb_3Sn will be used in the central solenoid and toroidal field coils in the ITER fusion reactor [47-50] and the dipole magnets in the large hadron collider (LHC) [51-53].

2.4.2. First generation HTS conductors

The first generation of commercial HTS conductors is BSCCO conductors, which has a critical temperature of 115K. Fig. 2.12 is a plot shows the transverse cross-section of a BSCCO conductor. The BSCCO conductor wire is generally made into a multi-filament structure [54]. BSCCO conductor is manufactured via a “powder-in-tube” method since it is a brittle ceramic. Power BSCCO is placed in a tube made from silver metal and then extruded along the wire length direction. The conductor is then processed and reacted at high temperature to form the final superconducting tape [55]. The BSCCO conductor was largely abandoned with the fast development of second-generation HTS conductor. But with the advancement of processing

techniques, the engineering current density is becoming higher. These BSCCO conductors are still attractive to some extent due to their low anisotropy and good high-field performance at a very low temperature.

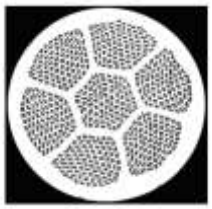

Fig. 2.12. The transverse cross-section of a BSSCO conductor wire with multi-filaments at 0.8 mm diameter, taken from [54].

2.4.3. Second generation HTS conductors

The second generation of commercial HTS conductors is the REBCO (Rare Earth Barium Copper Oxide) coated conductors, which has a critical temperature of 93K. Fig. 2. 13 shows the diagram of the REBCO conductor structure and layer composition [56].

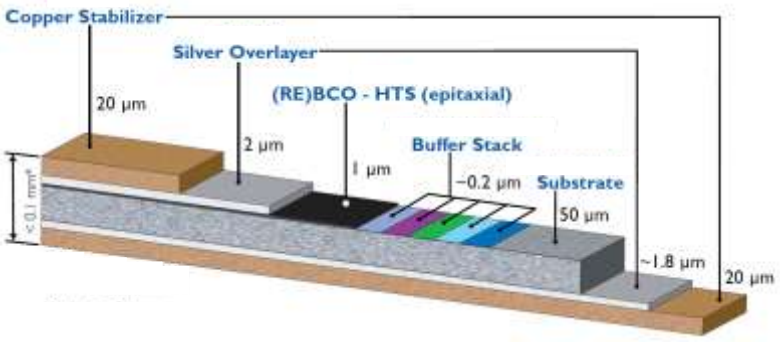

Fig. 2.13. Diagram of REBCO coated conductor structure and layer composition. The thickness of superconducting REBCO layer is around 1 µm. Taken from [56].

The REBCO conductor is manufactured in a multilayer structure, including a high temperature superconducting REBCO layer with 1 μm thickness, a substrate layer made of Hastelloy (50 μm), a buffer layer (0.2 μm), two silver overlayers (2 μm), and two copper stabilizer layers (20 μm). The REBCO layer is a single crystal grown on the substrate layer and coated with normal conductors, so it is also called “HTS coated conductors”. REBCO coated conductors are expensive to manufacture and this coated multilayer structure sacrifices engineering current density to provide HTS in a form that can be used by engineers and

customers. All present high temperature superconductors (HTS) are type-II superconductors, including the REBCO conductors and BSCCO conductors.

Compared with the first generation HTS BSCCO conductors, the REBCO conductor has an excellent critical current performance under the high field, a stronger mechanical property, a lower price, and requires no heat treatment. Due to these advantages, the REBCO coated conductors are widely used in many superconducting applications, such as high field magnets [57-60], MRI magnets [61-63], fault current limiters [64, 65], superconducting motor and generators [66, 67], and superconducting power cables [68-71]. REBCO conductors are currently under researches to a broader range of future applications, such as fusion tokamak [3], and particle accelerator magnets, and magnetic levitation high-speed strains. In 2019, a compact superconducting magnet containing a 14.4 T HTS REBCO magnet in a background field of 31.1 T broke the highest field world record at 45.5 T [2], which highlighted the capabilities of the second-generation HTS REBCO coated conductors.

Bulk REBCO HTS superconductors are grown as single crystals into small cylinders [72, 73]. Because the entire sample is superconducting, bulks can achieve high fields up to 17.6 T in a small volume due to high engineering current density [74]. It can be used to design compact and portable HTS devices, such as small MRI systems. However, the HTS bulk superconductors are not suitable for large field coil magnets or other components used in the cables, or power systems, because the bulk geometry limits their application scenarios.

2.5. Applications of superconducting magnets

The unique properties of superconductors make them very promising in many magnet applications. This section reviews the major applications for superconducting magnets, including healthcare devices magnetic resonance imaging (MRI), clean energy devices tokamak fusion magnets, particle accelerators, and high-power-density electrical machines. Most commercial applications currently use LTS conductors due to the low cost and highly mature technologies and manufacture. However, the fast-developing HTS conductors are demonstrating huge potentials due to the significant advantages and the reducing prices.

2.5.1. Magnetic resonance imaging

The magnetic resonance imaging (MRI) magnet is currently the biggest commercial market for the superconductors. The MRI system is widely used in healthcare and medical domain. MRI is based on nuclear magnetic resonance (NMR) technology, which gives scientists information about the molecular structure of materials. NMR is crucial for physical chemistry and many applied science fields. Fig. 2.14 shows a schematic view of an MRI system [75]. To achieve MRI, a background magnetic field is provided by using a superconducting magnet, the resonant frequency is dependent on the strength of the magnetic field. A higher resolution requires a higher field strength. Compared to resistive magnets, the superconducting magnets can achieve a very stable high field strength in a compact size with a very low resistive loss. Current commercial MRI magnets are manufactured by LTS conductors. But, scientists and engineers are researching on making MRI magnets by using HTS conductors due to their high critical current density under the high field. Plenty of valuable research has been done by the Francis Bitter Magnet Lab at MIT [61-63, 76]. At the University of Cambridge, two research groups led by Dr. Tim Coombs and Prof. David Cardwell are working on portable compact MRI systems by using the HTS REBCO coated conductors [77] and HTS REBCO bulk conductors [78] respectively.

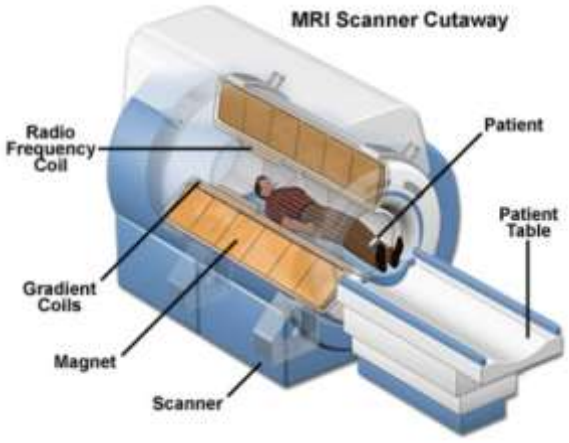

Fig. 2.14. Schematic view of an MRI scanner, taken from [75].

2.5.2. Magnetic confinement nuclear fusion

The superconductors are crucial for making the high field magnets for the magnetic confinement nuclear fusion devices. Nuclear fusion is the process of combining lighter elements from heavier ones. This process helps maintain the sunshine from the sun, which is

a form of the energy output of stars, where two hydrogen atoms fuse to form helium and release a huge amount of energy. Scientists are working on creating a controllable nuclear fusion process for providing limitless electricity. The tokamak is such a kind of device used to help scientists achieve controllable fusion energy. Fig. 2.15 shows a schematic view of a tokamak fusion device [79]. Tokamaks hold high temperature high energy plasmas in a vacuum with strong magnetic fields. The strong magnetic field is provided by an array of superconducting toroidal field coils. Scientists used to use the LTS conductors to manufacture the superconducting field coils in the ITER [80], however, the developing speed is quite slow and the cost keeps increasing and now far beyond its original budget. In recent years, scientists proposed a compact and economical Tokamak design by using HTS conductors and some small demos have been successfully developed [81-87]. The compact fusion use presents an impressively large potential market for the REBCO magnets.

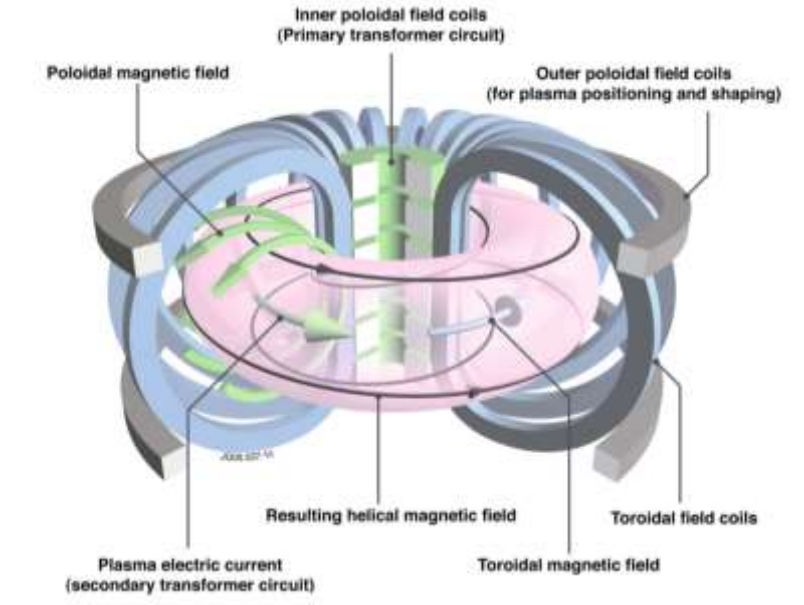

Fig. 2.15. Simplified schematic view of a tokamak fusion device, taken from [79].

2.5.3. Particle accelerator

Scientists use the very high energy particle accelerators to understand matter and the universe. Particle accelerators use magnetic fields to accelerate particles such as protons or electrons to high energies. Particles are accelerated to extremely high energies to collide with each other, and their behaviors are observed in these extreme conditions. To increase the final energy of the particles, the radius of the particle's path must increase or the magnetic field strength must increase. High field superconducting magnets help make accelerators in a

compact size. Fig. 2.16 shows a schematic view of the particle accelerator in Fermilab [88]. Its main accelerator complex comprises four particle accelerators and storage rings - the Linac, Booster, Recycler and Main Injector - the last of which produces the world's most powerful high-energy neutrino beam and provides proton beams for various experiments and R&D programs [88].

Fig. 2.16. Schematic view of the particle accelerator in Fermilab, taken from [88].

Another application of particle accelerators is for targeted radiation therapy, such as cancer tumors therapy. A more compact kind of particle accelerator, known as cyclotrons, is used to produce proton beams to kill the target cancer tumor [89]. One important advantage, compared to conventional x-ray radiation therapy, is protons do not penetrate as deeply into the tissue, and patients typically have fewer and less severe side effects. The particle accelerators used in proton therapy are increasingly using superconducting magnets, to help achieve a lighter, smaller, and cheaper systems [90].

2.5.4. Generators and motors

The superconducting generators and motors use the superconducting magnet to generate a higher field density compared to using the permanent magnets. Higher field density means a higher power density and a compact size. The weight and size are important for

some application scenarios such as wind turbine [66, 67, 91] and future hybrid-electric aircraft propulsion system [92].

Wind turbine size has grown significantly over recent decades. However, today's technology has trouble keeping up with this trend towards ever-increasing unit power levels. Adopting superconducting coils will enable a high-power-density low-weight generator. The EU H2020 EcoSwing project is working on the design, development, and manufacture of a full-scale 3.6 MW DD HTS generator, installing and operating it in an existing turbine [91]. Fig. 2.17 shows a schematic view of a superconducting wind turbine generator adopting HTS REBCO magnets. To reduce the AC loss, the superconducting magnets usually placed in the rotor.

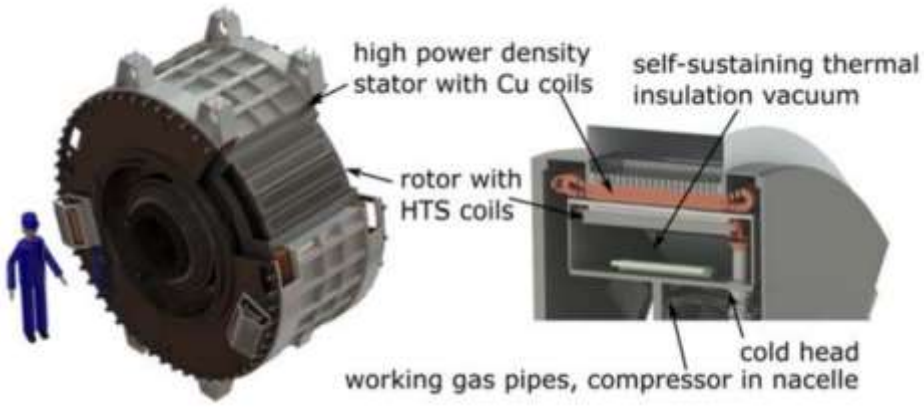

Fig. 2.17. A schematic of the EcoSwing superconducting generator, taken from [91].

The reduction of emissions is a key goal for the aviation industry. One enabling technology to achieve this goal could be the transition from conventional gas turbines to hybrid-electric propulsion systems. A prerequisite for short-range aircraft with hybrid-electric propulsion systems is that electric components such as electrical machines can meet the ambitious weight and efficiency requirements for this application. A potential technology is using the electrical machines built by HTS conductors [92]. While the best permanent magnets can have a magnetization of up to 1.3 T, superconducting coils made from HTS-tapes or magnets made from bulk HTS material can produce magnetic field densities up to 14 T [93] at their surface. Further, current densities over 200 A mm^{-2} can easily be achieved in HTS tapes or MgB_2 wires [94]. As the gravimetric power density of electric machines scales linearly with the magnetic field density in the air gap and the stator current loading, a compact size and a lightweight seem to be feasible.

2.6. Superconducting magnet technology

Superconducting magnets are key components in the superconducting devices. A superconducting magnet is a highly stressed device, which requires the best engineering to ensure reliable and economical operations. It is an interdisciplinary subject which requires knowledge in many fields: mechanical, electrical, cryogenic, and materials [95, 96].

Due to the high critical current under high fields, the strong mechanical property, and the high operating temperature of the HTS REBCO coated conductors, the HTS REBCO magnet has become the ideal candidate that can generate very high magnetic fields and operate at a higher temperature. HTS REBCO magnets become the ideal option for high field magnet systems because they are compact, robust, and capable of carrying large currents in high magnetic fields. Recently, the National High Magnetic Field Lab in the USA reported the world's highest DC magnetic field of 45.5 T, which was generated with a 14.4 T no-insulation HTS REBCO coil inside the bore of a 31.1 T resistive magnet [2]. The Francis Bitter Magnet Lab at MIT is also developing a 1.3 GHz NMR magnet project [97, 98], which requires a magnetic field strength of 30.5 T and uses the no-insulation type REBCO magnets. These high-field devices can only be built by using HTS REBCO magnets.

This section reviews important topics of the HTS magnets technology, including the detection and protection of thermal quench, mechanical reinforcement, no-insulation magnet technology, and persistent current mode.

2.6.1. Quench detection and protection

The superconducting magnet can be damaged by the thermal local hot spots due to the huge joule heat. The minimum quench energy (MQE) for LTS magnets is small, any subtle mechanical and thermal disturbance can lead to the quench of LTS magnets. This unstable property is a limitation towards a broader and more challenging application for LTS. In contrast, HTS magnet is more stable under mechanical and thermal disturbance because the MQE of HTS conductors is larger than LTS conductors. It leads to a broader application of HTS magnets. However, one remaining obstacle for the implementation of high temperature superconducting magnets into the system is the inability to rapidly detect a quench. The reason behind this is that the HTS conductors have a very slow normal zone propagation velocity (ZNPV), compared to LTS conductors. The quench of LTS magnets can be quickly detected by the fast voltage increases via the voltage taps across the magnets terminals. However, for

the HTS magnet, monitoring the voltage across the magnet taps is not effective because the quench and burn-out of the hotspot are developing much faster than the voltage rise.

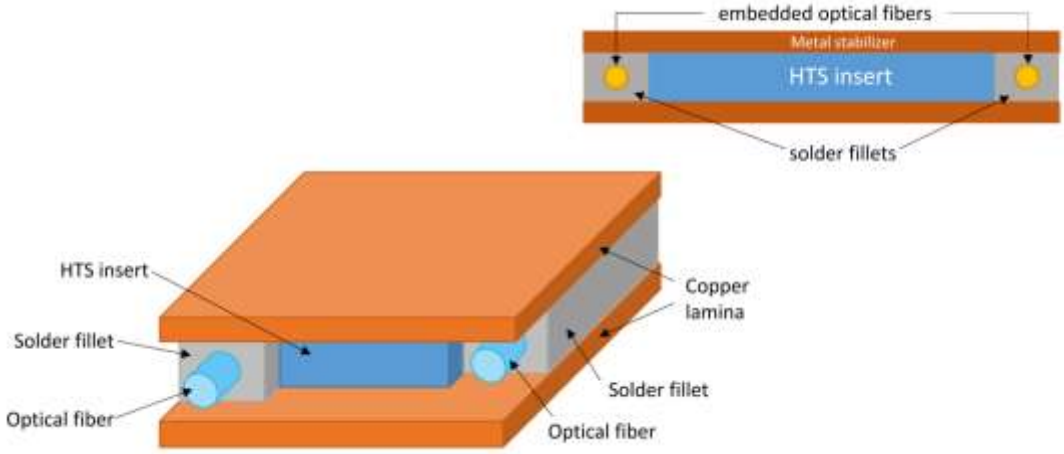

Cross-sectional drawing of the SMART REBCO conductor

Fig. 2.18. Schematic draw of the self-monitoring SMART REBCO conductor using optical fibers [102].

To monitor the temperature rise of the HTS magnets, a novel quench detection technology based on optical fibers has been proposed [99-102]. This detection technology has significant advantages over the traditional techniques, including very high spatial resolution and the ability to detect a hotspot well before the peak local temperature exceeds the current sharing temperature. Based on the quench detection system, the superconducting magnets will be cut off from the power supply if a hotspot is detected. The quench detection and protection technology is very important for the large-scale industrial superconducting applications.

2.6.2. Mechanical reinforcement

The mechanical damage is a significant problem for superconducting magnets. A typical 10 T magnet is subjected to an equivalent magnetic pressure of 40 MPa (nearly 400 atm) [95]. The operation in high fields at high current is sometimes not satisfied. The superconducting magnet can be damaged by the irreversible mechanical strain or the slitting damage due to the huge Lorentz Force [2, 103-105]. The risk of mechanical breakdown will be significant when the superconducting magnets are operating in the high-field high-current mode. High field magnets should be reinforced by extra mechanical support.

The mechanical characteristics in LTS conductors have been widely studied over the past decades [106-110]. Compared to LTS conductors, the HTS conductors, especially REBCO coated conductors, demonstrate much lower strain sensitivity with respect to the current

transport property and intrinsic higher tensile tolerance exceeding 600 MPa [111]. The excellent critical current performance under high magnetic field and the strong mechanical property of REBCO coated conductors enable scientists to fabricate more powerful superconducting magnets with ultra-high field density and compact construction [2]. A 32 T all-superconducting user magnet was constructed at the national high magnetic field laboratory (NHMFL) in 2017, and a new 40 T all-superconducting user magnet has been launched and currently under construction [105]. Under such high field and high operating current conditions, an excellent mechanical performance is super important for achieving a reliable magnet system.

Fig. 2.19. The mechanical deformation at the edges of the REBCO conductors after test in a high field test coil for the 40 T superconducting magnet project at the National High Magnetic Field Laboratory (NHMFL), taken from [105].

Fig. 2.19 shows a mechanical deformation at the edges of the REBCO conductors after test in a high field test coil for the 40 T superconducting magnet project at the NHMFL [105]. Mechanical stress due to screening current induced in HTS REBCO tape conductors will lead to reduced performance and lifetime of the superconducting magnet. The prediction and estimate of the mechanical stress and strain distribution are important, which helps understand the breakdown mechanism and optimize the magnet design and mechanical reinforcement. Scientists are currently working on mechanical analysis by using mechanical-electromagnetic coupled multi-physics modeling for the high field HTS magnets [111]. They found that varying magnetic field induced “screening current” significantly increases the peak value of mechanical stress and strain, and this problem could be alleviated by using multi-filamentary conductors.

2.6.3. No-insulation and self-protection

Most superconducting magnets are fabricated with turn-to-turn insulation layers. HTS conductors are known to have slow normal zone propagation velocity (NZPV) [112]. This NZPV in HTS is observed in the order of meters per second, whereas NZPV in LTS is in the order of centimeters (cm) per second. For the HTS magnets, a significant challenge is that the hotspot is not easy to be detected because the rise of voltage is not detected fast enough to prevent the damage. As a result, burnout will be developed at a local hotspot, which is shown in Fig. 2.20.

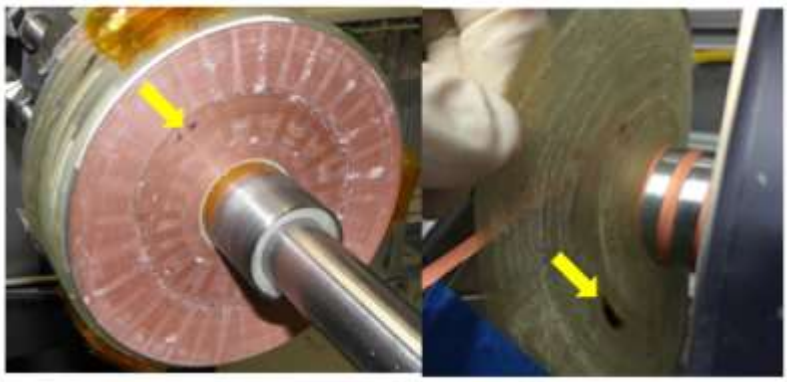

Fig. 2.20. Hot spot damage caused by the quench of HTS magnets, taken from [113].

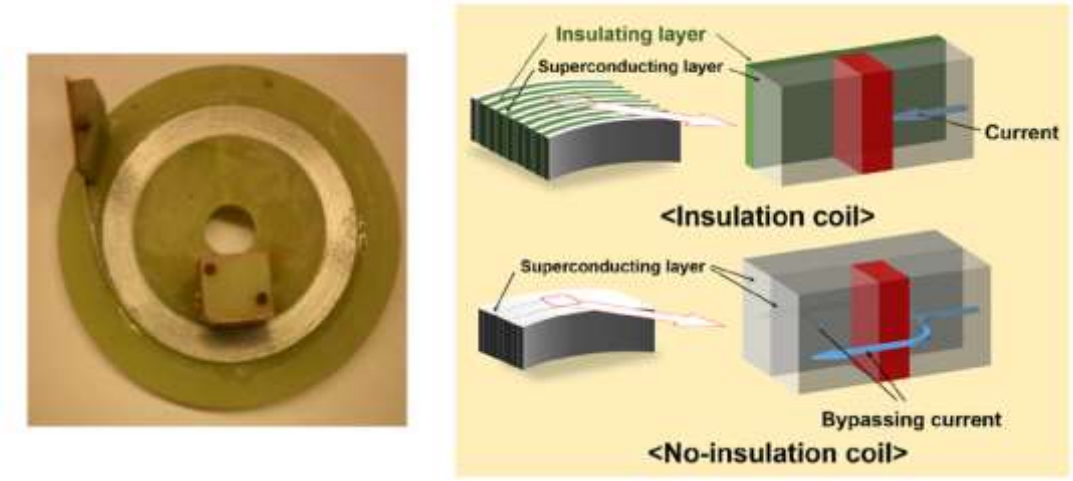

(a) (b)

Fig. 2.21. (a) (left) Picture of the no-insulation HTS REBCO coils, proposed by Hahn in 2011 [1]. (b) (right) The self-protecting ability of no-insulation HTS magnets. The absence of insulation in no-insulation winding allows current sharing between turns which in turn allows bypass of the defective zone and prevents a coil from localized hot spot heating, taken from [2, 113].

To solve this problem, Hahn proposed a novel HTS superconducting magnet without turn-to-turn insulation in 2011 [1]. This novel no-insulation type HTS REBCO magnet has gained great popularity in recent years due to its significantly improved reliability, compared to its counterpart "insulated HTS magnet". Fig. 2.21 (a) shows a picture of the no-insulation HTS REBCO coils. One significant advantage of the no-insulation HTS magnets is the self-protection ability [2, 114], which solves the long-standing hotspot damage problem. It means the transport current would automatically find its path of least resistance from end to end due to the absence of insulation. The absence of insulation allows current sharing between turns, which allows current bypass at the defective zone and prevents a coil from localized hotspot heating. The self-protecting ability makes the superconducting magnets highly reliable.

The no-insulation HTS magnet technology has facilitated the progress of high-field magnets, increasing the field strength from 7 T to 32T, and recently to a new world record of the strongest field strength at 45.5 T in 2019 [2]. The no-insulation HTS REBCO magnets show significant potentials in many industrial applications, such as tokamak fusion devices, MRI system, and ultra-high-field magnets for multidiscipline fundamental researches.

However, one side effect of the no-insulation HTS magnet is the slow charging speed [115]. In the equivalent circuit model of the no-insulation HTS magnets [1], there are three components: L_{coil} (inductance of HTS magnet), R_θ (azimuthal resistance including index loss and matrix resistance of HTS wire), and R_c (radial resistance including contact, insulation, and substrate resistances). The slow charging is caused by the turn-to-turn current bypass phenomenon, due to the absence of turn-to-turn insulation layers. To improve the charging speed, many variants of the no-insulation HTS magnet have been proposed, including HTS magnets with partial insulation [116], HTS magnets with metal insulation (MI) to increase the characteristic resistance [117, 118], HTS magnets with a graded-resistance method to achieve rapid and passive recovery of the NI coil [119], HTS magnets with "smart" insulation materials whose resistivity can change with the temperature rise [120], and so on. The core idea is to increase the R_c in the equivalent circuit, but keep the self-protection ability at the same time.

2.6.4. Persistent current mode

Existing superconducting magnets use DC supplies to drive current into the magnets. The DC power supplies are bulky, expensive, and heavy. DC power supplies work at room temperature but are connected to low temperature superconducting magnets via the thick

copper current leads, both in the charging mode and the normal constant operation mode. This means that the current leads introduce significant heat flow into the cryogenic superconducting magnets and greatly increase the work load on the cooling system.

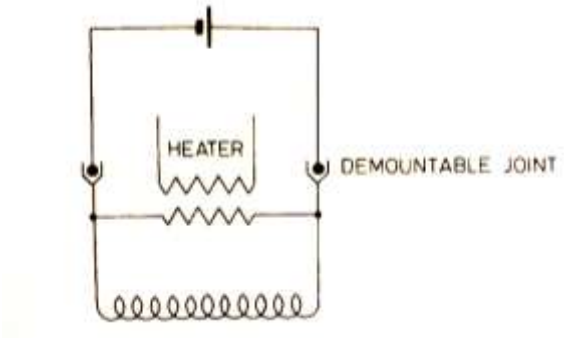

Fig. 2.22. Magnetic circuit with a persistent current switch and demountable current leads [121].

The LTS magnets are widely used in commercial MRI systems because they can operate in a persistent current mode because of the availability of the LTS superconducting joints. A persistent current switch (PCS) [121] as shown in Fig. 2.22 is used to charge the LTS magnets after a long period of working time. The PCS can help effectively remove the DC power supply from the superconducting magnets during the constant operation, and connect the magnets to the power supply again when the field needs compensation. An LTS PCS is usually a section of LTS conductor that is able to switch on and off between resistive state or superconducting state by a heater. When the PCS is in the resistive state, a DC voltage is generated across the PCS and used to charge the superconducting magnets. The LTS magnet can work in a persistent current mode for a very long time until the next field compensation.

However, one long-lasting problem has significantly impeded the widespread uptake of HTS coil technology: the HTS magnet cannot work in persistent current mode without the external power supply [122] because the lossless HTS joints cannot be fabricated due to the multi-layer structure of coated conductors. The joint resistance causes non-negligible current decay in the closed-loop HTS magnet circuit. So, HTS magnets are normally operated in open-loop mode, driven by an external electronic power supply via a pair of metal current leads. These current leads generate considerable heat load on the cryogenic system and the heat transfer makes the magnet less stable. It is very desirable to eliminate the current leads from the magnet and operate HTS coils in a closed-loop mode in a closed cryogenic environment.

One possible solution is to employ a cryogenic rectifier [123]. A high alternating current is induced in a closed cryogenic circuit and then rectified by diodes, MOSFETs, or other

switching elements that are located within the cryostat. Although these cryogenic rectifiers have managed to remove current leads, the on-state resistance of semiconducting electronic components is too high, so that the heat generated by the electronic switches in the cryogenic system is a major problem.

Another alternative solution is to use HTS flux pumps [124-133]. Flux pumps are superconducting devices that can inject flux into a closed superconducting circuit without physical electrical contact. Current HTS flux pumps are constructed by using HTS conductors and can be classified into two major types: traveling-wave flux pumps and transformer rectifier type flux pumps. Travelling-wave flux pumps include linear electromagnet flux pumps [124, 125] and rotating permanent magnets based flux pumps (HTS dynamos) [126-130]. Transformer-rectifier type HTS flux pumps [131-133] are similar to cryogenic rectifiers but employ different switching physics which is induced by flux motion in superconductors. This means that in their 'on-state' they are fully superconducting (zero resistance).

HTS flux pumps show many advantages over conventional DC power supplies by removing the current leads. Firstly, the wireless link providing thermal isolation between the cryogenic superconducting magnet and the room temperature external power supplies. Secondly, the wireless link also provides mechanical isolation between magnet and power supply, which is very useful in some applications such as rotating machines. Thirdly, the high current requirement of superconducting magnets can be difficult to achieve via conventional power supplies and flux pumps can be a more efficient and compact solution. Fourthly, flux pumps also provide the ability to operate on a "demand" basis. The flux pumps can be turned off if the HTS magnets have been pumped to its operating mode, because the flux pumps are not physically connected to the superconducting magnets. The HTS flux pumps have huge potentials in enabling efficient, economical, and compact superconducting magnet systems.

The HTS flux pumps have gained a rising interest in the field of applied superconductivity in recent years, and our next chapter gives a detailed review of this technology.

Chapter 3
Development of Flux Pumps

The concept of flux pumps was firstly proposed for LTS magnets by using LTS conductors several decades ago [134, 135]. However, due to the availability of lossless superconducting LTS joints and persistent current switches for LTS magnet systems, and the extra complexity of the flux pump system, these LTS flux pumps haven't been widely employed. In recent years, HTS magnet technology has been developing very fast due to the advance of HTS REBCO coated conductors. However, lossless HTS joints are still not available due to the multi-layer structure of REBCO coated conductors. HTS magnets working in persistent current mode must be charged by an external power supply via a pair of thick metal current leads. However, these current leads generate considerable heat load on the cryogenic system. As a result, the cooling capacity of the cryogenic system places limits on the achievable current capacity and energy density of the magnets. This heat ingress also makes the magnet less thermally-stable and less reliable. In this case, the HTS flux pump becomes an ideal solution to eliminate the current leads from the HTS magnet system and enable HTS magnets to operate in a closed-loop mode within a closed cryogenic environment. Due to these advantages, the HTS flux pump technology has attracted increasing attention recently. This chapter reviews the origin and progress of flux pump technology, including the LTS flux pumps and LTS flux pumps.

3.1. Concept of flux pumps

The concept of flux pumps has been proposed for many decades and the flux pump was firstly developed by using LTS conductors. A comprehensive review of LTS flux pumps was published in 1981 by Van Der Klundert and Ten Kate [134, 135]. The basic principle of flux pumps is shown in Fig. 3.1.

A time-varying flux (dΦ/dt) is produced from an external source in the left-hand loop of a two-loop circuit. This could be from any source such as a moving permanent magnet or an electromagnet. The changing flux gives rise to a positive (clockwise) EMF around the left-hand loop. If the circuit switch S2 is in a high impedance state and circuit switch S1 is in a zero-impedance state, the EMF in this cycle is dropped across S2. This will lead to a flux migration across S2 and an increase in the current through load *L*1. In the second half-cycle, a positive dΦ/dt gives rise to a negative (counter-clockwise) EMF in the left-hand loop. Now S2 is in zero-impedance, S1 is in high impedance and the EMF is dropped across S1 and S2 shorted the load *L*1. Over a full cycle, this leads to a net DC voltage developed across *L*1. Note that the circuit switch S1 and S2 do not have to present an open circuit to achieve the flux pumping, they merely need to change their impedance synchronously with the induced EMF in the left-hand loop.

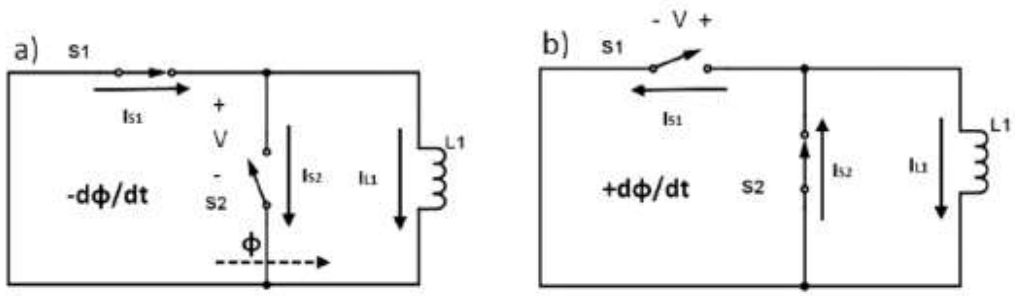

Fig. 3.1. The basic circuit of a flux pump [136]. (a) First half cycle, (b) second half cycle.

Based on the same fundamental concept, different implementations were developed for the last decades, including the DC dynamo flux pumps, transformer rectifier flux pumps, and automatic switching flux pumps. These different implementations can be classified into two categories: LTS flux pumps and HTS flux pumps.

3.2. LTS flux pumps

The flux pumps were originally based on LTS conductors and developed for LTS magnets. All LTS flux pumps are developed from the same concept in Fig. 3.1, but adopted different specific designs.

3.2.1. LTS DC dynamo flux pump

The LTS DC dynamo flux pump using a permanent magnet moving across an LTS superconducting plate or loop, to generate a varying flux (dΦ/dt) in the left-hand loop and create two switches S1 and S2 with varying resistance. Fig. 3.2 gives an example of an LTS DC dynamo flux pump [134].

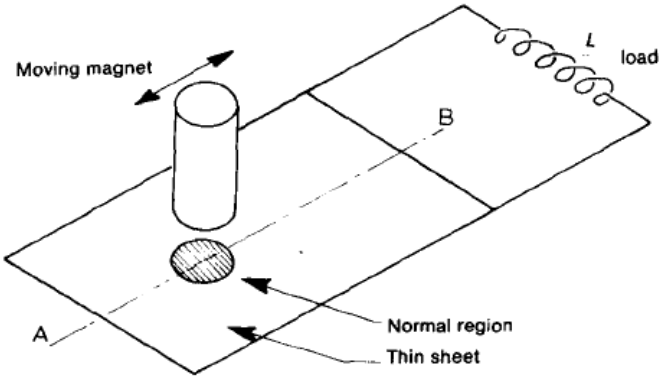

Fig. 3.2. Schematic drawing of an LTS DC dynamo flux pump, taken from [134].

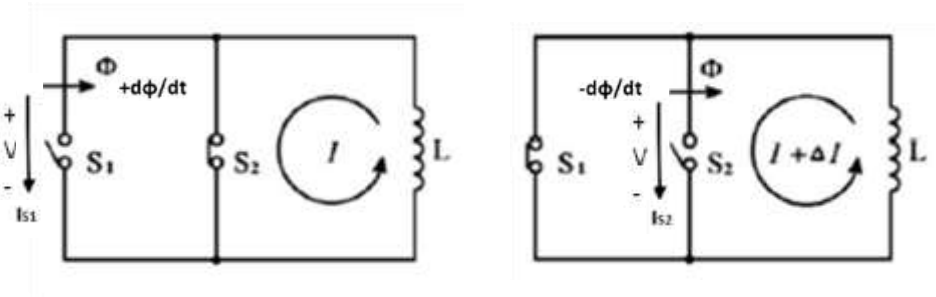

Fig. 3.3. The fundamental mechanism of the LTS DC dynamo flux pump.

The moving permanent magnet produces a moving normal or resistive spot in the superconducting plate due to the field sensitivity of the superconducting material. Fig. 3.3 shows the fundamental mechanism: S_1 and S_2 are LTS switches, and L is a superconducting load. When a permanent magnet moving towards the center of an LTS superconducting plate, an amount of external flux Φ is approaching, S_1 is off (in the resistive state) and S_2 is on (in the zero-resistance state) so that the S_2 short the EMF generated on S1 and the load current I pass through S_2, as shown in the left figure. When the permanent magnet moving away from the center of an LTS superconducting plate to the right-hand side, S_2 is off (in the resistive state) and S_1 is on (in the zero-resistance state), and the amount of total flux Φ in the left-hand loop is decreasing so an EMF is generated on S2. This EMF on S2 will charge the load L and

cause a net flux flow on S2 from the left-hand side to the right-hand side. As a result, a net amount of current increase ΔI is induced in the load.

These moving permanent magnets can be replaced by a traveling magnetic wave generated by a set of stationary copper windings as well [134].

3.2.2. LTS transformer rectifier flux pump

For the DC dynamo flux pump, the moving permanent magnet acts as both a source of varying flux ($d\Phi/dt$) in the left-hand loop and control of two switches using the field dependency of the LTS conductors. For the transformer rectifier flux pump (TRFP), the generation of flux and control of two switches are separated. The varying flux ($d\Phi/dt$) in the left-hand loop comes from a transformer. The two switches S1 and S2 are controlled separately to achieve variable resistance, enabling the current rectification. Fig. 3.4 shows the circuit of TRPF [134]. The resistance of the switches can be controlled by controlling the temperature via thermal pulses or by applying an external magnetic field.

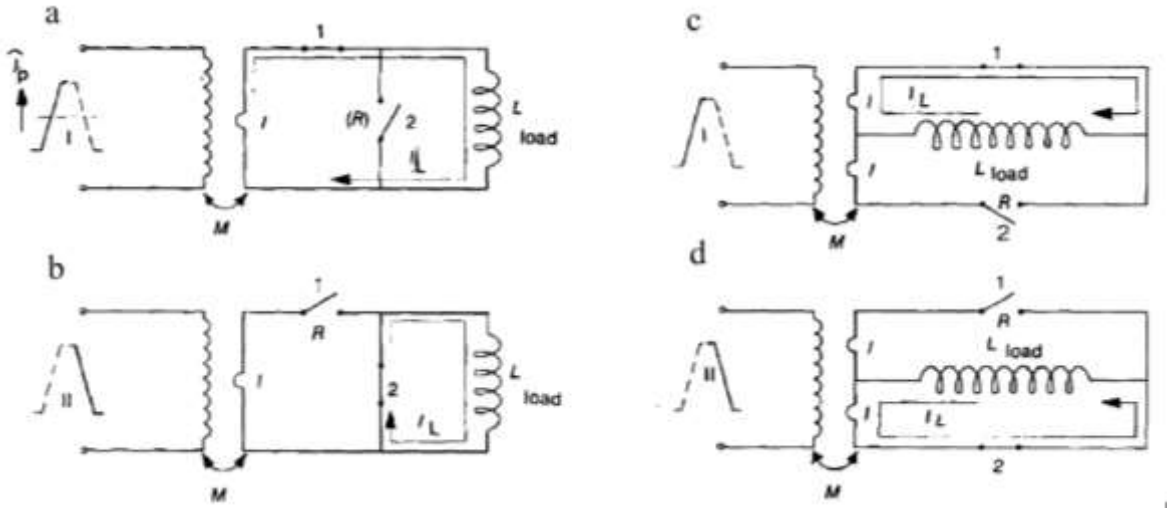

Fig. 3.4. The circuit view of the mechanism of TRFP: half-wave TRFP consists of (a) the first half-cycle and (b) the second half-cycle. Full-wave TRFP, (c) the first half-cycle, and (d) the second half-cycle. Taken from [134].

Many LTS TRFPs have been developed and some have operated in real applications. A thermally switched LTS TRFP was designed by Mulder [137] to deliver 100 kA and tested at 25 kA. Ten years of the successful operation of a TRFP for the detectors magnets of the CMD-2 detector on the VEPP-2M collider was reported by Barkov [138].

3.2.3. LTS self-switching transformer rectifier flux pump

Automatic switching flux pumps use automatic switches, which present an impedance by exceeding J_c [139]. Fig. 3.5 shows an example of the automatic switching flux pump [139]. A transformer is used to generate a varying flux and EMF in the load loop. In the load loop, a superconductor L_2 is connected in parallel to the load magnet L_1. In the first half cycle, I_s is lower than the I_c of L_2, so L_2 is in the superconducting state and no voltage is produced. In the second half cycle, I_s exceeds the I_c of L_2, L_2 is in resistive state and a DC voltage is produced across the load magnet L_1 and charge the magnet. The superconductor L_2 (R_2) works as an over-current switch. This type of flux pump has the advantage of requiring only very basic hardware with no dedicated switches and very simple control. However, this type of automatic switching flux pump is much less efficient than active switching TRFP (section 3.2.2) because of the high loss generated by the high simultaneous current and voltage produced by exceeding I_c. For the application scenarios where efficiency is less important than size and complexity, this automatic switching flux pump is very competitive.

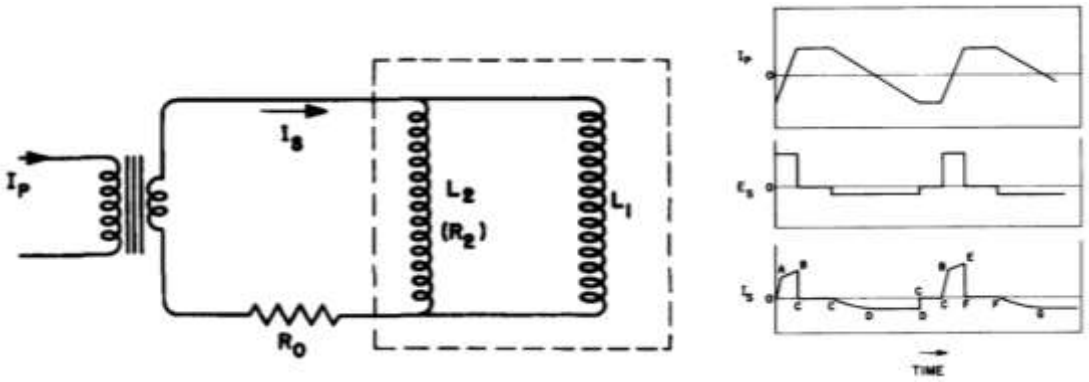

Fig. 3.5. Automatic switching flux pump, equivalent circuit and waveform [139].

3.3. HTS flux pumps

The HTS flux pumps were developed for HTS magnets and from the same fundamental concept presented in Fig. 3.1. The HTS flux pumps have gained rising interest due to the fast progressing HTS magnet technology in recent years. HTS magnets can operate over a broad range of temperature and magnetic field for industrial applications and have been proved to be the only solution for generating magnetic fields > 20 T. However, the lossless HTS joints cannot be practically fabricated due to the multi-layer structure of HTS coated conductors, which has been a long-lasting problem that has significantly impeded the widespread uptake

of HTS coil technology. It means that the HTS coils cannot work in the persistent current mode without an external power supply via a pair of thick metal current leads. However, these current leads generate considerable heat load on the cryogenic system. As a result, the cooling capacity of the cryogenic system places limits on the achievable current capacity and energy density of the magnets. Moreover, this heat ingress also makes the magnet less thermally-stable and less reliable. Under such circumstances, the HTS flux pumps [124−133] become an ideal solution to eliminate the current leads from the HTS magnet system and enable HTS magnets to operate in a closed-loop mode within a closed cryogenic environment.

3.3.1. HTS DC dynamo flux pumps

The HTS DC dynamo flux pump [126-130] is constructed by HTS conductors but follows the same fundamental structure and principles as the LTS DC dynamo flux pumps. The difference between HTS dc dynamo flux pumps and the LTS ones is that the moving magnets in the HTS DC dynamo flux pump don't have to drive the superconducting tape normal, so the moving field density is not required to be as high as the LTS DC dynamo flux pumps did. This is a potential advantage of the HTS DC dynamo flux pumps. Many explanations on the origin of DC voltage in the HTS DC dynamo flux pumps were reported recently [126-128, 140, 141].

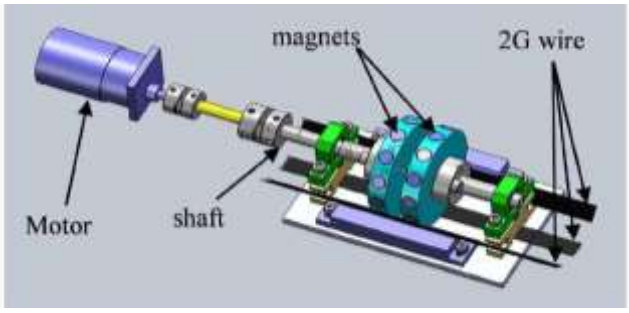

Fig. 3.6. HTS dynamo DC flux pump constructed by Hoffman in 2011 [126].

The first HTS DC dynamo flux pump was constructed by Hoffman [126] in 2011. The design of these devices is shown in Fig. 3.6, where several permanent magnets uniformly mounted on two discs are driven by a motor. Beneath the discs, HTS REBCO coated conductors are placed in parallel with the shaft and two ends connected to an HTS coil. When the magnets rotate above the REBCO tape, a DC voltage will appear across the REBCO tape and charge the HTS coil. Hoffman's HTS DC dynamo flux pump was able to pump a 2.7 mH HTS coil to its critical current of 49A in 112 seconds at 77K [126].

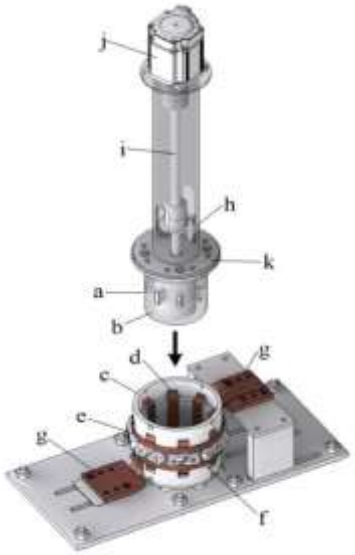

Fig. 3.7. A squirrel-cage HTS DC dynamo flux pump was constructed by Kent Hamilton in 2018 [129]. The illustration of disassembled test hardware showing: a. rotor with permanent magnets; d. superconducting stator parallel-connected REBCO tapes; j. Drive motor.

In 2018, a novel squirrel-cage HTS DC dynamo flux pump was constructed by Kent Hamilton [129], as shown in Fig. 3.7. This flux pump shares the same mechanism of DC dynamo flux pump constructed by Hoffman but exhibits an output capability of ~1.3 kA. This dynamo flux pump offers a practical feasible route to kA-class portable HTS magnet systems.

3.3.2. HTS linear travelling wave flux pumps

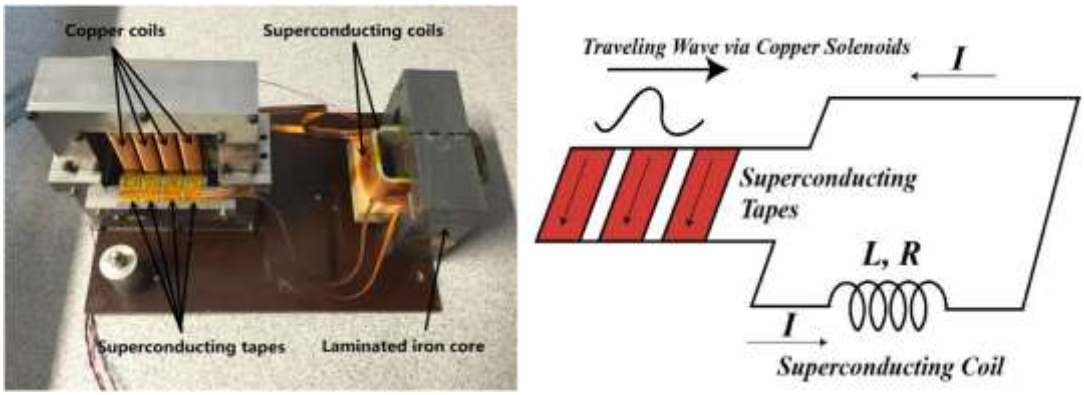

(a) (b)

Fig. 3.8. A linear travelling wave HTS flux pump and its working principle [125].

HTS linear traveling wave flux pumps [124, 125] uses multi-phase windings to generate an electrical controlled traveling magnetic wave to magnetize the HTS magnets. Fig. 3.8 shows

a linear traveling wave HTS flux pump and its working principle [125]. When the traveling wave travels across a series of superconducting tapes, a DC voltage is generated to charge the HTS coils. The mechanism is the same as the DC dynamo flux pumps. Compared to DC dynamo flux pumps, the linear traveling flux pumps give greater flexibility, because the field density and shape can be controlled flexibly by the electromagnet windings.

3.3.3. HTS transformer rectifier flux pumps

An HTS transformer rectifier flux pump (TRFP) was constructed by J. Geng in Tim Coombs' group [131, 132] in 2015. Fig. 3.9 shows the schematic view of the HTS TRFP and the equivalent circuit. The HTS TRFP shares the same principles with the half-wave LTS TRFP in section 3.2.2. The difference lies in the fundamental physics of the superconducting switches. The HTS switches in HTS TRFP uses the "dynamic resistance effect" [29-35] of the HTS conductors (Type-II superconductor), while the LTS TRFPs utilize the normal state of the LTS conductors in the switches. When an external AC magnetic field is applied perpendicular to a direct current carrying HTS coated conductor, a net flux flow motion will be triggered. Some magnetic flux enters the superconductor from one side, traverses across the central region where DC current flows, and leaves the conductor from the other side of the conductor. A DC electric field in the same direction of transport current appears and a DC voltage along the superconductor is induced. This phenomenon is known as the "dynamic resistance" effect, which is a key mechanism in the HTS TRFPs.

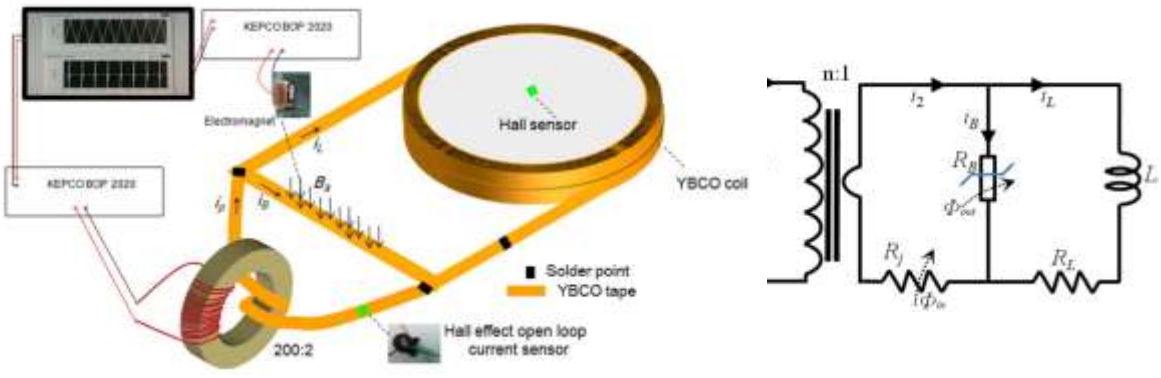

(a) (b)

Fig. 3.9. A schematic view of the HTS TRFP, which is actuated by applying the AC magnetic field (B_a) to the bridge switch, and the equivalent circuit of the TRFP [131]. In the circuit, R_j denotes joint resistance, and R_B denotes the flux flow resistance of the bridge superconductor.

This HTS TRFP can operate high field HTS magnets in ultra-high quasi-persistent current mode and reduce the size, weight, inductance, and cost of high field magnets, making them more accessible. It is promising for powering HTS magnets for NMR/MRI devices, which require a highly stable magnetic field.

3.3.4. HTS self-switching transformer rectifier flux pump

HTS self-switching transformer rectifier flux pump (TRFP) shares a similar mechanism with LTS automatic switching TRFP but uses the transition from zero-resistance state to resistive state by exceeding the I_c of HTS conductors. An HTS self-switching TRFP is constructed by J. Geng in our group in 2016 [133], which is very similar to the AC field controlled switches based TRFP in section 3.3.3. Fig. 3.10 shows the schematic drawing of the self-switching TRFP and the basic mechanism of the self-switching.

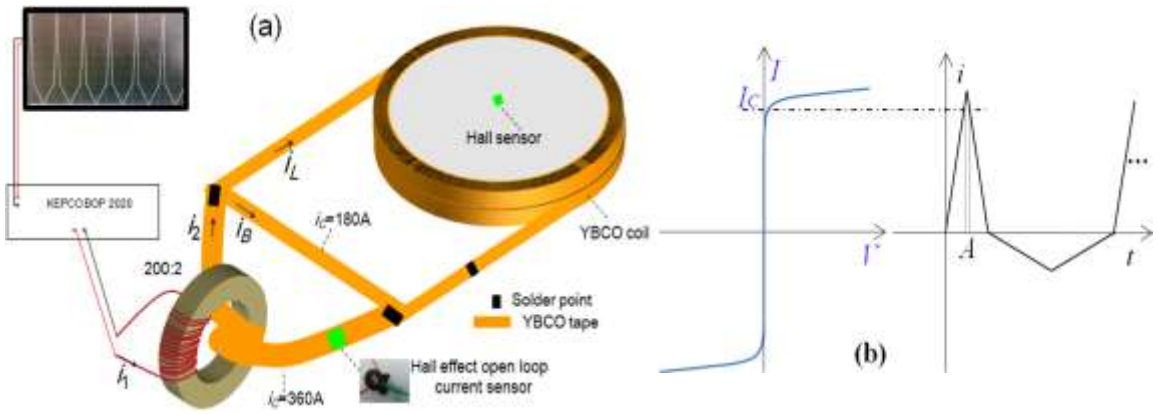

Fig. 3.10. (a) Schematic drawing of the proposed flux pump, (b) Basic principle of the automatic self-switching in the HTS TRFP [133].

A varying magnetic field is applied to an HTS loop which consists of a resistive joint. A superconducting load *L* is connected to the bridge branch which has a smaller critical current value than the rest of the HTS loop. Fig. 3.10 (b) shows the *V*-*I* curve of the HTS bridge branch and one example waveform of the circulating current *i*(t) (close loop contains i_2 and i_B). During each cycle of *i*(t), at time slot A, the critical current of the bridge branch is exceeded and a DC voltage develops across the bridge branch for the load coil (*L*). For the rest time of the waveform, abs(i(t)) < I_c and no DC voltage is generated for the load coil.

3.4. Chapter summary

The LTS flux pumps were proposed many decades ago but haven't been widely used in the LTS magnet system because of the availability of the lossless superconducting LTS joints and persistent current switches. However, the lossless HTS joints are currently unavailable due to the multi-layer structure of REBCO coated conductors. It has been a long-lasting problem that has significantly impeded the widespread uptake of HTS REBCO magnet technology. The HTS magnets working in persistent current mode must be charged by an external power supply via a pair of thick metal current leads. However, these current leads generate considerable heat load on the cryogenic system. As a result, the cooling capacity of the cryogenic system places limits on the achievable current capacity and energy density of the magnets. This heat ingress also makes the magnet less thermally-stable and less reliable. In this case, the HTS flux pump becomes an ideal solution to eliminate the current leads from the HTS magnet system and enable HTS magnets to operate in a closed-loop mode within a closed cryogenic environment.

Chapter 4
Active-switching HTS Transformer Rectifier Flux Pump

HTS flux pumps can inject flux into a closed superconducting circuit in a contactless way, making quasi-persistent current mode in closed HTS coils possible. This contactless charging technology removes the bulky current leads, which makes the superconducting magnet system compact, energy-efficient, and economical. Several types of HTS flux pumps have been developed since 2000, including HTS DC dynamo flux pumps [126-130], HTS linear traveling wave flux pumps [124, 125], HTS transformer rectifier flux pump (TRFP) based on AC field controlled HTS switches [131, 132], and a self-switching HTS TRFP [133]. Among different types of HTS flux pumps, the HTS TRFP using active-controlled power switches has significant advantages: powerful output capability, high controllability, and low energy loss. These advantages enable a highly stable magnetic field of the HTS magnets.

This chapter introduces the design and fabrication of an active-switching HTS TRFP, including the fundamental physics "dynamic resistance effect", the key components of the HTS TRFP "AC field controlled switch", and the overall design of the HTS TRFP. In the end, an operational test is presented to validate the control of this active-switching HTS TRFP.

4.1. Design of active-switching HTS TRFP

4.1.1. Key physics: "Dynamic resistance"

The "dynamic resistance effect" is the key physics for the TRFP using active-controlled HTS power switches. This dynamic resistance effect is a unique phenomenon of the type-II superconductors. HTS REBCO coated conductor is a type-II superconductor. When an external AC magnetic field is applied perpendicular to a direct current carrying HTS coated

conductor, a net flux flow motion will be triggered. Some magnetic flux enters the superconductor from one side, traverses across the central region where DC current flows, and leaves the conductor from the other side of the conductor. A DC electric field in the same direction of transport current appears and a DC voltage along the superconductor is induced. This phenomenon is known as the "dynamic resistance" effect [29-35]. The DC voltage arises from the interaction between the transport DC current and moving magnetic fluxons within the superconductor, which is a modulation of the vortex spatial distribution [32]. Dynamic resistance is very useful and is utilized as a key mechanism of making HTS power switches.

The "dynamic resistance effect" is different from the "flux flow effect" when DC transport current I_t exceeds the critical current I_c. For the "flux flow effect", the flux flow resistance can be well calculated by the *E-J* power law. However, the dynamic resistance doesn't follow the *E-J* power law and has to be calculated by an empirical equation [33].

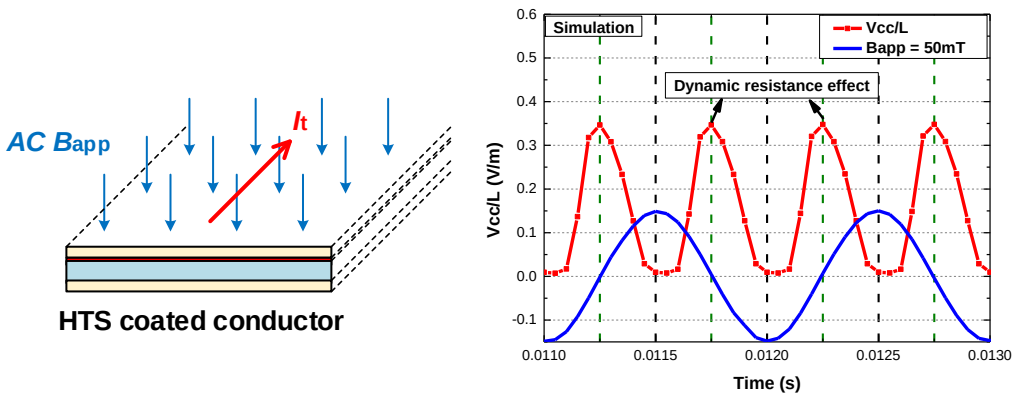

Fig. 4.1. (Left) Schematic view of a direct current carrying HTS coated conductor tape subjecting to a perpendicular AC magnetic field. (Right) "Dynamic resistance" effect: Induced dc "dynamic voltage" and the applied AC perpendicular magnetic field. The data is obtained from a simulation model that has been verified via experiments in [142].

Fig. 4.1 (a) shows a schematic view of a direct current carrying HTS coated conductor tape subjecting to a perpendicular AC magnetic field. Fig. 4.1 (b) shows the induced dc "dynamic voltage" along the direction of the transport current. The data is obtained from a simulation model which has been verified via experiments in [142]

When a perpendicular AC magnetic field is applied to the YBCO coated conductor tape, a dc voltage will be induced along the tape length direction. The induced dc voltage has two peaks in one cycle of the applied magnetic field (B_{app}), and the dc voltage curve peaks at the zero-crossing of the applied field when the field has the fastest-changing rate. In contrast, the

dc voltage is zero at the peaks of the applied field when the field changing rate is the lowest. This "double peak" phenomenon is a unique feature of the "dynamic resistance" effect. This "dynamic resistance" effect is different from the "flux flow" resistance effect, where the dc voltage will peak at the maximum (peak) value of the applied magnetic field. The "flux flow" resistance effect is caused by the drop of the critical current (I_c) due to the field dependency of the critical current density $J_c(B)$.

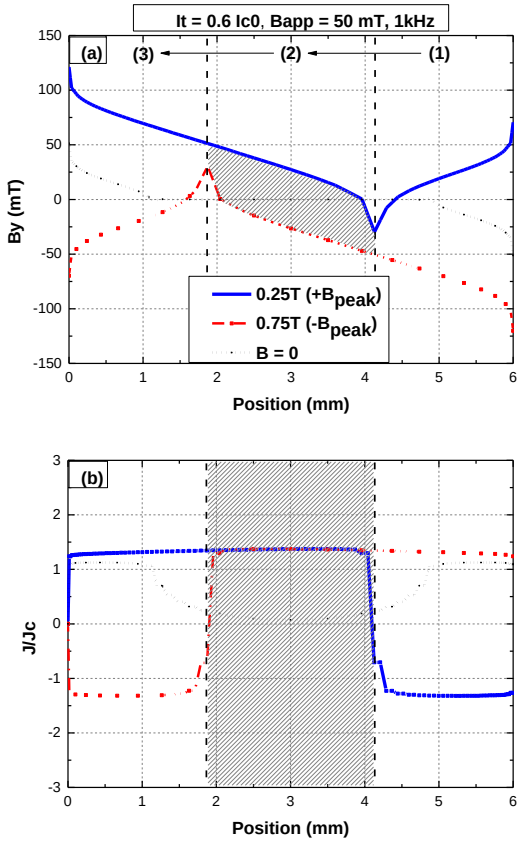

Fig. 4.2. (a) *B* profile: Distribution of the magnetic field and (b) *J* profile: distribution of current density of an HTS REBCO coated conductor, at the transport current of 0.6 I_{c0} under a magnetic field of $B = B_{app}\sin(2000\pi t)$ with B_{app} = 50 mT. The solid lines (blue) are obtained when the external magnetic field reaches its negative peak (+ B_{peak}), and the dash-dot lines (red) are at the positive peak (-B_{peak}), with the dot lines (black) at B_{app} = 0 (no external magnetic field). The data is obtained from the central line of the YBCO layer [143].

Fig. 4.2 shows the distributions of magnetic field (*B* profiles) and current density (*J* profiles) of the HTS coated conductor, which are obtained from the simulation model [142].

As shown in Fig. 4.2, the enclosed shadowed area in Fig. 4.2 (a) represents the hysteretic flux change within one cycle of the periodic *B* curve, which refers to the magnetic flux traversing from the region (1) through (2) to (3) (from one side to the other side of the YBCO coated conductor). A larger enclosed shadow area means a larger amount of net flux flow and

a higher value of dynamic loss [35], which is determined both by dc transport current and ac magnetic field. The "dynamic resistance effect" arises from the interaction of the transport dc current and moving magnetic fluxons within the superconductor. The shadowed belt in Fig. 4.2 (b) is the region where dc current flows and "dynamic resistance" occurs. In contrast, the screening current induced by the perpendicular AC field only flows at the two marginal areas of the superconductor, which is surrounding the dc transport current (I_t) in the central shadowed belt area.

Scientists have already obtained an empirical equation for the "dynamic resistance" generated on the HTS REBCO coated conductors, which is reported in [33] in 2017. The expression for "dynamic resistance" is shown in equation 4.1 and equation 4.2, which are taken from [33]. In equation 4.1, $R_{d,\perp}$ is the "dynamic resistance", L is the length of REBCO tape, a is the half-width of the REBCO tape, f is the frequency of the applied perpendicular AC field, $B_{a,\perp}$ is the magnitude of the perpendicular component of applied AC field, I_{c0} is the self-field critical current of the REBCO tape. $B_{th,\perp}$ is the threshold value of the perpendicular AC field. In equation 4.2, the J_{c0} is the self-field critical current density, μ_0 is the permeability of free space, t is half-thickness of the REBCO tape, $i = I_t/I_{c0}$.

$$\frac{R_{d\perp}}{L} = \frac{4af}{I_{C0}}(B_{a,\perp} - B_{th,\perp}) \tag{4.1}$$

$$B_{th,\perp} = \frac{4.9284\mu_0 J_{c0} t}{\pi}(1-i) \tag{4.2}$$

From equations 4.1 and 4.2, we know that the "dynamic resistance" ($R_{d,\perp}$) in a certain fixed width HTS REBCO tape is mainly determined by the magnitude of perpendicular component ($B_{a,\perp}$) of applied AC field and the frequency of the AC field. The transport current will influence the threshold value ($B_{th,\perp}$) of the perpendicular field, but the impact is not so that significantly compared to the AC field, including the magnitude and frequency.

To sum up, a DC dynamic voltage can be generated across the DC current carrying HTS REBCO tape when an AC perpendicular field is applied, which is called the "dynamic resistance" effect. The "dynamic resistance" of REBCO tape can be easily controlled by changing either the magnitude or the frequency of the perpendicular AC field. The value of the DC dynamic voltage is determined by both the magnitude of the dc transport current and

the "dynamic resistance" which is controlled by the AC perpendicular field. This unique "dynamic resistance" effect of the HTS REBCO coated conductor tape makes the fundamental mechanism of the AC field controlled HTS power switches.

4.1.2. AC magnetic field controlled switch

Based on the "dynamic resistance" effect, we built an AC perpendicular magnetic field controlled HTS power switch. Fig. 4.3 shows the AC magnetic field controlled HTS power switch. A DC current-carrying YBCO coated conductor is placed in the air gap of the electromagnet. An AC magnetic field perpendicular to the surface of the YBCO coated conductor tape is generated by the electromagnet. The frequency and magnitude of the perpendicular AC magnetic field are controlled by the AC current flowing through the copper winding of the electromagnet. By changing the frequency and magnitude of the AC current in the electromagnet, we can easily adjust the resistance of the HTS power switch.

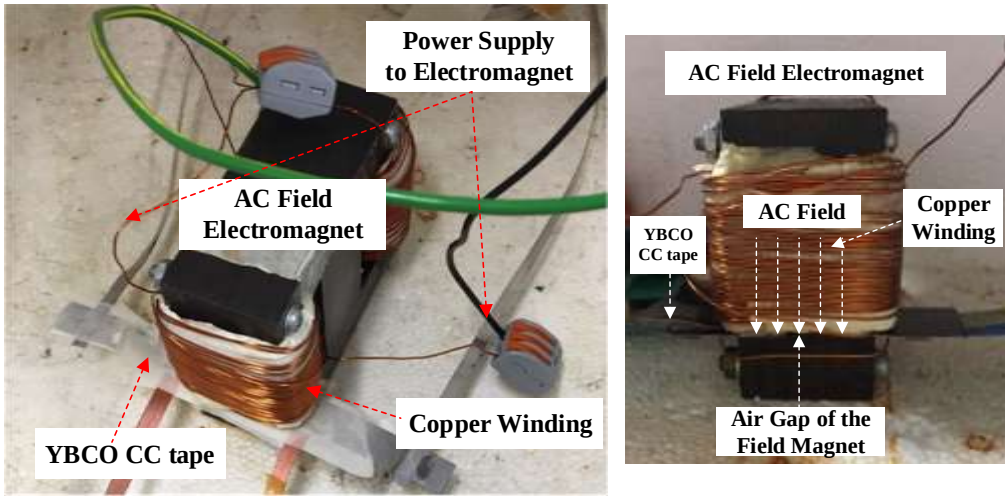

Fig. 4.3. Photos of an AC magnetic field controlled power switch. A dc transport current is flowing through the YBCO coated conductor tape and a perpendicular AC magnetic field is applied to the REBCO tape via an electromagnet. The frequency and magnitude of the AC magnetic field are controlled by the AC current in the copper winding of the electromagnet. So the resistance of the HTS power switch can be easily controlled by changing the frequency and magnitude of the AC current in the electromagnet.

Fig. 4.4 shows the DC voltage of the HTS switch made by REBCO coated conductor tape. Different field magnitudes (peak value) from 50 mT to 400 mT are applied. In this HTS switch, a 10 cm long and 6 mm wide *SuperPower SCS4050* YBCO coated conductor tape is used, which has two 20 μm thick copper stabilizer layers on both sides. The self-field critical current

is around 135 A (at 77 K, with 10^{-4} V/m criterion) when the YBCO coated conductor tape is placed in the narrow gap (~ 1 mm) of the iron core of the electromagnet. The transport current is set at around 0.6 I_{c0} = 80A (I_{c0} = 135 A), and 20 cycles of 1 kHz AC magnetic field is applied perpendicularly to the YBCO coated conductor tape.

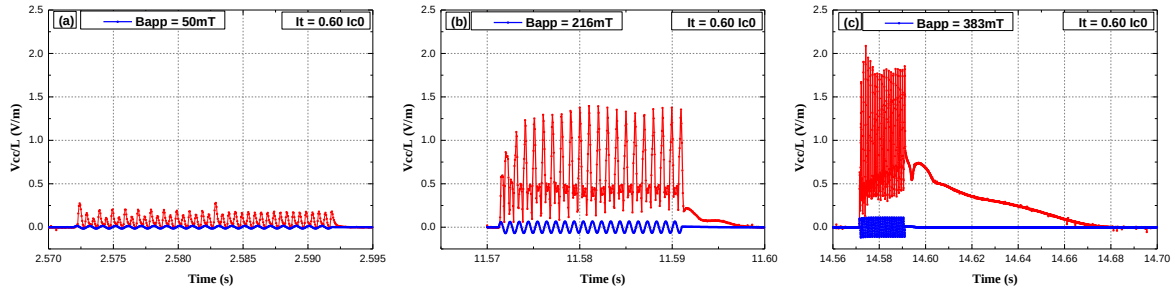

Fig. 4.4. The DC voltage (per unit length) response of the HTS switch to 20 cycles of 1 kHz applied AC magnetic field when the applied field (peak) is around 50 mT, 200 mT, and 400 mT. The transport current is set at around 0.6 I_{c0} (80A), the I_{c0} = 135 A. The DC voltage measured via a pair of voltage taps across the two ends of the YBCO tape [142].

We found that the dc voltage increases significantly with the increases of the applied field magnitude. The dc voltage (peak value) is around 0.3 V/m when the field (peak value) B_{app} = 50 mT; the dc voltage (peak value) increases to around 1.3 V/m when the field (peak value) B_{app} = 216 mT; and the dc voltage (peak value) increases up to around 1.8 V/m when the field (peak value) B_{app} = 383 mT. The results show that the dc voltage of the HTS switch can be effectively controlled by the AC field magnitude. These results agree well with the theoretical analysis in section 4.1.1.

Fig. 4.5 shows the details of the dc voltage curves when the AC field (peak value) B_{app} = 50 mT and B_{app} = 383 mT. When we plot the curve detail, we found that the dc voltage curve in Fig. 4.4 has coupled some background AC magnetic field. So we remove the coupled background noise and got the Fig. 4.5, which shows the details of the dc voltage curve. Under relatively high magnetic field (216 mT and 383 mT) as shown in Fig. 4.5 (b), since the coupling is strong, the dc voltage in Fig. 4.5 (b) is smaller than that in Fig. 4.4 after removing the background noise.

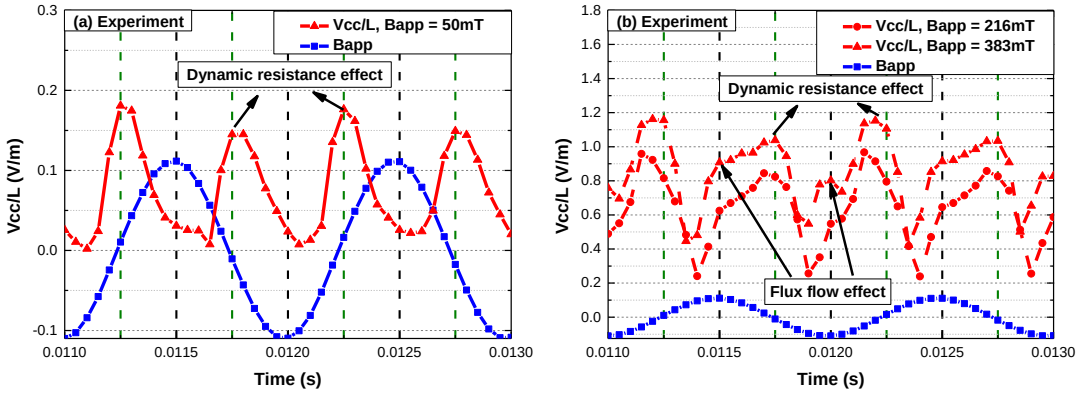

Fig. 4.5. The details of the dc voltage curves (per unit length) generated on the HTS switch, when: AC field magnitude (peak) is around 50 mT, 200 mT, and 400 mT [142].

As shown in Fig. 4.5, two differences can be found between Fig. 4.5 (a) and Fig. 4.5 (b). Firstly, the dc voltage does not go back to zero at the peaks of the applied magnetic field, so that the electrical field value is always over zero, and the voltage curve seems to be "floating". Secondly, there are four peaks (not two peaks) in the curve of dc voltage during one field cycle: two "main peaks" caused by the dynamic resistance effect and two "side peaks" caused by the flux flow effect. The "side peaks" appears at the peaks of the applied field. By comparing the voltage curves at 216 mT and 383 mT, we found that the "side peaks" value increases with the increase of the applied field. This phenomenon can be explained by the field dependency of the critical current density: the YBCO tape is intermittently driven into flux flow region when the instantaneous value of the applied field is high, especially around its peaks. In Fig. 4.5 (b), we can see both "dynamic resistance effect" and "flux flow effect" at the same time when the applied field is very high. So, Fig. 4.5 shows that the AC field controlled HTS switch actually uses both two physics to produce the dc voltage: the "dynamic resistance" effect and the "flux flow" effect when the AC field is very strong. This is slightly different from our original idea and design. In Fig. 4.4, when the B_{app} = 383 mT, a recovery time of 90 ms is found for the HTS switch. The recovery process and the "flux flow" effect indicate that the power loss and temperature rise in the HTS switch are significant and are impacting negatively on the performance of the HTS switch, such as the switching frequency and the reliability. In the real operation of the TRFP, the HTS switch should avoid working in such high power loss mode for a long time.

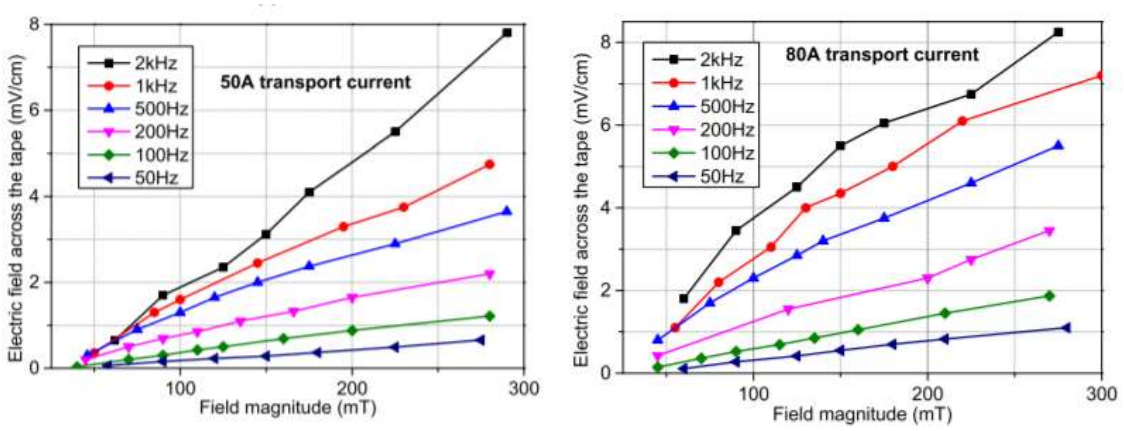

(a) (b)

Fig. 4.6. DC voltage (per unit length) of the HTS switch under different field frequencies and magnitudes. (a) YBCO coated conductor tape carries a 50 A transport current (0.37 I_{c0}). (b) YBCO coated conductor tape carries an 80 A transport current (0.60 I_{c0}). I_{c0} = 135 A. This work was finished by our group in [144].

Fig. 4.5 just shows one of the three controlling methods: increasing the AC field density. Besides, there are two alternative methods to increase the dc voltage of the HTS switch: (1) increase the frequency of the applied AC field; and (2) increase the transport current of the YBCO coated conductor tape in the HTS switch. Fig. 4.6 shows the dc voltage (per unit length) of the HTS REBCO switch under different field frequencies and different transport current (50 A and 80 A). This work was finished by our group in [144]. From Fig. 4.6, we can see that both increasing the AC field frequency and the transport current can increase the dc voltage of the HTS switch. However, the transport current should not exceed the critical current and a very high transport current is also not recommended, because a high transport current mode has a high risk of "thermal quench" during long time operation.

To sum up, an AC magnetic field controlled HTS power switch is successfully developed based on the "dynamic resistance effect". Results show that the DC voltage on the HTS switch can be controlled by adjusting the magnitude and frequency of the AC perpendicular field as well as the magnitude of the transport current flowing through the YBCO coated conductor tape. However, the AC field controlled HTS switch is not recommended to work in the very high-field and high-current mode because the high power loss will lead to a significant temperature rise and a long recovery process. These long recovery time and high temperature rise will eventually slow down the switching frequency and reduce the reliability of the HTS switch. But, generally speaking, this AC field controlled HTS switch has high controllability and fast switching speed. It is an ideal candidate for the power switches in the HTS TRFP.

4.1.3. Circuit design of active-switching TRFP

From previous sections, an AC magnetic field controlled HTS switch has been built by using the "dynamic resistance" effect. This section presents a circuit design of an active-switching HTS transformer rectifier flux pump (TRFP) based on the AC field controlled HTS switch, as shown in Fig. 4.7.

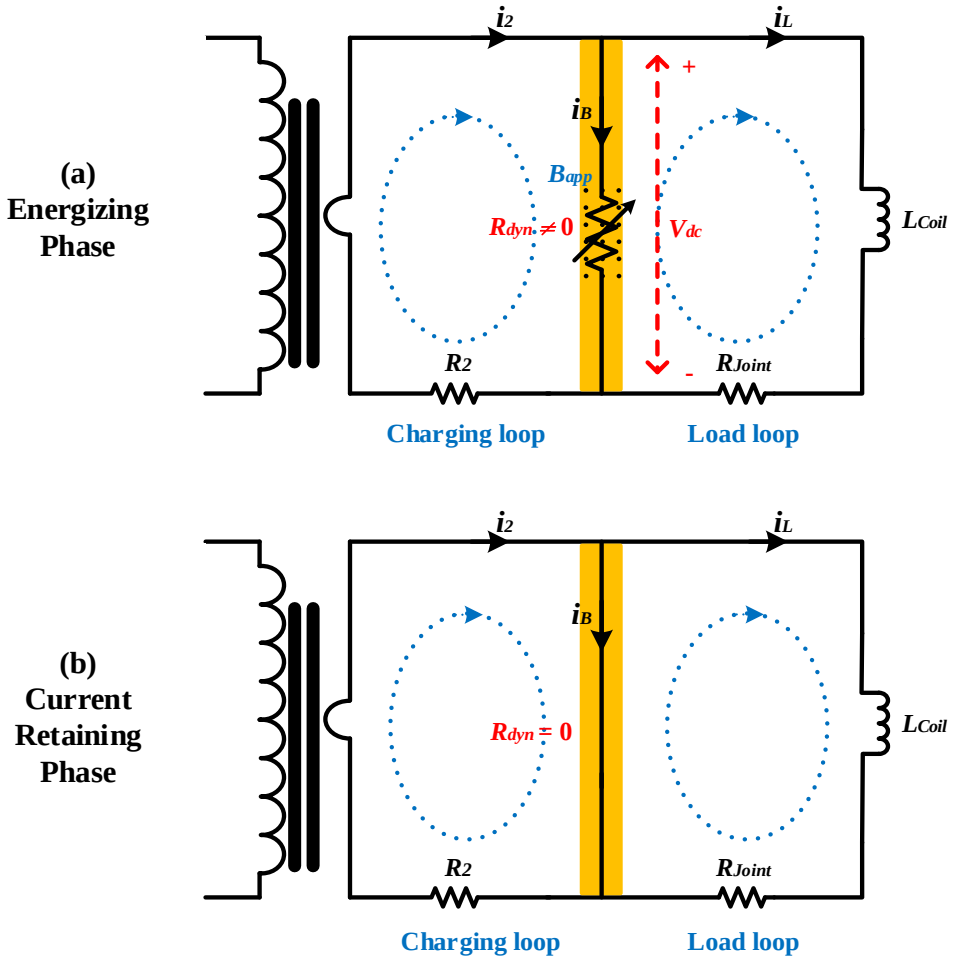

Fig. 4.7. Circuit design of the HTS transformer rectifier flux pump. For the HTS transformer rectifier flux pump, there are two working phases in one charging cycle (T): (a) the energizing phase; (b) the current retaining phase.

The active-switching HTS TRFP consists of two current loops: a charging loop and a load loop. Two loops are joined together by an HTS bridge, which is actually an AC field HTS switch. In the charging loop, high AC current i_2 is induced via a transformer in the secondary winding. i_L is the load loop current flowing through the load HTS magnet, i_B is the current flowing through the bridge section.

The flux pumping mechanism of the active-switching HTS TRFP is also presented in Fig. 4.7. There are two working phases in one charging cycle (T): (a) the energizing phase, and (b) the current retaining phase.

In the energizing phase (a), a perpendicular AC magnetic field (B_{app}) is applied to the HTS bridge (switch), so that the HTS bridge (switch) turns into the resistive state ($R_{dyn} \neq 0$) due to the "dynamic resistance effect". Then, a DC voltage ($V_{dc} = R_{dyn} i_B$) is generated on the HTS bridge (switch), which charges the load coil magnet. Alternatively, we can also say the resistive-state HTS bridge (switch) enables a net flux flow into the load magnet loop.

In the current retaining phase (b), the AC perpendicular field is removed, so that the load loop is shorted by the superconducting state (zero-resistance state: $R_{dyn} = 0$) HTS bridge (switch). However, the joint resistance (R_{joint}) in the load loop will lead to a continuous current decay in the HTS magnet. If the energy input is smaller than the energy consumption on the joint resistance, then the load magnet won't be successfully flux pumped up. R_2 is the resistive component in the charging loop, which is mainly the joint resistance and partly the resistance of the HTS tape caused by the winding process of the transformer secondary winding. However, this R_2 is essential for the transformer to induce a current in the secondary winding, otherwise, the secondary winding will be short-circuited.

The flux increase during one charging cycle can be calculated as follow:

(a) During the energizing phase (the bridge switch is on, or the bridge switch in the resistive state: $R_{dyn} \neq 0$), the frequency of the B_{app} is much higher than the frequency of i_2, the time when the B_{app} is applied is very short (around 10 % T, and T = the time of one charging cycle), so i_2 can be considered as quasi-DC. During this phase, the amount of flux injected into the load is shown in equation (4.3). T is the period of i_2, p is the proportion of T during which B_{app} is applied. I_2 is the average value of i_2 for the time during which B_{app} is applied.

(b) During the current retaining phase, the amount of flux that flows out of the load loop is shown in equation (4.4).

Therefore, during one charging cycle (T), the net flux increase in the HTS load magnet can be expressed as equation (4.5).

$$\Delta\phi_{on} = pT \cdot [(I_2 - i_L) R_{dyn} - i_L R_{joint}] \tag{4.3}$$

$$\Delta\phi_{\text{off}} = -(1-p)T \cdot (i_{\text{L}} R_{\text{joint}}) \tag{4.4}$$

$$\Delta\phi_{\text{T}} = \Delta\phi_{\text{on}} + \Delta\phi_{\text{off}} = pTI_2 R_{\text{dyn}} - i_{\text{L}} T(pR_{\text{dyn}} + R_{\text{joint}}) \tag{4.5}$$

According to the load coil inductance (L), we get equation (4.6).

$$\frac{\Delta\phi_{\text{T}}}{T} = L\frac{di_{\text{L}}}{dt} \tag{4.6}$$

By combing equation (4.5) and equation (4.6), we get the governing equation (4.7) for i_{L}, the load magnet current. In equation (4.7), the variation of i_L in a single cycle can be neglected (i_L can be regarded as a constant during a very short time), because T is very short in comparison to the time taken to charge the load.

$$L\frac{di_{\text{L}}}{dt} = pI_2 R_{\text{dyn}} - i_{\text{L}}(pR_{\text{dyn}} + R_{\text{joint}}) \tag{4.7}$$

Equation (4.7) is a 1st order equation, and the solution is shown in equation (4.8).

$$i_{\text{L}} = A(1 - e^{-t/\tau}) \text{ , where } \begin{cases} A = I_2 / (1 + R_{\text{joint}} / R_{\text{dyn}} p) \\ \tau = L / (R_{\text{joint}} + R_{\text{dyn}} p) \end{cases} \tag{4.8}$$

According to equation (4.8), the final load current (i_{L}) is proportional to I_2, which means: if B_{app} is always applied at i_2 reaching one peak, a high final value of i_L can be achieved. This strategy [7] is useful and will be used in the control system for the active-switching HTS TRFP.

4.2. Fabrication of HTS transformer rectifier flux pump

4.2.1. Overall experimental system

Based on the circuit design, an experimental system for the active-switching HTS TRFP has been built by Jun Ma in the Coombs group [145], as shown in Fig. 4.8.

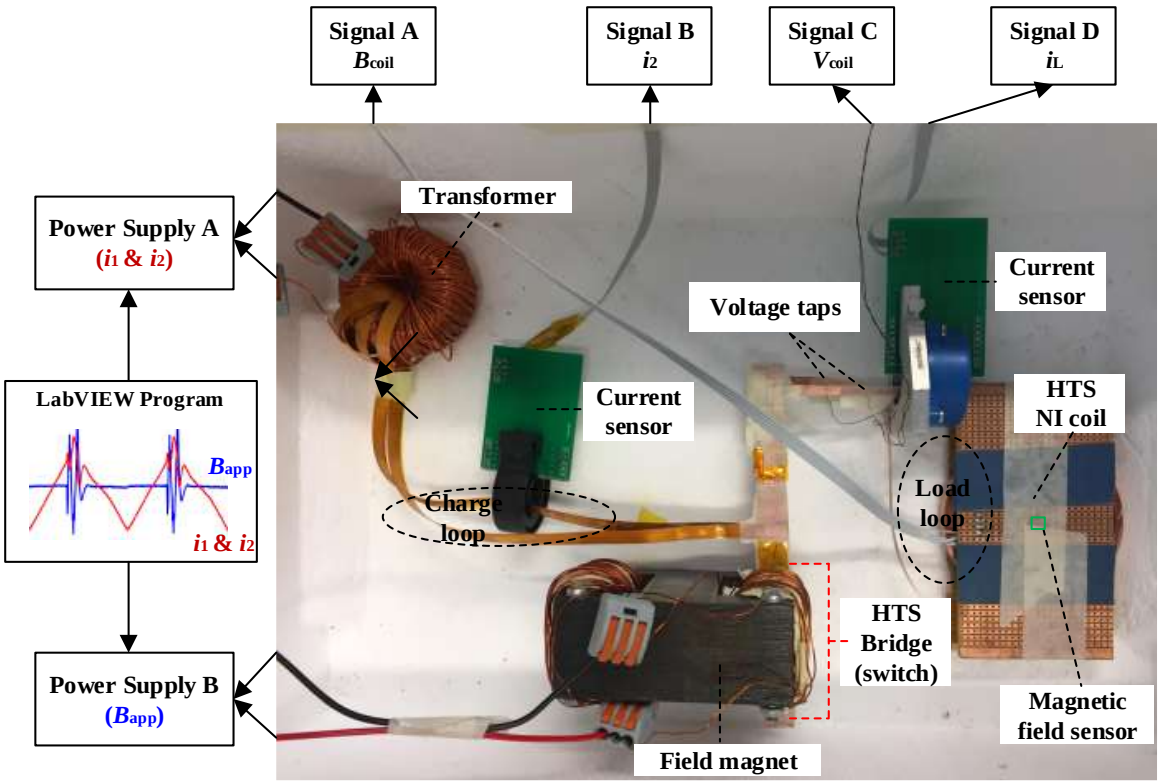

(a) Experimental set-up

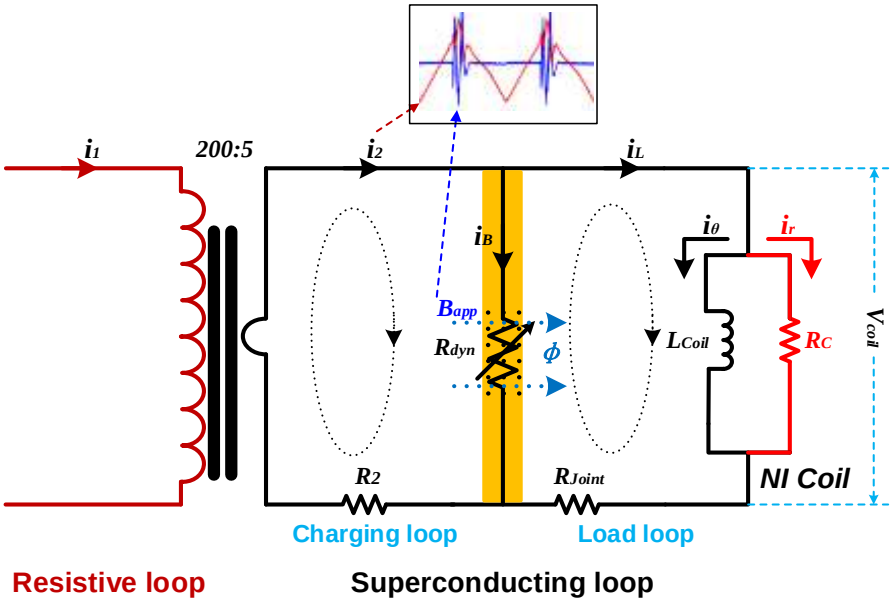

(b) Equivalent circuit

Fig. 4.8. (a) (Top) Overall experimental set-up of the active-switching HTS transformer rectifier flux pump system for an HTS magnet. In this photo, the HTS magnet is an HTS REBCO no-insulation coil. The data acquisition system is also presented in this photo. (b) (Bottom) The equivalent circuit of the active-switching TRFP system. A symmetrical triangular waveform of i_2 is generated by a transformer, and a perpendicular AC magnetic field perpendicular to the HTS bridge switch is generated by the electromagnet. To help achieve a high final value of i_L, the AC field is applied to the HTS bridge when i2 reaches around its positive peak.

A copper/HTS transformer is used to generate the varying flux dΦ/dt in the charging loop. An HTS switch (marked as an HTS bridge) is controlled by the perpendicular AC field to achieve variable resistance, enabling the current rectification. In this set-up, a data acquisition system has been installed to monitor four important parameters, including the magnetic field on the center of the HTS load magnet (B_{coil}), the dc voltage to charge the HTS load magnet (V_{coil}), the current in the charging loop (i_2), and the current in the load loop (i_L). As shown in the equivalent circuit of the HTS TRFP, a symmetrical triangular waveform of i_2 is generated by a copper/HTS transformer with a turn ratio of 200:5, and a perpendicular AC magnetic field perpendicular to the HTS bridge switch is generated by the electromagnet. To help achieve a higher DC charging voltage and a higher final value of i_L, the AC field is applied to the HTS bridge when i_2 reaches around its positive peak (see last part of section 4.1.3). The field duration is around 10% of the period of i_2. This control strategy is executed by a LabVIEW program.

In the equivalent circuit, R_{dyn} is the resistance of the HTS bridge switch (an AC field controlled HTS switch). R_2 represents total resistance in the charging loop, including joint resistance and flux penetration induced resistance. The value of this resistance is estimated to be 60 $\mu\Omega$. This resistance is essential for the flux pump because it allows flux to become linked to the charging loop from outside. The equivalent circuit of the no-insulation HTS REBCO coil is based on Hahn's model [1]. R_{joint} denotes the joint resistance in the load loop. L_{Coil} is the inductance of the YBCO coil magnet. R_c represents the characteristic resistance of the HTS YBCO no-insulation coil (for the Kapton tape insulated coil, there is no R_c parallel branch). Other basic parameters presented in the circuit include the transformer primary current i_1, the secondary current i_2, the voltage across the load coil V_{coil}, the bridge current i_B, the load current i_L, the azimuthal current (i_θ) flowing through the YBCO tape, and radial bypass current i_r flowing through the turn-to-turn bypass path in the no-insulation coil. The relationship between these currents is shown in the formulas (4.9) and (4.10).

$$i_2 = i_B + i_L \tag{4.9}$$

$$i_L = i_\theta + i_r \tag{4.10}$$

4.2.2. Power supply and control system.

A schematic view of the power supply and control system for the active−switching TRFP system is presented in Fig. 4.9. One programmable power supply (A) is used to power the transformer and another programmable power supply (B) is used to control the HTS switch. A LabVIEW program is built to execute the control strategy for the current (i_2) and field (B_{app}): To achieve a higher DC charging voltage and a higher final value of i_L, the AC field (B_{app}) is applied to the HTS bridge switch when i_2 reaches around its positive peak.

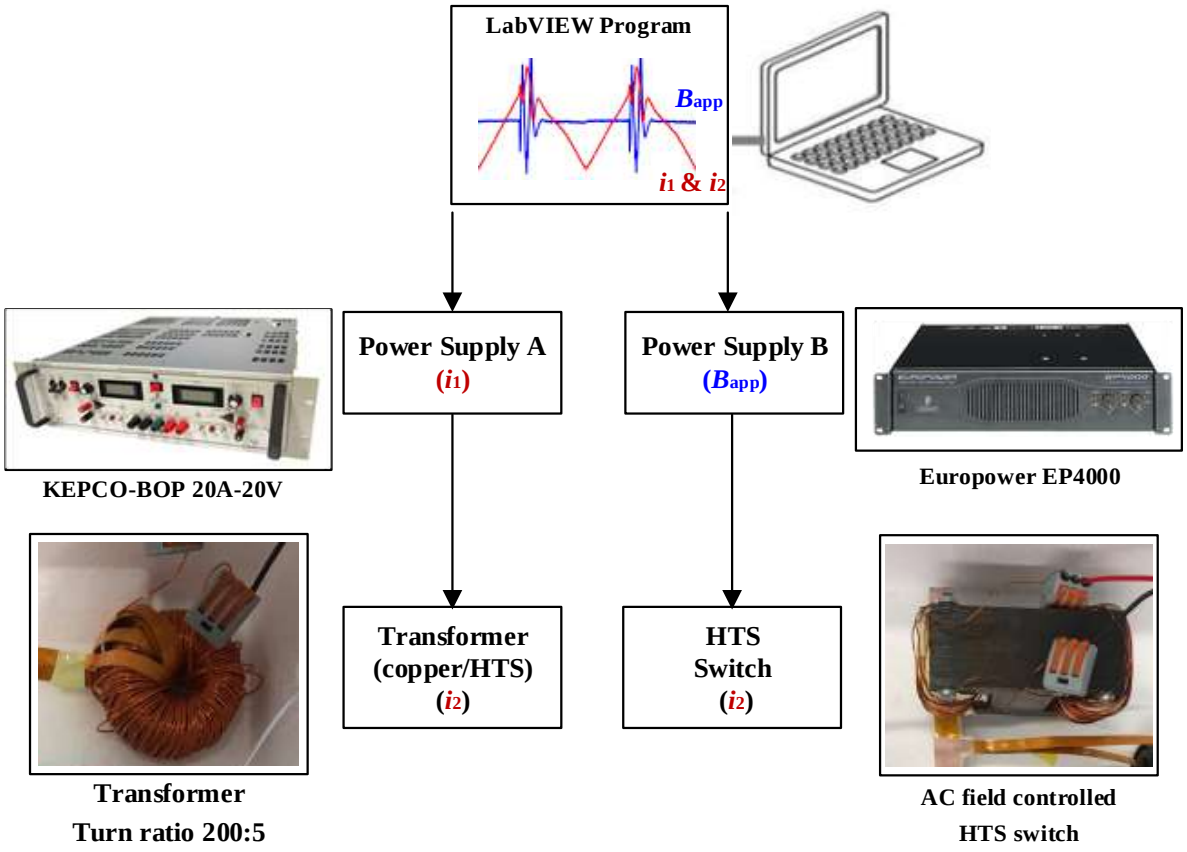

Fig. 4.9. Schematic view of the power supply and control system for the transformer and HTS switch in the active-switching TRFP system. One programmable power supply (A) is used to power the transformer and the other programmable power supply (B) is used to control the HTS switch. A LabVIEW program is built to execute the control strategy for the current (i2) and field (B_{app}): The AC field (B_{app}) is applied to the HTS bridge switch when i_2 reaches around its positive peak, to achieve higher DC charging voltage and a higher final value of i_L.

A LabVIEW control program.

A digital control system is built by the LabVIEW software. Fig. 4.10 shows the front panel and the logical diagram of the LabView program. In the front panel, we can adjust the magnitude and frequency of the current powered into the primary winding of the transformer, and the magnitude and frequency of the AC current into the winding of the electromagnet of the AC field controlled HTS power switch. An AC current with a symmetrical triangular waveform is generated for the programmable power supply for the transformer, and an AC sinusoidal waveform is generated for the programmable power supply for the switch magnet. The duty cycle for the applied AC field can be adjusted in the front panel of the LabVIEW program. In the experiments, we set the duty cycle at 10%.

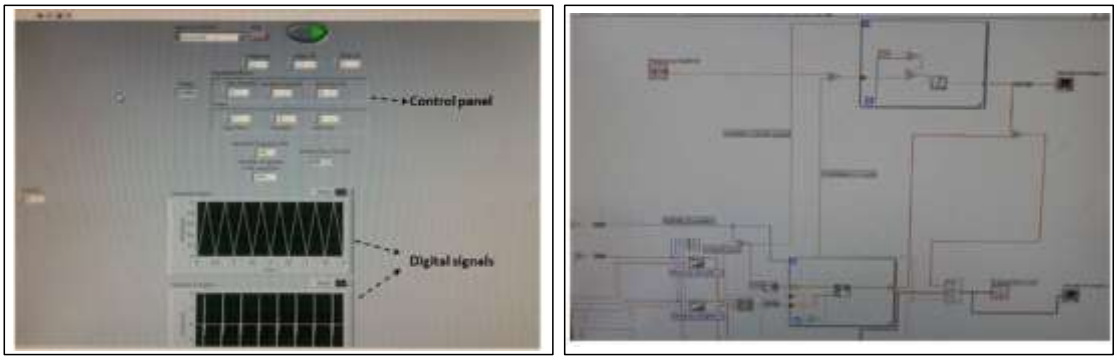

(a) Front panel **(b) Logical diagram**

Fig. 4.10. Front panel and logical diagram of the LabVIEW control program for the TRFP.

Two programmable power supplies.

Fig. 4.11. Two power supplies used to power the transformer and HTS power switch: (a) KEPCO-BOP 400W 20A-20V bipolar operational power supply, and (b) Europower EP4000 power supply.

Two programmable power supplies are used in the experimental system, as shown in Fig. 4.11. The KEPCO-BOP 400W 20A-20V bipolar operational power supply is used to power the copper/HTS transformer. The Europower EP4000 power supply is used to power and control the AC field controlled HTS power switch. Both two power supplies are controlled by one LabVIEW program.

A copper/HTS transformer.

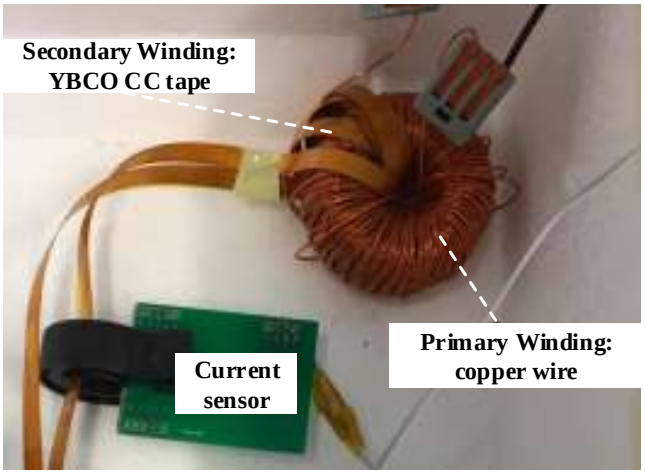

Fig. 4.12. The copper/HTS transformer with a turn ratio of 200:5. The Primary winding is made of copper wire. The secondary winding is made of an HTS YBCO coated conductor tape manufactured by SuperPower. A current sensor is placed in the secondary winding of the transformer.

A copper/HTS transformer is fabricated to generate the symmetrical triangular waveform of i_2. The transformer is shown in Fig. 4.12. This transformer has a high turn ratio of 200:5, aiming to generate a high alternating current in its secondary winding. The primary winding of the transformer is made of copper wire. The primary winding of the transformer is powered by the KEPCO-BOP 2020 power amplifier. The KEPCO is controlled by programmable analog signals from LabVIEW via a NI-USB 6221 data acquisition card. The secondary winding of the transformer is made of an HTS YBCO coated conductor tape manufactured by *SuperPower*, which has a critical current of 180 A. The secondary winding is soldered on the HTS bridge switch (an AC field controlled current switch).

An AC field controlled HTS power switch.

An AC field controlled HTS power switch based on the "dynamic resistance" effect mechanism is built, as shown in Fig. 4.13. This HTS switch is designed to generate the $R_{dyn,}$ on the bridge section in the equivalent circuit in Fig. 4.8. This HTS switch is actually a direct

current carrying YBCO bridge tape subjected to a controllable perpendicular AC magnetic field. In this HTS switch, the YBCO tape is 12 mm wide and is manufactured by *Sunam*. It has a self-field critical current of above 500A at 77K. This HTS switch is used to charge and short-circuit the HTS load magnet. In order to reduce the signal coupling, a bifilar structure, as shown in Fig. 4.13 (b), is adopted in the design of bridge tape: two closely attached YBCO tapes (insulated from each other) were soldered together at one end. The bifilar bridge design narrows the load loop in the magnet air gap, reducing the B_{app} induced voltage in the load loop. B_{app} is provided by an AC field electromagnet as shown in Fig. 4.13 (a). This electromagnet is made of an iron core. There is a narrow air gap (1.5 mm thick, 50 mm long and 15 mm wide) in one core of the magnet, where the B_{app} is applied. The magnet is powered by the Europower EP4000 power supply.

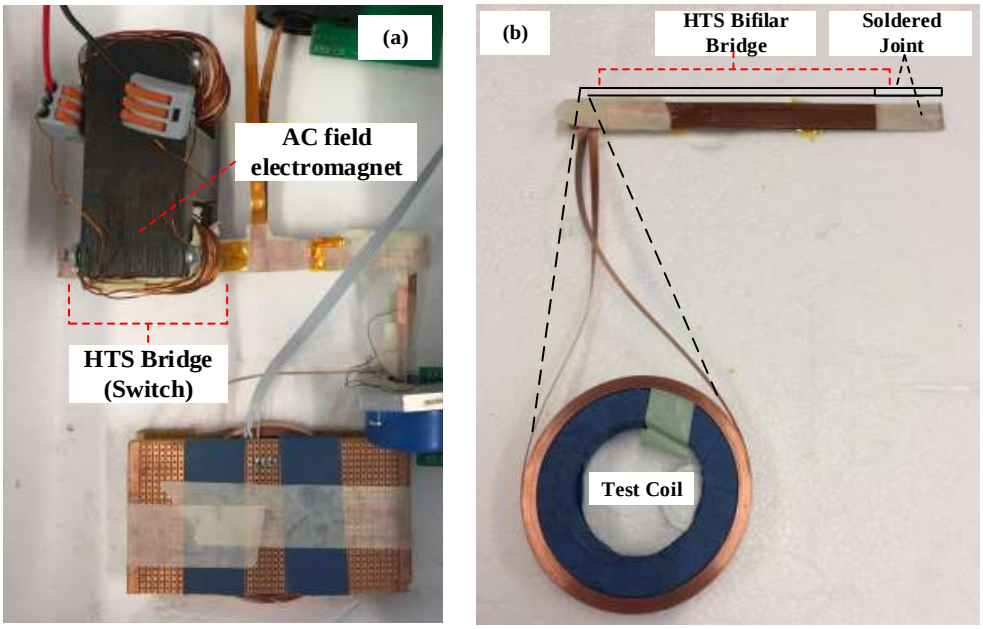

Fig. 4.13. (a) A photo of the AC field controlled HTS power switch based on the "dynamic resistance" effect, and (b) a photo of the bifilar bridge structure, which is used to reduce the signal coupling.

Fig. 4.14 shows the relationship between the peak value of the perpendicular AC field B_{app} and the peak value of the AC sinusoidal current flowing through the copper winding of the electromagnet of the HTS switch. The frequency and the peak value of the perpendicular AC field B_{app} are controlled by adjusting the frequency and the magnitude of the AC sinusoidal current in the winding of the electromagnet of the HTS switch. Accordingly, the resistance of the HTS power switch can be easily adjusted.

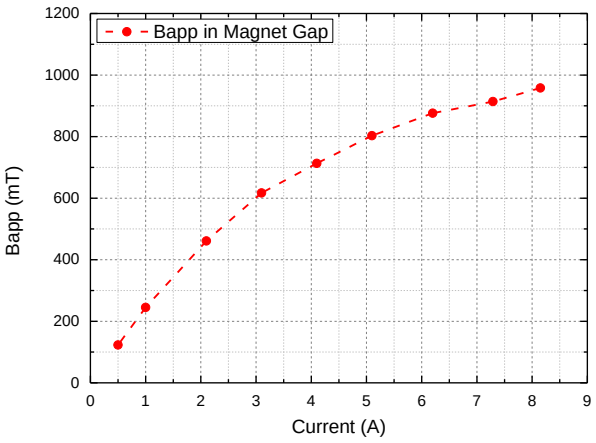

Fig. 4.14. The relationship between the peak value of the perpendicular AC field B_{app} and the peak value of the AC sinusoidal current flowing through the copper winding of the electromagnet of the HTS switch. The current is monitored via a 0.5 Ω resistor, which is connected in series with the copper winding of the electromagnet.

4.2.3. Signal acquisition

A schematic view of the signal acquisition system for flux pumping system is presented in Fig. 4.15. It includes the real-time data display and recording software *Signal Express*, and data acquisition card manufactured by *National Instrument*, one magnetic field Hall sensors for monitoring HTS magnet central field strength (B_{coil}), two current sensors for monitoring i_2 and i_L, and one pair of voltage taps for V_{coil}. The position of these sensors and their set-ups can be found in Fig. 4.8.

Data acquisition card.

The signal output is recorded via a National Instrument NI-USB 6221 data acquisition (DAQ) card. The sampling frequency was set to 2k Hz to guarantee a detailed recording of each signal. The minimum resolution of the NI-USB 6221 data acquisition card was 69 μV. The voltage of the HTS magnet (V_{coil}) was measured directly by the NI-USB 6221 data acquisition card via two voltage taps on the two ends of the coil magnet. Fig. 4.16 is a picture of a USB type data acquisition card (DAQ) card manufactured by National Instrument we often used in our lab.

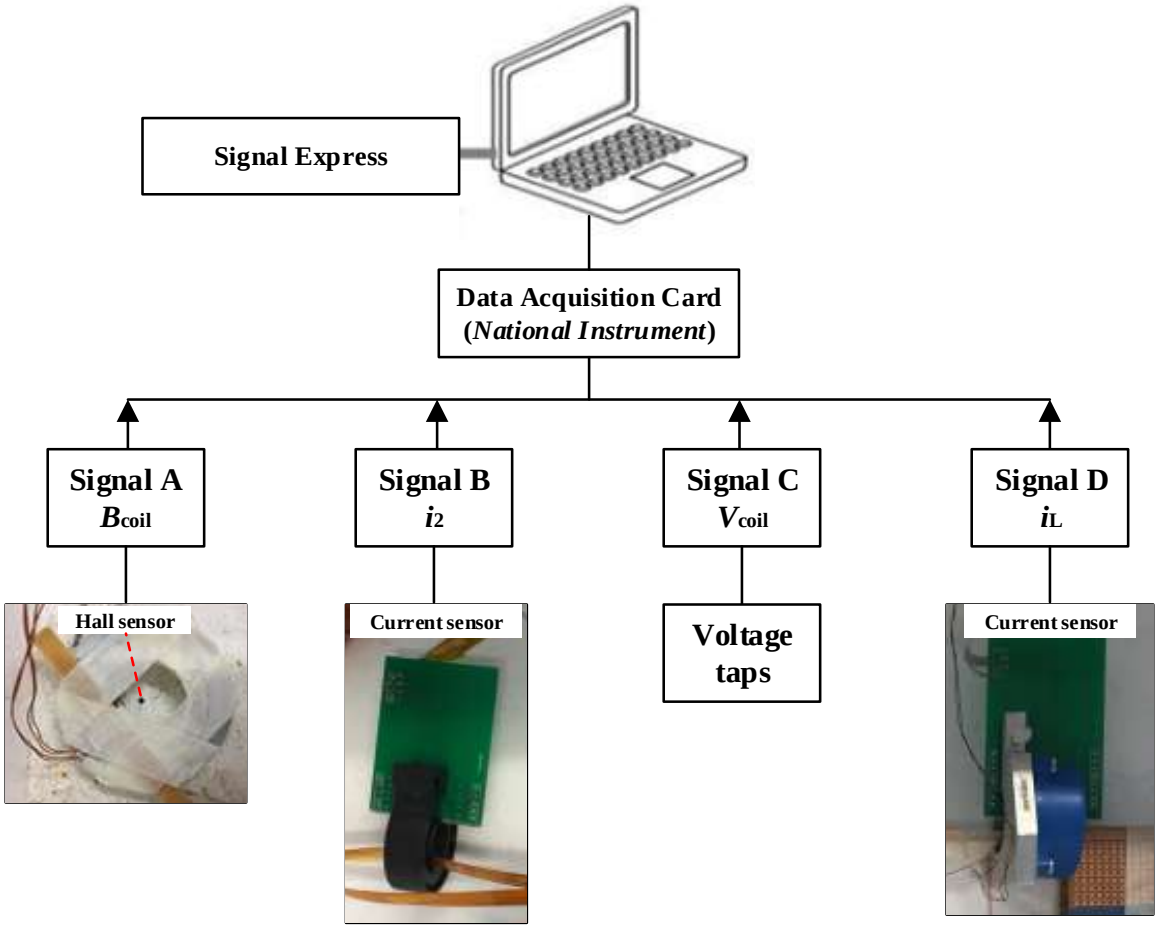

Fig. 4.15. A schematic view of the signal acquisition system for the flux pumping system. It consists of the real-time data display and recording software *Signal Express*, and data acquisition card manufactured by *National Instrument*, one magnetic field Hall sensors for monitoring HTS magnet central field strength (B_{coil}), two current sensors for monitoring i_2 and i_L, and one pair of voltage taps for V_{coil}.

Fig. 4.16. A picture of a USB type data acquisition card (DAQ) card manufactured by National Instrument, which is used in our lab.

Magnetic field Hall sensor.

A Hall sensor is fixed on the center point of the HTS magnet, to monitor the magnitude of the magnetic field (B_{coil}) generated by the HTS magnet. Fig. 4.17 shows the photo of the Hall sensor. The Hall sensor is very sensitive to the magnetic field. It has two current power input pins and two voltage output pins. During the experiment, this Hall sensor is powered by a constant 10 mA DC current by a current source and the conversion ratio is 1 mV = 0.75 mT.

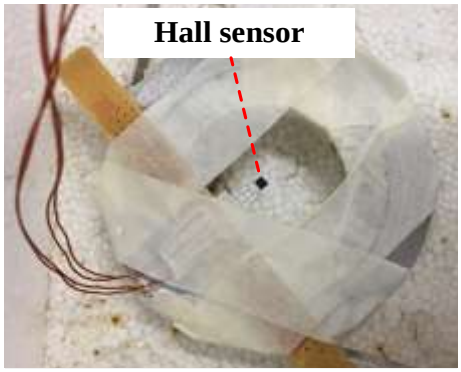

Fig. 4.17. A photo of the Hall sensor for monitoring the magnetic field of the HTS magnet.

Current sensor.

The current (i_2) in the secondary winding of the transformer and the load loop current (i_L) is monitored via two Hall-effect current sensors respectively. Fig. 4.18 shows a photo of the Hall-effect current sensor and the relationship between the output voltage and the current flowing through the two Hall-effect current sensors.

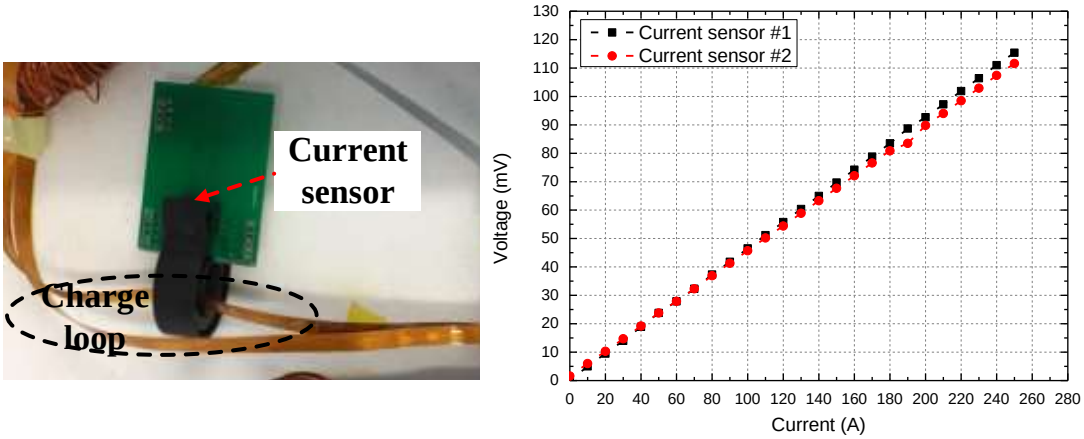

(a) (b)

Fig. 4.18. (a) A photo of the Hall-effect current sensor, and (b) the relationship between the measured current flowing through the current sensor and the output voltage signal for two current Hall sensors (labeled as Current sensor #1 and Current sensor #2 in the figure).

4.3. Operational test

This section presents the operational test results of this active-switching TRFP system. The operational test is generally the last step of building a new device. In this test, the active-switching HTS TRFP is tested with different field density and different field frequencies for the HTS power switch. A Kapton tape insulated REBCO double pancake coil, as shown in Fig. 4.19, is used as a load HTS magnet in the operational test. It has 60 turns in total, and 30 turns in one pancake. The critical current of the HTS coil is 62 A, the coil inductance is 123 μH.

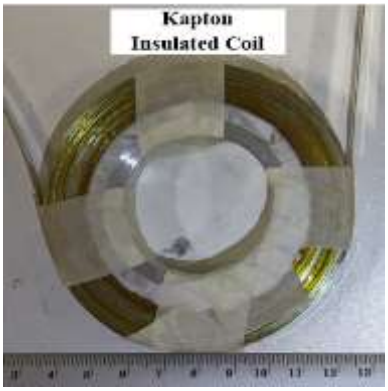

Fig. 4.19. HTS REBCO coil with Kapton tape insulation. It has 60 turns in total, and 30 turns in one pancake. The critical current of the HTS coil is 62 A, the coil inductance is 123 μH.

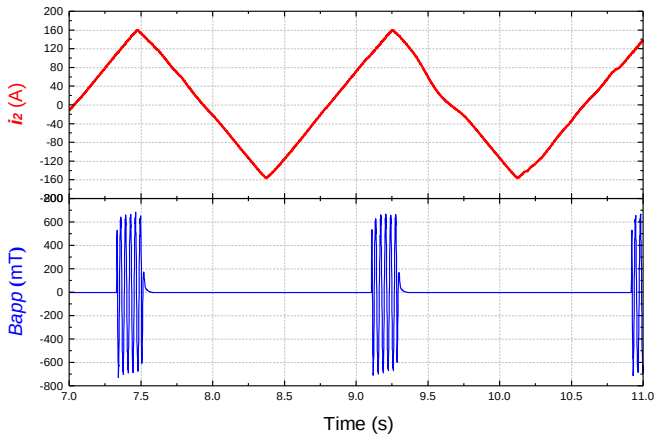

Fig. 4.20. Waveforms of the secondary current i_2 (symmetrically triangular) in the transformer and applied switching AC field B_{app}. The peak value of i_2 is 160 A. B_{app} is applied around the positive peak of i_2, the field duration is 0.1 times of the period of i_2. Here, the frequency of i_2 is set as 1 Hz via the front panel of the LabVIEW program. (Actual output is at 0.56Hz. The reason probably is the equipment error.). The magnitude of B_{app} is 685 mT, and the frequency is set as 50 Hz, but the actual output is 28 Hz (due to the same equipment error).

Fig. 4.20 shows the waveform of i_2 and B_{app}. The waveform of i_2 is symmetrically triangular, and the frequency of i_2 is set as 1 Hz via the front panel of the LabVIEW program. (Actual output is at 0.56Hz, which is obvious according to the waveform in Fig. 4.20. The reason probably is the equipment error.). The peak value of i_2 is 160 A. B_{app} is applied around the positive peak of i_2, the field duration is 0.1 times of the period of i_2.

4.3.1. Magnitude of AC switching field

The flux pumping performance for the insulated HTS REBCO magnet with different AC switching field density is presented in Fig. 4.21. The field frequency is set as 50 Hz, the field magnitude increases from 475 mT to 685 mT, and 850 mT.

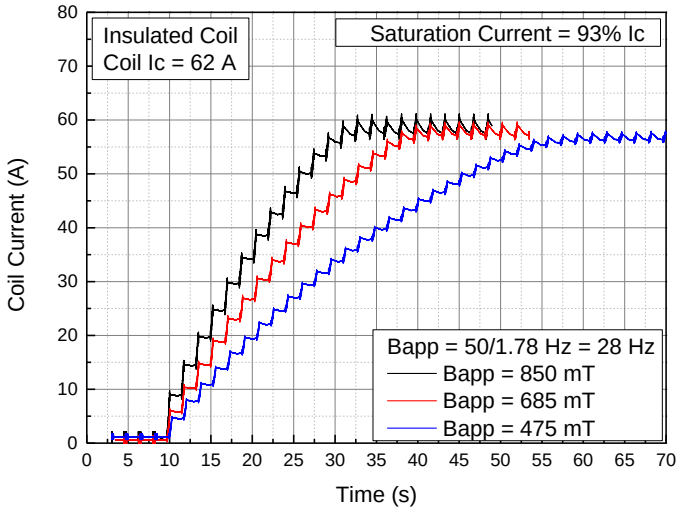

Fig. 4.21. The flux pumping performance for the insulated HTS REBCO magnet with different switching field density. The frequency of the switching AC field is set as 50 Hz. For the triangular shape AC current (i_2) in the transformer, frequency is set as 1 Hz.

Fig. 4.21 shows that a higher switching field leads to a faster pumping speed and a slightly higher final saturation current. The reason behind is that a higher switching field leads to a higher "dynamic resistance" and therefore a higher DC charging voltage (V_{coil}) for the HTS coil. When Bapp = 850mT, 50Hz, the REBCO HTS insulated coil can be quickly charged up to 57.5 A (93% coil I_c) in 22 s.

Take a further look at the curve details when coil current reaches a quasi-steady state, there are current ripples in the quasi-steady state and the current ripples are different under different field magnitudes.

The ripples show that, in the final quasi-steady state, the coil current still increases and decreases in one charging cycle. This means that the field of the HTS magnet will fluctuate slightly in the final quasi-steady state. This can be explained by the existence of joint resistance (R_{joint}) in the load loop and/or the flux flow resistance of the HTS coil, as shown in equivalent circuit in Fig. 4.8 (b). When a DC charging voltage is generated in the bridge switch, the coil is charged and the current increases, but this only lasts for about 10 % of the whole charging cycle (T). When the AC field applied to the bridge switch is removed, the DC charging voltage disappears and the coil current decays because energy is consumed by the joint resistance (R_{joint}) in the load loop and/or the flux flow resistance of the HTS coil.

When the AC field magnitude is relatively higher, a higher DC charging voltage (V_{coil}) is generated for the HTS coil. In this case, the ripples of coil current (black curve, B_{app} = 850 mT) is larger than of the coil current under a smaller AC field magnitude (such as 475 mT). The reason is that, a higher DC voltage pushes the coil current further into a higher level (61 A, ~98% coil I_c) up to the flux flow state (region) (which can be understood by the E-J power law curve), and an extra flux flow resistance together with the joint resistance (R_{joint}) in the load loop will lead to a faster decay speed in the current ripples. When the AC field magnitude is relatively small such as 475 mT, the peak current (57A, ~92% coil I_c) is smaller than the peak value (61 A, ~98% coil I_c) when B_{app} = 850 mT, so the flux flow resistance can be very small or can be ignored. In this case, the current decay or the current ripple is smaller because the flux flow resistance can be ignored and current decay is mainly caused by the joint resistance (R_{joint}) in the load loop. So, these reasons can explain the phenomenon: current ripples are different under different field magnitudes. We can learn that, if we want to sustain a more stable field, then a smaller AC field magnitude is preferred. This strategy is very indicative for achieving a more stable field and a smaller ppm value for the MRI magnet system.

To conclude, the output capability of the active-switching HTS TRFP can be effectively controlled by the magnitude of the AC switching field (B_{app}): A faster charging speed can be achieved by applying a higher AC field magnitude, while a more stable field can be sustained by applying a smaller AC field magnitude.

4.3.2. Frequency of AC switching field

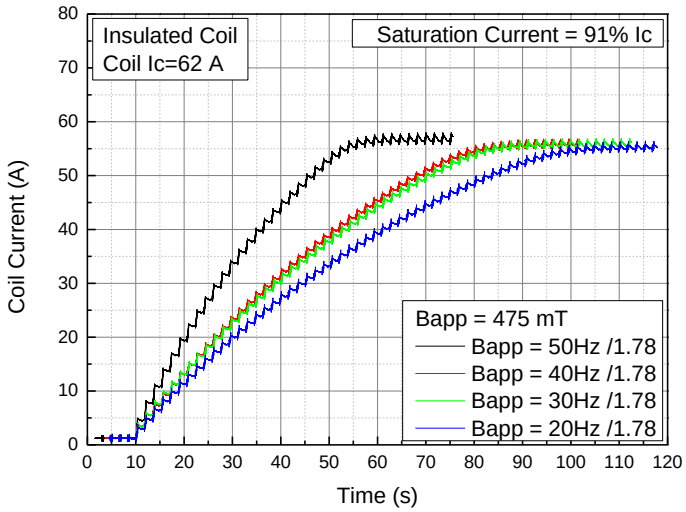

Fig. 4.22. The flux pumping performance for the insulated HTS REBCO magnet with different switching field frequency. The magnitude of the switching AC field is set as 475 mT. For the triangular shape AC current (i_2) in the transformer, frequency is set as 1 Hz.

The flux pumping performance for the insulated HTS REBCO magnet with different AC switching field frequency is presented in Fig. 4.22. The field (peak) magnitude is set as 475 mT, the field frequency increases from 20 Hz to 50 Hz. Fig. 4.22 shows that a higher switching field frequency leads to a faster pumping speed and a slightly higher final saturation current. The reason behind is similar: a higher switching field frequency leads to a higher "dynamic resistance" and therefore a higher DC charging voltage (V_{coil}) for the HTS coil. When B_{app} = 475 mT, 50Hz, the REBCO HTS insulated coil can be quickly charged up to 56.5 A (91% coil I_c) in 50 s.

Besides, the impact of the field frequency on the field stability in the final quasi-steady state is not obvious from these curves in Fig. 4.22. The reasons probably are that the AC field magnitude (B_{app} = 475 mT) is not high enough and the field frequency (20Hz - 50 Hz) is also not high enough to generate huge difference. According to equation (4.1), both a higher field frequency and a higher AC field magnitude can lead to a higher "dynamic resistance" and therefore a higher DC charging voltage. The magnitude of the DC charging voltage determines the current fluctuation in the HTS load magnet. So theoretically speaking, a higher field frequency will result in a higher DC charging voltage and reduce the field stability in the final quasi-steady state.

To sum up, the output capability of the active-switching HTS TRFP can also be effectively controlled by the frequency of the AC switching field (B_{app}). A higher AC field frequency will lead to a faster charging speed, but a lower AC field frequency probably will lead to a more stable field in the final quasi-steady state.

4.3.3. Conclusion

To conclude, operational tests show that this active-switching HTS TRFP has been successfully constructed and it can be easily controlled by adjusting the magnitude and frequency of the AC field of the HTS power switch.

4.4. Chapter summary

This chapter introduces the design and fabrication of an active-switching HTS TRFP, including the fundamental physics “dynamic resistance effect”, the key components of the HTS RRFP “AC field controlled switch”, and the overall design and fabrication of the HTS RRFP. This active-switching HTS TRFP shows high controllability, fast pumping speed, high output current. These advantages will enable a highly stable magnetic field of the HTS magnets. This TRFP will be used in the pumping experiments for different types of HTS coil magnets in the following chapters.

Chapter 5
No-insulation HTS Magnets

The HTS REBCO magnets have a high operating temperature, a high critical current under high magnetic fields, and excellent mechanical properties, these advantages make REBCO magnets very promising in practical superconducting applications. The no-insulation winding technology has further enhanced the overall performance of HTS REBCO magnets by adding the unique self-protection ability [2, 114], which greatly improved the reliability of the HTS magnets. The absence of insulation layers also enables a compact size and a high current-field density. Recently, the fast development of NI HTS REBCO magnets has facilitated the rapid progress of high field magnet technology, increasing the field strength of superconducting or hybrid magnets gradually from 7T to 32T, and to a new world record of the strongest field strength at 45.5 T in 2019 [2]. The fast-developing NI HTS REBCO magnets have shown significant potential in future applications and are the ideal candidate to achieve compact and reliable high-field superconducting devices.

This chapter presents the design and innovation of the no-insulation HTS RECO magnets. It presents the design and fabrication of the conventional no-insulation HTS REBCO magnet. Based on the conventional no-insulation HTS REBCO magnet, a novel solder impregnated no-insulation HTS REBCO magnet is designed and fabricated. The solder impregnated no-insulation HTS REBCO magnet has strong mechanical properties and excellent overcurrent performance. This novel magnet design can solve the long-lasting mechanical breakdown problem for the superconducting magnets. We believe that this novel type of solder impregnated no-insulation HTS REBCO magnet will have a promising and broad application in the high field magnet systems, including tokamak fusion devices, the particle accelerator magnet system, and the NMR/MRI systems.

5.1. Conventional NI HTS magnets vs solder impregnated NI HTS magnets

Typically the Kapton-tape insulated HTS magnets are mechanically strengthened by impregnation with epoxy resin or occasionally they are edge glued. This helps the superconducting magnets withstand high Lorentz Force under high field and high current working condition. But current conventional no-insulation coil magnets are simply wound from tape which has not been previously insulated with Kapton tape or similar. They don't have reinforcement between layers. Lack of mechanical reinforcement will greatly reduce the reliability of the no-insulation HTS magnets.

This chapter presents a novel design of no-insulation HTS magnet, which adopts solder as turn-to-turn impregnation. Solder impregnated no-insulation HTS magnets are further strengthened using solder. The manufacturing process is different for the two types and so are their properties. Sections 5.2 and 5.3 below detail the processes and the properties.

5.2. Conventional no-insulation HTS magnets

This section presents the fabrication of a conventional no-insulation (NI) HTS REBCO magnet. As a comparison, a Kapton tape insulated REBCO coil is also fabricated. Fig. 5.1 shows the winding process and final samples of a Kapton-tape insulated HTS REBCO coil and a no-insulation HTS REBCO coil. In this thesis, they are named as "INS REBCO coil" and "NI REBCO coil" respectively.

One high-quality 30-metre long REBCO coated conductor tape with uniform I_c is cut into two 15-metre long RECBO coated conductor tapes. Two tapes are used to wind the INS REBCO coil and NI REBCO coil. These REBCO CC tapes have two 100 μm copper tapes laminated on both sides, which are manufactured by the *Shanghai Superconductor Technology Company (SSTC)*. The critical current of the REBCO CC tape is around 100 A. The schematic plot of the multilayer structure of the REBCO coated conductor is presented in Fig.1.13. For the traditional HTS Kapton tape insulated coil magnet, insulation must be provided for the HTS tapes before coil winding. A high-temperature material call "Kapton tape" is used as the insulation layer. The REBCO tape co-wounded with one layer of Kapton tape can be found in Fig. 5.1 (a), where the Kapton tape is in brown. The Kapton tape is resistant at very low temperatures, such as 77 K, so that it can provide high-quality inter-turns insulation in a very low-temperature environment. For no-insulation HTS magnet, no insulation layer is used for

HTS tape before being wound into NI coils, which is shown in Fig. 5.1 (b). A double pancake (DP) coil structure is adopted for the HTS INS coil and the HTS NI coil. An insulation layer is inserted into the gap between two pancakes, as shown in Fig. 5.1 (a) and (b). Fig. 5.1 also shows the photos of the experimental sample coils: a REBCO Kapton tape insulated (INS) coil and a REBCO NI coil after coil winding. The white adhesive tapes are used to fasten the coil magnet. The inner diameter of the NI REBCO coil is 63 mm, the outer diameter of the NI REBCO coil is 88 mm. The inner diameter of the INS REBCO coil is 63 mm, the outer diameter of the INS REBCO coil is 85 mm. The total number of turns is 60 for both INS and NI coils, which means that every single pancake has 30 turns.

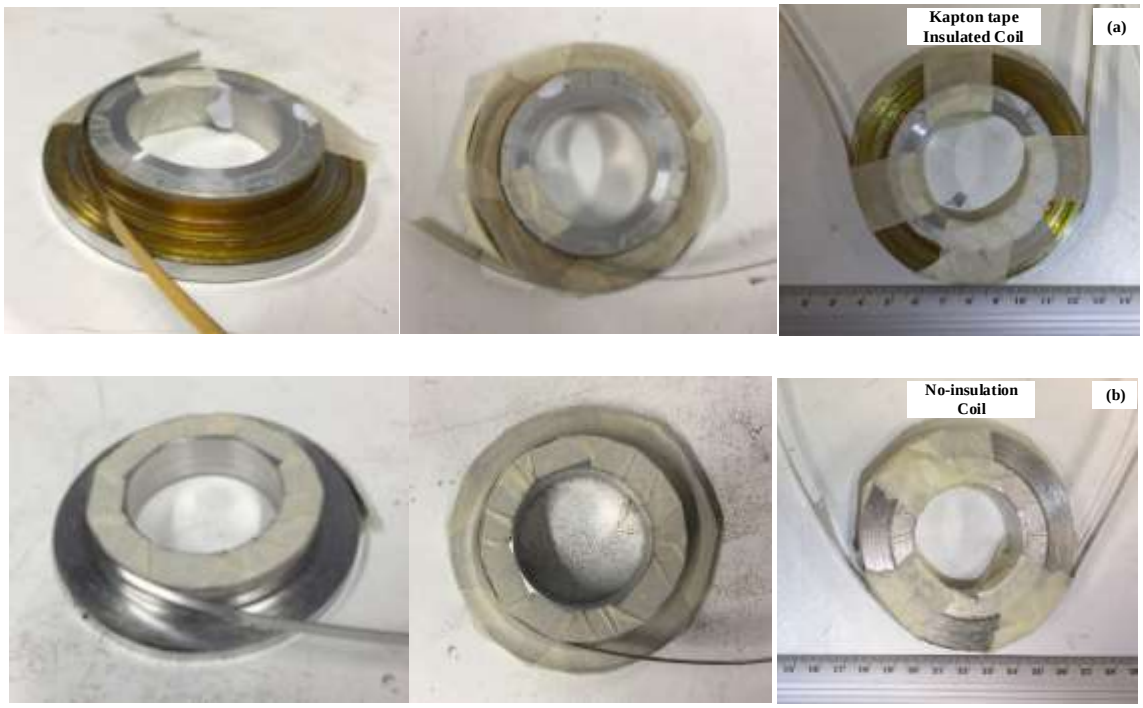

Fig. 5.1. Winding process of (a) a Kapton-tape insulated HTS coil made by REBCO coated conductor, which is named as "INS REBCO coil" in this thesis; and (b) a traditional no-insulation HTS coil also made by REBCO coated conductor, named as "NI REBCO coil".

Fig. 5.2 shows the V-I (voltage-current) curves of the NI REBCO coil and INS REBCO coil. The critical current of the NI coil is around 65 A, the critical current of the INS coil is 62 A. A criteria of 10^{-4} V/m is used to determine the critical current of the coil. The length of HTS tape for both coils is the same: ~15 m. So the critical voltage for both coils should be around 1.5 mV.

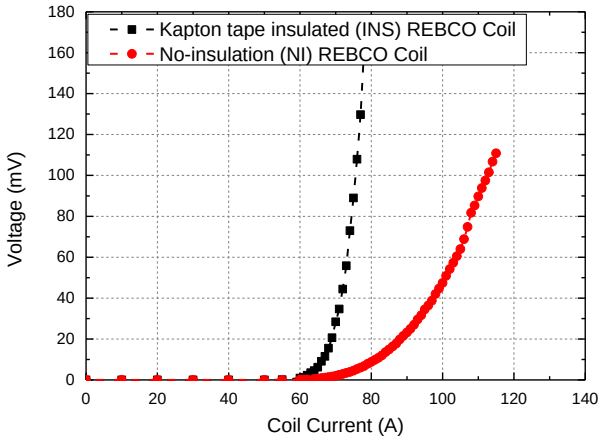

Fig. 5.2. The *V-I* (voltage-current) curves of the NI REBCO coil and INS REBCO coil. The I_c of the INS REBCO coil is 62 A, the I_c of NI REBCO coil is 65 A. Both coils are wound with the same 15-meter-long REBCO coated conductor, whose critical current is around 100 A.

(a) (b)

Fig. 5.3. (a) Power supply and (b) nanovolt meters for measuring the *V-I* curve of HTS coils.

Fig. 5.4 shows the equivalent circuits for the INS REBCO coil and NI REBCO coil [1]. R_c is called "characteristic resistance", which is an equivalent component in the electrical circuit. It is a result of the turn-to-turn contact resistance and the resistance of the substrate layer in the REBCO coated conductors. When the current bypass through the turn-to-turn contact resistance and the substrate layers, a dissipative loss will be generated and the overall impact is represented by the "characteristic resistance" (R_c). Characteristic resistance leads to a charging delay of HTS NI coil magnet, compared to the INS coil. A lower R_c will lead to a slower charging process for the HTS NI magnet. In order to control the value of the R_c, a constant large force is required to be applied, during the winding process, to the winding tape to prevent a loose coil winding. The winding force will determine the quality of the turn-to-turn contact, which influences the value of the characteristic resistance (R_c) of the NI coil. This process is especially important for making a NI HTS REBCO magnet.

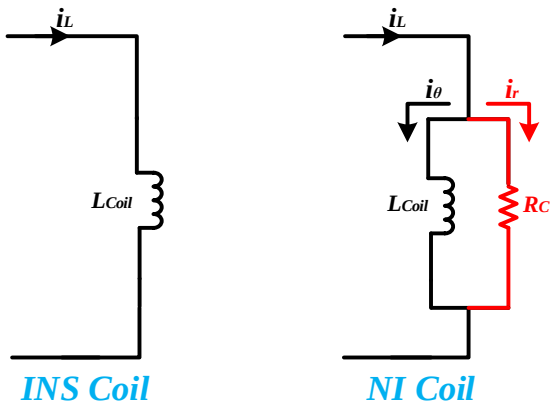

Fig. 5.4. The equivalent circuits for the INS REBCO coil and NI REBCO coil [1].

Characteristic resistance R_c can be measured by the following experimental measurements:

Step (1): Measure the coil inductance (L_{coil}) of the INS REBCO coil with the same geometry and number of turns with the HTS NI coil. These two coil magnets with the same geometry and number of turns will have the same coil inductance in the superconducting state. The inductance of the INS coil can be measured by an inductance meter, while it doesn't work for HTS NI coil because the inductance meter is shorted by the inter-turns contact, or we can say the R_c as shown in the equivalent circuit of NI coil. Fig. 5.5 shows the inductance meter we used. The coil inductance (L_{coil}) of the INS REBCO coil is 122.8 μH. We assume that the coil inductance (L_{coil}) of the NI REBCO coil in the superconducting state is around 120 μH.

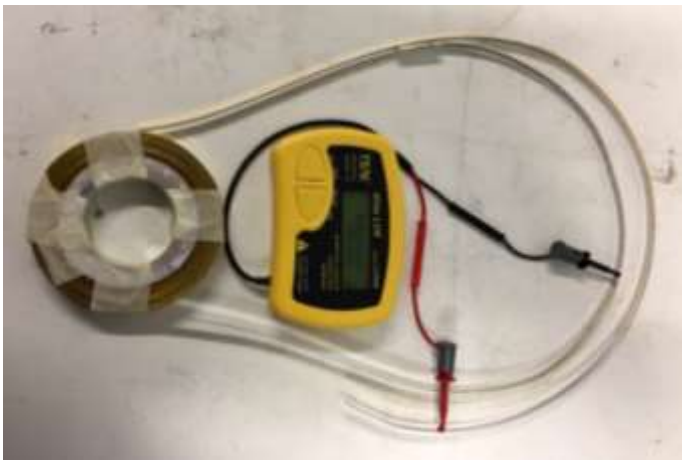

Fig. 5.5. Measurement of coil inductance (L_{coil}) of the INS REBCO coil via an inductance meter: "*atlas model LCR40*" manufactured by *PEAK electronic design ltd.*

Step (2): Measure the Time Constant (τ) through the sudden discharge test for the NI coil. Time constant refers to the time taken for the magnetic field density (or coil current) to decrease by a factor of *1-1/e* (approximately 0.6321), which can be calculated from the sudden discharge curve. The sudden discharge curves of the NI REBCO coil and the INS REBCO coil are shown in Fig. 5.6. From Fig. 5.6, the time constant (τ) for NI REBCO coil is 0.4 s. The double peaks in the coil voltage (blue line) could be triggered by the instability of the power supply, which doesn't impact on our results significantly.

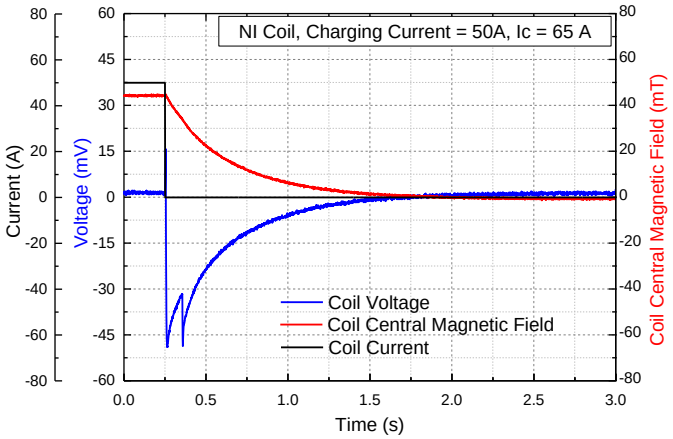

Fig. 5.6. The sudden discharge curves of the NI REBCO coil. A 50 A DC constant charging current is supplied and suddenly removed.

Step (3): Calculate the characteristic resistance (R_c) according to experimentally measured coil inductance (L_{coil}) and time constant (τ) of magnetic field decay of the NI REBCO coil, as mentioned in above steps. R_c can be calculated from the equation (5.1): R_c = 120 μH / 0.4 s = 300 $\mu\Omega$.

$$Rc = \frac{Lcoil}{\tau} \tag{5.1}$$

Table 5.1. summarizes the specifications of the INS REBCO coil and NI REBCO coil.

Table.5. 1. Specifications of INS REBCO Coil and NI REBCO Coil.

	Kapton Tape Insulated REBCO Coil	No-insulation REBCO Coil
I_c of YBCO tape	100 A	100 A
I_c of coil	62 A	65 A
Outer Diameter	85 mm	88 mm
Inner Diameter	63 mm	63 mm
Number of Turns	30SP/60DP	30SP/60DP
L_{coil}	123 μH	$\approx$ 120 μH
R_c	∞	300 $\mu\Omega$

5.3. Solder impregnated no-insulation HTS magnet

The initial aim of solder impregnation here is to reduce the characteristic resistance (R_c) of the NI REBCO coil by reducing the turn-to-turn contact resistance. But luckily, we found other excellent properties of this novel type of no-insulation HTS coil design, such as excellent mechanical robustness, significantly enhanced thermal and electrical stability, and reinforced self-protection and defect-free abilities. The manufacturing process of this novel solder impregnated no-insulation HTS REBCO coil is illustrated as below:

Step (1): Winding no-insulation coil before solder impregnation: To ensure that this new coil magnet has the same coil inductance, we wind this new coil magnet with the same double pancake structure and with the same number of turns (30SP/60DP). The critical current of the RECBO tape is 95 A, which is manufactured by *SuperPower*. Before the solder impregnation, the REBCO NI coil after winding is presented in Fig. 5.7 (a).

Step (2): Solder impregnation: A low-temperature solder (6337 Alloy) is used to achieve a relatively low heating temperature of the heater. It consists of 63% Sn (stannum) and 37% PB (plumbum). A solder pot (SWT-2000 lead-free solder pot) is used to maintain the melting temperature of the 6337-alloy solder. The power of the solder pot is 2 kW, the working (heating) temperature is 0-600 ℃. The solder and heater are presented in Fig. 5.8 (a) and (b). The 6337-alloy solder is firstly heated to the melting point at around 185 ℃, and the temperature is maintained at around 185 ℃ by the solder pot. Then the REBCO NI coil is placed in the tank

of the solder pot for a while (around 15 s -20 s) to let the liquid solder impregnate into turn-to-turn air gap of the REBCO NI coil. Afterward, the solder impregnated REBCO NI coil is taken out from the solder pot. After totally cools down, the new solder impregnated REBCO NI magnet coil is polished by sandpaper. Fig. 5.7 (b) shows a photo of the no-insulation REBCO coil after solder impregnation.

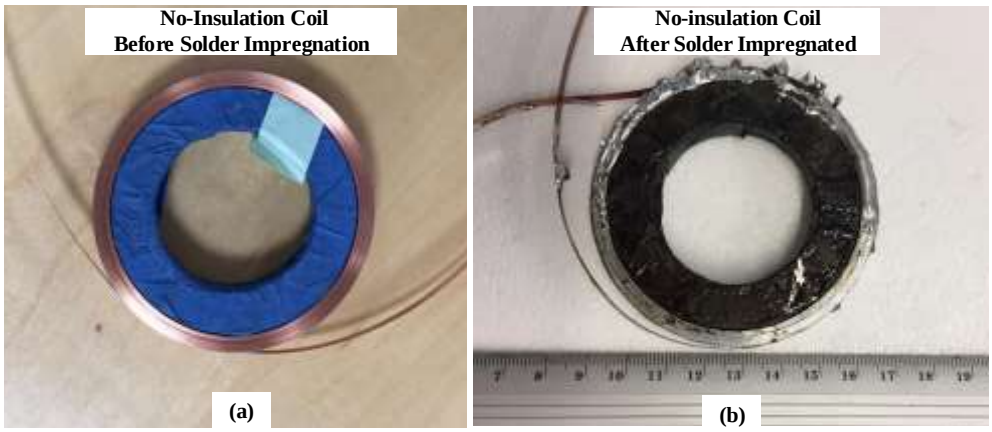

Fig. 5.7. Photos of no-insulation REBCO coil magnet (a) before solder impregnation and (b) after solder impregnation.

Fig. 5.8. Photos of the 6337 alloy (63% Sn (tin), 37% Pb (lead)) low temperature solder and solder port for solder impregnation process.

The original critical current of the RECBO CC tape is 95 A, however, after solder impregnation, the critical current of the no-insulation REBCO coil is only around 35 A, which is much smaller than the critical current of the INS REBCO coil (62 A) and NI REBCO coil (65 A) which are made from RECBO CC tape with a similar critical current of 100 A. The reason is that: the solder impregnation process has a high temperature up to ~185 ℃ to ~190 ℃, which caused I_c degradation of the REBCO layer in the coated conductors [145, 146]. This is a disadvantage of the solder impregnated no-insulation REBCO coil. Future work should

research on how to protect the HTS REBCO coated conductors from the high temperature during the solder impregnation process. Adopting a soldering material with a lower melting point seems to be a good solution, and this can be meaningful future work.

The solder impregnation has greatly increased the mechanical property of the no-insulation REBCO magnet. As shown in Fig. 5.7 (b), the liquid solder becomes a solid solder after it is cooled down, and it makes the impregnated no-insulation REBCO coil a whole solid bulk magnet which has excellent mechanical properties. Strong mechanical property is very important for high field magnet applications, especially when field > 20 T. In the high field applications, the insulated HTS magnet breaks down due to both thermal quench and mechanical damage caused by huge Lorenz Force. The huge Lorenz Force is induced by the large transport current under ultra-high magnetic field [71, 103-110]. For the conventional no-insulation HTS magnets, the problem of thermal breakdown has been solved, but the mechanical breakdown problem still exists. The novel solder impregnation technology for no-insulation HTS REBCO magnets will help solve the long-lasting mechanical breakdown problem and improve the reliability of the HTS magnet systems.

The sudden discharge curve for the solder impregnated REBCO NI coil is presented in Fig. 5.9. The time constant (τ) is 120 s. The coil inductance is assumed as the same value with the REBCO INS (120 μH), because they share similar geometries and a similar number of turns. The characteristic resistance of the solder impregnated NI REBCO coil is calculated according to equation (5.1): R_c = 120 μH / 120 s = 1 $\mu\Omega$.

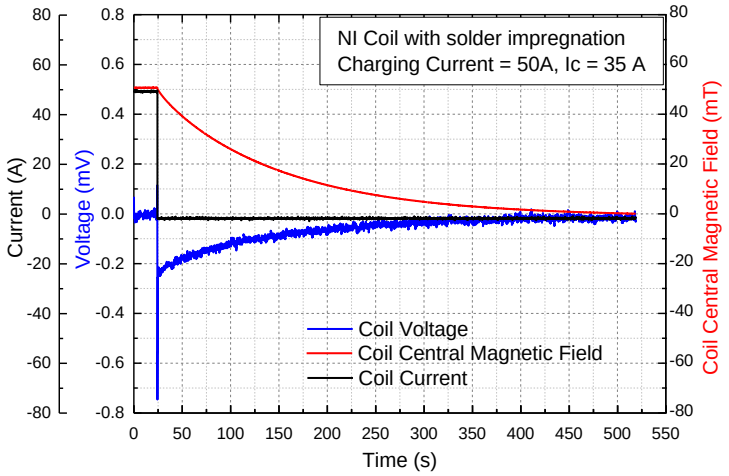

Fig. 5.9. Sudden discharge curves of NI REBCO coil after solder impregnation. A very slow decay process is observed, which means a very small characteristic resistance (R_c).

Table.5. 2. Specifications of the Kapton tape insulated (INS) REBCO coil, the conventional no-insulation (NI) REBCO coil, and the novel solder impregnated NI REBCO coil.

	INS Coil	Conventional NI Coil	Solder Impregnated NI Coil
I_c of YBCO tape	100 A	100 A	95 A
I_c of coil	62 A	65 A	35 A
Outer Diameter	85 mm	88 mm	78 mm
Inner Diameter	63 mm	63 mm	63 mm
Number of Turns	30SP/60DP	30SP/60DP	32SP/64DP
Inductance	123 μH	$\approx$ 120 μH	$\approx$ 120 μH
R_c	∞	300 $\mu\Omega$	1 $\mu\Omega$

The specifications of the novel solder impregnated REBCO NI coil is presented in Table.5.2. Specifications of the Kapton tape insulated (INS) REBCO coil and the traditional REBCO NI coil are also presented in Table. 5.2.

Compared to the conventional no-insulation REBCO coil wound by similar REBCO CC tape and with the same geometry and number of turns, the solder impregnated no-insulation REBCO coil has significantly smaller characteristic resistance (R_c). The reason is that the solder impregnation significantly increases the quality of turn-to-turn contact, and greatly reduces the inter-turns contact resistance. But one advantage of the solder impregnation is that: the characteristic resistance (R_c) is constant and won't change due to the oxidization of the metal contact.

In order to increase the characteristic resistance (R_c) of the solder impregnated no-insulation HTS magnet, there are two potential solutions: (1) use one layer or more layers of metal co-wound tape to increase the turn-to-turn bypass resistance. (2) use a higher resistive soldering material. These solutions could be studied in future work.

A series of overcurrent tests are performed on the solder impregnated no-insulation HTS REBCO coil. Fig. 5.10 shows the charging curves of the solder impregnated no-insulation HTS REBCO coil under different overcurrent, up to 1.4 times (50A), and 1.7 times (60A) of the coil I_c (coil I_c =35 A). Results show that the solder impregnated no-insulation HTS REBCO coil has excellent overcurrent performance, which is a significant advantage for reliable and stable HTS applications.

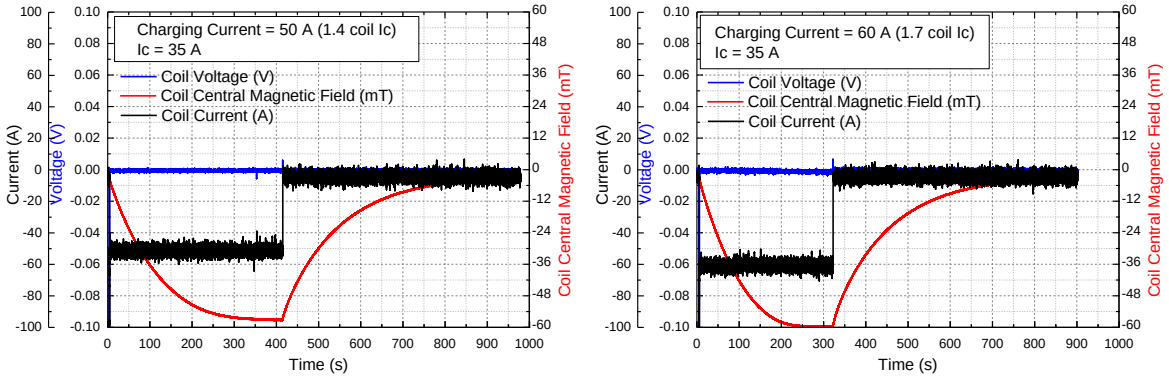

Fig. 5.10. Overcurrent tests for the solder impregnated no-insulation HTS REBCO coil: (a) charging current = 50 A = 1.4 I_c of coil, (b) charging current = 60 A = 1.7 I_c of coil. Under overcurrent up to 1.7 I_c of coil, the solder impregnated no-insulation HTS REBCO coil still works in good condition.

The solder impregnated no-insulation REBCO coil has several significant advantages:

1. The solder impregnation significantly increases the mechanical property of the magnet. In high field applications, the superconducting magnets break down mainly due to thermal quench and mechanical damage caused by huge Lorenzo Force. For conventional no-insulation HTS magnets, the thermal breakdown problem has been solved, but the mechanical breakdown problem still exists. The novel solder impregnated no-insulation REBCO magnets will solve the long-lasting mechanical breakdown problem and improve the reliability of the HTS magnet systems.

2. Excellent overcurrent performance. The solder impregnation enables an excellent electrical and thermal turn-to-turn contact, which leads to a better current bypass ability and a better internal heat transfer. These two characteristics help prevent the development of hotspots inside the HTS magnet and increase reliability.

3. The solder impregnation can occupy the turn-to-turn air gap space, which leads to high-quality turn-to-turn contact and prevent turn-to-turn oxidization. The turn-to-turn oxidization could potentially lead to R_c increase after a long operating time, and the solder impregnation could be a solution, which makes R_c a constant value.

The solder impregnated NI REBCO coil, however, has two major disadvantages:

1. Solder impregnation makes R_c smaller than the conventional NI REBCO coil without solder impregnation, which leads to a bigger charging delay.

2. The impregnation process requires a high temperature environment for solder-melting, and this process will cause thermal damage to the REBCO conductors and leads to a considerable I_c degradation. In our experiments, the I_c of the solder impregnated REBCO NI coil (35 A) is around half value of the I_c for traditional INS (62 A) and NI coils (65 A).

To conclude, the advantages of solder impregnated no-insulation REBCO coil outweigh its disadvantages. The excellent mechanical property and high thermal and electrical reliability will solve the long-lasting mechanical breakdown problem and enhance the reliability of HTS magnets. Its disadvantages such as the low characteristic resistance (R_c) and decline of coil I_c can be possibly improved by using a higher resistive soldering material with a lower melting point or using co-wound metal layers. We believe that this novel solder impregnated no-insulation REBCO HTS magnet has a huge potential in the high-field magnet systems.

5.3. Chapter summary

This chapter presents the design and fabrication of a conventional NI HTS REBCO magnet and a novel solder impregnated NI HTS REBCO magnet. The solder impregnated NI HTS REBCO magnet has strong mechanical properties and excellent overcurrent performance. This novel magnet design can solve the long-lasting mechanical breakdown problem for the superconducting magnets. We believe that this novel type of solder impregnated NI HTS REBCO magnet has a promising and broad application in the high field magnet systems, including tokamak fusion devices, the particle accelerator magnet system, and the NMR/MRI systems.

Chapter 6
Flux Pumping for No-insulation HTS REBCO Magnets

The NI REBCO magnet has many unique advantages, including high operating temperature, excellent critical current performance under high magnetic fields, strong mechanical properties, and a unique self-protection ability. Due to these excellent properties, NI REBCO magnet is believed to have the ability to pave the way for a compact, economical, and highly reliable superconducting magnet system. Currently, very limited research work can be found on flux pumping technology for NI HTS REBCO magnets.

This chapter studies the flux pumping characteristics of the active switching HTS TRFP for NI HTS magnets. We compared the flux pumping characteristics of three different types of HTS REBCO magnets, including the insulated REBCO magnet and the NI REBCO magnets. We focused on the study of NI REBCO coil with a large R_c and a novel solder impregnated NI REBCO coil with a very small R_c. We will show that the active-switching HTS TRFP is very suitable for charging the NI REBCO coil magnet, including the conventional NI REBCO coil (without solder impregnation) and the novel soldered impregnated NI REBCO coil magnet. Optimization methods were proposed to improve the flux pumping performance for the NI HTS magnets with a very small R_c, making it comparable to using external DC current power supplies.

6.1. Flux pumping characteristics for no-insulation HTS magnets

This section studies the flux pumping characteristics of the active-switching HTS TRFP for no-insulation type HTS magnets. We use the active switching HTS TRFP constructed in chapter 4 to pump three different HTS REBCO coil magnets, including two no-insulation HTS coil magnets with a high R_c and a low R_c, and an insulated HTS RECBO coil. The two NI HTS

REBCO coils are the conventional NI HTS REBCO coil and the novel solder impregnated NI HTS REBCO coil presented in chapter 5. The pumping characteristics of three different HTS coils are studied and compared comprehensively. This study will help researchers understand the electro-magnetic transient behaviors of pumping no-insulation type HTS magnets, and build a solid foundation for the future optimization on the TRFP for NI HTS magnets.

6.1.1. Comparison between no-insulation coil and insulated coil

In this section, we present a comparison of the charging characteristics between three different HTS coils. The specifications of three different HTS coils are presented in Table. 6.1.

Table. 6.1. Specifications of the Kapton tape insulated (INS) HTS coil, the conventional no-insulation (NI) HTS coil, and the novel solder impregnated NI HTS coil.

	INS Coil	Conventional NI Coil	Solder Impregnated NI Coil
I_c of YBCO tape	100 A	100 A	95 A
I_c of coil	62 A	65 A	35 A
Outer Diameter	85 mm	88 mm	78 mm
Inner Diameter	63 mm	63 mm	63 mm
Number of Turns	30SP/60DP	30SP/60DP	32SP/64DP
Inductance	123 μH	$\approx$ 120 μH	$\approx$ 120 μH
R_c	∞	300 $\mu\Omega$	1 $\mu\Omega$

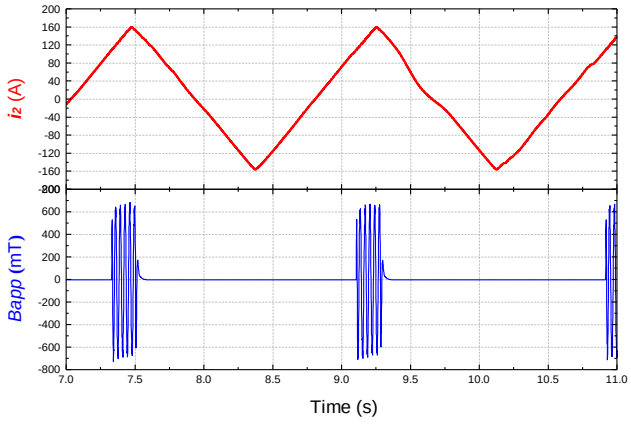

Fig. 6.1. Waveforms of the secondary current i_2 in the copper/HTS transformer and the AC switching field B_{app} of the HTS switch on the bridge section.

Fig. 6.1 shows the waveform of i_2 and B_{app}. The waveform of i_2 is symmetrically triangular, the peak value of i_2 is 160 A, and the frequency of i_2 is 0.56 Hz. B_{app} is applied around the positive peak of i_2 with a phase difference of 30 degrees. The field duration is 0.1 times of the period of i_2. The magnitude of B_{app} is 685 mT, and the frequency is 28 Hz. The waveforms of i_2 and B_{app} are carefully adjusted to minimize the differences during charging the three different coils.

The current in no-insulation HTS magnet consists of two parts: the azimuthal current i_θ flowing through the YBCO tape, and radial bypass current i_r flowing through the turn-to-turn bypass current path in NI coil. Therefore, we monitor the i_θ from the magnitude of the coil central magnetic field B_{coil}, because the radial bypass current i_r cannot contribute to the coil central magnetic field.

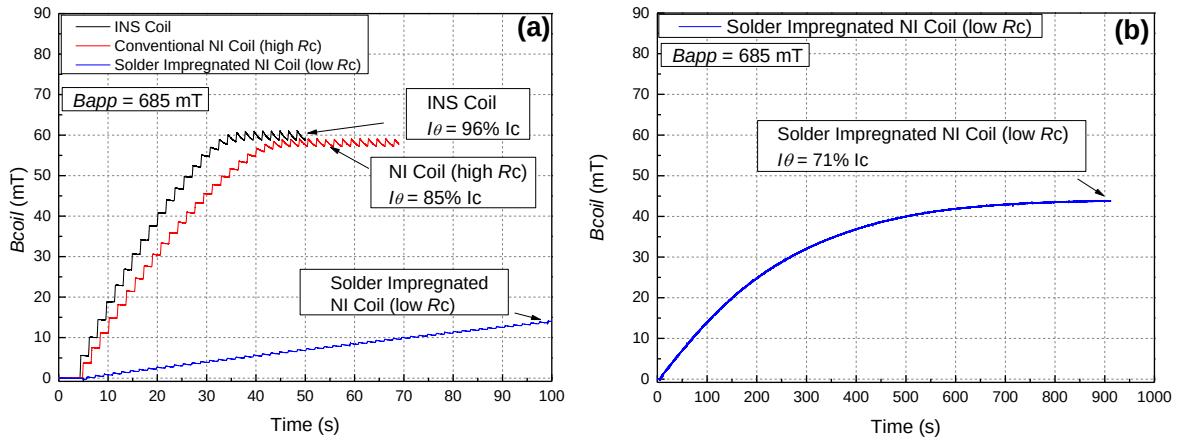

Fig. 6.2. Charging curve comparison between INS coil, NI coil with high R_c, and solder impregnated NI coil with low R_c: (a) Overall comparison for three HTS coils, (b) charging curve for the solder impregnated NI coil with a low R_c. The frequency of i_2 is 0.56 Hz. B_{app} is applied around the positive peak of i_2. The field duration is 0.1 times of the period of i_2. The magnitude of B_{app} is 685 mT, and the frequency is 28 Hz [145].

Fig. 6.2 shows the pumping curve (B_{coil}, coil center field) comparison between the INS coil, the conventional NI coil with a high R_c, and the solder impregnated NI coil with a low R_c. Fig. 6.2 shows that the pumping speed of the no-insulation HTS coils is slower than that of INS HTS coils. And the pumping process of the low-R_c solder impregnated NI coil is much slower than that of the high-R_c conventional NI coil. The pumping processes of the INS coil and the high-R_c NI coil take 32s and 40s respectively, whereas the pumping process of the low-R_c solder impregnated NI coil takes up to about 720s, almost 22.5 times of the INS coil's pumping time and 18 times of the high-R_c NI coil's pumping time. The characteristic resistance (R_c) of

the conventional NI coil and the solder impregnated NI coil are 300 $\mu\Omega$ and 1 $\mu\Omega$ respectively. The huge difference in R_c leads to a significantly different pumping speed.

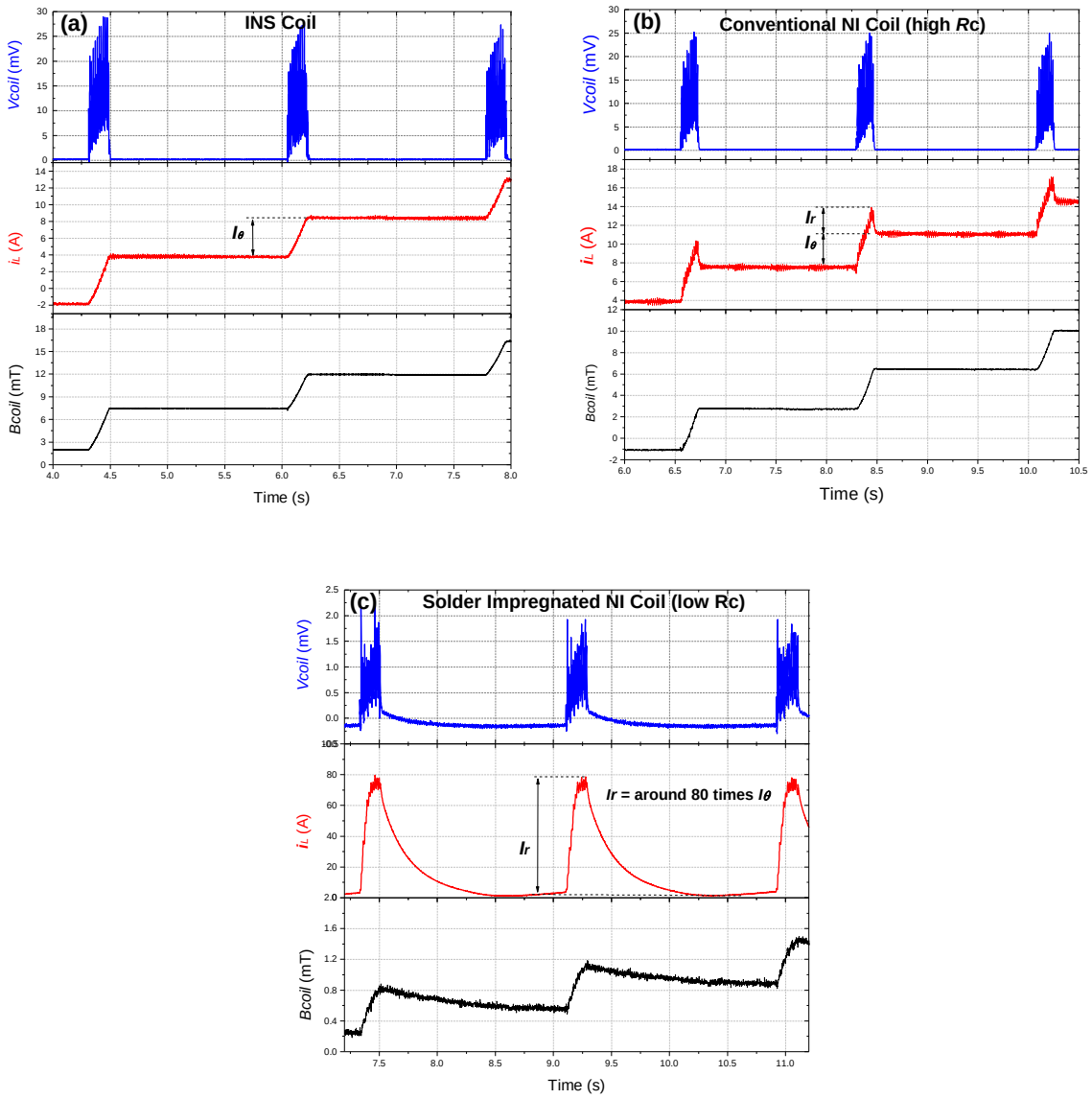

Fig. 6.3. Pumping details of the INS coil, conventional NI coil (high-R_c), and low-R_c novel solder impregnated NI coil, where B_{app} = 685 mT [145].

To investigate the pumping characteristics, we plotted the pumping details of each coil during the initial stage of the pumping process in Fig. 6.3. In each set of figures, the upper curve is the induced voltage V_{coil} on the HTS switch across the load HTS coil, the curve in the middle is the coil current i_L, and the lower curve is the magnetic field in the coil center B_{coil}. As we can see in Fig. 6.3, the curves differ greatly for three HTS coils.

Voltage of the coils:

As shown in Fig. 6.3, the peak voltage (V_{coil}) is 29 mV for the INS coil, and 25 mV for the high-R_c conventional NI coil, but only around 2.0 mV for the low-R_c solder impregnated NI coil. The huge difference in DC voltages (V_{coil}) leads to the different pumping speeds.

The reason for a much smaller coil voltage (V_{coil}) for low-R_c solder impregnated NI coil can be understood from the equivalent circuit in Fig. 6.4. The load impedance of the INS coil is dominated by the inductance which is 123 μH. The load impedance of the NI coil (including conventional NI coil and solder impregnated NI coil) is determined by the characteristic resistance (R_c) and coil inductance (L_{coil}) in parallel. Considering R_c of the conventional NI coil is 300 $\mu\Omega$, which is 2 times higher than the coil inductance, the impedance of the conventional NI coil is also dominated by the inductance. In contrast, the R_c of the solder impregnated NI coil is only 1 $\mu\Omega$, which means the overall load impedance is very low. When an AC field is applied to the bridge switch, a dynamic resistance (R_{dyn}) is generated, which is dependent on the bridge transport current i_B when the applied field magnitude is not much higher than the threshold value [30, 33]. The dynamic resistance is in parallel with the load impedance, sharing a current proportional to the load impedance. In this case, with the same i_2, i_B is much lower for the solder impregnated NI coil than for the conventional NI coil or INS coil, and the dynamic resistance (R_{dyn}) is also lower. Since V_{coil} equals to $i_B \times R_{dyn}$, it is easy to understand that the voltage across the low-R_c solder impregnated NI coil is much lower than that of the other two coils (high-R_c conventional NI coil, and INS coil).

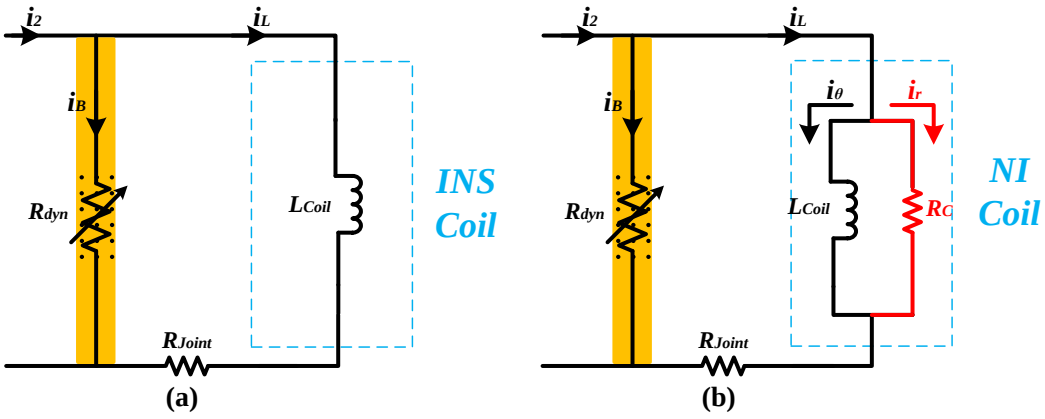

Fig. 6.4. Simplified circuits of flux pumping system for (a) the INS coil and (b) the NI coil.

Current and magnetic field of the coils:

Fig. 6.3 also shows the load current i_L and magnetic field in the center of the coils B_{coil}.

For the INS coil, i_L is always proportional to B_{coil}. Due to the turn-to-turn insulation, all coil current flows azimuthally. Each time the bridge voltage is induced, the current i_L increases by over 4.3A.

For the high-R_c conventional NI coil, each time the DC voltage (V_{coil}) is induced, the coil center field B_{coil} rises monotonically, whereas the current i_L presents an overshoot. The current increases by 6A, followed by a sharp decrease of about 2.5A. The difference between the curves of i_L and B_{coil} indicates a radial bypass current is i_r induced. The value of this current is about 2.5A, which contributes to 41.6% of the total current increase of 6A. The difference between i_r and Δi_L is the actual increase of the azimuthal current i_θ, which is 3.5A.

For the low-R_c solder impregnated NI coil, the pumping curves are very different from those of the INS coil and conventional NI coil. During each cycle of the secondary current, when the DC voltage on the bridge (switch) is induced by the applied AC field, the load current i_L ramps to 79.5A, and then reduced by over 78.5A. The azimuthal current increase is less than 1A during each cycle, whereas the radial bypass current is over 80 times larger than this azimuthal current increase. The radial bypass current i_r decreases rather slowly after removing the applied field. The time constant of the decay of i_r is determined by the characteristic resistance R_c as well as an inductance formed by the leads of the coil (total inductance in the load loop minuses the coil inductance). Because R_c is only 1 $\mu\Omega$, it is reasonable that the radial current decay is slow. In terms of the slow charging speed of the low-R_c solder impregnated NI coil, it can also be explained by the huge amount of bypass current flowing through the radial turn-to-turn current path, or the equivalent parallel branch R_c. Another interesting phenomenon is that the center field of the NI coil also has a considerable decrease during the time the bridge field is not applied. This does not happen for the INS coil or high-R_c conventional NI coil. We are still not very clear about the reason of the field decay. It could be possible that the radial bypass current causes the decay in azimuthal current, but it still needs further investigation.

6.1.2. Impact of AC switching field: magnitude and frequency

This section presents a comparison of the impact of the applied magnetic field (B_{app}) on the flux pumping performance of active switching HTS TRFP for INS REBCO coil and solder impregnated NI REBCO coil.

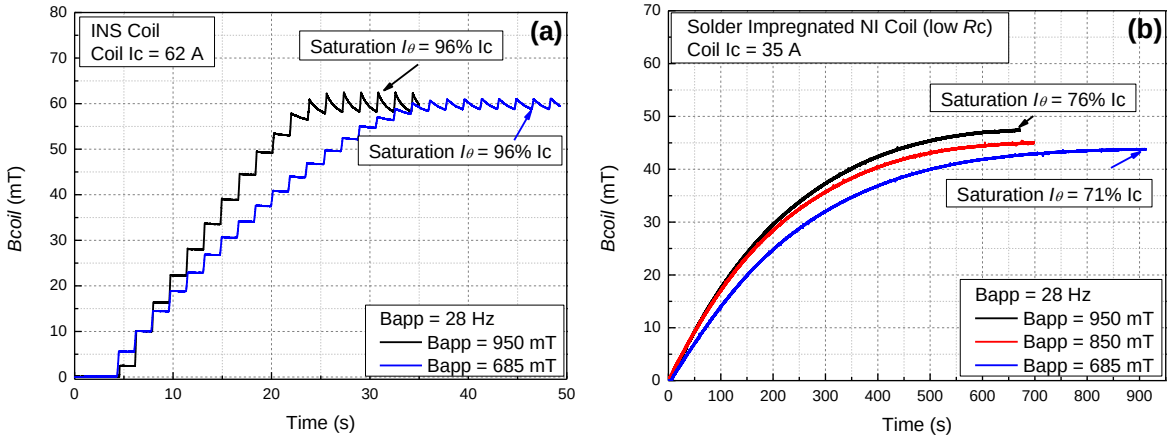

Fig. 6.5. Field magnitude dependence of flux pumping behaviour for (a) INS coil and (b) solder impregnated NI Coil. The frequency of i_2 is 0.56 Hz.

The impact of the magnitude of the AC switching field is shown in Fig. 6.5. Since the pumping behaviors of the INS coil and the high-R_c conventional NI coil are similar, as shown in Fig. 6.2 (a), we only present results for the INS coil and the solder impregnated NI coil (low-R_c). The magnitude of the applied magnetic field increased from 685 mT to 950 mT. Other experiment parameters were the same as those in previous sections.

As shown in Fig. 6.5, as the magnitude of the applied magnetic field increased from 685 mT to 950 mT, the charging time of the INS coil reduced from 32s to 21s, and the charging time of the solder impregnated NI coil reduced from about 720s to about 600s. It shows that increase the magnitude of the AC switching field can speed up the pumping process, but the speed is still very slow for low-R_c solder impregnated NI coil.

Take a further look at the details when the coil field curve reaches a quasi-steady state, there are field ripples for INS coil but no obvious field ripples for the novel solder impregnated NI coil (low-R_c). The ripple means the field will fluctuate, and the field fluctuation is smaller the better. The results show that the field is more stable in the novel solder impregnated NI coil. The reason for no obvious field ripples for the novel solder impregnated NI coil is that: the extra over-shot current will bypass the NI coil if a large voltage is applied to the NI coil.

For the INS coil, results show that the field ripples are smaller under smaller AC field magnitudes. It means that: If we want to sustain a more stable field, then a smaller AC field magnitude is preferred. This finding will help achieve a more stable field for the magnet. The reason is that: When the AC field magnitude is relatively higher, a higher DC charging voltage is generated for the HTS coil, which pushes the coil current further into a higher level to the flux flow region (which can be found in the curve of *E*-*J* Power Law), but an extra flux flow resistance together with the joint resistance (R_{joint}) in the load loop will lead to a faster decay speed in the field ripples. When the AC field magnitude is relatively small, the peak current is smaller so the flux flow resistance can be smaller or be ignored. In this case, the field ripple is smaller because the field decay is mainly caused by the joint resistance in the load loop.

To figure out the reasons behind the slow pumping process for the low-R_c solder impregnated NI coil, we plotted the curves of load loop current i_L for both the INS coil and the solder impregnated NI Coil in Fig. 6.6 and the curves of coil voltage V_{coil} for solder impregnated NI Coil in Fig. 6.7.

As shown in Fig. 6.6 (a) and (b), i_L for the solder impregnated NI Coil fluctuates greatly while i_L for the INS coil is very stable. This huge difference is caused by the bypass current phenomenon in the solder impregnated NI Coil. When a DC voltage is applied to the low-R_c solder impregnated NI coil, a huge overshot bypass current (i_r) was generated through the R_c brunch, as shown in Fig. 6.4 (b).

As time increases, the peak value of i_L decreases but the minimum value of i_L increases. This characteristic can be explained as: The minimum value of i_L increases because the coil current increases as pumping time increases, and the increase of the load loop current i_L leads to higher total resistance in the load loop. This resistance can be the flux flow resistance on some low I_c areas in the REBCO tape (because of the tape's nonuniformity) and the increases of the flux flow resistance in the REBCO coils (whose I_c is ~ 35 A).

In addition, as shown in Fig. 6.6 (b), the peak value of i_L increases as the magnitude of the AC applied magnetic field (B_{app}) on the "Bridge switch" increases. During the first 20s of the charging process, when the magnitude of the applied magnetic field (B_{app}) increases from 685 mT to 950 mT, the peak value of i_L increases from 75A to 93A, which are much smaller than the peak value of i_2 (160 A, as shown in Fig. 6.1). In contrast, the coil voltage (V_{coil}) increases from 2mV to 7.5mV in the first 20s, and from 2.5 mV to 13 mV in the quasi-steady state (400s

- 600s), as shown in Fig. 6.7. The coil voltage increase is much more significant than the current increase in the load loop (i_L).

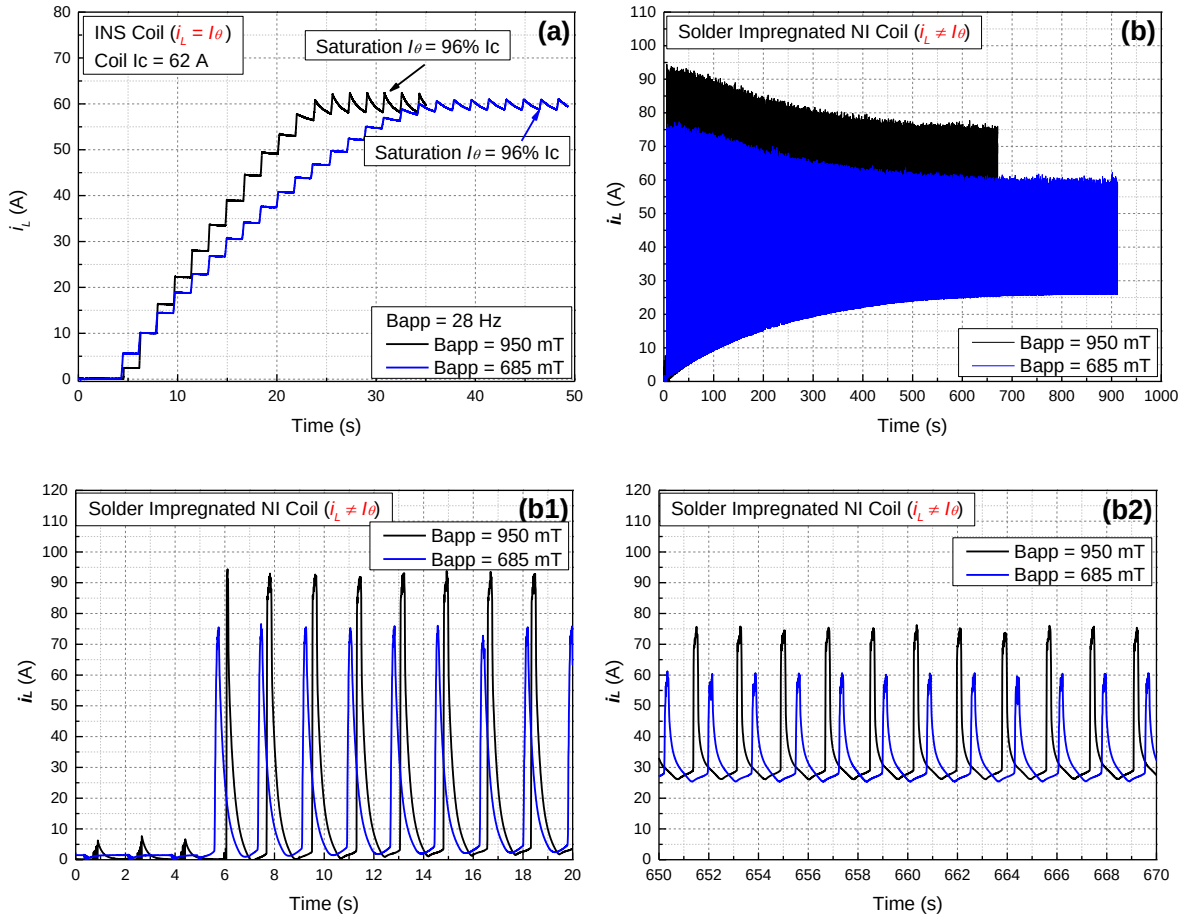

Fig. 6.6. Curves of load loop current i_L for (a) the INS coil and (b) the solder impregnated NI Coil. Different magnitudes of AC magnetic field are applied on the HTS "Bridge switch". (b) Overview curves; (b1) Detailed curves at start-up stage (0s-20s) and (b2) detailed current curves at saturation stage (650s-670s). B_{app} = 28 Hz.

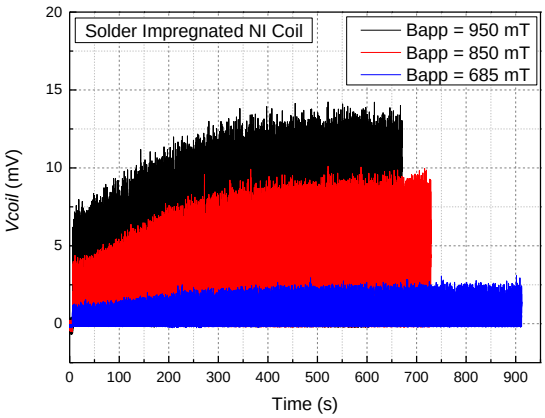

Fig. 6.7. DC voltage on the solder impregnated NI coil when different magnitudes of magnetic field is applied on the HTS "Bridge switch". B_{app} = 28 Hz.

We noticed that the peak value of i_L (75A - 93A, as shown in Fig. 6.6 (b)), which is much smaller than the peak value of i_2 (160 A, as shown in Fig. 6.1). This phenomenon could be explained as: YBCO tape of coil lead turned into the flux flow state when the coil current increases close to critical current. From the experimental results, the critical current of the YBCO tape is around 92A to 95A. In this case, a resistance (R_{tape}) can be generated, which is shown in Fig. 6.8. The R_{tape} shared a certain portion of the coil voltage, which limits the peak value of the coil current, not exceeding the critical current of tape too much. In addition, there is a small inductance in the load loop apart from the coil due to extra several turns of YBCO tapes (This is accidental due to the small size of the liquid nitrogen tank but the long length YBCO current leads), as shown in Fig. 6.8. This small inductance also shared a proportion of charging voltage in the load loop, reduced the DC voltage shared on the solder impregnated NI coil, and also limited the peak value of the load loop current (i_L).

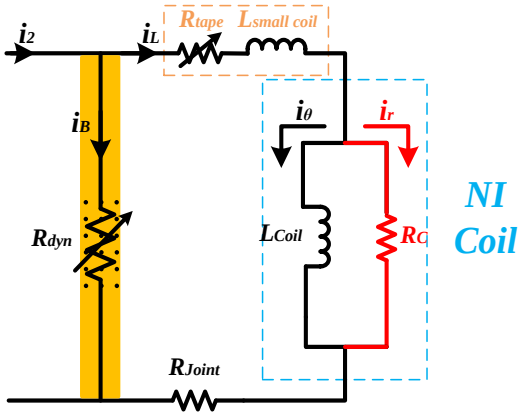

Fig. 6.8. Simplified equivalent circuit of the active switching TRFP system for the solder impregnated NI coil. (Two coil current lead YBCO tapes turn into the critical state when the load loop current increases close to critical current (95A), showing a resistance R_{tape} which cannot be ignored anymore. This resistance follows the *E-J* Power Law [9]. There are also several turns of YBCO tape (can be considered as a small coil, refers to the yellow $L_{small\ coil}$ in the load loop) in load loop close to the NI coil because the YBCO current lead is too long for the LN_2 container).

The impact of the frequency of the AC switching field is the same with the impact of the magnitude of the AC switching field, both magnitude and frequency play the same role: changing the dynamic resistance of the HTS bridge switch, and therefore adjusting the output capability of the TRFP.

6.1.3. Impact of secondary current in transformer

This section studies the impact of the secondary current in the copper/HTS transformer on the pumping performance for different types of HTS coils. A comparison of the secondary current i_2 frequency dependence of the TRFP for the INS coil and the low-R_c solder impregnated NI coil is presented in Fig. 6.9. The frequency of the secondary current increased from 0.56 Hz (1Hz/1.78) to 2.63 Hz (5Hz/1.78). Other experiment parameters were the same as the previous section.

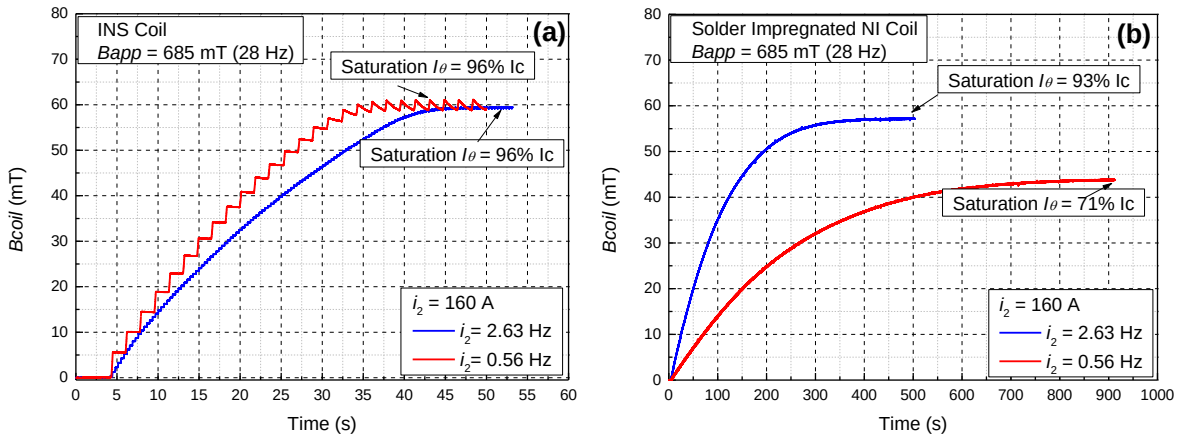

Fig. 6.9. Magnetic field (B_{coil}) curves of (a) the INS coil and (b) the solder impregnated NI coil with different frequencies of secondary current.

As shown in Fig. 6.9, increasing the frequency of i_2 can significantly reduce the pumping time of the solder impregnated NI coil, whereas the pumping time of the INS coil becomes slightly longer with the frequency increase.

The reason for the significant influence of the i_2 frequency on pumping speed for the solder impregnated NI coil can be figured out from the waveform of i_L. As shown in Fig. 6.10, the average value of i_L in 2.63 Hz is much higher than that in 0.56 Hz. In the 0.56 Hz charging test, during each cycle of i_2 the bridge field duration is 5 times that in 2.63 Hz test. However, i_L increase is much less than 5 times. This is on one hand because the amount of flux injection into the load loop via the bridge of 0.56 Hz is less than that of 2.63 Hz due to the bridge current dependence of flux motion; on the other hand i_L in 0.56 Hz test is driven to a high value which is likely to induce flux flow in the leads of the load coil, limiting the further increase of i_L. After the AC switching field on the bridge switch is removed, i_L decay time in 2.63 Hz test is 1/5 of that in 0.56 Hz test, resulting in a higher final i_L at the end of an i_2 cycle. The higher average i_2 value leads to faster charging speed. This finding may be an effective strategy for

speeding up the charging process for the low-R_c NI coils, such as the solder impregnated NI HTS magnet. We expect the TRFP to be equivalent to a low-voltage but high-current power source. The ultimate aim is to maintain i_L at a high value throughout the period of i_2 no matter the bridge switch is on-state or off-state. The ideal value of i_L is just below the value which can induce resistance in the coil leads.

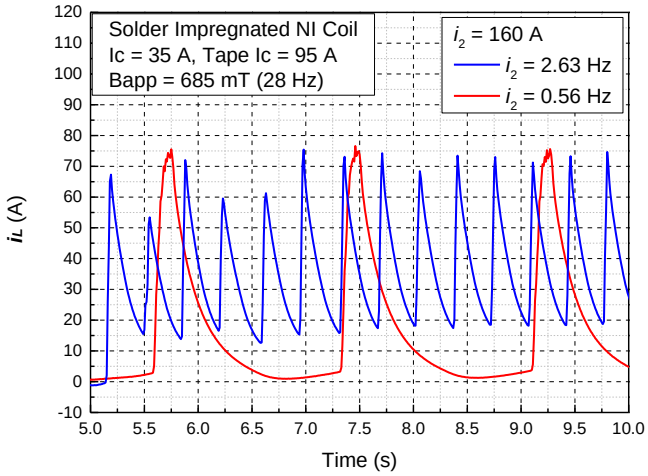

Fig. 6.10. Load current i_L of the solder impregnated NI coil with different frequencies of secondary current i_2 in the transformer.

6.1.4. Conclusion

This section studies the flux pumping characteristics of the active switching HTS TRFP for NI HTS REBCO magnets. A conventional NI REBCO coil with a high R_c, a novel soldered impregnated NI REBCO coil with a low R_c, and an insulated REBCO coil are pumped separately as a comparison. The experimental results show that the active-switching HTS TRFP works well for all three REBCO coils. However, compared with the conventional NI coil (without solder impregnation), the pumping speed of the solder impregnated NI coil with a small R_c is much lower. The main reason for the low charging speed of the solder impregnated NI coil is the low DC voltage generated for pumping the low-R_c solder impregnated NI coil, which is actually resulted from the low R_c of solder impregnated NI REBCO coil. A great proportion of the coil current flows through the low resistance radial turn-to-turn current path (R_c parallel brunch in the equivalent circuit) instead of through the relatively high inductance azimuthal current path. The result is similar to charging delay of NI coil by using external DC power supplies.

Impacting factors of the TRFP on flux pumping performance for different coils were also investigated. Increasing output voltage of the TRFP by increasing the magnitude and frequency of the AC switching field helps improve the pumping speed and final coil current. We also found that increasing the frequency of the secondary current (i_2) of the transformer can speed up the pumping process, and the effect is significant especially for pumping the low R_c solder impregnated NI coil. The mechanism of this method is that: the higher average value of the coil current leads to a faster charging.

The experimental results in this section provide a comprehensive understanding of the flux pumping characteristics as well as the technical limits of the TRFP for NI HTS magnet, especially those with very low R_c. This study has greatly deepened our understanding of the electro-magnetic transient behaviours of pumping for NI HTS magnets, built a solid foundation and provided important clues for the future optimization on the TRFP for NI HTS magnets, especially the NI HTS magnets with a very low R_c. The strategies and lessons learnt from the optimisation also works for pumping traditional insulated type HTS magnets.

6.2. Optimization on flux pumping for NI HTS magnets with low R_c

In the last section, we found the flux pumping performance for the low-R_c no-insulation HTS coil (soldered impregnated) needs to be further improved. The low R_c limits the pumping (charging) voltage and slows down the pumping speed significantly. This section focuses on further improving the flux pumping performance of the TRFP for the low-R_c solder impregnated NI REBCO coils, aiming at making it comparable to using external DC power supplies. In this section, we proposed and examined a new method [146] to speed up the flux pumping performance for the low-R_c (solder impregnated) NI coil by using the active switching TRFP. After the optimization, the flux pumping performance of the TRFP for the low-R_c solder impregnated NI HTS coil is comparable to using external DC power supplies.

6.2.1. Methodology: optimization on circuit design of TRFP

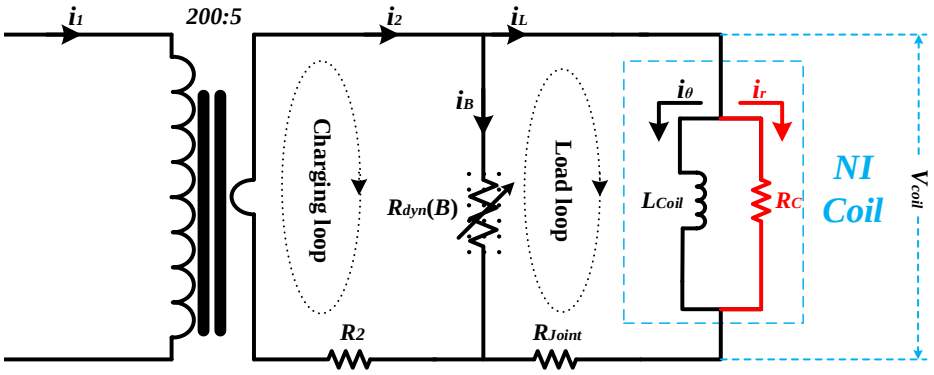

Fig. 6.11. An equivalent circuit of the TRFP for the HTS NI coil.

Fig. 6.11 shows the equivalent circuit of the TRFP with a NI coil. An alternating current i_2 with high magnitude is induced in the transformer secondary. Each AC cycle can be divided into two stages: during the first stage, an AC magnetic field is applied to the HTS switch on the bridge section, inducing a dynamic resistance $R_{dyn}(B)$ and a dc voltage across the bridge to charge the load HTS coil. During the rest of the time, the external magnetic field is removed and $R_{dyn}(B) = 0$, so the load HTS coil was shorted and current in the load maintains. In the last section, the charging details already presented**.**

Although the flux pump can charge the NI coil to close to its critical current, the charging speed is very slow. Since the value of R_c of the solder impregnated NI HTS coil is rather small ($1\mu\Omega$ level), the bridge current i_B tends to migrate to i_L when $R_{dyn}(B)$ appears, thus greatly reducing the induced dc voltage (V_{coil})e. The migration of current may also cause i_L to exceed the critical current of the coil terminations, causing a flux leakage in the load loop.

To cope with this problem (or to achieve fast charging), the core idea is to limit i_L. This may be achieved by adding a filtering inductor $L_{filtering}$ into the load loop, which is connected in series with the NI coil, as shown in Fig. 6.12. In the first stage, when the bridge switch is resistive (AC field is on), the filtering inductor and the NI coil are both charged. The existence of $L_{filtering}$ resists the migration of bridge current to i_L and limits the value of i_L. This helps to acquire a higher voltage (V_{coil}) across the bridge switch. In the second stage when the bridge switch superconducting (field is off), the energy stored in $L_{filtering}$ will transfer to the NI coil as long as the coil current is lower than i_L. In this way, due to the existence of the filtering inductor, the NI coil can be charged in both stages throughout the entire pumping process. In contrast,

if the filtering inductor does not exist, the NI coil can only be charged in the first stage when the bridge switch is resistive (the field is on). Adding in a filtering inductor may help boost the flux pumping speed of the TRFP for the low-R_c NI coil.

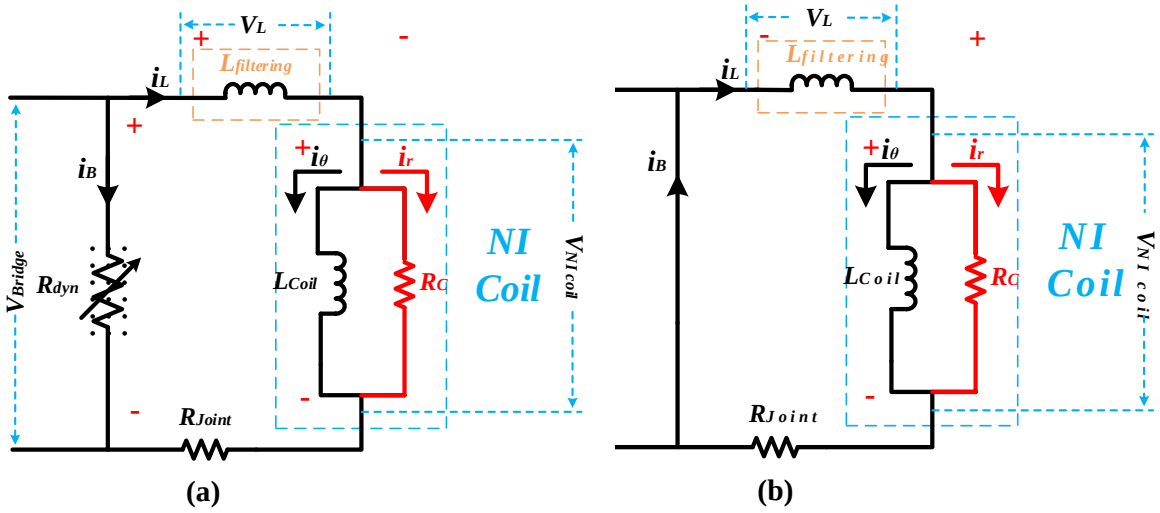

Fig. 6.12. Equivalent circuit of two stages in one charging cycle for NI coil when filtering inductor is added into the load loop of the flux pumping system: (a) The first stage: charging stage when bridge-field is on and (b) the second stage: recharging stage when bridge-field is off [146].

Specifically, when there is no filtering inductor as shown in Fig. 6.11, in the first stage the external magnetic field B_{app} is applied and the dynamic resistance $R_{dyn} \neq 0$, the bridge switch functions as a DC voltage source and the NI coil is being charged:

$$i_B R_{dyn} = i_r R_c = L_{coil} \frac{di_\theta}{dt} \tag{6.1}$$

$$i_L = i_r + i_\theta \tag{6.2}$$

The solder joint resistance is so small that it is ignored in the above equations.

In the second stage, the AC magnetic field B_{app} on the switch is removed, the dynamic resistance $R_{dyn} = 0$, the NI coil is shorted by the superconducting bridge switch and cannot be charged during this period. Since R_c is much larger than the joint resistance R_{Joint}, the NI coil current mainly flows through the bridge, instead of through the R_c branch. In this case, a very small proportion of stored electrical energy of NI coil is dissipated in the soldered joint R_{Joint}, causing a slow current decay, as shown in Equation (6.3).

$$i_L R_{Jo\,\mathrm{int}} = L_{coil}\frac{di_\theta}{dt} \tag{6.3}$$

When there is a filtering inductor $L_{\mathrm{filtering}}$, as shown in Fig. 6.12.

In the first stage, the dynamic resistance $R_{dyn} \neq 0$, both the filtering inductor and NI coil are being charged.

$$i_B R_{dyn} = L_{filtering}\frac{di_L}{dt} + L_{coil}\frac{di_\theta}{dt} \tag{6.4}$$

$$irR_C = L_{coil}\frac{di_\theta}{dt} \tag{6.5}$$

$$i_L = ir + i_\theta \tag{6.6}$$

In the second stage (recharging stage), the dynamic resistance $R_{dyn} = 0$. The filtering inductor releases its stored magnetic energy and works as a current power supply to charge the NI coil.

$$L_{filtering}\frac{di_L}{dt} = L_{coil}\frac{di_\theta}{dt} \tag{6.7}$$

To sum up, with the help of filtering inductor, the NI coil can be charged continuously at both stages. Besides, the filtering inductor can limit the peak value of i_L, making it smaller than the critical current of the coil terminations. Therefore, it is expected that the flux pumping speed will be improved by adding a filtering inductor. This method is validated via experiments in the following sections.

6.2.2. Experimental set up

We built an experimental system to verify the above method. In the system, a filtering inductor ($L_{\mathrm{filtering}}$) was added into the load loop, connected in series with the solder impregnated NI REBCO coil (with a low R_c = 1 $\mu\Omega$). The overall experimental as shown in Fig. 6.13.

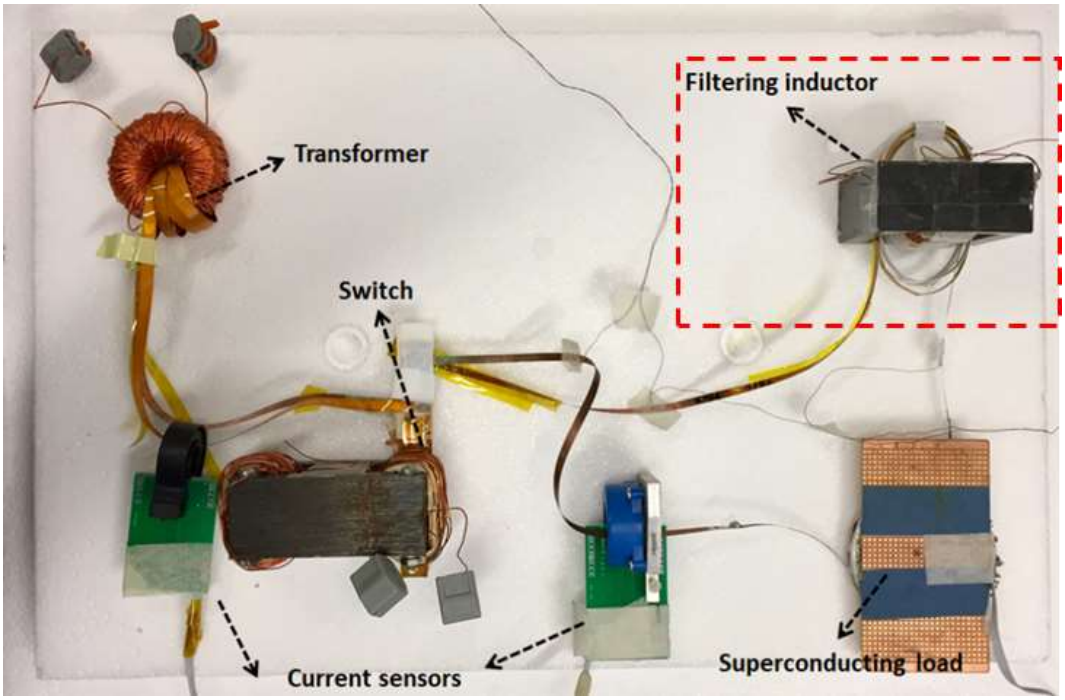

Fig. 6.13. Photo of the transformer-rectifier flux pump charging the solder impregnated NI coil (with low R_c = 1 $\mu\Omega$). A superconducting filtering inductor ($L_{filtering}$) is connected in series with the solder impregnated NI coil to speed up charging process.

Fig. 6.13 shows the structure of the superconducting filtering inductor ($L_{filtering}$). The filtering inductor ($L_{filtering}$) was fabricated in the form of an insulated small HTS coil with a gapped ferrite insert core. The value of $L_{filtering}$ can be changed by changing the number of turns of YBCO CC tape.

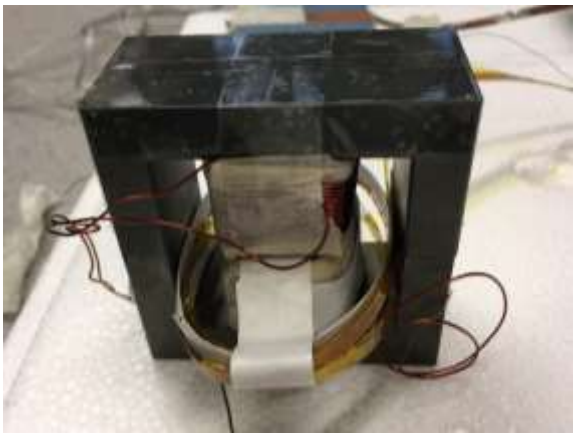

Fig. 6.14. The structure of the superconducting filtering inductor ($L_{filtering}$): Several turns of YBCO coated conductor tape are wound on a ferrite core. The value of $L_{filtering}$ can be changed by changing the number of turns of YBCO CC tape.

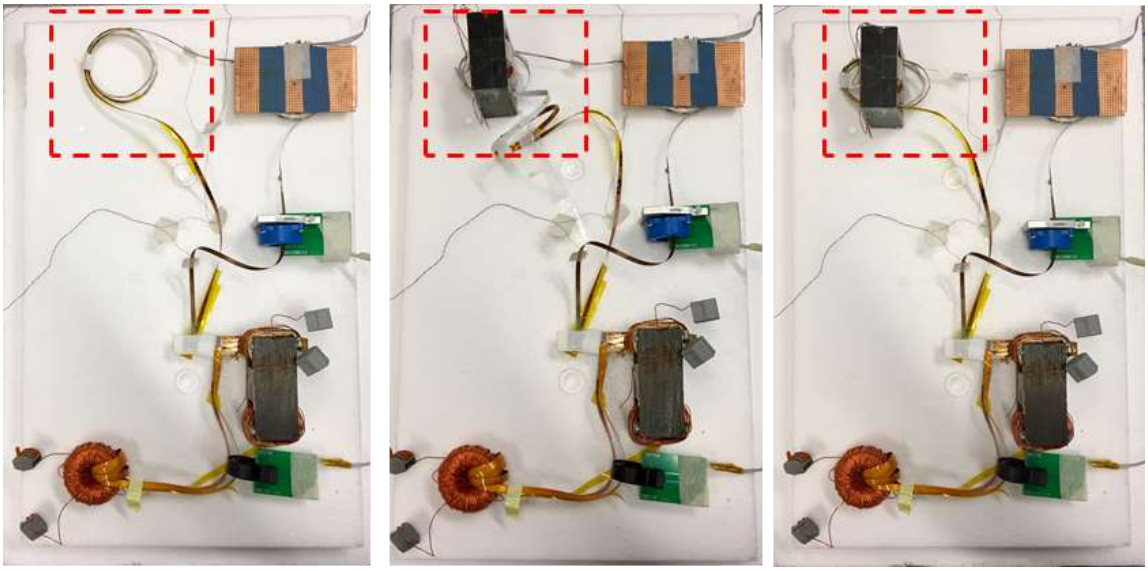

(a) (b) (c)

Fig. 6.15. The photos of flux pump system with different values of superconducting filtering inductor ($L_{\text{filtering}}$) made by REBCO tape: (a) $L_{\text{filtering}}$ = not measurable small value, where no ferrite core is inserted; (b) $L_{\text{filtering}}$ = 4 μH, where a ferrite core is partly linked; (c) $L_{\text{filtering}}$ = 16 μH, where a ferrite core is fully linked (inserted). The superconducting filtering inductor is marked with a red frame.

To further investigate the influence of filtering inductor to the flux pump system, the inductance was made variable by changing its number of turns that linked to the ferrite core. Fig. 6.15 shows the photos of flux pump system with different values of superconducting filtering inductor ($L_{\text{filtering}}$) made by REBCO tape: (a) $L_{\text{filtering}}$ = Not measurable small value, where no ferrite core is inserted; (b) $L_{\text{filtering}}$ = 4 μH, where a ferrite core is partly linked; (c) $L_{\text{filtering}}$ = 16 μH, where a ferrite core is fully linked (inserted). The superconducting filtering inductor ($L_{\text{filtering}}$) is marked with a red frame. It should be noted that there was a parasitic inductor in the load loop before we artificially added in the ferrite core because there were 4 loose turns in one of the coil terminations. The key parameters of the filtering inductor and the NI load coil are summarized in Table. 6.2.

Table. 6.2. Specifications of the filtering inductors and the solder impregnated NI coil.

	Parasitic inductor (Fig. 6.15 (a))	Filtering inductor #1 (Fig. 6.15 (b))	Filtering inductor #2 (Fig. 6.15 (c))	Solder impregnated NI Coil
Number of Turns	4 (no ferrite core)	2 (linking ferrite core)	4 (linking ferrite core)	32 SP/ 64 DP
Inductance	Not measurable	4 μH	16 μH	≈ 120 μH

(SP = single pancake, DP = double pancake)

6.2.3. Experimental results and analysis

6.2.3.1. Charging characteristics

Firstly, we present the pumping performance comparison of the flux pumping for the solder impregnated low R_c NI coil magnet with and without the filtering inductor ($L_{filtering}$). The waveform of i_2 is symmetrically triangular, and the frequency of i_2 is 0.56 Hz. B_{app} is applied at the positive peak of i_2. The field duration is 0.1 times the period of i_2. The magnitude of B_{app} is 850 mT, and the frequency is 28 Hz. The waveforms of i_2 and B_{app} are carefully adjusted to minimize the differences during different charging tests. The detailed waveforms of secondary current i_2 and applied magnetic field B_{app} are already presented in section 6.1.1.

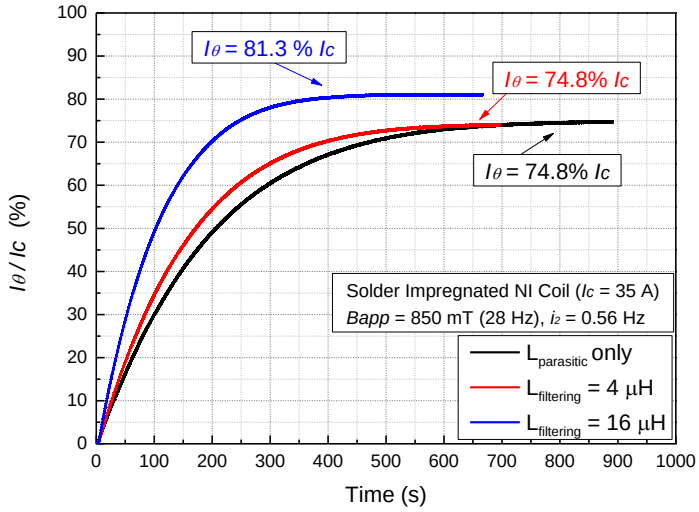

Fig. 6.16. Charging curves of NI coil when filtering inductor was placed in the load loop of flux pump.

Fig. 6.16 shows the pumping performance comparison of the flux pump for the solder impregnated NI coil with and without the filtering inductor. As shown in Fig. 6.16, both the pumping speed and the saturated azimuthal current (I_θ) of the NI coil was improved significantly when the filtering inductor was added into the load loop. Without the filtering inductor, the pumping time is up to about 700s, and I_θ reached only 74.8% of the critical current of the NI coil (I_c). When the filtering inductor was 4 μH, the pumping time reduced slightly to 600s, and I_θ saturated at 74.8% I_c. But when the filtering inductor was 16 μH, the pumping time was shortened significantly to 400s, only 57% of the original pumping time. The I_θ reached up to 81.3% of I_c. These results show that both the charging speed and the final I_θ can be improved significantly when a filtering inductor with appropriate value is added in

series with the load into the load loop of the flux pumping system. The experimental results validate the methodology proposed in section 6.2.1.

Fig. 6.17 and Fig. 6.18 present the flux pumping details of the solder impregnated NI coil when filtering inductors ($L_{\text{filtering}}$) with different value were added into the load loop of the TRFP system.

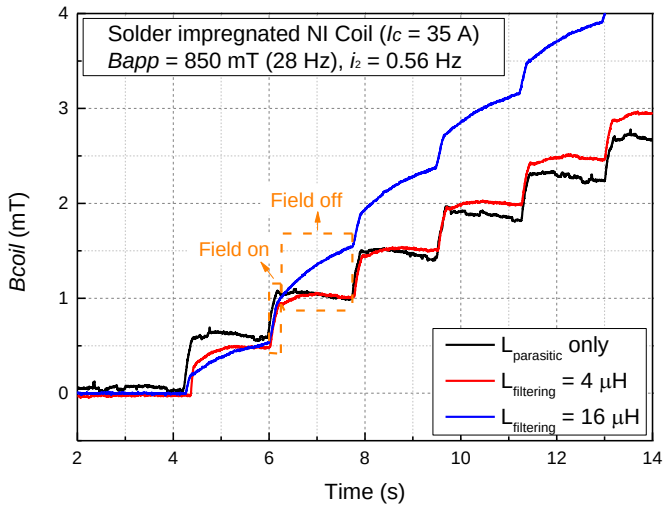

Fig. 6.17. Details of load coil center field during flux pumping process under different filtering inductance values. When filtering inductor $L_{\text{filtering}}$ = 16 μH, the load coil kept being pumped by the filtering inductor when the bridge field is off.

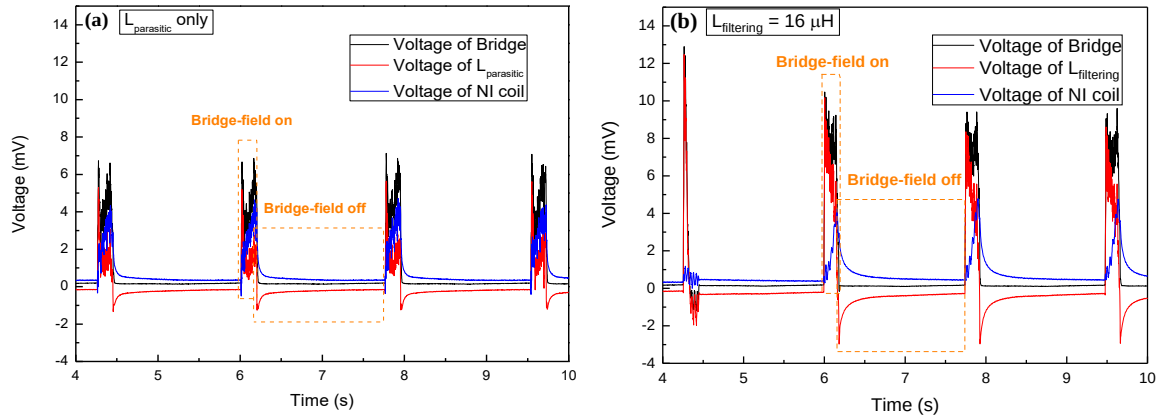

Fig. 6.18. Voltage share in the load loop when (a) no filtering inductor and (b) a 16 μH filtering inductors ($L_{\text{filtering}}$) were added into the load loop.

As shown in Fig. 6.17, each pumping cycle can be divided into two stages: during the first stage, the AC magnetic field was applied to the bridge switch and the NI coil was pumped quickly. The three cases showed similar charging behaviors. However, during the second stage

when the AC switching field was removed from the bridge, different charging behaviors were observed. The coil center field B_{coil} decreased to some extent when there was no filtering inductor, whereas the B_{coil} almost kept the same value when there was a 4 μH filtering inductor in the load loop. But it is noteworthy that the B_{coil} kept increasing quickly when a 16 μH filtering inductor was added into the load loop.

Fig. 6.18 presents the detailed voltage distribution in the load loop. During the first stage when the bridge-field was on, the filtering inductor shared a large proportion of the load loop voltage generated on the HTS bridge switch, and it was charged. During the second stage when the bridge-field was off, the voltage on the filtering inductor inversed immediately after the bridge voltage disappeared. At this stage, the filtering inductor released its stored energy and functioned as a power supply charging the NI coil. This is the reason why the B_{coil} curve kept increasing quickly during the second stage when a 16 μH filtering inductor was added into the load loop. The filtering inductor maintained continuous charging of the NI for both stages of pumping. This resulted in improved pumping speed.

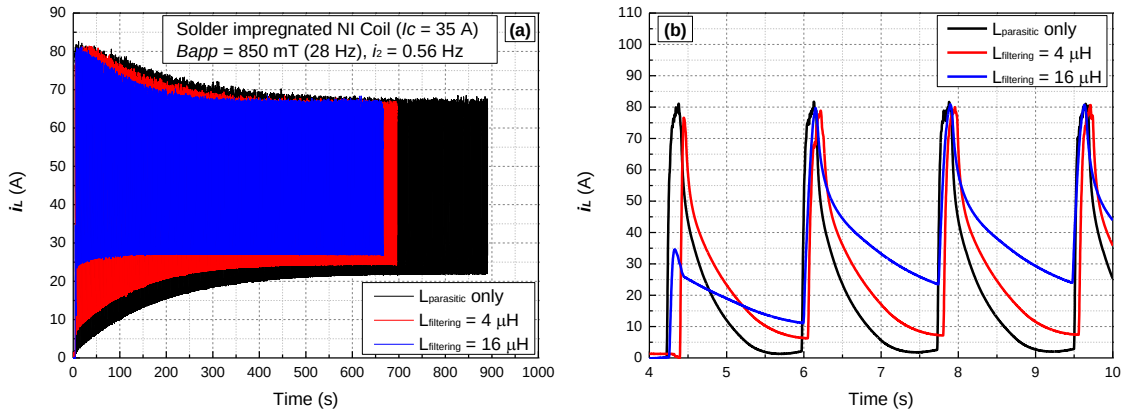

Fig. 6.19. Load loop current i_L when filtering inductors ($L_{filtering}$) with different inductances were added into the load loop: (a) Overall current curves; (b) Detailed current curves.

Fig. 6.19 shows the load loop current i_L comparison. Fig. 6.19 (a) shows the detailed curves for the beginning cycles and Fig. 6.19 (b) shows the overall current curves. As shown in Fig. 6.19 (b), the average value of the load current i_L with 16 μH filtering inductor ($L_{filtering}$) was much larger than the other two cases because load current decay during the second stage of each pumping cycle was much slower than other two cases. The slow decay rate was resulted from the current retaining ability of the filtering inductor, which led to a larger time constant. The increase in the average load loop current can result in an increase in charging voltage on the NI coil (V_{coil}), which results in fast pumping speed and better pumping effect for the NI

coil. This result also agrees well with the experimental results mentioned above (as shown in Fig. 6.16, Fig. 6.17, and Fig. 6.18. All the experiment results, shown from Fig.6.16 to Fig. 6.18, demonstrated that adding a filtering inductor with appropriate inductance value is a very simple and effective method to improve the pumping speed and performance of the TRFP for the low R_c NI coil.

To conclude, the results in figure 6.16, figure 6.17, figure 6.18, and figure 6.19 agree well with the theoretical analysis in section 6.2.1 and validated the methodology: insert a series-connected filtering inductor ($L_{filtering}$) can improve the flux pumping performance of the TRFP for the solder impregnated NI coil with low characteristic resistance R_c.

6.2.3.2. Impact of secondary current in transformer

To further improve the flux pumping performance, we also changed the frequency of the secondary current in the transformer. Fig. 6.20 shows the pumping curves of the solder impregnated NI coil with different transformer secondary current frequency. A 16 μH filtering inductor ($L_{filtering}$) was added into the load loop of the TRFP to improve the flux pumping performance. The frequency of the secondary current i_2 increased from 0.56 Hz to 2.63 Hz. Other experiment parameters were the same as the previous sections.

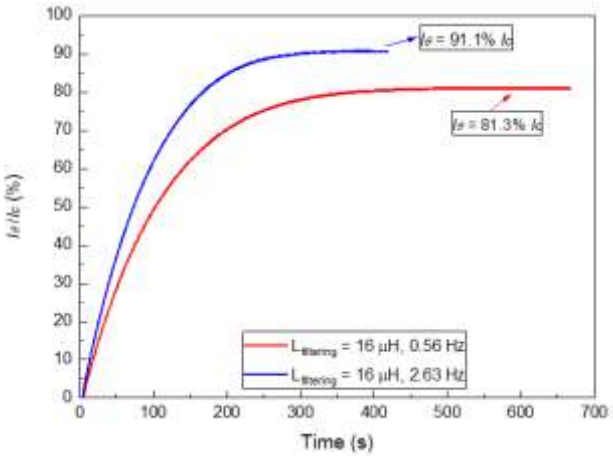

Fig. 6.20. Flux pumping curves of the solder impregnated NI coil with different secondary current frequency when a 16 μH filtering inductor ($L_{filtering}$) was added into the load loop of the TRFP.

Fig. 6.20 shows that: when the frequency of the secondary current i_2 increased from 0.56 Hz to 2.63 Hz, the pumping time reduces from around 400s to around 300s and the saturated azimuthal current I_θ of the NI coil increased from 81.3% I_c to 91.1% I_c of the NI coil. The improvement of the pumping performance results from the increase in the average value of

the load loop current. The increase of the average load loop current leads to an increase of average charging voltage on the solder impregnated NI coil (V_{coil}), which results in fast pumping speed and higher saturated azimuthal current of the low R_c NI coil. An alternative way to understand this is that the reactance of the inductor is proportional to frequency, higher frequency results in a higher reactance and a better filtering effect. Increasing the inductance of the filtering inductor is another method to improve the flux pumping performance for the low R_c NI coil when the flux pump is working in low secondary current frequency mode. But since the inductance of our load coil is only 120 μH, we did not further increase the filtering inductance in this work.

Our experimental results in this section show that: after adding filtering inductor ($L_{\text{filtering}}$) and increasing frequency of the secondary current in the transformer, the flux pumping performance had been improved significantly from original 700s charging time, I_θ = 74.8% I_c to 300s charging time, I_θ = 91.1% I_c.

6.2.3.3. Comparison with DC power supply

The flux pumping performance of the TRFP for the low-R_c solder impregnated NI coil was compared with using an external power supply. An Agilent 6680A DC current source was used to charge the NI coil. The power supply outputs a step DC, instead of ramping the current up. Several charging tests were conducted with different DC magnitudes from 40A (114% coil I_c) to 60A (170% coil I_c). The DC step current is faster in charging the coil compared with using a current ramp. The charging curves are presented in Fig. 6.21.

For the external power source, when the charging current increases from 114% I_c to 170% I_c, the charging time reduces from 480 s to 250 s while the saturated azimuthal current I_θ increases from 79.7% I_c to 96% I_c. The best pumping result using the TRFP among these tests is: charging time 300s, and I_θ = 91.1% I_c. This is achieved with 16 μH filtering inductor under 2.63 Hz secondary current frequency. This result is not as good as using the power supply with DC of 170% I_c, in terms of both charging speed and saturated I_θ. But it is still remarkable that its charging time 50s shorter than the using the power supply with 143% I_c, and the saturated I_θ reaches a similar level to 91.1% I_c. These results show that the TRFP is a competitive alternative to external power supplies in charging a low R_C NI coil.

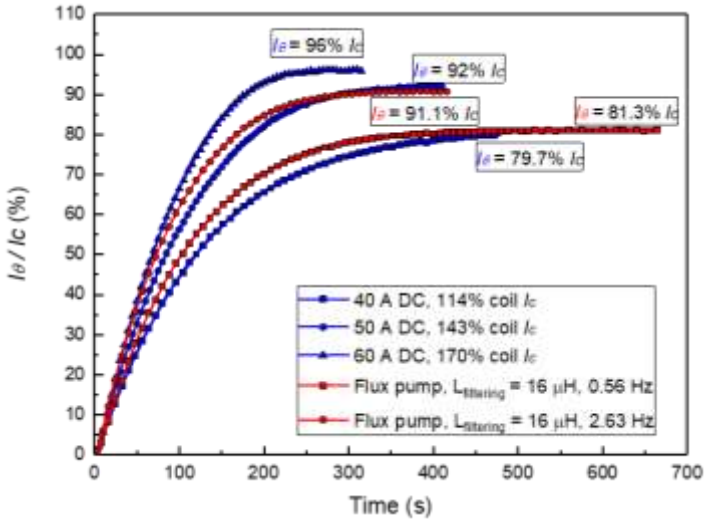

Fig. 6.21. A comparison of the charging performance for the NI coil between using the transformer-rectifier flux pump and an external super supply. The result shows that the flux pumping speed is comparable to using a DC of 143% coil I_c to charge the coil.

6.2.4. Conclusion

This section improves the flux pumping performance of the active-switching HTS TRFP for the solder impregnated HTS NI coil with very low R_c. We added a filtering inductor in series with the NI coil, which considerably improves the flux pumping performance by speeding up the pumping process and increasing the final coil current.

We found two reasons why the filtering inductor can improve flux pumping performance: Firstly, the filtering inductor increase in the bridge voltage by resisting bridge current migration, and limit the load current under the critical current of the coil terminations. So the extra flux flow resistance in the load loop is avoided and removed, so the energy is saved from the extra unnecessary dissipative component and the DC bridge voltage can be delivered to HTS NI coil more effectively. Secondly, the filtering inductor stores the energy when the DC bridge voltage is on and acts as a power source to charge the low R_c NI coil when the bridge voltage is off (bridge-field is off), therefore the charging happens throughout an AC cycle. The storage of the energy in the filtering inductance doesn't cost any electricity as well.

We made a comparison between using the optimized flux pumping technique and a traditional DC power supply to charge the low R_c solder impregnated NI REBCO coil. Results show that the optimized active-switching HTS TRFP performs as well as the traditional DC

power supply. It indicates that the flux pumping method is an ideal alternative to traditional DC power supplies for charging NI HTS magnet with low R_c.

Based on experiment results, we found that the active-switching HTS TRFP has a low voltage but a high output current, which is very suitable for charging the low R_c NI REBCO coil. This active-switching HTS TRFP can be scaled up by using a more powerful transformer with a higher secondary current, and the output current can be lifted up to >1kA level. It is expected to be competitive for charging high current NI HTS magnets.

6.3. Chapter summary

This chapter studies the flux pumping performance and characteristics of the active-switching HTS TRFP for different NI HTS REBCO magnets, with a conventional NI REBCO coil magnet with a large R_c and a novel soldered impregnated NI REBCO coil magnet with a very small R_c. The flux pumping performance for the conventional NI HTS coil (without solder impregnation) with a large R_c is very satisfying. But, the flux pumping performance for the novel soldered impregnated NI REBCO coil magnet with a very small R_c needs further improvement. Because the low R_c limits the pumping (charging) voltage and slows down the charging speed significantly.

A very important work of this chapter is improving the performance of the active-switching HTS TRFP for charging the novel solder impregnated NI REBCO coil with a very low R_c. We proposed and verified an effective solution: adding a filtering inductor connected in series with the NI coil can considerably improve the flux pumping performance, by speeding up the pumping process and achieving a higher final coil current. Our experiment results show that: after the optimization, the flux pumping performance of the HTS TRFP for the low R_c solder impregnated NI REBCO coil is comparable to using external DC power supplies. It indicates that the active-switching HTS TRFP is an ideal alternative to traditional DC power supplies, for charging NI HTS magnet with low R_c.

Based on studies of this chapter, we can conclude that the active-switching HTS TRFP with a high output current is very suitable for charging the NI coils both with a high R_c and a low R_c. This chapter provided the important clues for the future optimization on the large active-switching HTS TRFP, making it available for different types of HTS magnets, no matter it is insulated or no-insulation REBCO magnet, or NI REBCO magnet with a high R_c or a low R_c.

The NI HTS magnet can enable compact and highly reliable HTS high field magnets, and the HTS TRFP has the ability to replace the external room temperature power supplies and remove the bulky and low-efficient current leads from the cryogenic superconducting system. The NI HTS magnet together with the flux pumping technology will enable future compact, economical, and highly reliable superconducting magnet systems.

Chapter 7
High Performance Switch for TRFP

To improve the performance of the active-switch HTS TRFP, the core idea is to improve the output current and output voltage. The HTS power switch is a key component in the active switching HTS TRFP system, which significantly determines the output current and voltage. A better switch can improve the overall performance of the active-switching HTS TRFP. High-performance switch means high off-state resistance, high switching frequency, fast response, and high reliability. To design high performance HTS switches, we built a multi-physics FEM model by using COMSOL Multiphysics software. By using this multi-physics model, we found the shielding effect of the stabilizer layers in the HTS switch. We analysed many impacting factors of the HTS switch and proposed several optimized designs for achieving high switching performance. The high performance switches can improve the output capability, and overall reliability, and reduce the size of the HTS TRFP.

7.1. Multi-physics model for AC field HTS switch

7.1.1. Aim of multi-physics modelling

When an external AC magnetic field is applied perpendicular to a direct current carrying HTS coated conductor (CC), a DC electric field in the same direction of transport current appears, and a DC voltage along the superconductor is induced. This phenomenon is known as the “dynamic resistance effect”. However, the dynamic resistance incurs a dissipative loss effect and generates heating power in the superconductor. When carrying large transport current and working in the high background field, heat will accumulate in the HTS CC. The superconductivity of the HTS CC is sensitive to the temperature variation. The temperature rise will impact on the electromagnetic behaviors of the HTS CC significantly. The HTS CC may even be damaged by a temperature increase during a local quench. The quench

phenomenon is a long-lasting issue for all superconducting devices [23, 24, 70, 99-101, 113, 114]. "Quench" means the superconductor loses its conductivity. For the HTS TRFP, the HTS switch is the key component of the whole system, and dynamic resistance is utilized as a key mechanism in HTS power switches. In the TRFP, the HTS switch has the highest risk of quench, and the quench of the switch will lead to the breakdown of the whole TRFP system. The output capability of the TRFP will also be limited by the quench and recovery process of the HTS switches. Therefore, quench analysis for the HTS switch is important for achieving a high-performance TRFP.

There has been much previous research on dynamic resistance. A theoretical analysis of the dynamic resistance effect has been done by Oomen et al [30]. Numerous solid experimental investigations into dynamic resistance had been presented by Uksusman et al [32] and Jiang et al [33]. Numerical models for the dynamic resistance have also been built by Ainslie et al [34] and Li et al [35]. However, previous numerical models [34, 35] for the dynamic resistance haven't considered the impact of the temperature rise, which is of great importance to the performance, safety, and stability of the HTS power switches and obviously other applications.

Moreover, in previous numerical models [34, 35] for the dynamic resistance, the multilayer structure of 2G HTS CC has been oversimplified into a single layer structure, where the impact of each layer and the interaction between different layers in the real 2G HTS CC cannot be simulated. It hinders our further understanding and in-depth investigation into the complicated characteristics inside the HTS CCs, such as current sharing among different layers of the CCs, and different loss components in different layers of the CCs. These characteristics are also vital to the design of HTS applications.

In this chapter, we build a 2D thermal-coupled multilayer model [142] for the HTS CC based on the H-formulation [147] and a heat transfer equation [23, 24]. It has successfully resolved the above two major problems. Both temperature dependency and field dependency have been considered in this model. Our results show that the thermal-coupled model can correctly simulate the electro-thermal response of the DC carrying CC conductor to the external applied field with various magnitudes. Dynamic resistance effect, flux flow effect, quench and recovery phenomena can be successfully simulated. This multilayer model is very close to the real structure of the 2G HTS CCs, making it very useful in analyzing the impact of different layers in the 2G HTS CCs, especially the metal stabilizer layers. It has been proven to be a very powerful tool to help understand more complicated characteristics inside the CCs

which could not be accurately measured, such as the temperature distribution, current sharing among different layers of the CCs, and different loss components in different layers of the CCs.

This section presents the modelling techniques and our experimental verification for this model. The powerful analytical functions of this model are presented and explained in detail. This model is a powerful tool in designing AC magnetic field controlled HTS switches, in terms of increasing the off-state resistance, analyzing different sources of losses, minimizing detrimental losses, and enhancing safety and stability.

7.1.2. Model description

Fig. 7.1 shows the structure and working principles of the AC field controlled HTS switches. The AC field controlled HTS switches is a direct current carrying HTS CC tape subjecting to AC external applied field. The dc voltage (V_{dc}/L) generated on the HTS switch can be adjusted by changing the frequency and magnitude of the perpendicular magnetic field (B_{app}) and the magnitude of the transport current (I_t).

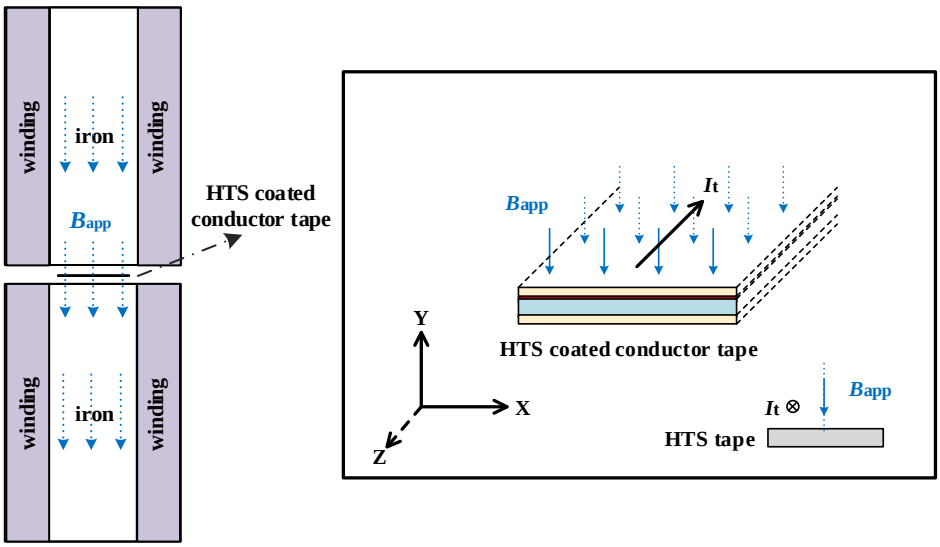

Fig. 7.1. A schematic view of the working principle and structure of the AC magnetic field-controlled HTS switch made of YBCO coated conductor.

Fig. 7.2 shows the schematic drawing of the 2D temperature-dependent multilayer model for simulating the thermal-electromagnetic behaviors of a 2G HTS coated conductor when carrying a direct current and subjected to an AC perpendicular magnetic field. As we know, the 2G HTS CC has a multilayer structure, including an HTS ReBCO layer (1 μm), a substrate (Hastelloy) layer (50 μm), a buffer stack layer (≈0.2 μm), two silver overlayers (≈ 2 μm), two copper (Cu) stabilizer layers (20 μm). In this model, the multilayer 2G HTS CC is simplified

into a four-layer model, which contains a YBCO (superconducting) layer (1 μm), a substrate layer (50 μm), and two copper (Cu) stabilizer layers (20 μm) on both sides of the tape. The silver overlayers and the buffer stack layer are neglected since they are too thin compared to the substrate layer and copper stabilizer layers. The width of the CC is 6 mm. This multilayer model is very close to the real structure of the 2G HTS CCs, making it very useful in analyzing the impact of different layers in the 2G HTS CCs, especially the metal stabilizer layers. It will be proved to be a very powerful tool to help understand more complicated characteristics inside the CCs which could not be accurately measured or simulated by previous numerical models [31, 32], such as the temperature distribution, current sharing among different layers of the CCs, and different loss components in different layers of the CCs.

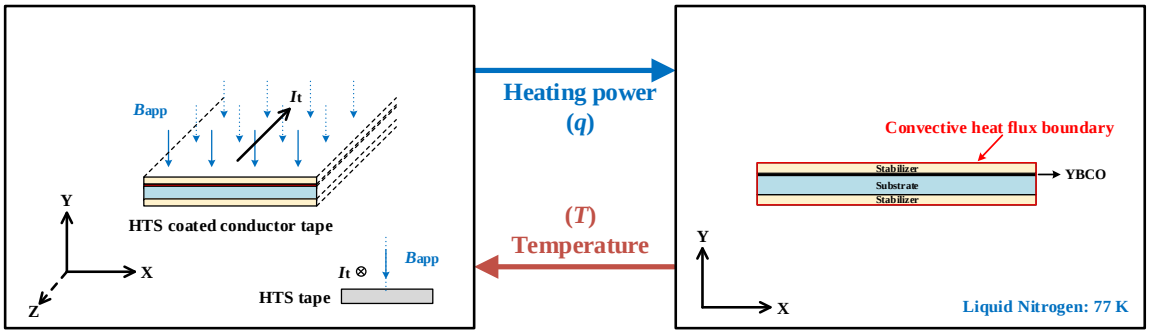

Fig. 7.2. Schematic drawing of the 2D temperature-dependent multilayer model [142] for a direct current carrying HTS coated conductor wire under perpendicular AC magnetic fields. (a) is the electromagnetic module, which is responsible for calculating electromagnetic variables including the heating power (q) in each element; (b) is the thermal module for calculating the temperature (T) of each element. The B_{app} is the instantaneous external AC magnetic field perpendicular to the HTS tape surface. I_t is the DC transport current flowing along the HTS coated conductor tape.

The model consists of two mutually coupled modules: an electromagnetic module and a thermal module. They are mutually coupled through the calculated heating power (q) and the temperature-dependence of critical current density $J_c(B,T)$ of the superconductor. In each calculation step, the electromagnetic module calculates the heating power (q) in each element; at the same time, the thermal module calculates the temperature (T) of each element based on the heating power (q) from the electromagnetic module. The temperature dependent critical current density $J_c(B,T)$ of each element in the electromagnetic module is simultaneously updated according to the temperature (T) results calculated by the thermal module in each step. The model is built and solved by commercial finite element software COMSOL Multiphysics.

It is worth mentioning that: This model is also extensible and multifunctional for simulating a variety of different working conditions, such as (i) transporting an AC or DC or zero current, (ii) subjecting to an AC, DC, or zero perpendicular magnetic field, (iii) subjecting to an external magnetic field at an arbitrary angle by rotating the HTS CC wire in the X-Y plane.

7.1.3. Electromagnetic physics

7.1.3.1. Governing equations

Governing equations for the electromagnetic physics are derived from Faraday's law and Ampere's law:

$$\begin{cases} \nabla \times E = -\mu_0 \mu_r \dfrac{\partial H}{\partial t} \\ \nabla \times H = J \end{cases} \tag{7.1}$$

where μ_0 is the permeability of free space, μ_r is the relative permeability. For the superconducting layer and non-magnetic layers, the relative permeability is $\mu_r = 1$. The equations are solved by using the *H*-formulation [147]. In 2D geometry, $H = [H_x, H_y]$, which represents the components of the magnetic field in the x and y directions. The induced electric field and the current density are perpendicular to the cross-section and are defined as E_z and J_z. By substituting $H = [H_x, H_y]$, $E = E_z$ and $J = J_z$ into Eq. (7.1), we obtain:

$$\begin{cases} \begin{bmatrix} \dfrac{\partial E_z}{\partial y} \\ -\dfrac{\partial E_z}{\partial x} \end{bmatrix} = -\mu_0 \mu_r \begin{bmatrix} \dfrac{\partial H_x}{\partial t} \\ \dfrac{\partial H_y}{\partial t} \end{bmatrix} \\ J_z = \dfrac{\partial H_y}{\partial x} - \dfrac{\partial H_x}{\partial y} \end{cases} \tag{7.2}$$

The resistivity (ρ) of the superconducting element in YBCO layer follows the *E-J* power law:

$$E = E_0 \left(\frac{J}{J_c(B,T)}\right)^n \tag{7.3}$$

where $E_0 = 10^{-4}\, V\, m^{-1}$, n = 21 [23, 24, 147], and $J_c(B, T)$ is the temperature and magnetic field dependent critical current density. The resistivities (ρ) for the non-superconducting elements

are set as constant values. The resistivity (ρ) is 8×10^{-9} Ωm for Cu-stabilizer layer, 1×10^{-6} Ωm for substrate layer, and 100 Ωm for air region.

7.1.3.2. Magnetic field and temperature dependence

The critical current density of the 2G HTS coated conductor is sensitive to and influenced by the variation of both the temperature and the magnetic field density. The magnetic field and temperature-dependent critical current density are given as:

$$J_c(B,T) = J_{c0} \cdot J_c(B) \cdot J_c(T) \tag{7.4}$$

where J_{c0} is the self-field critical current density at 77 K, $J_c(B)$ represents the coefficient of magnetic field dependence, and $J_c(T)$ represents the coefficient of temperature dependence. $J_c(B) \in [0, 1]$, and $J_c(T) \in [0, 1]$. The self-field critical current is set as 140 A, according to the experimental measured self-field critical current from a 2G HTS CC wire manufactured by *SuperPower* [144]. J_{c0} is set as 2.33×10^{10} A/m^2, which is calculated according to self-field critical current (140A) and the cross-section area of the YBCO layer (6 mm wide × 1 μm thick).

$J_c(B)$ is calculated through an anisotropic model [18-21], which is given as:

$$J_c(B) = \frac{1}{\left(1 + \frac{\sqrt{(kB_{para})^2 + B_{perp}{}^2}}{B_c}\right)^b} \tag{7.5}$$

where B_{para} and B_{perp} represent the flux density parallel and perpendicular to the wide tape surface, respectively. k, B_c, and b are three parameters controlling the $J_c(B)$ curve. These three parameters are obtained by curve-fitting on experimental measured critical current data for a specific 2G HTS CC wire from the HTS CC manufacturers. In our model, we use the values for k, B_c, and b from a *SuperPower* coated conductor wire in Ref. [21]: B_c = 0.3 T, k = 0.25 and b = 0.6. In the experimental verification section, a *SuperPower SCS4050* 2G HTS coated conductor is used, which is the same 2G HTS coated conductor wire with the one used in Ref. [21].

$J_c(T)$ is calculated according to Eq. (7.6), which has been adopted in ref. [23, 24].

$$J_c(T) = \begin{cases} 1, T \le T_0 \\ \dfrac{T_c - T}{T_c - T_0}, T_0 < T < T_c \\ 0, T \ge T_c \end{cases} \tag{7.6}$$

where T is the temperature for each element in the superconducting (YBCO) layer, which is calculated through the thermal module. T_0 = 77 K is the starting temperature of the 2G HTS CC in the model, which is the same with the temperature of the surrounding liquid nitrogen, T_c = 92 K is the critical temperature, above which the HTS element totally losses its superconductivity.

7.1.3.3. Boundary conditions

For the real multilayer 2G HTS coated conductor wire, a portion of transport current will flow into protective metal layers such as Cu-stabilizer layers under certain conditions. These conditions include when the YBCO layer enters a resistive stage due to the "dynamic resistance effect", due to a large overcurrent exceeding the YBCO critical current, due to a temperature rise of the YBCO layer, or due to high external DC or AC field. Our four-layer model can simulate the current sharing among different layers of the CC, which will help further our understanding of the interaction between different layers in the 2G HTS CC. The transport current (I_t) is set as the sum of the current in each layer:

$$I_t = I_{YBCO} + I_{Cu\_upper} + I_{Cu\_lower} + I_{Sub} = \int J_{YBCO} ds + \int J_{Cu\_upper} ds + \int J_{Cu\_lower} ds + \int J_{Sub} ds \tag{7.7}$$

where, s refers to the cross-section area of each layer. I_{YBCO}, I_{Cu_upper}, I_{Cu_lower}, and I_{Sub} is the DC transport current in the YBCO layer, the upper Cu-stabilizer layer, the lower Cu-stabilizer layer, and the substrate layers respectively. J_{YBCO} J_{Cu_upper}, J_{Cu_lower}, and J_{Sub} are the current density in each element of the above four layers. The transport current I_t is applied to the CC through a "Pointwise Constraint" in COMSOL. To avoid non-convergence in the model calculation, it takes 0.01s for the transport current to ramp linearly from zero to the preset constant value.

The applied ac perpendicular magnetic field (B_{app}) is generated by a pair of electro-magnets with a narrow flux gap (≈ 1 mm). Each magnet consists of a pair of windings and an iron core, which is similar to that described in Ref. [148]. A series of a sinusoidal magnetic waveform

(B_{app}) with different peak magnitudes and frequencies are applied perpendicular to the surface of the HTS CC tape in the model. The boundary of the air region is far away from the superconductor, therefore the perpendicular component of the magnetic field to the boundary is very small and can be set as zero in the model.

7.1.3.4. Loss, voltage, and resistance

The loss (q) per length meter (W m^{-3}) generated in each element of the CC is the heating power source for each element in the thermal module. It is also a key parameter linking the electromagnetic physics and thermal physics. q is calculated by Eq. (7.8):

$$q = E \cdot J \tag{7.8}$$

In the multilayer 2G HTS coated conductor wire, different layers produce different types of loss: the superconducting (YBCO) layer generates a transportation loss and a magnetization loss. The transportation loss originates from the dynamic resistance and flux flow resistance. The magnetization loss normally refers to hysteresis loss during the magnetization process of the superconductor (YBCO). Meanwhile, metal layers such as Cu-stabilizer will incur a transportation loss due to the metal's (copper's) resistivity if carrying a transport current, and an eddy current loss if subjected to a perpendicular AC magnetic field (B_{app}). The existence of the eddy current in the Cu-stabilizer has a significant impact on the behavior of the direct current carrying HTS CC when subjected to a perpendicular AC magnetic field. It will be analyzed in detail in the following sections. To sum up, the loss of the HTS CC contains three types of loss, including transportation loss, magnetization loss, and eddy current loss.

Total loss of each layer per length meter (Q_{layer}) (W m^{-1}) can be calculated by a surface integral, as shown in Eq. (7.9), where s refers to the cross-section area of each layer. The total loss of the CC (Q_{cc}) can be obtained from the sum of loss in four layers. Since the resistivity of the substrate layer is much larger than the Cu-stabilizer layer, current in substrate (I_{Sub}) layer is negligible. Q_{Sub} is also very small and negligible. In order to distinguish the transport loss from magnetization loss or the eddy current loss, the voltage per length-meter (V_{cc}/L) (V m^{-1}) of the CC along the tape length direction should be calculated first. It is the average electric field density along the length direction of the CC wire, which can be calculated by Eq. (7.10). s_{YBCO} refers to the cross-section area of the YBCO layer. The transportation loss (Q_{trans}) in a certain layer can be calculated by Eq. (7.11), where $I_{transport}$ refers to the transport current in the same layer, for example I_{YBCO} in YBCO layer, I_{Cu_upper} and I_{Cu_lower} in upper and lower Cu-

stabilizer layer in Fig. 7.3. Afterward, as shown in Eq. (7.12), the magnetization loss (Q_{mag}) in YBCO layer can be calculated by removing out the transportation loss (Q_{trans}) from the total loss of YBCO layer (Q_{YBCO}) which can be calculated through Eq. (7.9). Similarly, as shown in Eq. (7.13), the eddy current loss (Q_{eddy}) in the Cu-stabilizer layer can be calculated by removing the transportation loss (Q_{trans}) from the total loss of Cu-stabilizer layer (Q_{Cu}) which can be calculated through Eq. (7.9).

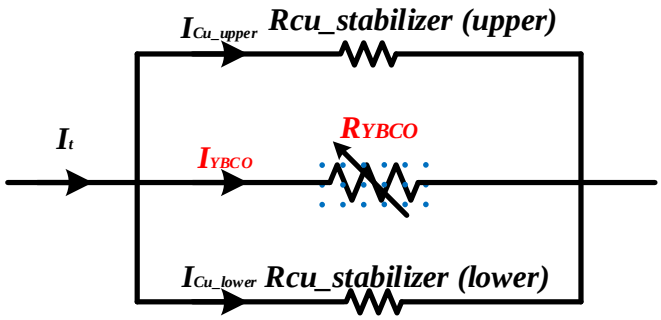

Fig. 7.3. The equivalent circuit of the multilayer HTS CC wire.

$$Q_{\text{layer}} = \int qds = \int EJds \tag{7.9}$$

$$\frac{V_{\text{CC}}}{L} = \frac{\int E_{\text{YBCO}} ds}{s_{\text{YBCO}}} \tag{7.10}$$

$$Q_{\text{trans}} = I_{\text{transport}} \cdot \frac{V_{\text{cc}}}{L} \tag{7.11}$$

$$Q_{\text{mag}} = Q_{\text{YBCO}} - I_{\text{YBCO}} \cdot \frac{V_{\text{cc}}}{L} \tag{7.12}$$

$$Q_{\text{eddy}} = Q_{\text{Cu}} - I_{\text{Cu}} \cdot \frac{V_{\text{cc}}}{L} \tag{7.13}$$

$$\frac{R_{\text{YBCO}}}{L} = \frac{\frac{V_{\text{CC}}}{L}}{I_{\text{YBCO}}} \tag{7.14}$$

The resistance per length-meter (R_{YBCO}/L) (Ω m^{-1}) of the YBCO layer along the tape length direction can be calculated by Eq. (7.14). The waveform of the R_{YBCO}/L is an important

parameter to determine the status of the YBCO layer, such as a simple status only containing a dynamic resistance, or a mixed-status containing both the dynamic resistance effect and flux flow effect. The total resistance of the HTS CC is mainly determined by the parallel resistances, mainly the YBCO layer and two Cu-stabilizer layers. The impact of the high resistivity substrate layer is very small and can be ignored. The equivalent circuit is presented in Fig. 7.3, from which we know that $V_{cc}/L = V_{ybco}/L = V_{cu}/L$.

7.1.4. Thermal physics

7.1.4.1. Governing equation

The thermal module calculates the temperature for each element in the coated conductor. In each calculation step, it is responsible for updating the temperature of the CC wire, which is important for updating the coefficient of temperature dependence $J_c(T)$ as shown in Eq. (7.4) and (7.6). The thermal module is based on the general heat transfer equation (7.15):

$$dC\frac{\partial T}{\partial t}=\nabla\cdot(k\nabla T)+q \tag{7.15}$$

where d is the mass density (kg m^{-3}), C is the heat capacity (J $kg^{-1}K^{-1}$)), k is the thermal conductivity (W $m^{-1}K^{-1}$). The mass density for the YBCO layer is 5900 kg m^{-3}, it is 8000 kg m^{-3} for the Cu-stabilizer, and 8280 kg m^{-3} for the substrate. The heat capacity C and thermal conductivity k of the YBCO, substrate, and copper (Cu-stabilizer) in this model are temperature dependent, which is presented in Fig. 7.4.

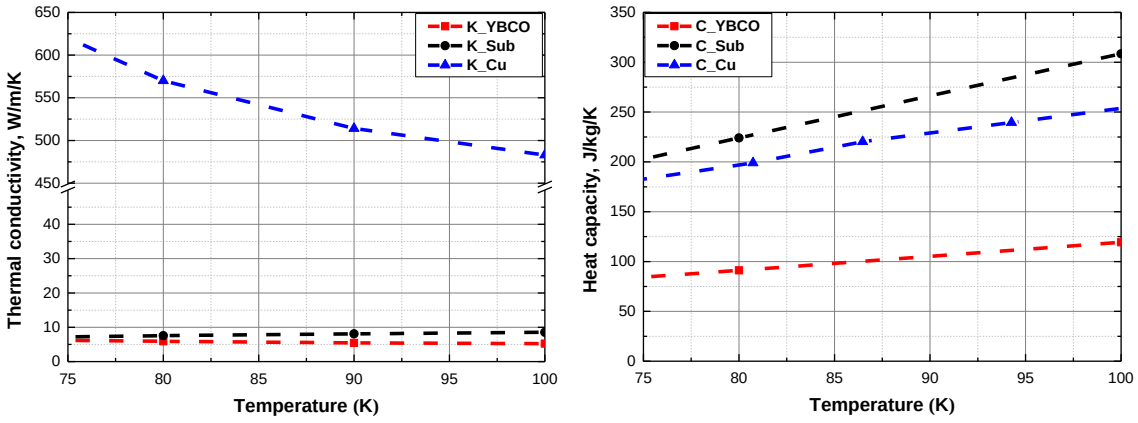

Fig. 7.4. Thermal conductivity (k) and heat capacity (C) of the YBCO, Cu-stabilizer, and substrate.

The data for C and k are obtained from reference [157-160]. q (W m^{-2}) is the heating power source in each element, which is calculated by Eq. (7.8) in the electromagnetic module. This general heat transfer equation (7.15) means that the temperature variation is a final result from two impacting factors: the heating power (q) generated inside the element, and the heat transfer between the element itself and the surrounding elements.

7.1.4.2. Heat transfer boundary condition

An accurate setting for the heat transfer boundary condition is critical for the accuracy of the thermal-coupled model. It significantly influences the thermal-electromagnetic behavior of the 2G HTS CC in the simulation model. In our model, a convective heat flux type boundary condition is adopted, which is highlighted by the red line in Fig 7.2 (b). The convective heat flux boundary condition can be expressed as:

$$Q = h\,(T_{ext} - T) \tag{7.16}$$

where Q is the heat transfer (W m^{-2}) between the liquid nitrogen and the surface of the HTS CC tape, T_{ext} is the temperature of liquid nitrogen surrounding the coated conductor, and h is the heat transfer coefficient (W m^{-2} K^{-1}) representing the cooling (heat transfer) capability of the liquid nitrogen by liquid-to-solid surface contact. T_{ext} is set as a constant value at 77 K. h value is an important parameter in the heat transfer boundary condition. In reference [23], h is set as 10000 W m^{-2} K^{-1}. But in our verification experiment, the CC tape is placed in a narrow gap of the magnet, so the cooling condition is not as good as in an open space in the liquid nitrogen. When the heating power is large, bubbles will be generated in the liquid nitrogen, which is very detrimental to the heat dissipation of the CC tape in the narrow gap. So, h value should be lower in this model. We have tried different values for h between 500 and 10000, but finally got reasonable simulation results when h = 800 W m^{-2} K^{-1}. Table.7.1 gives a brief summary of the specifications of the HTS coated conductor model.

Table. 7.1. Specifications of the HTS coated conductor model

Parameters	Value
Tape width	6 mm
Thickness of superconducting layer	1 μm
Thickness of substrate layer	50 μm
Thickness of stabilizer layer	20 μm
μ_0	$4\pi \times 10^{-7}$ H m^{-1}
n (E-J power law index)	21
Tape self-field I_{c0} at 77K	140 A
J_{c0}	2.33×10^{10} A m^{-2}
E_0	10^{-4} V m^{-1}
B_c	0.3 T
k	0.25
b	0.6
T_0	77 K
T_c	92 K
h	800 W m^{-2} K^{-1}

7.1.5. Experimental verification

To validate this model, we experimentally measured the voltage response of a DC carrying 2G HTS CC sample wire when subjecting to a series of perpendicular AC magnetic field with various magnitudes. A 10-cm long and 6 mm wide *SuperPower SCS4050* coated conductor is used, which has two 20 μm thick copper stabilizers on both sides. Table.7.2 presents the specifications of the Superpower SCS4050 coated conductor wire. The self-field critical current is around 135 A (at 77 K, with 10^{-4} Vm^{-1} criterion) when the coated conductor is placed in the narrow gap (≈ 1 mm) of the iron core of the electromagnet. The gap of the iron core is very narrow, and the iron core can concentrate the magnetic flux, which increases the self-field of the coated conductor tape when transporting a DC current. The increased self-field will lead to the decrease of the self-field critical current of the CC tape. The original self-field critical current should be slightly higher than 135 A. That is the reason why I_{c0} (at 77K, self-field) in the simulation model is set as 140 A. Our results in Fig. 7.10 can verify our explanation about this phenomenon. The tape critical current I_c in narrow gap degrades to around 0.95 I_{c0} (around 135A) when the applied field (B_{app}) is removed. The AC field is generated by an electromagnet with a copper winding of 80 turns. The CC is placed in a narrow air gap of the electromagnet. The cross-section of the gap is 2 cm × 1.2 cm. The AC field is

normal to the CC's wide surface. The voltage response of the CC is measured via a pair of voltage taps soldered to the CC surface with a 2-cm separation. The ac field magnitude is monitored by a pick-up coil winding on the gapped ferrite core. The transport current is supplied by an Agilent 6680A constant current source. The field is magnet is powered by an EP4000 audio amplifier with a wide frequency range. All signals are acquired by a NI-PCIe 6221 DAQ card. More details about the experimental setup can be found in Ref. [144].

Table. 7.2. Specifications of the Superpower SCS4050 coated conductor wire

Parameters	Value
Tape width	6 mm
Superconducting layer thickness	1 μm
Substrate layer thickness	50 μm
Stabilizer layer thickness	20 μm
Tape self-field I_c at 77K in the magnet gap	135 A

7.1.6. Result and analysis

7.1.6.1. Dynamic resistance effect and flux flow effect

Representative electromagnetic phenomena such as dynamic resistance effect and flux flow effect can be well simulated by our model.

Fig.7.5 (a1) and (b1) show the electric field response of the CC to a 1 kHz, 50 mT (peak) applied field. Fig. 7.5 (a1) is the simulation result and Fig. 7.5 (b1) is the experimental data for comparison. The chosen field magnitude is relatively low so that the superconductor is not driven to flux flow state at the peak of the applied field. The simulation result for the "dynamic resistance effect" is in good agreement with the experimental data in terms of the waveform: There are two peaks in the electric field waveform during each cycle of the applied field. Both peaks appear around the zero-crossing of the applied field when the field changing rate is the highest. And the electric field is close to zero around the peaks of the applied field when the field rate of change is the lowest. In terms of the magnitude of the electric field waveform, there is still a slight difference between the simulation and experiments. The difference is acceptable and could be caused by many factors: The adoption of a $J_c(B)$ formula (Eq. 7.5) in instead of experimentally measured data, the simplified temperature dependence $J_c(T)$ formula (Eq. 7.6), and the neglect of silver overlayers and the buffer stack layer, and so on.

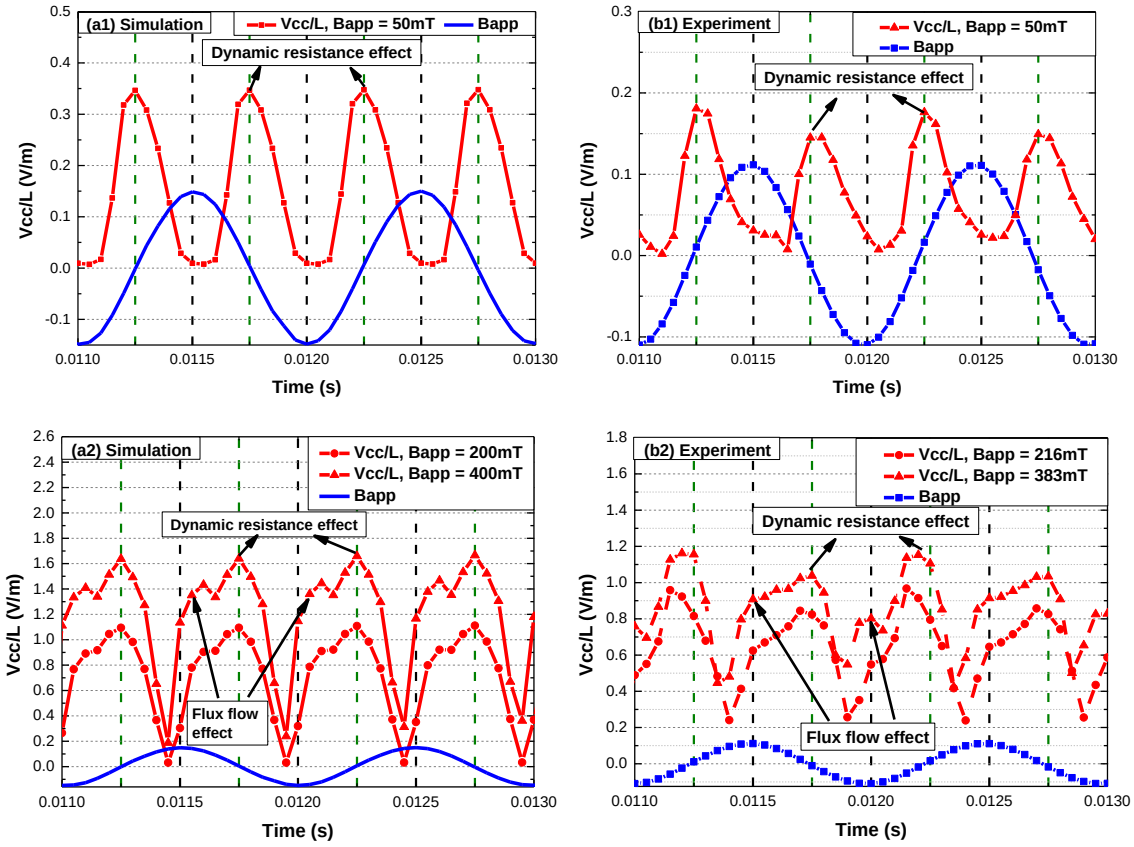

Fig. 7.5. Electrical field generated on the CC in simulation (a1, a2) and experiment (b1, b2) when: field magnitude (peak) is around 50 mT (a1, b1), 200 mT (a2, b2), and 400 mT (a2, b2).

Fig. 7.5 (a2) and (b2) show the result when the applied field magnitude is increased to around 200 mT and 400 mT, respectively. The waveforms are very different from the previous ones when the applied field is low. The first difference is that the electric field does not go back to zero at the peaks of the applied magnetic field, so that the electric field value is always over zero, and the curve seems to be "floating". The second difference is that there are more than two peaks in the electric field during each cycle of the applied magnetic field. There are "side peaks" in the electric field appearing at the peaks of the applied field. Comparing the 200 mT result and the 400 mT result, we can clearly see that the "side peak" value increases with the applied field. These two significant differences can be explained by the "flux flow effect": Due to the strong dependence of critical current density to the perpendicular applied field, the tape is intermittently driven into flux flow region when the instantaneous value of the applied field is high, especially around its peaks. When the applied field magnitude is increased to 200 mT and 400 mT, we can observe both the "dynamic resistance effect" and "flux flow effect". Therefore, we can see multi-peaks in the electric field waveform both at the applied field zero-crossings time-point as well as at its peak time-point.

Both the waveforms under low applied field and high applied fields are in good agreement with the previous theoretical analysis [30], test results [32, 33], and simulation results [34, 35].

7.1.6.2. Quench and recovery

This temperature-dependent multilayer model is a very powerful tool to help us better understand complicated characteristics in the HTS CCs. which could not be accurately measured, such as the temperature distribution, current sharing between different layers, the resistance of the superconducting layer, instant critical current variation, and different loss components in different layers of the CCs.

Voltage response:

In either the previous dynamic resistance model or flux flow model, the temperature rise in the superconductor is not considered. This is not valid when the applied field is with high frequency, high magnitude, and long duration. In this case, quench behavior may happen in the CC. By using our temperature-dependent model, the thermal-electromagnetic behaviors of 2G HTS coated conductors can be successfully simulated**.**

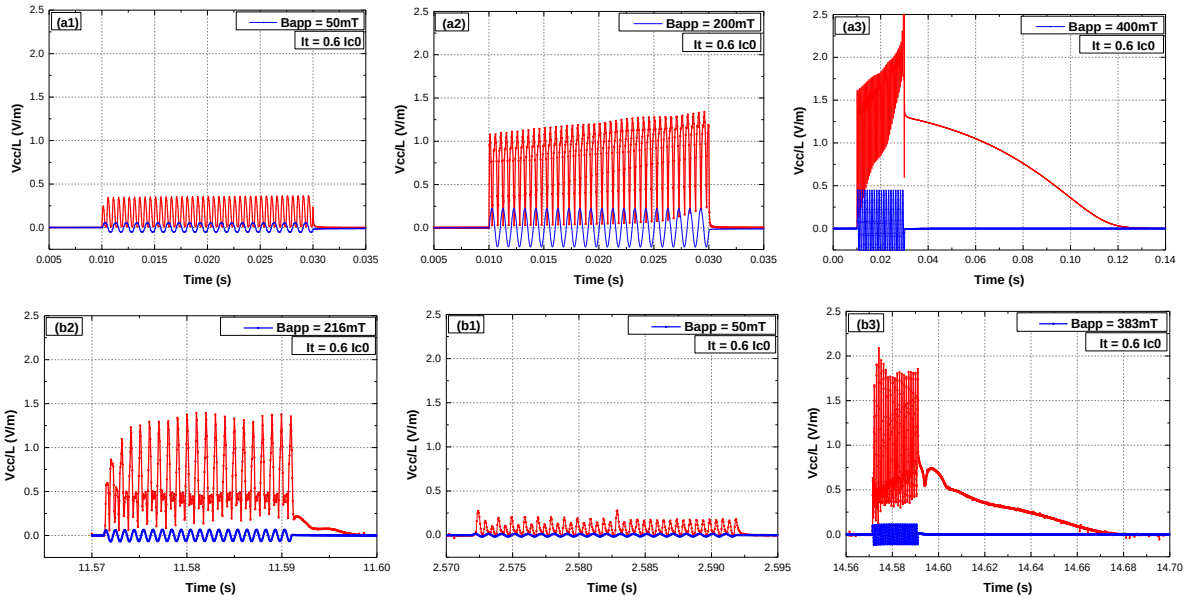

Fig. 7.6. The electric field response of the CC to 20 cycles of 1 kHz applied field when the applied field (peak) is 50 mT, 200 mT, and 400 mT. (a1), (a2) and (a3) are simulation results, (b1), (b2), and (b3) are the experimental data for comparison.

Fig. 7.6 shows the electric field response of the CC to 20 cycles of 1 kHz applied field. Our experimental results show that the impact of the temperature rise is not obvious when the field

frequency is low. So, we focus on the high-frequency range around 1 kHz here. Fig. 7.6 (a1, a2, and a3) are the simulation results when the applied field (peak) is 50 mT, 200 mT, and 400 mT. Fig. 7.6 (b1, b2, and b3) are the experimental data for comparison. The transport current is set as 80A (around 0.6 I_{c0}) in both simulation and experiment. The simulation results are in good accordance with the experimental data, especially in terms of waveform shape and recovery time. The difference in magnitude between the simulation and experiments is acceptable.

When the field magnitude is relatively low, the electric field response of the CC is stable. And it recovers to zero immediately when the applied field is removed. When the applied field magnitude is increased to 200 mT, the electrical field peak value increases gradually with time, which is different from the case when the applied field is low. At the same time, the valley value gradually increases and doesn't return to zero ("floating") after a time period. Both are different phenomena as well. But the electric field still can recover to zero quickly when the field is removed. When the applied field increases to 400 mT, the electrical field is both increasing and "floating" at the same time. When the field is removed, an obvious 90 ms time-delay of electrical field returning to zero is observed, which is regarded as thermal quench and recovery behavior. Both our numerical and experimental results show that the CC becomes unstable and even quenches when a magnetic field with high frequency, high magnitude, and long duration is applied. By comparing the simulation and experimental waveforms, our thermal-coupled model has been successfully validated to be capable of correctly simulating the electro-thermal response of the DC carrying CC conductor to the external applied field with various magnitudes.

Temperature variation:

Monitoring the temperature variation of the 2G HTS CC wire is another important function of this temperature-dependent model. Fig. 7.7 (a) shows the temperature rise of the CC when 20 cycles of 1 kHz applied field is applied. When the field magnitude is relatively low (50 mT), the temperature of the CC rises slightly, from 77 K to 78 K. When the field is 200 mT, the temperature rise is moderate (6 K, from 77 K to 83 K). But when the field increases to 400 mT, the temperature rise is considerable (12 K, from 77 K to 89 K), and it decreases slowly after the field is removed. The high temperature rise and very slow cooling speed lead to the fast increase of the electrical field (Vcc/L) and the long recovery time (90 ms) of the HTS CC as shown in Fig. 7.6 (a3 and b3)

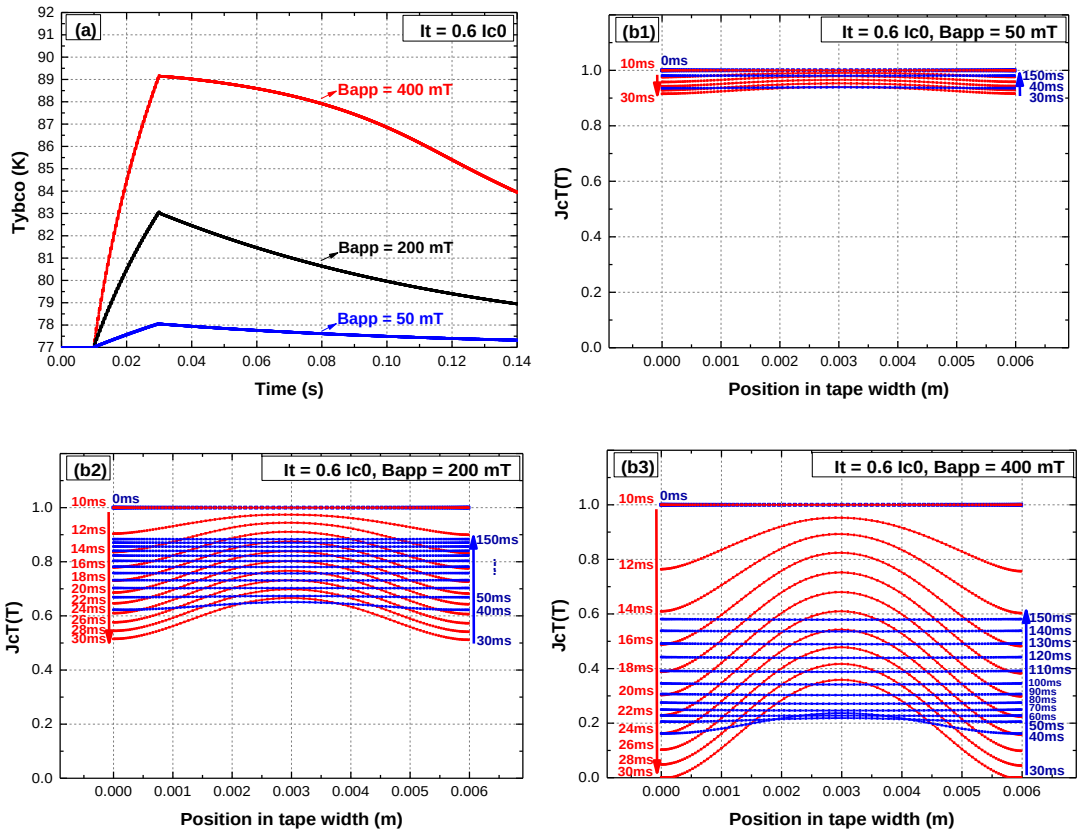

Fig. 7.7. (a) The average temperature of coated conductor, and (b1-b3) the coefficient of temperature dependence $J_c(T)$ distribution along the length direction in the YBCO layer at different instants of time when the field magnitude is 50 mT, 200 mT, and 400 mT.

Fig. 7.7 (b1), (b2), and (b3) show the coefficient of temperature dependence $J_c(T)$ distribution along the length direction in the YBCO layer at different instants of time when the field magnitude is 50 mT, 200 mT, and 400 mT. Results show that the degradation of $J_c(T)$ is more severe at two edges of the CC wire. It is caused by the faster and higher temperature rise at two edges of the CC wire than the temperature rise in the center. This is because the current density on the two ends is higher, then the electrical field is higher, and therefore the loss in two ends is larger. Our results indicate that the most vulnerable part of the HTS CC wire is at the two edges when carrying a DC transport current and subjected to a perpendicular AC field. This finding is very indicative for the design of HTS current switches and switches-based flux pumps. Our model is also very useful in analyzing the quench and recovery process of HTS CC switches.

Current distribution:

This multilayer structured model is very powerful to help study the current sharing and different loss components in different layers, which could not be accurately measured. Fig. 7.8 shows the current distribution of the CC in the YBCO layer and one Cu-stabilizer layer. We have verified that the current in the upper and lower Cu-stabilizer layers are exactly the same, so here only the current in one Cu-stabilizer (upper or lower) layer is plotted. When the field magnitude is relatively low (50 mT), the transport current of the CC mainly flows in the YBCO layer and a very small proportion flows into Cu-stabilizer. When the field increases to 200 mT, a larger proportion of transport current enters Cu-stabilizer. When the field increases to 400 mT, a great proportion of the transport current flows into the Cu-stabilizer. Moreover, when the temperature of the CC increases, more and more current enters Cu-stabilizer due to the temperature dependency of the critical current density of the YBCO layer. When the 400 mT field is removed, a long recovery time is needed for the transport current in Cu-stabilizer to return to the YBCO layer, which is a typical characteristic of the thermal quench and recovery behavior.

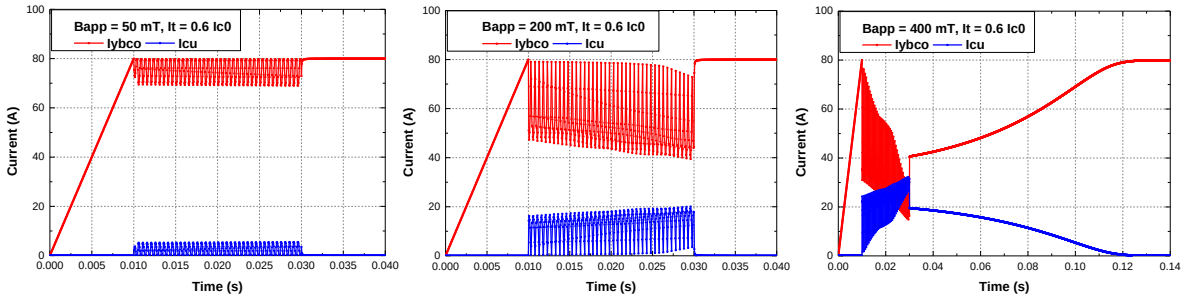

Fig. 7.8. Current distribution in YBCO and the upper (or lower) Cu-stabilizer layer. We have verified that the current in upper and lower Cu-stabilizer layers are totally the same, so here only the current in one Cu-stabilizer (upper or lower) layer is plotted.

Resistance of superconducting layer:

Fig. 7.9 shows the resistance of the YBCO layer and Cu-stabilizer. When the field magnitude is relatively low (50 mT), the resistance of the YBCO layer is very small and is solely due to dynamic resistance. When the field increases to 200 mT, the resistance of the YBCO layer increases to a higher level. When the field magnitude rises to 400 mT, the resistance of the YBCO layer is comparable to the constant resistance of the Cu-stabilizer layer and the instantaneous value finally surpasses the resistance of Cu-stabilizer due to the temperature rise. The waveform shows that the resistance of the YBCO layer consists of both dynamic

resistance and flux flow resistance. When the 400 mT field is removed, the resistance of the YBCO layer doesn't recover to zero immediately because the YBCO layer is still in flux-flow region. The resistance variation of the YBCO layer compared to the constant resistance of Cu-stabilizer in Fig. 7.9 can explain the current distribution between the YBCO layer and the Cu-stabilizer in Fig. 7.8. Since the total resistance of the HTS CC is determined by the parallel resistances, mainly the YBCO layer and two Cu-stabilizer layers, the variation of the resistance of the YBCO layer will result in the change of the total resistance of HTS CC.

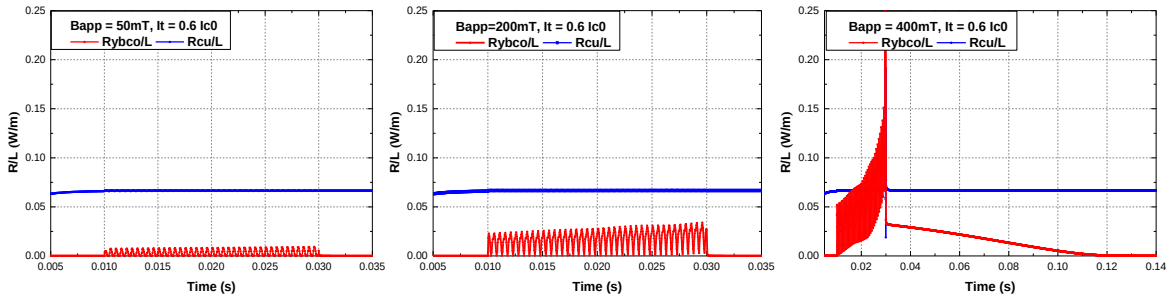

Fig. 7.9. Resistance (Ω/m) of YBCO layer and Cu-stabilizer layer.

Critical current

Fig. 7.10 shows the critical current response of the YBCO layer to the applied field. The critical current waveform can help determine the working condition of the 2G HTS CC wire. When the field magnitude is relatively low (50 mT), the degradation in the critical current of the YBCO layer is very slight. When the field magnitude increases to 200 mT and 400 mT, the critical current decreases greatly to a different extent, which results in the current sharing in Fig. 7.8 (b) and (c). When the 400 mT field is removed, the critical current of the YBCO layer is still much lower than transport current, so consequently the current flows through the Cu layer. During the recovery process, the critical current gradually increases, surpasses the transport current, and finally recovers to its initial state.

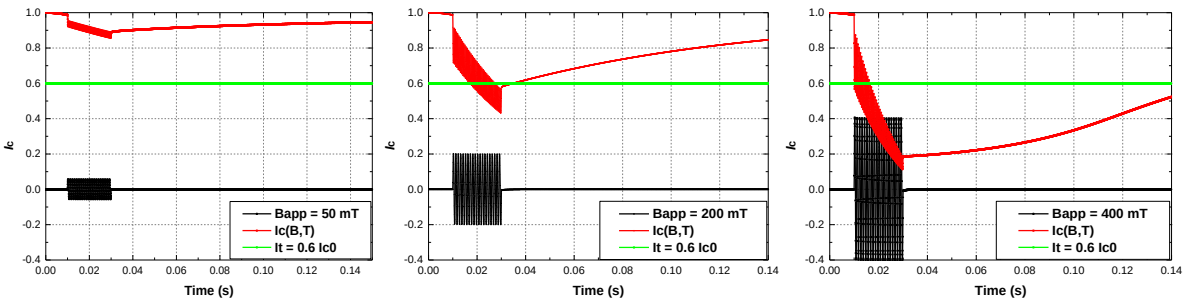

Fig. 7.10. Critical current (I_c) response of YBCO layer to the applied field (B_{app}).

7.1.6.3. Losses in different layers

In the applications of dynamic resistance such as HTS switches in flux pumps, losses are a very important issue. It would be desirable to know the sources of the losses and to minimize them. Compared to previous models, our multilayer thermal coupled model can help calculate the different loss components from different layers. It can also help understand the loss variation when the temperature rises.

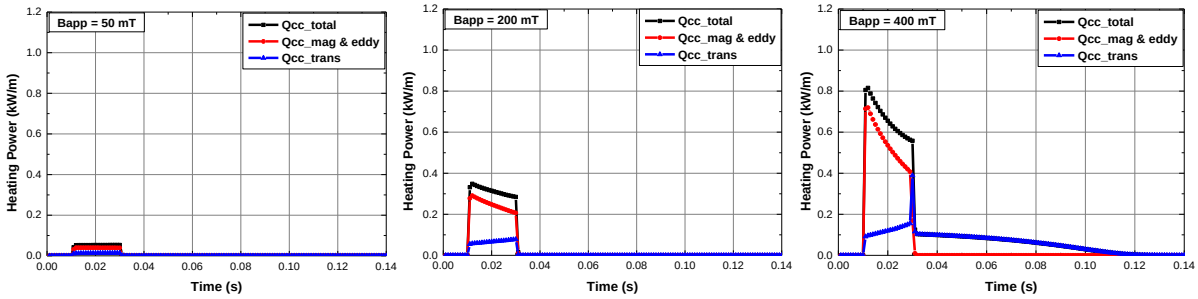

Fig. 7.11. The total loss, transport loss, and the total amount of magnetization loss and eddy loss of the CC when a perpendicular AC magnetic field is applied.

Fig. 7.11 shows the total loss, transport loss, magnetization, and eddy loss of the CC when a perpendicular AC magnetic field is applied. The eddy loss is induced in the Cu-stabilizer layer. When the field magnitude increases, the total loss increases. When the field magnitude is relatively large (400 mT), the total loss decreases with time, among which the total amount of the magnetization loss and eddy loss drops while the transport loss increases.

Moreover, if the impact of temperature rise is not considered, the ratio of transport loss to total loss drops when the field magnitude increases: the Q_{cc_trans} = 0.238 Q_{cc} (B_{app} = 50 mT), Q_{cc_trans} = 0.157 Q_{cc} (B_{app} = 200 mT), and Q_{cc_trans} = 0.124 Q_{cc} (B_{app} = 400 mT). This phenomenon doesn't agree well with the traditional theory. According to the traditional theory: critical state model proposed by Bean [13], the ratio of transport loss to total loss should rise and the ratio of magnetization loss to total loss should decrease when the transport current (I_t) rises closer to critical current (I_c) because more space in the superconducting layer is occupied by the transport current and therefore the magnetization loss is less.

In order to understand the above phenomenon, we further investigate the losses in different layers of the CC, mainly the YBCO layer and two Cu-stabilizer layers because losses are mainly generated these two layers. Fig. 7.12 shows the transport loss and magnetization loss of the YBCO layer, as well as the transport loss and eddy loss of Cu-stabilizer. The ratio of

loss in the YBCO layer to the total loss in the whole CC varies greatly when the field magnitude increases. When the field is relatively small (50 mT), the loss of the CC mainly comes from the YBCO layer, including magnetization loss and transport loss. When the applied field magnitude increases to 200 mT and 400 mT, the loss generated in Cu-stabilizer increases and eventually becomes the dominant component.

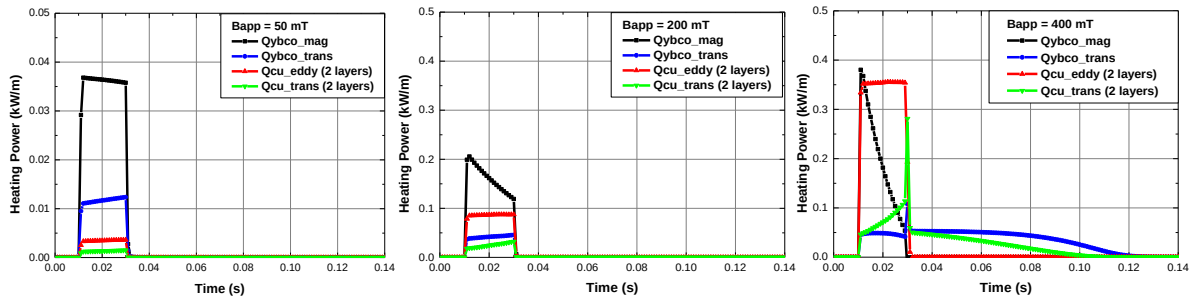

Fig. 7.12. Transport loss and magnetization loss of YBCO layer and Cu-stabilizer.

Fig. 7.12 also shows that the magnetization and transportation losses change greatly when the temperature rises, while the eddy current loss in the Cu-stabilizer layer is not affected by temperature. When the field magnitude is 400 mT, the magnetization loss in the YBCO layer decreases quickly as the temperature of the CC rises. It results from the decrease of the current-carrying ability of the YBCO layer. The transport loss in Cu-stabilizer increases greatly because the current is entering the stabilizer layer as the temperature rises. The eddy current is induced by the perpendicular applied AC field, and the resistivity of the copper doesn't change much during a small temperature rise. So, the eddy current loss in the Cu-stabilizer layer is not affected by temperature.

From the results above, we found that the Cu-stabilizer impacts significantly on the total loss of the CC. The transport loss of Cu-stabilizer is an unavoidable by-product of its helpful current sharing ability. The existence of large eddy loss in the Cu-stabilizer indicates that the Cu-stabilizer layer has a shielding effect of the AC external magnetic field. The shielding effect will impact on the dynamic resistance of the YBCO layer, which is worth being studied more carefully. The section 7.2.1 will present our study on the shielding effect of the Cu-stabilizer, based on which the optimization designs for AC field-controlled switches are proposed.

7.1.7. Conclusion

This chapter presents a 2D temperature-dependent multilayer model of the 2G HTS CC based on the *H*-formulation and a general heat transfer equation. This model successfully coupled electromagnetic and thermal physics and can simulate the thermal-electromagnetic response of the DC carrying CC conductor to the external applied field with various magnitudes. It is a powerful tool to study the behavior of the 2G HTS CC, especially when the impact of temperature rise must be considered. This multilayer model is also a very useful tool in analyzing the impact of the different layers of 2G HTS CCs. Complicated characteristics in the CCs which could not be accurately measured, such as the current sharing, and different loss components from different layers, can be carefully analyzed. The multi-physics model is very powerful in analyzing the quench and recovery characteristics of the AC field-controlled switches, which can help analyze the performance and reliability of the whole flux pump.

7.2. Impacts of stabilizer layers

By analyzing different loss components via using this model in the previous section, we found that the Cu-stabilizers have both the current sharing ability and the shielding effect. Thesis two phenomena probably will impact on the dynamic resistance, dynamic voltage, the loss, and the risk of quench of the AC field-controlled switches made by HTS coated conductors. In this section, we will further study the shielding effect and the current sharing ability of the Cu-stabilizer. The impact of the Cu-stabilizer incurred by these multiple effects has been analyzed comprehensively.

7.2.1. Current sharing

The current sharing ability of the stabilizer layer has been shown in Fig.7.8. When the resistance of the YBCO layer increases, due to the dynamic resistance effect and the temperature rise, the stabilizer layer will share a part of the dc transport current. This can be understood by the equivalent circuit of the coated conductors as shown in Fig. 7.3. This can help protect the YBCO layer from further thermal quench and loss increase. However, the absence and the current sharing ability of the metal-stabilizer layers decrease the total resistance of the coated conductor, and therefore reduce the dc charging voltage of the HTS switch.

7.2.2. Field shielding effect

The shielding effect of the metal stabilizers has been found in the loss analysis of the last section. The shielding effect may greatly impact the behaviors of the HTS switch, but the influence is not quite clear now and need to be studied. This part investigates the shielding effect of the Cu-stabilizer layer.

To better understand the impact of the Cu-stabilizer layer, it's better to separate the impact of the current sharing ability and field shield effect. In order to achieve this goal, a new set of comparison models are designed and simulated: (i) An HTS tape which only contains the YBCO layer and substrate layer, whose upper and lower Cu-stabilizer layers have been removed. (ii) An HTS CC tape which contains both upper and lower Cu-stabilizer layers, but the transport current (I_t) has been constrained to flowing in the YBCO (Superconducting) layer. In this case, the current sharing ability of the Cu-stabilizer has been removed. (iii) An HTS CC tape which contains both up and down Cu-stabilizer layers and the transport current (I_t) constraint has been cancelled, so I_t can be naturally shared by the Cu-stabilizers. It is the same as the model setting in previous sections. Above experiments and simulations have already shown that the temperature rise influences the behaviors of the HTS CC tape significantly.

In order to get rid of the influence of the temperature difference between comparison simulations, the heat transfer coefficient h is increased from 800 W m^{-2} K^{-1} to 10000 W m^{-2} K^{-1} (a more than 10 times higher level). Our simulation results below will prove that this very high heat transfer coefficient (h) value can help guarantee the same temperature rise for comparison simulation models, which is quite an important precondition for studying the shielding effect of the Cu-stabilizer layer. The peak magnitude of B_{app} is 35mT and the frequency is set as 2 kHz for a more obvious shielding effect. The low-frequency range like around 50 Hz has been studied, but the shielding effect is not as significant as in the high-frequency range (kHz level). The transport current is still 80 A.

Fig. 7.13 (a) shows the temperature curves of three HTS tapes. They are almost the same, which is an important precondition for further analysis and discussion of the shielding effect. Fig. 7.13 (b) is the transport current (I_{ybco}) flowing in the YBCO (superconducting) layer in three HTS tapes. Only in the tape model (iii), I_{ybco} fluctuates due to the current sharing of the Cu-stabilizer layer. Both Fig. 7.13 (a) and Fig. 7.13 (b) verifies our temperature control and current injection in three comparison models for different HTS tapes.

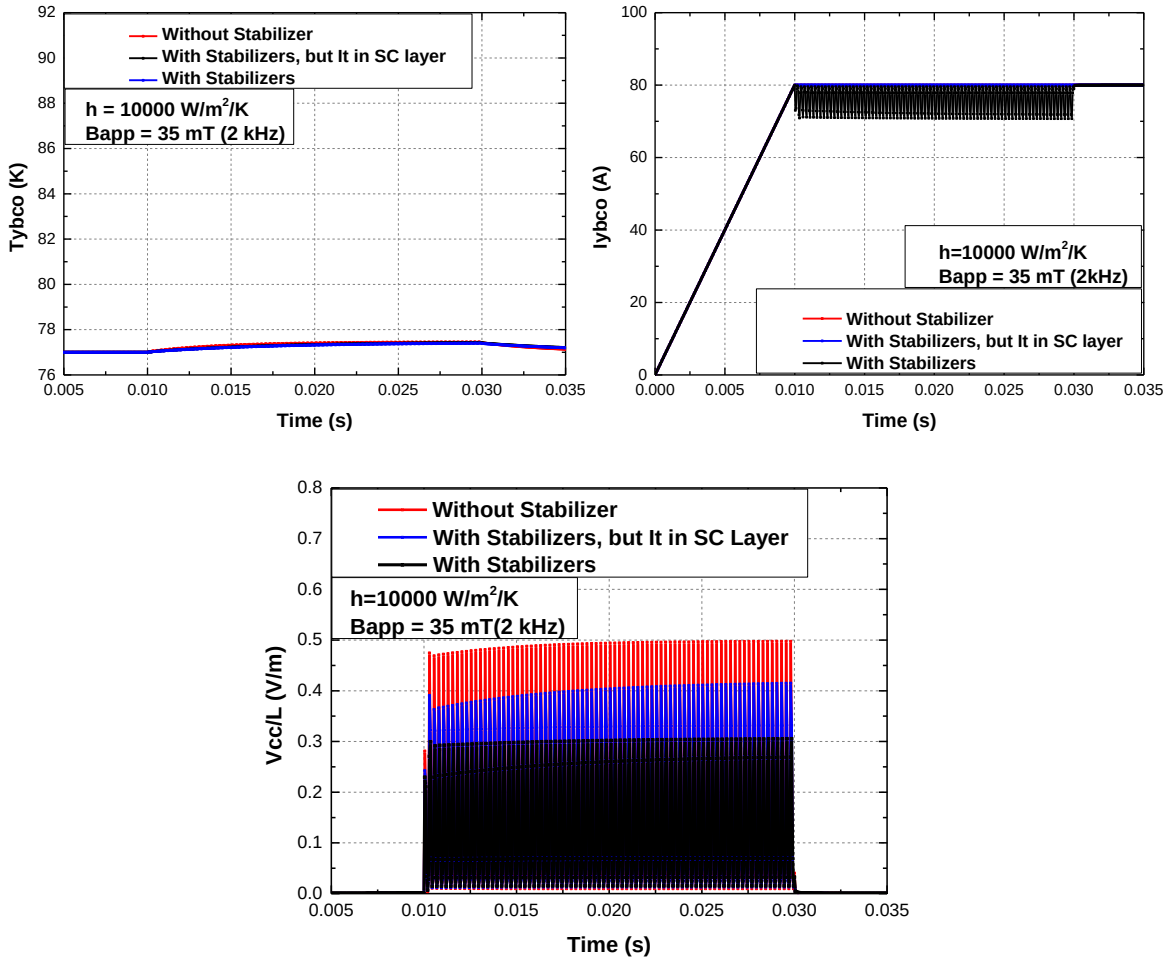

Fig. 7.13. Temperature curves (T_{ybco}) of the YBCO (superconducting) layer in three AC field switches made of HTS YBCO CC tapes, transport current (I_{ybco}) flowing in the YBCO layers, and the electrical field (or voltage per meter length) (V_{cc}/L) generated on three HTS tapes [142].

Fig. 7.13 (c) shows the electrical field (or voltage per meter length) (V_{cc}/L) generated on three HTS tapes. Results show that the existence of the Cu-stabilizer layer greatly reduces the electrical field (V_{cc}/L) generated on DC carrying HTS CC tapes subjecting to AC external applied field (B_{app}). It is easy to understand that the current sharing ability of Cu-stabilizer will decrease the electrical field (V_{cc}/L) because the electrical field or is a product of the resistance (R_{ybco}/L) and current (I_{ybco}) in YBCO (superconducting) layer. However, the mechanism is not so simple for the decrease of the electrical field (V_{cc}/L). Our results in Fig. 7.14 reveal the existence of the magnetic field shielding effect of the Cu-stabilizer and its impacts on the dynamic resistance of the superconducting (YBCO) layer.

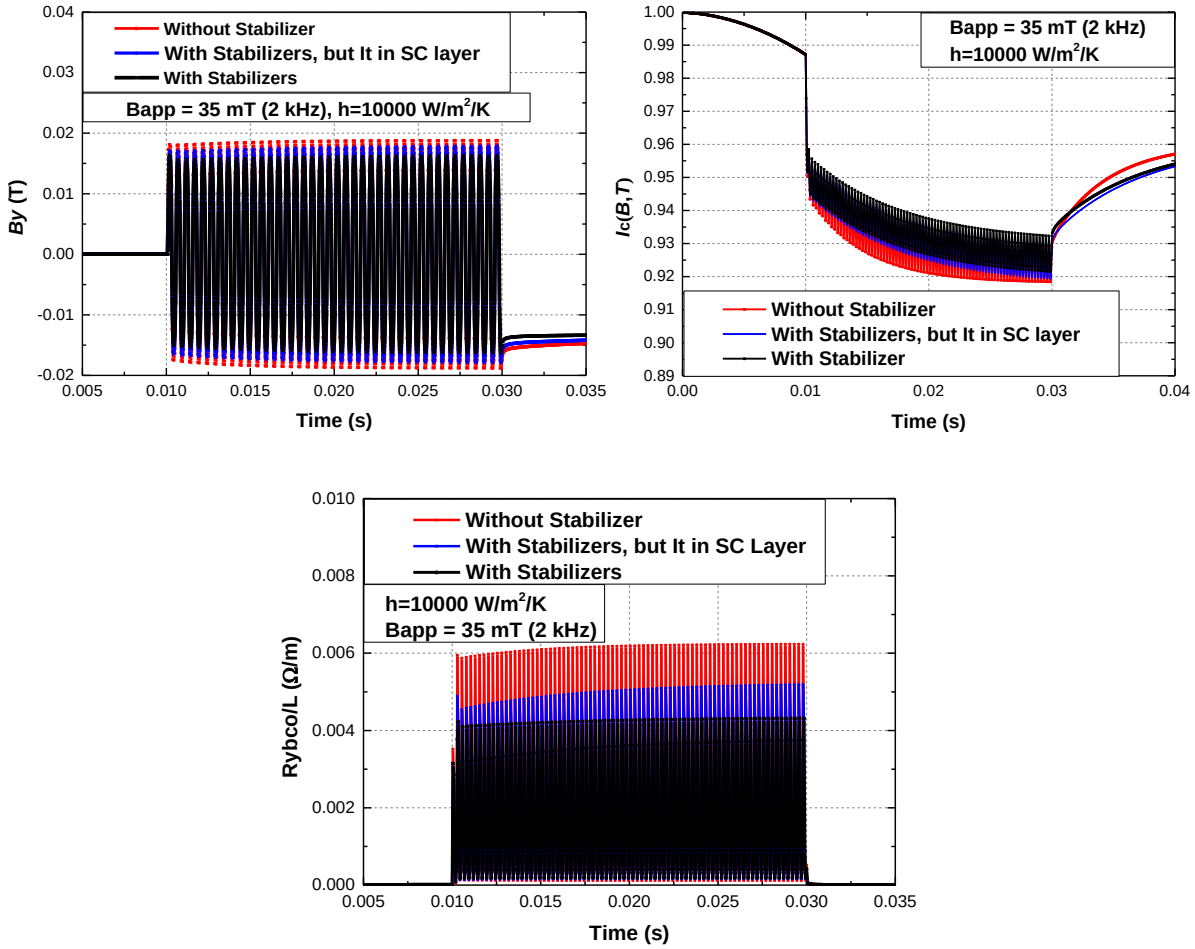

Fig. 7.14. The perpendicular field magnitude (B_y) at the center point of YBCO layer's up surface of three HTS tapes, the temperature and magnetic field dependent critical current ($I_c(B,T)$) of three HTS tape, and the resistance (R_{ybco}/L) of superconducting (YBCO) layer of three HTS tapes.

Fig. 7.14 (a) shows the perpendicular field magnitude (B_y) at the center point of the YBCO layer's up surface, which can tell the intensity of the field shielding effect of Cu-stabilizers. Fig. 7.14 (b) shows the temperature and magnetic field dependent critical current ($I_c(B,T)$) of HTS tape. The temperature curves are the same for three HTS tapes, therefore $I_c(B,T)$ is a good monitor for field shielding effect. Both Fig. 7.14 (a) and Fig. 7.14 (b) successfully show that the perpendicular field magnitude at the center point of YBCO layer's up surface is reduced due to the upper and lower Cu-stabilizers' shielding effect. Fig. 7.14 (c) shows the resistance (R_{ybco}/L) of the superconducting (YBCO) layer. Their waveforms show that the resistances are totally dynamic resistance. From ref. [33], we know that the dynamic resistance in a certain fixed width HTS tape is determined by the magnitude of perpendicular component (B_y) of AC applied external magnetic field, if the field frequency is fixed as well:

$$\frac{R_{d\perp}}{L} = \frac{4af}{I_{C0}}(B_{a,\perp} - B_{th,\perp}) \tag{7.17}$$

So, for tape (ii) (the transport current (I_t) only flows in the YBCO (Superconducting) layer), the dynamic resistance (R_{ybco}/L) decreases a lot simply because the up and down Cu-stabilizers shield a portion of the perpendicular field (B_y). For tape (iii), the transport current (I_t) can be shared by the Cu-stabilizers naturally. This situation is more complicated. Both the current sharing phenomenon and shielding effect of the Cu-stabilizers lead to a further reduced dynamic resistance (R_{ybco}/L). On one hand, the shielding effect of the Cu-stabilizer can reduce the perpendicular field (B_y) to some extent, which has already been verified in above discussion. On the other hand, when the dynamic resistance appears in the superconducting (YBCO) layer due to the AC perpendicular field, a portion of transport current (I_t) flows into the upper and lower Cu-stabilizer layers. As a result, I_{ybco} decreases and so the YBCO layer can screen more applied field. The screening effect of the YBCO layer becomes stronger under the same AC field, compared to tape (ii). This also further reduces the AC perpendicular field (B_y). Fig. 7.14 (a) provides good evidence for this explanation, where AC perpendicular field (B_y) in tape (iii) is further reduced, compared with tape (ii). The further reduced AC perpendicular field (B_y), caused by both the Cu-stabilizers' shielding effect directly and by their current sharing ability indirectly, finally results in a higher $I_c(B,T)$ and a lower dynamic resistance (R_{ybco}/L) of superconducting (YBCO) layer, which are clearly presented in Fig. 7.14 (b) and Fig. 7.14 (c) respectively.

Now, let's move back to Fig. 7.13 (c): the electric field (V_{cc}/L) generated on three HTS tapes. After the analysis and discussion above, the mechanism behind the decrease of electrical field (V_{cc}/L) for tape (iii) is clear now: (a) Firstly, Cu-stabilizers' shielding effect directly reduces the dynamic resistance (R_{ybco}/L) of superconducting (YBCO) layer, and the Cu-stabilizers' current sharing ability also indirectly reduces dynamic resistance (R_{ybco}/L) of superconducting (YBCO) layer. (b) Secondly, the Cu-stabilizers share a portion of transport current (I_t), which reduces the transport current (I_{ybco}) in YBCO (superconducting) layer. As a result, compared to tape (i) and tape (ii), the electrical field (V_{cc}/L) generated on HTS tape (iii) is further reduced due to the drop in both the resistance (R_{ybco}/L) and transport current (I_{ybco}) in YBCO (superconducting) layer. (For the multilayer coated conductor, V_{cc}/L = V_{ybco}/L=$V_{cu\_stabilizer}$/L because the multilayers are electrically connected in parallel.)

To conclude, our simulation results deepened the understanding of the impact of the Cu-stabilizers on the performance of the AC field-controlled HTS switch made of YBCO CC tape. The simulation results have verified the shielding effect and current sharing ability of Cu-stabilizers. The Cu-stabilizers decrease the dynamic resistance and dc voltage of the HTS switch due to both the shielding effect and current sharing ability, directly and indirectly. Our analysis is useful for optimizing the design of AC field-controlled HTS switches for TRFP.

7.2.3. Frequency dependence of shielding effect

This part presents the frequency dependence of the shielding effect. Fig. 7.15 (a1-a3) shows the perpendicular field magnitude (B_y) at the center point of YBCO layer's up surface under 1 kHz, 2kHz, and 4 kHz field frequency, for tape (i) and tape (iii). Fig. 7.15 (b1-b3) shows the dynamic resistance (R_{ybco}/L) of superconducting (YBCO) layer accordingly. Tape (ii) is not the real situation for the HTS coated conductor, so it is not discussed here. The magnitude of the applied perpendicular AC field is 35 mT, but the measured perpendicular field magnitude (B_y) at the center point of YBCO layer's up surface is around or less than 20mT. It is caused by the shielding effect of the whole coated conductor, including the superconducting layer (predominately) and Cu-stabilizer layers (slightly).

Fig. 7.16 shows the percentage of the total eddy current loss (two Cu-stabilizer layers) to the total loss of the HTS CC wire when carrying DC current and subjecting to perpendicular AC external applied field. As a comparison, the percentage of the transport current loss of the two Cu-stabilizer layers is also presented. Results show that: as the field frequency increases from 1 kHz to 4 kHz, the percentage of the eddy current loss in two Cu-stabilizer layers increases significantly from 4% to 12.5%. It means that the shielding effect of the Cu-stabilizers has a strong field frequency dependence in the high-frequency working zone like kHz level. In contrast, the percentage of the transport loss of the two Cu-stabilizers increases slightly as the field frequency goes up. It shows that the current sharing ability of the Cu-stabilizers doesn't have an obvious field frequency dependence. The reason for the slight increases in the percentage of the transport loss of two Cu-stabilizers might be: when the field frequency increases from 1 kHz to 4 kHz, the dynamic resistance (R_{ybco}/L) of superconducting layer increases from 2.8 mΩ/m to around 7.0 mΩ/m. A higher dynamic resistance (R_{ybco}/L) of the superconducting layer pushes more transport current into the two Cu-stabilizer layers, which results in a slightly higher percentage of the transport loss from Cu-stabilizers.

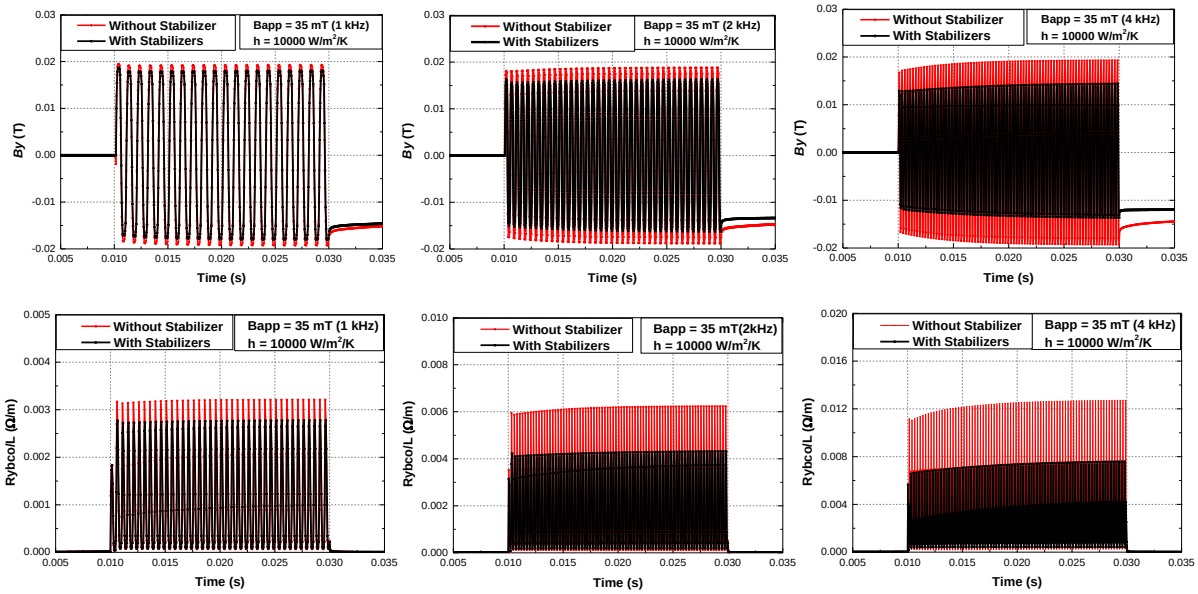

Fig. 7.15. The perpendicular field magnitude (B_y) at the center point of YBCO layer's up surface for tape (i) and tape (iii) under 1 kHz, 2kHz, and 4 kHz field frequency; and the dynamic resistance (R_{ybco}/L) of superconducting (YBCO) layer accordingly.

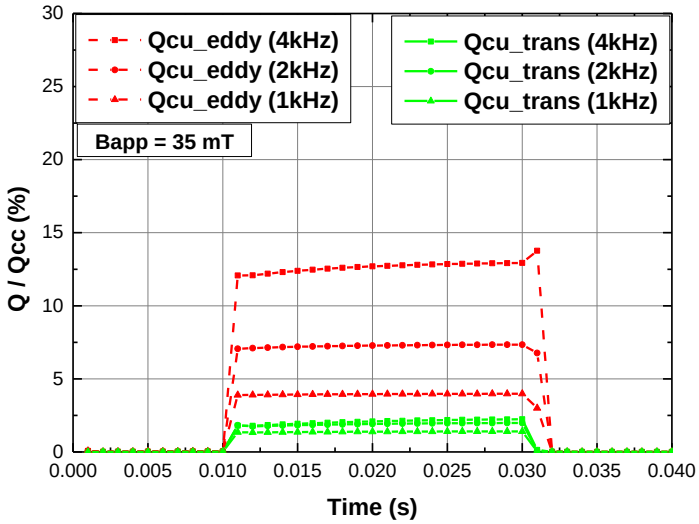

Fig. 7.16. The percentage of the total eddy current loss (two Cu-stabilizer layers) to the total loss of the HTS CC wire when carrying DC current and subjecting to perpendicular AC external applied field: (Q_{cu_eddy}/Q_{cc}), and the percentage of the transport current loss of two Cu-stabilizer layers to the total loss: (Q_{cu_trans}/Q_{cc}) [142].

To conclude, this section reveals the strong frequency dependence of the field shielding effect of the Cu-stabilizer layer under the kHz level high-frequency field. As the frequency of the applied perpendicular AC field rises, the shielding effect becomes stronger, and the proportion of the eddy current loss from Cu-Stabilizer becomes higher and higher. Moreover, the strong shielding effect also decreases the dynamic resistance of the superconducting layer,

and finally reduces the dynamic voltage (V_{cc}/L) of the HTS coated conductor. From the above results, we found that both the shielding effect of the Cu-stabilizers and its directly triggered eddy current loss are detrimental to the performance of the AC field-controlled switch.

7.3. Optimization on switch design

The AC field-controlled switch is the key component in the active-switching transformer rectifier flux pumps, and it has the highest risk of thermal quench among all components. In this section, we will focus on optimizing the design of the AC field HTS switch, aiming at designing high-performance AC magnetic field controlled switches. A high-performance AC magnetic field controlled persistent current switch means high off-state resistance, low loss, and high excellent stability. The multi-physics model is used in optimizing the design of AC field-controlled switches.

7.3.1. With and without stabilizer layers

In this section, we compare the performance of the switches with and without the stabilizer layers.

Fig. 7.17 shows the differences in temperature rise under different external magnetic fields and dc voltage under a 200 mT magnetic field. The resistivity of the stabilizer layer is set as 10^{-8} Ωm. 20 cycles of 1 kHz AC magnetic field is applied with different (peak) magnitudes, including 50 mT, 200 mT, and 400 mT.

Fig. 7.17 (a) shows that: with the stabilizer layers, the temperature rise is smaller and slower. This means stabilizer layers can help increase the stability and safety of the switches. Fig. 7.17 (b) shows that: without the stabilizer layers, the dc voltage is much higher. This means that the stabilizer layers will reduce the dc voltage (off-state resistance) of the switch, which will be a disadvantage. Based on the results shown in Fig. 7.17, we have released that the choice of the stabilizer layers should be made according to the specific application scenario. Because the stabilizer layers have both advantages and disadvantages on the performance of the switch made by REBCO coated conductors.

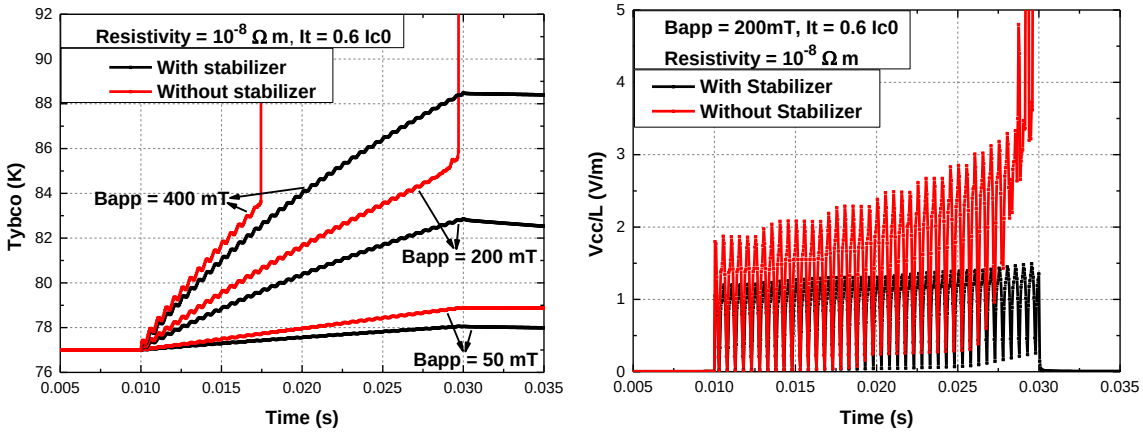

Fig. 7.17. A comparison between the 2G HTS tapes with stabilizer and without stabilizer layers when carrying a direct current under perpendicular AC magnetic fields: The temperature rise (T_{ybco}) and Electrical field (V_{cc}/L). 20 cycles of 1 kHz AC magnetic field is applied with different (peak) magnitudes.

To design a high resistance and compact switch, the stabilizer is not preferred. Without stabilizer layers, the dc voltage (and off-state resistance) per unit length of the switch is higher, which can make the switch more compact. However, this switch design is easy to quench, especially under high-field and high-frequency working mode.

To design a safe and stable switch, the switch with stabilizer layers is more advantageous, especially when working in a high-field and high-frequency mode. So such a switch design is more suitable for high switching frequency, high current transformer-rectifier flux pumps due to its high thermal-electromagnetic stability and reliability.

7.3.2. Resistivity of stabilizer layers

In most cases, copper (Cu) tapes are used as the stabilizer layers. However, copper is not the only candidate for stabilizer layers. A study on different values of resistivity for the stabilizer layers can help better choose the metal material for the 2G HTS tape. This section presents our study on the impacts of the resistivity of stabilizer layers on the thermal-electromagnetic characteristics of the AC magnetic field controlled switches [143]. The performance of the switch will be evaluated via four basic parameters: including (1) Temperature rise, (2) DC voltage, (3) Dynamic resistance, and (4) Total loss.

Temperature rise, DC voltage, and Dynamic resistance:

Fig. 7.18 shows the temperature of the YBCO layer (T_{ybco}, K), the electrical field of the HTS CC (V_{cc}/L, V/m), the dynamic resistance of the YBCO layer (R_{ybco}/L, Ω/m), and the current

flowing in the YBCO layer (I_{YBCO}, A), when the HTS switch is subjected to a perpendicular 1 kHz, 50 mT (peak) magnetic field (B_{app}). The stabilizer layers with different resistivity (10^{-9} Ωm, 10^{-8} Ωm, and 10^{-7} Ωm.) are adopted. 20 cycles of AC field magnetic field with different peak magnitudes are applied, including 50 mT and 200 mT. The transport current of the HTS CC is 80A (around 0.6 I_{c0}). The waveform has 40 peaks in 20 cycles, or two peaks per AC field cycle, which is a representative symbol for the "dynamic resistance effect".

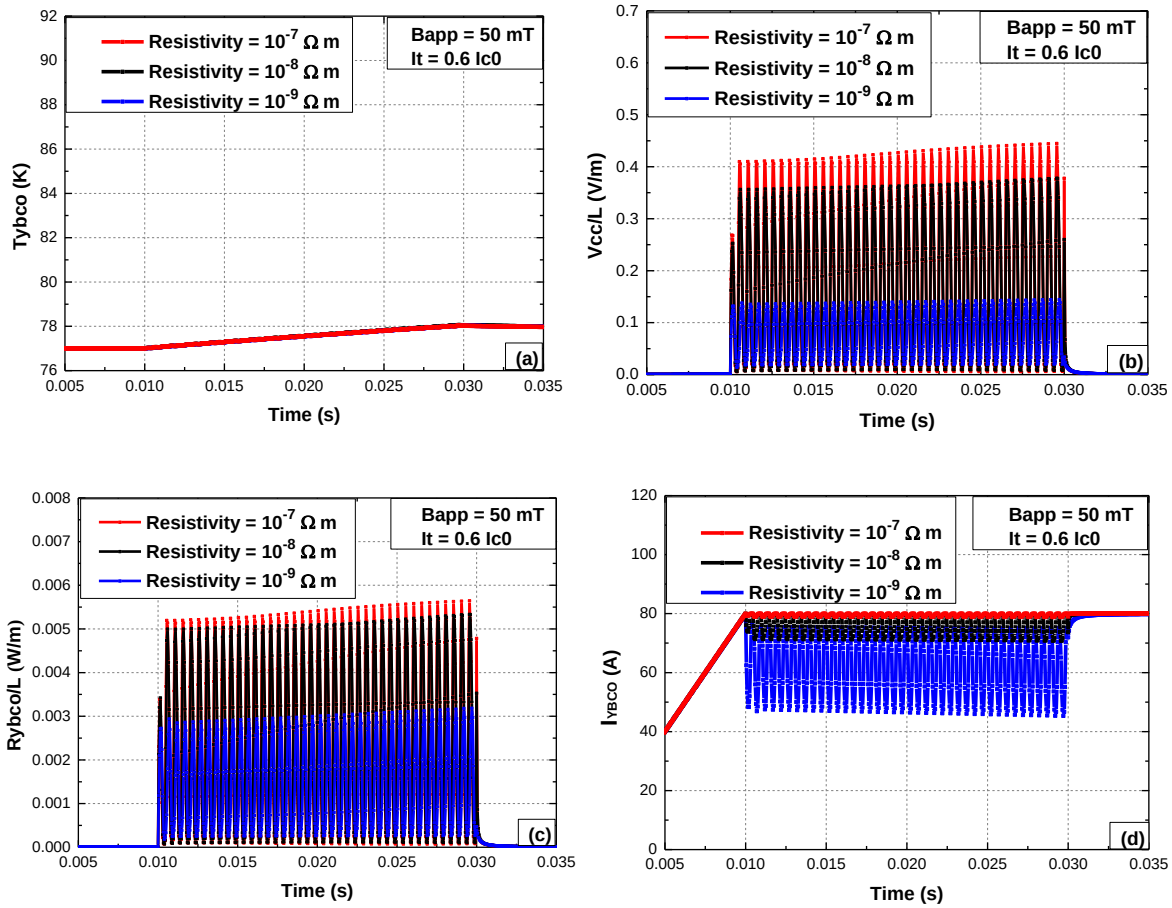

Fig. 7.18. (a) The temperature rise of the YBCO layer. (b) The electrical field of the HTS CC. (c) The dynamic resistance of the YBCO layer. (d) The current flowing in the YBCO layer. The HTS switch is subjected to a 1 kHz, 50 mT (peak) perpendicular magnetic field. The resistivity of the stabilizer increases from 10^{-9} Ωm to 10^{-7} Ωm. Taken from [143].

As shown in Fig. 7.18 (a), the temperature rise is small for all three HTS switches: 1 K, from 77 K to 78 K in 20 ms, and the temperature waveforms are almost the same. The same waveforms can help better analyze the differences in the electrical field of the HTS CC (V_{cc}/L) and the dynamic resistance of the YBCO layer (R_{ybco}/L), since the superconductivity of the YBCO layer is temperature-dependent.

As shown in Fig. 7.18 (b), the electrical field (V_{cc}/L) of the HTS switch increases when the resistivity of the stabilizer layers increases from 10^{-9} Ωm to 10^{-7} Ωm. There are two reasons for this: (i) the increase of the dynamic resistance of the YBCO layer (R_{ybco}/L), as shown in Fig. 7.18 (c), and (ii) the increase of the current flowing in the YBCO layer (I_{YBCO}), as shown in Fig. 7.18 (d). Firstly, the increase of dynamic resistance (R_{ybco}/L) of the YBCO layer is caused by the gradual weakening of shielding effect of the stabilizer layers when their resistivity gradually increases from 10^{-9} Ωm to 10^{-7} Ωm, because the eddy current induced by the AC magnetic field is smaller in a metal stabilizer layer with higher resistivity. Secondly, more transport current is pushed back into the YBCO layer when the resistivity of the stabilizer layers increases. These two factors lead to a higher electrical field (V_{YBCO}/L, or V_{cc}/L) for the HTS switch when the resistivity of the stabilizer layers increases from 10^{-9} Ωm to 10^{-7} Ωm. It is worth to mention that $V_{YBCO}/L = V_{cc}/L$ because different layers in the HTS coated conductor are electrically connected in parallel.

However, the case is different when the magnitude of the AC magnetic field (B_{app}) increases to 200 mT. The results for B_{app} = 200 mT are presented in Fig. 7.19. As shown in Fig. 7.19 (a), the temperature rise of three HTS switches are different. The HTS switch has the fastest temperature accumulation (0.67 K/ms, 10 K in 15 ms) and quenches in a very short time (~16.5 ms) when the resistivity of the stabilizer layers is 10^{-9} Ωm. The temperature rise is 0.3 K/ms (6 K in 20 ms) and 0.25 K/ms (5 K in 20 ms) when the resistivity of the stabilizer layers is 10^{-8} Ωm and 10^{-7} Ωm respectively. As shown in Fig. 7.18 (a), the temperature rise is 0.05 K/ms (1 K in 20 ms) when B_{app} = 50 mT for three HTS tapes. Fig. 7.19 (a) shows that the HTS switch is thermal-electromagnetically more stable and reliable when it has relatively higher resistive stabilizer layers.

As shown in Fig. 7.19 (b), the electrical field (V_{cc}/L) increases when the resistivity of the stabilizer layers increases, which agrees well with Fig. 7.18 (b). Fig. 7.18 (b) and Fig. 7.19 (b) show that the HTS switch has a higher electrical field (V_{cc}/L) when it has relatively higher resistive stabilizer layers. However, one very interesting phenomenon is found by comparing Fig. 7.19 (a) and Fig. 7.19 (b): In general, the heating power should be higher if the electrical field (V_{cc}/L) is higher when the HTS switch carries the same transport current. However, Fig. 7.19 (a) shows that it seems not the same case here. It mainly results from a high eddy current loss in the stabilizer layers, which is induced by the high frequency (1 kHz) external AC magnetic field. A loss analysis is presented in the following section to explain this phenomenon.

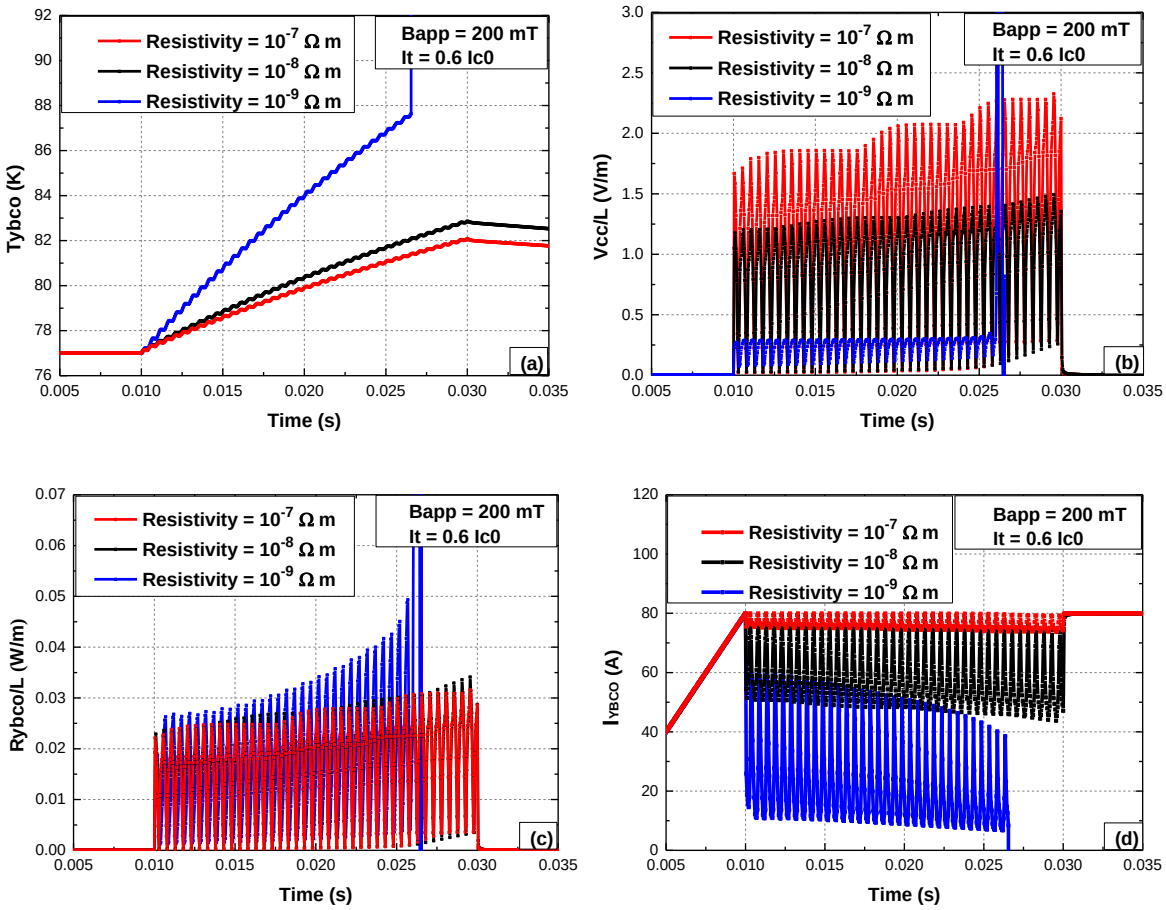

Fig. 7.19. (a) The temperature rise of the YBCO layer. (b) The electrical field of the HTS CC. (c) The dynamic resistance of the YBCO layer. (d) The current flowing in the YBCO layer. The HTS switch is subjected to a 1 kHz, 200 mT (peak) perpendicular magnetic field. The resistivity of the stabilizer increases from 10^{-9} Ωm to 10^{-7} Ωm.

Fig. 7.19 (c), the dynamic resistance of the YBCO layer (R_{ybco}/L), is also different from Fig. 7.18 (c): (i) R_{ybco}/L is the highest when the resistivity of the stabilizer layers is the lowest (10^{-9} Ωm); (ii) the difference in R_{ybco}/L is neglectable when the resistivity of the stabilizer layers is 10^{-8} Ωm and 10^{-7} Ωm. Phenomenon (i) is predominately caused by the quicker and higher temperature rise of the YBCO layer when the resistivity of the stabilizer layers is 10^{-9} Ωm, due to the temperature dependence $J_c(T)$ of the YBCO layer. The main reasons for the phenomenon (ii) are: Firstly, the shielding effect of the stabilizer layers is relatively weak compared to a relatively higher field (200 mT); Secondly, a slightly higher temperature rise, as shown in Fig. 7.19 (a), also contributes to a slightly higher R_{ybco}/L when the resistivity of the stabilizer layers is 10^{-8} Ωm.

Fig. 7.19 (d) is the current flowing in the YBCO layer. Compared to Fig. 7.18 (d), a higher AC perpendicular magnetic field (200 mT) pushes more transport current into the stabilizer layers on both sides of the CC tape. Generally speaking, Fig. 7.19 (b), (c), and (d) agree well with each other.

To conclude, increasing the resistivity of the stabilizer layers has two major benefits: (1) increase the electrical field (V_{cc}/L), or the dc voltage per meter length, of the HTS switch. (2) slow down the temperature rise and increase the thermal-electromagnetic stability and reliability.

Loss analysis:

A loss analysis will help evaluate the performance of switches with different stabilizer layers with different resistivity.

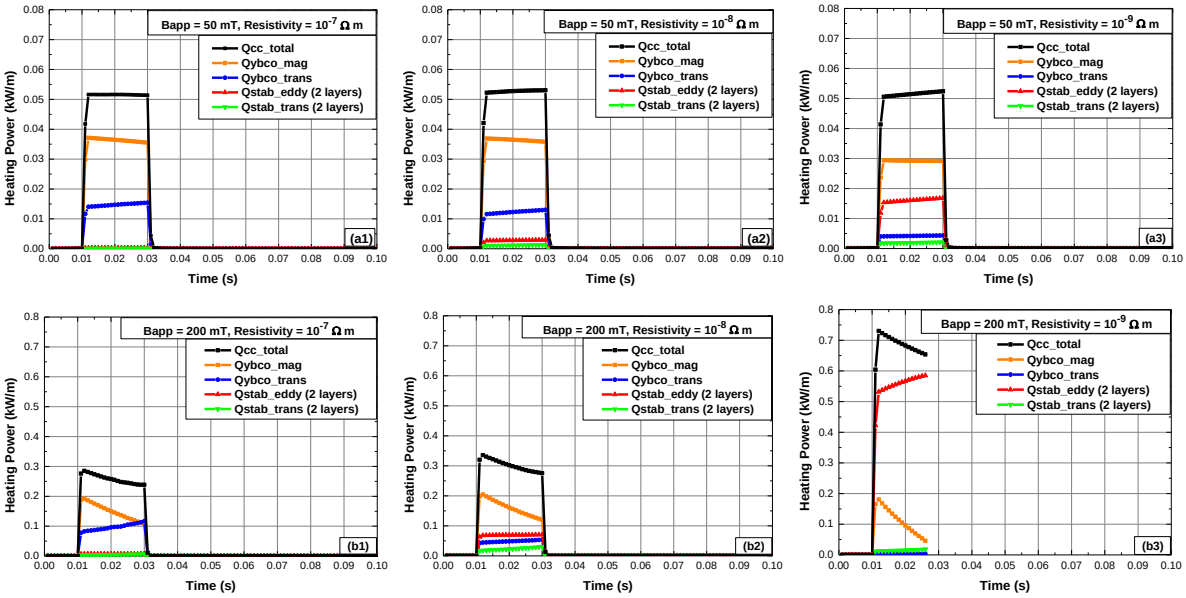

Fig. 7.20. Heating power (loss) analysis when the perpendicular AC magnetic field (peak) magnitude is 50 mT (a1-a3) and 200 mT (b1-b3) respectively [143].

Fig. 7.20 presents an elaborative analysis on the loss, or heating power, of the HTS switch under 50 mT and 200 mT perpendicular AC magnetic fields. Different values of stabilizer resistivity are studied. The different loss components in YBCO layer and stabilizer layers are presented. The total loss (Q_{cc_total}) consists of four parts: (1) the magnetization loss in YBCO layer (Q_{ybco_mag}), (2) the transport loss in YBCO layer (Q_{ybco_trans}), (3) the eddy current loss in two stabilizer layers (Q_{stab_eddy}), and (4) the transport loss in two stabilizer layers (Q_{stab_trans}).

The loss analysis helps further understand the thermal-electromagnetic characteristics of the HTS switch under perpendicular AC magnetic fields.

The total loss (Q_{cc_total}) of the HTS switch subjecting to a perpendicular 1 kHz 50 mT (peak) magnetic field is almost the same, when the stabilizer layer's resistivity increases from 10^{-9} Ωm to 10^{-7} Ωm. It is the reason for the same temperature curves for all three HTS switches in Fig. 7.18 (a). However, when the field (peak) magnitude is 200 mT as shown in Fig. 7.20 (b1) - (b3), the total loss (Q_{cc_total}) is much higher, compared with Fig. 7.20 (a1) - (a3) when the field (peak) magnitude is 50 mT. This is the reason for the higher temperature rise for all three HTS switches in Fig. 7.19 (a), compared with Fig. 7.18 (a). More importantly, the total loss (Q_{cc_total}) increases with the decrease of stabilizer layers' resistivity, which explains the fastest temperature rise of the HTS switch when the resistivity of the stabilizer layers is 10^{-9} Ωm.

Take a further look at the variation of four different loss components, we found that:

(i) The eddy current loss decreases significantly when the stabilizer layers' resistivity increases from 10^{-9} Ωm to 10^{-7} Ωm, which is obvious from Fig. 7.20 (b1) - (b3) and (a1) - (a3). The shielding effect is detrimental: it not only decreases the dynamic resistance and the dynamic voltage of the HTS switch, but also introduces an extra eddy current loss, which increases the risk to quench. Our results show that using relatively higher resistive stabilizer layers in the HTS switch is an effective solution to weaken the magnetic shielding effect and reduce the eddy current loss.

(ii) Increasing the stabilizer layers' resistivity will increase the transport loss in YBCO layer (Q_{ybco_trans}) and reduce the transport loss in stabilizer layers (Q_{stab_trans}). Strictly speaking, the ratio of the magnetization loss in YBCO layer (Q_{ybco_mag}) to the total loss (Q_{cc_total}) also increases when the stabilizer layers' resistivity increases. The main reason for these phenomena is: more transport current is pushed back into the YBCO layer when the resistivity of the stabilizer layers increases, which is shown in Fig. 7.18 (d) and Fig. 7.19 (d).

Results in this part show that: high resistive stabilizer layers help achieve low eddy current loss and low total loss for the HTS switch, which helps achieve high thermal-electromagnetic stability.

In conclusion, the resistivity of the stabilizer layers significantly impacts the thermal-electromagnetic characteristics of the HTS switch, including dynamic resistance, dc voltage,

temperature rise, losses, and stability. High resistive stabilizer layers can help achieve: (1) High dynamic resistance and dc voltage per meter length, (2) Low loss and temperature rise.

7.3.3. Sliced stabilizer layers

Based on previous studies in section 7.2.1, we know that the key idea to improve the performance of the HTS switch is weakening the shielding effect of the stabilizer layers but keeping the current sharing ability. This can help increase the dynamic resistance, reduce the total loss, and keep the excellent thermal stability under quench condition.

In this section, we further study the impact of the stabilizer layers by changing the geometrical design of the stabilizer layers. Fig. 7.21 shows the schematics of three switch designs with different stabilizer layouts: (a) original non-sliced stabilizer layer, (b) sliced stabilizer layers consisted of 4 wide strips (1.5 mm), and (c) sliced stabilizer layers consisted of 4 narrow strips (0.75 mm). We will focus on two core technical parameters: (1) temperature rise and (2) dc voltage V_{dc} and dynamic resistance.

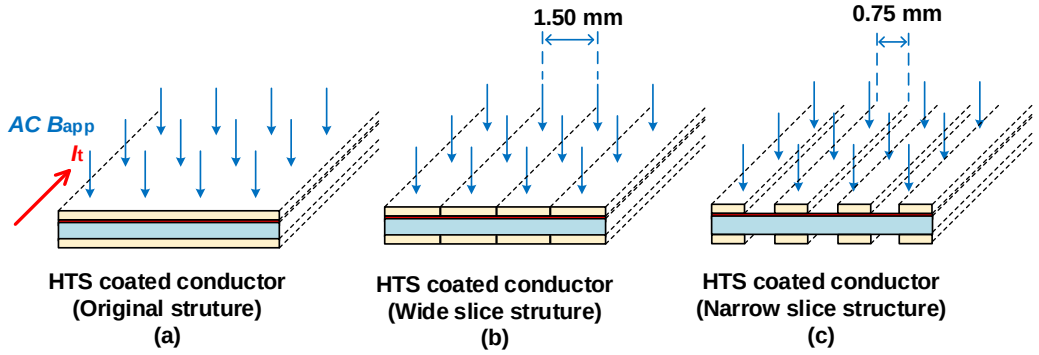

Fig. 7.21. The schematics of three switch designs with different stabilizer layouts: (a) original non-sliced stabilizer layer, (b) sliced stabilizer layers consisted of 4 wide strips (1.5 mm), and (c) sliced stabilizer layers consisted of 4 narrow strips (0.75 mm).

Temperature rise, DC voltage, and Dynamic resistance:

Fig. 7.22 shows the temperature rise and dc voltage (V_{cc}/L) of the switches with three different stabilizer layouts. Fig. 7.22 (a) shows that the temperature rise of the switches with a stabilizer layer consisted of 4 wide slices and with a normal non-sliced stabilizer layer are the same, while the temperature rise of the switch with stabilizer layer consisted of 4 narrow slices is slightly higher. Fig. 7.22 (b) shows that the dc voltage of the switches with the

stabilizer layer consisted of 4 wide slices and with normal non-sliced stabilizer layer are the same, while the dc voltage of the switch with stabilizer layer consisted of 4 narrow slices is much higher. These results from Fig. 7.22 show that the switch with the stabilizer layer consisted of narrow slices can be a good design to help increase the dc voltage of the switch at the cost of slightly higher temperature rise. This optimization method removes a part of the stabilizer layers, which is a little bit similar to removing the stabilizer layers (as shown in Fig. 7.17) to some extent but is much more advantageous in terms of temperature rise. In contrast, the switch adopting stabilizer layers consisted of 4 wide slices is not a good design for improving the performance of the HTS switch.

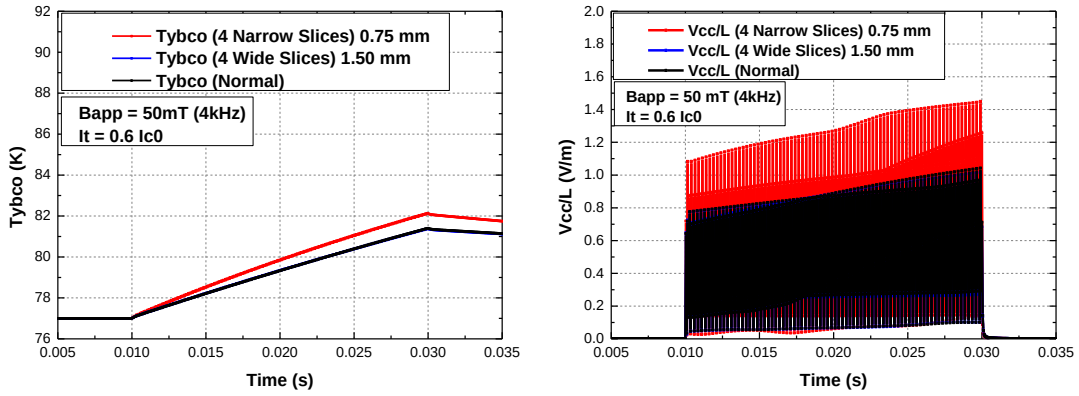

Fig. 7.22. Performance analysis of switches: temperature rise (T_{ybco}) and the dc voltage (V_{cc}/L). A 4 kHz, 50 mT (peak) perpendicular magnetic field is applied for 20 ms. The transport current is 0.6 I_{c0}. The resistivity of the stabilizer layers is set as 8×10^{-9} Ωm.

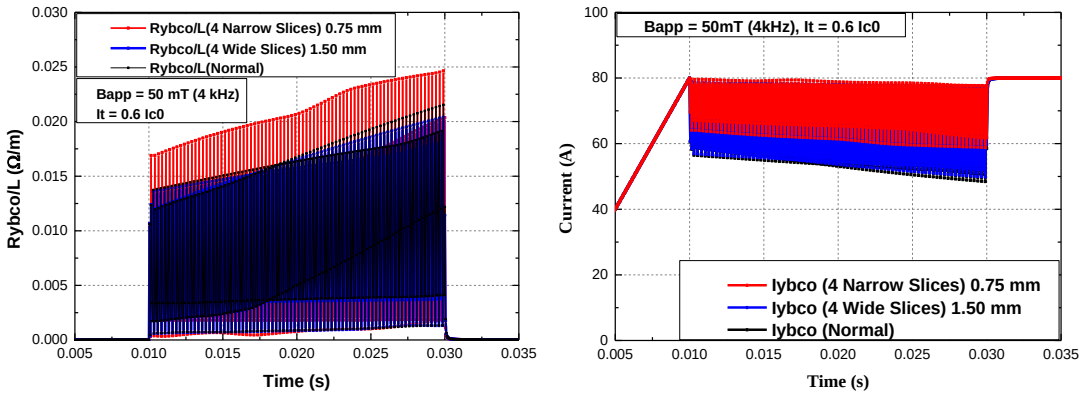

Fig. 7.23. The dynamic resistance (R_{ybco}/L) and the current in YBCO layer.

In order to further understand the mechanism, the dynamic resistance (R_{ybco}) and the current in YBCO layer (I_{ybco}) are plotted in Fig. 7. 23 (a) and (b) respectively.

Fig. 7.23 shows that the dynamic resistance is higher when the switch adopts stabilizer layers consisted of 4 narrow slices. This means that the shielding effect of the stabilizer layers has been weakened by adopting narrowly sliced stabilizer layers.

Fig. 7.23 (b) shows that the current in YBCO layer is higher when the switch adopts stabilizer layers consisted of 4 narrow slices. This means that the resistance of the narrowly sliced stabilizer layers is much higher so that more transport current is pushed back to YBCO layer even when the dynamic resistance of the YBCO layer has already increased. The current sharing ability will be weakened if the switch uses stabilizer layers consisted of narrow slices.

Because of both the increased dynamic resistance of the YBCO layer due to a weakened shielding effect and a higher resistance of the stabilizer layers, the total resistance of the YBCO coated conductor tape (or the HTS switch) will increase. At the same transport current, the dc voltage (V_{cc}/L) will be higher (when the HTS switch adopts stabilizer layers consisted of narrow slices).

Loss analysis:

Fig. 7.24 shows the loss analysis of the three switches with different stabilizer layer layouts, which will help understand the temperature rise of the three different switch designs.

The three designs have a similar total loss (~ 0.22 kW/m), and it should result in the same level of temperature rise. But we realize that the temperature rise is the same only for the HTS switch with stabilizer layer consisted of 4 wide slices and the HTS switch with a normal non-sliced stabilizer layer. The most likely reason for the higher temperature rise for the HTS switch with the stabilizer layer consisted of 4 narrow slices is the small heat tank of the stabilizer layers with narrow slices. Narrow slices mean less mass and therefore smaller heat tank, which results in a higher temperature rise if the HTS switch absorbs the same amount of heat, just as shown in Fig. 7.22 (a).

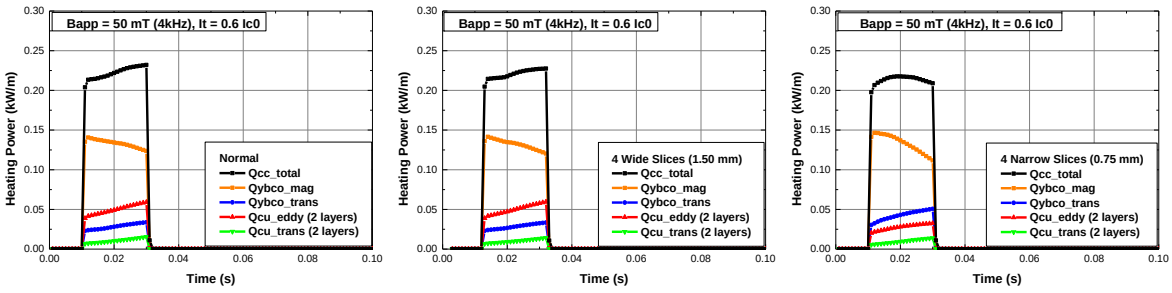

Fig. 7.24. Loss analysis of the three switches with different stabilizer layer layouts.

In terms of eddy current loss in stabilizer layers, the HTS switch with stabilizer layer consisted of 4 narrow slices has the smallest eddy current loss and it accounts for ~11% of the total loss, while the HTS switches with stabilizer layer consisted of 4 wide slices and with normal non-sliced stabilizer layer have a higher eddy current loss at the same level at ~22% of the total loss. Results agree well with the expectation of the optimized design: a narrowly sliced stabilizer layer can effectively reduce the eddy current loop, and therefore reduce the eddy current density and its induced eddy loss. In contrast, the transport loss (Q_{cu_trans}) in stabilizer layers almost keeps the same for three switch designs. So, the ratio of the total loss in the Cu-stabilizer layers to the total loss of coated conductor tape decreases when CC tape has a narrowly sliced stabilizer layer.

In the YBCO layer: the transport loss of the YBCO layer increases greatly when adopting a stabilizer layer consisted of 4 narrow slices. The reason behind this is that: the dynamic resistance of the YBCO layer increases greatly and the dc transport current in YBCO layer increases due to the resistance increase of the stabilizer layers. Compared to the increase of the transport loss in YBCO layer, the magnetization loss in YBCO layer almost keeps the same for three designs. So the ratio of total loss in the YBCO layer to the total loss of coated conductor tape increases when CC tape has a narrowly sliced stabilizer layer.

To sum up, the higher temperature rise in the HTS switch with the stabilizer layer consisted of 4 narrow slices is mainly caused by the small heat tank due to the reduced mass of the stabilizer layers, not by the differences in the total loss.

In this section, we compared three different switch designs with different stabilizer geometrical layouts, among which we found that the HTS switch design with a stabilizer layer consisted of narrow slices is a good design. This switch design can help achieve much higher dc voltage at a relatively low cost of temperature rise.

7.4. Chapter summary

This chapter focuses on the design optimization for high-performance HTS AC-field-controlled switches for the HTS TRFP. Our goal is to design switch with high dynamic resistance, low loss, low temperature rise, and excellent reliability. Our studies in this chapter will help design high-performance, compact, and reliable active-switching HTS TRFP.

In section 7.1, we build a 2D multi-physics model for the HTS REBCO coated conductor (CC), which can simulate the electro-thermal behaviors of the DC carrying coated conductor

to the external applied field with various magnitudes. This model is very close to the real multilayer structure of the REBCO CC and is very useful in analyzing the impact of different layers in the REBCO CC, especially the metal stabilizer layers. It is a powerful tool to understand complicated characteristics inside the REBCO CC that could not be accurately measured, such as the temperature, current, and different loss components in different layers of the REBCO CCs. This model is used for optimizing the switch design.

In section 7.2, we analyzed the impacts of stabilizer layers and found that the Cu-stabilizer has both the current sharing ability and the shielding effect. These two phenomena significantly impact on the dynamic resistance, dynamic voltage, and the loss of the switch. While the current sharing ability is good for safety issues, the shielding effect is detrimental: It not only decreases the dynamic resistance and dynamic voltage, but also introduces an extra eddy current loss to the switch and increases the risk to quench. So, the shielding effect should be suppressed while the current sharing ability should be kept. These findings are important for designing high-performance AC-field-controlled HTS switch.

In section 7.3, based on the understanding of the impacts of the metal stabilizer layers, different switch designs are discussed, including removing the stabilizer layers, changing the material of the stabilizer layers with different resistivity, and changing the geometry design of the stabilizer layers. But the core idea is the same: to weaken the detrimental shielding effect but keep the current sharing ability of the stabilizer layer.

Section 7.3.1 shows that: to design a high resistance and compact switch, the stabilizer is not preferred. Without stabilizer layers, the dc voltage (and off-state resistance) per unit length of the switch is higher, which can make the switch more compact. However, the switch design without stabilizer layers is easy to quench, especially under high-field and high-frequency working mode. To design a reliable switch, the stabilizer layers should be kept. It is advantageous when working in a high-field and high-frequency mode and is suitable for TRFP with a high switching frequency and a high operating current.

Section 7.3.2 shows that the resistivity of the stabilizer layers impacts significantly on the thermal-electromagnetic characteristics of the HTS power switch, including dynamic resistance, DC voltage, temperature rise, losses, and stability. High resistive stabilizer layers help achieve high dynamic resistance and DC voltage per meter length, low loss and temperature rise, and high thermal-electromagnetic stability.

Section 7.3.3 shows that the switch with a stabilizer layer consisted of narrow slices is a good design option. This switch design can achieve high DC voltage at a low cost of slightly higher temperature rise. In this design, the current sharing ability is kept and the shielding effect is weakened.

Chapter 8
Thesis Conclusion and Future Work

8.1. Summary

Flux pumping is an energy-efficient and highly controllable contactless charging technology for superconducting magnets. With its help, the superconducting magnet system can be more compact, reliable, and energy-efficient. This thesis provides a comprehensive study on the flux pumping technology for the no-insulation (NI) type HTS REBCO magnets, which fills the research gap by connecting the state of the art flux pumping technology to the novel NI HTS REBCO magnets.

The main contributions of this PhD thesis include:

1. Proposed a novel NI HTS REBCO magnet adopting solder impregnation technology. This novel NI HTS magnet has huge potential in high-field high-current applications due to excellent mechanical and thermal reliability.
2. Analyse the flux pumping characteristics of the active-switching HTS transformer rectifier flux pump (TRFP) for NI HTS REBCO magnets.
3. Improve the flux pumping performance for the novel solder impregnated NI HTS REBCO magnets with a very small Rc.
4. Optimize the design of the "HTS switch", which is the key component of the active-switching HTS transformer rectifier flux pump.
5. Build a multi-physics model for the HTS REBCO coated conductor. This model is very useful in analyzing the impact of different layers in the REBCO CC. It is also a powerful tool to understand complicated characteristics inside the REBCO CC that cannot be accurately measured, such as the temperature, current, and different loss components in different layers of the REBCO CCs.

The major work of this thesis is summarized as below.

Chapter 4 designs and fabricates an active-switching HTS TRFP. It introduces the fundamental physics, key components, and overall experimental system. The design, experimental fabrication, and an operational test of the TRFP system are presented.

Chapter 5 introduces the NI HTS magnet technology and a novel NI HTS REBCO magnet adopting solder impregnation technology. This novel NI HTS magnet was proposed for the first time, and has huge potential in high field high current applications due to its excellent mechanical and thermal reliability.

Chapter 6 present the pioneering study on the flux pumping experiments for NI HTS REBCO magnet. It presents a comprehensive analysis on the flux pumping characteristics for different types of HTS coil magnets, including insulated HTS REBCO coil, no-insulation REBCO coil, and solder impregnated REBCO coil. An effective improving strategy based on circuit design is proposed and validated. Experimental results show that the flux pumping performance can reach a comparable level to the traditional DC power supplies.

Chapter 7 shows how to design high-performance HTS AC-field-controlled switches with high dynamic resistance, low loss, low temperature rise, and excellent reliability. The HTS power switch determines the overall performance of the active-switching HTS TRFP, including the output capability and reliability. This chapter builds a multi-physics model for REBCO coated conductors, which successfully coupled the thermal physics and the electromagnetic physics. This model is powerful in analysing the thermal-electromagnetic behaviours of the AC-field-controlled HTS switches, including the quench and recovery process, temperature rise, DC voltage, resistance, and loss components. By analyzing various impact factors of the HTS switches via model simulation, different switch designs are analysed and discussed. This chapter will help design high-performance, compact, and reliable active-switching HTS TRFP.

8.2. Future work

This thesis has formed the basis for many exciting future work:

1. Developing stronger flux pumps with higher current and higher voltage is an important future work. The optimized AC field HTS switch design can be utilized in the large-scale active-switching HTS transformer rectifier flux pumps. This thesis presents the numerical study of the AC-field-controlled HTS switches. Practical HTS switch can be developed via experiments.

2. For the AC-field-controlled HTS switches, the impact of the superconducting layer and the substrate layer haven't been studied in this thesis, which can be interesting future research work as well.

3. "Dynamic resistance" effect is also very common for HTS REBCO magnets that work in a time-varying AC magnetic field, such as in HTS motors and generator, HTS maglev, and HTS power cables. Our multi-physics model for REBCO coated conductors can be extended to simulating HTS magnets and cables, including the dynamic loss, temperature rise, and quench phenomenon. These can be very meaningful work as well.

4. Solder impregnated no-insulation HTS REBCO magnet has huge potential in building up safe and reliable superconducting magnet applications. Scaling up the solder impregnated no-insulation REBCO magnets to industrial applications can be a very meaningful future work to our applied superconductivity field.

References

[1]. Hahn, Seungyong, et al. "HTS pancake coils without turn-to-turn insulation." *IEEE transactions on applied superconductivity* 21.3 (2010): 1592-1595.

[2]. S. Hahn et al., "45.5-tesla direct-current magnetic field generated with a high-temperature superconducting magnet," Nature, vol. 570, no. 7762, pp. 496–499, Jun. 2019, doi: 10.1038/s41586-019-1293-1.

[3]. Tokamak Energy [Online]. Available: https://www.tokamakenergy.co.uk/st40/

[4]. H. Onnes, "The resistance of pure mercury at helium temperatures," Commun Phys Lab Univ Leiden, vol. 12, p. 120, 1911.

[5]. W. Meissner and R. Ochsenfeld, "Ein neuer Effekt bei Eintritt der Supraleitfähigkeit," Naturwissenschaften, vol. 21, pp. 787–788, Nov. 1933, doi: 10.1007/BF01504252.

[6]. M. D. Ainslie, "Transport AC loss in high temperature superconducting coils," Thesis, University of Cambridge, 2012.

[7]. Jianzhao Geng. "*Flux Pumping for High-Tc Superconducting (HTS) Magnets"*. Thesis, University of Cambridge, 2017.

[8]. Chao Li, "Dynamic Resistance of High-Tc Superconductor and Its Application in Flux Pumped Superconducting Magnets," Thesis, University of Cambridge, 2019.

[9]. K. Maki, "The magnetic properties of superconducting alloys I," Physics Physique Fizika, vol. 1, no. 1, pp. 21, 1964.

[10]. E. J. Kramer, "Scaling laws for flux pinning in hard superconductors," Journal of Applied Physics, vol. 44, no. 3, pp. 1360-1370, 1973.

[11]. A. Caplin, L. Cohen, G. Perkins, and A. Zhukov, "The electric field within high-temperature superconductors: mapping the EJB surface," Superconductor Science and Technology, vol. 7, no. 6, pp. 412, 1994.

[12]. J. Rhyner, "Magnetic properties and AC-losses of superconductors with power law current—voltage characteristics," Physica C: Superconductivity, vol. 212, no. 3-4, pp. 292-300, 1993.

[13]. C. P. Bean, "Magnetization of hard superconductors," Physical review letters, vol. 8, no. 6, pp. 250, 1962.

[14]. Y. Kim, C. Hempstead, and A. Strnad, "Critical persistent currents in hard superconductors," Physical Review Letters, vol. 9, no. 7, pp. 306, 1962.

[15]. Y. Kim, C. Hempstead, and A. Strnad, "Magnetization and critical supercurrents," Physical Review, vol. 129, no. 2, pp. 528, 1963.

[16]. P. W. Anderson, and Y. Kim, "Hard superconductivity: theory of the motion of Abrikosov flux lines," Reviews of Modern Physics, vol. 36, no. 1, pp. 39, 1964.

[17]. Available online (open access): https://nationalmaglab.org/magnet-development/applied-superconductivity-center/plots#critical-current.

[18]. Grilli, F., Sirois, F., Zermeno, V.M. and Vojenčiak, M., 2014. Self-consistent modeling of the *Ic* of HTS devices: How accurate do models really need to be?. *IEEE Transactions on Applied Superconductivity, 24*(6), pp.1-8.

[19]. Jiang, Z., Thakur, K.P., Staines, M., Badcock, R.A., Long, N.J., Buckley, R.G., Caplin, A.D. and Amemiya, N., 2011. The dependence of AC loss characteristics on the spacing between strands in YBCO Roebel cables. *Superconductor Science and Technology*, *24*(6), p.065005.

[20]. Zhang, X., Zhong, Z., Ruiz, H. S., Geng, J., & Coombs, T. A. (2016). General approach for the determination of the magneto-angular dependence of the critical current of YBCO coated conductors. *Superconductor Science and Technology*, *30*(2), 025010.

[21]. Shen, B., Li, C., Geng, J., Zhang, X., Gawith, J., Ma, J., Liu, Y., Grilli, F. and Coombs, T.A., 2018. Power dissipation in HTS coated conductor coils under the simultaneous action of AC and DC currents and fields. *Superconductor Science and Technology*, *31*(7), p.075005.

[22]. Fujishiro, Hiroyuki, and Tomoyuki Naito. "Simulation of temperature and magnetic field distribution in superconducting bulk during pulsed field magnetization." *Superconductor Science and Technology* 23.10 (2010): 105021.

[23]. Chan, Wan Kan, et al. "Three-Dimensional Micrometer-Scale Modeling of Quenching in High-Aspect-Ratio YBaCuO Coated Conductor Tapes—Part I: Model Development and Validation." *IEEE Transactions on Applied Superconductivity* 20.6 (2010): 2370-2380.

[24]. Chan, Wan Kan, and Justin Schwartz. "A Hierarchical Three-Dimensional Multiscale Electro–Magneto–Thermal Model of Quenching in REBCO Coated-Conductor-Based Coils." *IEEE transactions on applied superconductivity* 22.5 (2012): 4706010-4706010.

[25]. Gao, P., Chan, W. K., Wang, X., Zhou, Y. H., & Schwartz, J. (2020). Stress, strain and electromechanical analyses of (RE) Ba2Cu3Ox conductors using three-dimensional/two-dimensional mixed-dimensional modeling: fabrication, cooling and tensile behavior. *Superconductor Science and Technology*.

[26]. M. P. Oomen, J. Rieger, V. Hussennether, and M. Leghissa, “AC loss in high-temperature superconducting conductors, cables and windings for power devices,” Supercond. Sci. Technol., vol. 17, no. 5, p. S394, 2004, doi: 10.1088/0953-2048/17/5/061.

[27]. Z. Hong, A. M. Campbell, and T. A. Coombs, “Computer Modeling of Magnetisation in High Temperature Bulk Superconductors,” IEEE Trans. Appl. Supercond., vol. 17, no. 2, pp. 3761–3764, Jun. 2007, doi: 10.1109/TASC.2007.899108.

[28]. W. T. Norris, “Calculation of hysteresis losses in hard superconductors carrying ac: isolated conductors and edges of thin sheets,” J. Phys. Appl. Phys., vol. 3, no. 4, pp. 489– 507, Apr. 1970, doi: 10.1088/0022-3727/3/4/308.

[29]. V.V.Andrianov, V. B. Zenkevich, V.V.Kurguzov, V.V.Sychev, and (last) aooF. F.Ternovskii, “Effective Resistance of an Imperfect Type II Superconductor in an Oscillating Magnetic Field,” Sov. Phys. JEPT, vol. 31, no. 5, Nov. 1970.

[30]. Oomen, M.P., Rieger, J., Leghissa, M., ten Haken, B. and ten Kate, H.H., 1999. Dynamic resistance in a slab-like superconductor with Jc (B) dependence. *Superconductor Science and Technology*, *12*(6), p.382.

[31]. Mikitik, G.P. and Brandt, E.H., 2001. Generation of a dc voltage by an ac magnetic field in type-II superconductors. *Physical Review B*, *64*(9), p.092502.

[32]. Uksusman, A., Wolfus, Y., Friedman, A., Shaulov, A. and Yeshurun, Y., 2009. Voltage response of current carrying Y–Ba–Cu–O tapes to alternating magnetic fields. *Journal of Applied Physics*, *105*(9), p.093921.

[33]. Jiang, Z., Toyomoto, R., Amemiya, N., Zhang, X. and Bumby, C.W., 2017. Dynamic resistance of a high-Tc coated conductor wire in a perpendicular magnetic field at 77 K. *Superconductor Science and Technology*, *30*(3), p.03LT01.

[34]. Ainslie, M.D., Bumby, C.W., Jiang, Z., Toyomoto, R. and Amemiya, N., 2018. Numerical modelling of dynamic resistance in high-temperature superconducting coated-conductor wires. *Superconductor Science and Technology*, *31*(7), p.074003.

[35]. Li, Q., Yao, M., Jiang, Z., Bumby, C.W. and Amemiya, N., 2017. Numerical modeling of dynamic loss in HTS-coated conductors under perpendicular magnetic fields. *IEEE Transactions on Applied Superconductivity*, *28*(2), pp.1-6.

[36]. Andy Extance, "The race is on to make the first room temperature superconductor," Chemistry World, 31-Oct-2019. [Online]. Available: https://www.chemistryworld.com/news/the-race-is-on-to-make-the-first-roomtemperature-superconductor/4010591.article. [Accessed: 02-Dec-2019].

[37]. J. M. Kosterlitz and D. J. Thouless, "Long range order and metastability in two dimensional solids and superfluids. (Application of dislocation theory)," J. Phys. C Solid State Phys., vol. 5, no. 11, p. L124, 1972, doi: 10.1088/0022-3719/5/11/002.

[38]. P. Drozdov, M. I. Eremets, I. A. Troyan, V. Ksenofontov, and S. I. Shylin, "Conventional superconductivity at 203 kelvin at high pressures in the sulfur hydride system," Nature, vol. 525, no. 7567, pp. 73–76, Sep. 2015, doi: 10.1038/nature14964.

[39]. H. Y. Zhai et al., "Superconducting magnesium diboride films on Si with Tc0∼24 K grown via vacuum annealing from stoichiometric precursors," Appl. Phys. Lett., vol. 79, no. 16, pp. 2603–2605, Oct. 2001, doi: 10.1063/1.1410360.

[40]. Y. Kamihara, T. Watanabe, M. Hirano, and H. Hosono, "Iron-Based Layered Superconductor La[O1-xFx]FeAs (x = 0.05−0.12) with Tc = 26 K," J. Am. Chem. Soc., vol. 130, no. 11, pp. 3296–3297, Mar. 2008, doi: 10.1021/ja800073m.

[41]. Hahn, Seungyong, et al. "No-insulation (NI) winding technique for premature-quench-free NbTi MRI magnets." *IEEE transactions on applied superconductivity* 22.3 (2011): 4501004-4501004.

[42]. Bottura, Luca, et al. "Advanced accelerator magnets for upgrading the LHC." *IEEE Transactions on Applied Superconductivity* 22.3 (2012): 4002008-4002008.

[43]. Hassenzahl, W. "A Comparison of the Costs of Superconducting Accelerator Dipoles Using NbTi, Nb3Sn and NbTiTa." (1981).

[44]. Mitchell, N., et al. "The ITER magnets: Design and construction status." *IEEE transactions on applied superconductivity* 22.3 (2011): 4200809-4200809.

[45]. Miyazaki, T., et al. "Development of bronze-processed Nb_3Sn superconductors for 1GHz NMR magnets." *Advances in Cryogenic Engineering Materials*. Springer, Boston, MA, 1998. 935-941.

[46]. Matsumoto, S., et al. "Generation of 24 T at 4.2 K using a layer-wound GdBCO insert coil with Nb3Sn and Nb–Ti external magnetic field coils." *Superconductor Science and Technology* 25.2 (2012): 025017.

[47]. Boso, Daniela P., Marek Lefik, and Bernhard A. Schrefler. "Multiscale analysis of the influence of the triplet helicoidal geometry on the strain state of a Nb3Sn based strand for ITER coils." *Cryogenics* 45.9 (2005): 589-605.

[48]. Ciazynski, Daniel. "Review of Nb3Sn conductors for ITER." *Fusion Engineering and Design* 82.5-14 (2007): 488-497.

[49]. Nishi, M., Yoshida, K., Ando, T., Takahashi, Y., Isono, T., Nunoya, Y., ... & Yasukawa, Y. (1994). Nb3Sn superconducting strand development in Japan for ITER. *Cryogenics*, *34*, 505-508.

[50]. Devred, Arnaud, et al. "Status of ITER conductor development and production." *IEEE transactions on applied superconductivity* 22.3 (2012): 4804909-4804909.

[51]. Ambrosio, Giorgio. "Nb3Sn high field magnets for the high luminosity LHC upgrade project." *IEEE Transactions on Applied Superconductivity* 25.3 (2014): 1-7.

[52]. Ferracin, P., Ambrosio, G., Anerella, M., Ballarino, A., Bajas, H., Bajko, M., ... & Chlachidze, G. (2015). Development of MQXF: The Nb_3Sn Low-β Quadrupole for the HiLumi LHC. *IEEE Transactions on applied superconductivity*, *26*(4), 1-7.

[53]. Savary, Frederic, et al. "Progress on the Development of the Nb3Sn 11T Dipole for the High Luminosity Upgrade of LHC." *IEEE Transactions on Applied Superconductivity* 27.4 (2017): 1-5.

[54]. Marken, K. R., et al. "BSCCO-2212 conductor development at Oxford Superconducting Technology." *IEEE transactions on applied superconductivity* 13.2 (2003): 3335-3338.

[55]. C. L. Briant, E. L. Hall, K. W. Lay, and I. E. Tkaczyk, "Microstructural evolution of the BSCCO-2223 during powder-in-tube processing," J. Mater. Res., vol. 9, no. 11, pp. 2789– 2808, Nov. 1994, doi: 10.1557/JMR.1994.2789

[56]. SuperPower® 2G HTS Wire Specifications. Available online (open access): http:// superpower-inc.com/content/wire-specification.

[57]. Weijers, Hubertus W., et al. "Progress in the development and construction of a 32-T superconducting magnet." *IEEE Transactions on Applied Superconductivity* 26.4 (2016): 1-7.

[58]. "32 Tesla all-superconducting magnet," [Online]. Available: https:// nationalmaglab.org/magnet-development/magnet-science-technology/ magnet-projects/32-tesla-scm.

[59]. Bai, Hongyu, et al. "The 40 T Superconducting Magnet Project at the National High Magnetic Field Laboratory." *IEEE Transactions on Applied Superconductivity* 30.4 (2020): 1-5.

[60]. Liu, Jianhua, Qiuliang Wang, et al. "World record 32.35 tesla direct-current magnetic field generated with an all-superconducting magnet." *Superconductor Science and Technology* 33.3 (2020): 03LT01.

[61]. Iwasa, Yukikazu, et al. "High-temperature superconducting magnets for NMR and MRI: R&D activities at the MIT francis bitter magnet laboratory." *IEEE Transactions on Applied Superconductivity* 20.3 (2010): 718-721.

[62]. Michael, P. C., Park, D., …, Iwasa, Y. (2019). Assembly and test of a 3-nested-coil 800-MHz REBCO insert (H800) for the MIT 1.3 GHz LTS/HTS NMR magnet. *IEEE Transactions on Applied Superconductivity, 29*(5), 1-6.

[63]. Park, Dongkeun, et al. "MIT 1.3-GHz LTS/HTS NMR Magnet: Post Quench Analysis and New 800-MHz Insert Design." *IEEE Transactions on Applied Superconductivity* 29.5 (2019): 1-4.

[64]. Noe, Mathias, and Michael Steurer. "High-temperature superconductor fault current limiters: concepts, applications, and development status." *Superconductor science and technology* 20.3 (2007): R15.

[65]. Hong, Z., et al. "The structure, performance and recovery time of a 10 kV resistive type superconducting fault current limiter." *IEEE transactions on applied superconductivity* 23.3 (2012): 5601304-5601304.

[66]. Xiaowei Song et al., "Ground Testing of the World's First MW-Class Direct Drive Superconducting Wind Turbine Generator," *IEEE Trans. Energy Conv. (Early Access)*, doi: 10.1109/TEC.2019.2960255.

[67]. Xiaowei Song et al., "Designing and Basic Experimental Validation of the World's First MW-Class Direct-Drive Superconducting Wind Turbine Generator," *IEEE Trans. Energy Conv.*, vol. 34, no. 4, pp. 2218–2225, Dec. 2019.

[68]. Van der Laan, Daniel C. "YBa2Cu3O7− δ coated conductor cabling for low ac-loss and high-field magnet applications." *Superconductor Science and Technology* 22.6 (2009): 065013.

[69]. Van der Laan, Danko C., Jeremy D. WEISS, and Dustin McRae. "Status of CORC® cables and wires for use in high-field magnets and power systems a decade after their introduction." *Superconductor Science and Technology* (2019).

[70]. Wang, Yawei, et al. "Quench behavior of high-temperature superconductor (RE) $Ba_2Cu_3O_x$ CORC cable." *Journal of Physics D: Applied Physics* 52.34 (2019): 345303.

[71]. Wang, Xiaorong, et al. "A viable dipole magnet concept with REBCO CORC® wires and further development needs for high-field magnet applications." *Superconductor Science and Technology* 31.4 (2018): 045007.

[72]. Frankel, D. J. (1979). Critical-state model for the determination of critical currents in disk-shaped superconductors. *Journal of Applied Physics, 50*(8), 5402-5407.

[73]. Hull, J. R., & Murakami, M. (2004). Applications of bulk high-temperature superconductors. *Proceedings of the IEEE, 92*(10), 1705-1718.

[74]. Durrell, J. H., Dennis, A. R., Jaroszynski, J., Ainslie, M. D., Palmer, K. G., Shi, Y. H., ... & Cardwell, D. A. (2014). A trapped field of 17.6 T in melt-processed, bulk Gd-

Ba-Cu-O reinforced with shrink-fit steel. *Superconductor Science and Technology*, *27*(8), 082001.

[75]. [Online]. Available: https://nationalmaglab.org/education/magnet-academy/learn-the-basics/stories/mri-a-guided-tour

[76]. Iwasa, Yukikazu. "HTS and NMR/MRI magnets: Unique features, opportunities, and challenges." *Physica C: Superconductivity and its applications* 445 (2006): 1088-1094.

[77]. Shen, B., Ozturk, Y., Wu, W., Lu, L., Sheng, J., Huang, Z., ... & Menon, D. (2020). Development of an HTS Magnet for Ultra-compact MRI System: Optimization using Genetic Algorithm (GA) Method. *IEEE Transactions on Applied Superconductivity*.

[78]. Durrell, J. H., Ainslie, M. D., Zhou, D., Vanderbemden, P., Bradshaw, T., Speller, S., ... & Cardwell, D. A. (2018). Bulk superconductors: A roadmap to applications. *Superconductor Science and Technology*, *31*(10), 103501.

[79]. De Tommasi, Gianmaria. "Plasma magnetic control in tokamak devices." *Journal of Fusion Energy* 38.3-4 (2019): 406-436.

[80]. Magnet design of tokamak in ITER. [Online]. Available: https://www.iter.org/mach/magnets

[81]. Costley, A. E. "Towards a compact spherical tokamak fusion pilot plant." *Philosophical Transactions of the Royal Society A* 377.2141 (2019): 20170439.

[82]. Windridge, Melanie J., Mikhail Gryaznevich, and David Kingham. "Nuclear fusion research at Tokamak Energy Ltd." *Purazuma, Kaku Yugo Gakkai-Shi* 93.1 (2017): 28-31.

[83]. Slade, Robert. "Cable design in hts tokamaks." U.S. Patent Application No. 16/346,072.

[84]. Windridge, Melanie. "Smaller and quicker with spherical tokamaks and high-temperature superconductors." *Philosophical Transactions of the Royal Society A* 377.2141 (2019): 20170438.

[85]. Sykes et al., “Compact fusion energy based on the spherical tokamak,” Nucl. Fusion, vol. 58, no. 1, p. 016039, Nov. 2017, doi: 10.1088/1741-4326/aa8c8d.

[86]. R. Mumgaard et al., “The High Field Path to Practical Fusion Energy,” APS, vol. 2017, p. JP11.081, Oct. 2017.

[87]. Greenwald, M., et al. *The high-field path to practical fusion energy*. PSFC Report, 2018.

[88]. Fermilab's Accelerator Complex, [Online] Available: https://www.fnal.gov/pub/science/particle-accelerators/accelerator-complex.html

[89]. W. P. Levin, H. Kooy, J. S. Loeffler, and T. F. DeLaney, “Proton beam therapy,” Br. J. Cancer, vol. 93, no. 8, pp. 849–854, Oct. 2005, doi: 10.1038/sj.bjc.6602754.

[90]. J. B. Farr, J. B. Flanz, A. Gerbershagen, and M. F. Moyers, “New horizons in particle therapy systems,” Med. Phys., vol. 45, no. 11, pp. e953–e983, 2018, doi: 10.1002/mp.13193.

[91]. Bergen, Anne, et al. "Design and in-field testing of the world’s first ReBCO rotor for a 3.6 MW wind generator." *Superconductor science and technology* 32.12 (2019): 125006.

[92]. Filipenko, Mykhaylo, et al. "Concept design of a high power superconducting generator for future hybrid-electric aircraft." *Superconductor Science and Technology* 33.5 (2020): 054002.

[93]. Durrell, John H., et al. "A trapped field of 17.6 T in melt-processed, bulk Gd-Ba-Cu-O reinforced with shrink-fit steel." *Superconductor Science and Technology* 27.8 (2014): 082001.

[94]. Ballarino A and Flückinger R 2017 Status of MgB_2 wire and cable applications in europe IOP Conf. Ser.: J. Phy. 871 012098.

[95]. Iwasa, Yukikazu. *Case studies in superconducting magnets: design and operational issues*. Springer Science & Business Media, 2009.

[96]. Maeda, Hideaki, and Yoshinori Yanagisawa. "Recent developments in high-temperature superconducting magnet technology." *IEEE Transactions on applied superconductivity* 24.3 (2013): 1-12.

[97]. Y. Iwasa et al., "A high-resolution 1.3-GHz/54-mm LTS/HTS NMR magnet," IEEE Trans. Appl. Supercond., vol. 25, no. 3, pp. 1–5, Jun. 2015.

[98]. J. Bascun˜an, S. Hahn, T. Lecrevisse, J. Song, D. Miyagi, and Y. Iwasa, "An 800−MHz all-REBCO insert for the 1.3-GHz LTS/HTS NMR magnet program - a progress report," IEEE Trans. Appl. Supercond., vol. 26, no. 4, Art. no. 4300205, Jun. 2016.

[99]. Jiang, Junjie, et al. "Experimental study on quench detection of a no-insulation HTS coil based on Raman-scattering technology in optical fiber." *IEEE Transactions on Applied Superconductivity* 28.3 (2018): 1-5.

[100]. Jiang, Junjie, et al. "Spatial and Temporal Resolution Optimization on Raman Distributed Temperature Sensor System for Quench Detection in a No-Insulated Coil." *IEEE Transactions on Applied Superconductivity* 29.5 (2019): 1-5.

[101]. Scurti, F., et al. "Quench detection for high temperature superconductor magnets: a novel technique based on Rayleigh-backscattering interrogated optical fibers." *Superconductor Science and Technology* 29.3 (2016): 03LT01.

[102]. Scurti, Federico, et al. "Self-monitoring 'SMART' (RE)$Ba_2Cu_3O_{7-x}$ conductor via integrated optical fibers." *Superconductor Science and Technology* 30.11 (2017): 114002.

[103]. Kajita, Kentaro, et al. "Degradation of a REBCO coil due to cleavage and peeling originating from an electromagnetic force." *IEEE Transactions on Applied Superconductivity* 26.4 (2016): 1-6.

[104]. Kajita, K., et al. "Degradation of a REBCO conductor due to an axial tensile stress under edgewise bending: a major stress mode of deterioration in a high field REBCO coil's performance." *Superconductor Science and Technology* 30.7 (2017): 074002.

[105]. Bai, Hongyu, et al. "The 40 T Superconducting Magnet Project at the National High Magnetic Field Laboratory." IEEE Transactions on Applied Superconductivity 30.(4),1-5, 2020.

[106]. Mitchell N 2002 Analysis of the effect of Nb3Sn strand bending on CICC superconductor performance Cryogenics 42 311–25

[107]. Nijhuis A, Ilyin Y, Abbas W, Ten Haken B and Ten Kate H H J 2004 Performance of an ITER CS1 model coil conductor under transverse cyclic loading up to 40,000 cycles IEEE Trans. Appl. Supercond. 14 1489–94

[108]. Nijhuis A 2008 A solution for transverse load degradation in ITER Nb3Sn CICCs: verification of cabling effect on Lorentz force response Supercond. Sci. Technol. 21 054011

[109]. Zhai Y and Bird M D 2008 Florida electro-mechanical cable model of Nb3Sn CICCs for high-field magnet design Supercond. Sci. Technol. 21 115010.

[110]. Bajas H, Durville D, Ciazynski D and Devred A 2010 Numerical simulation of the mechanical behavior of ITER cable-inconduit conductors IEEE Trans. Appl. Supercond. 20 1467–70.

[111]. Xia, Jing, et al. "Stress and strain analysis of a REBCO high field coil based on the distribution of shielding current." Superconductor Science and Technology 32, no. 9 (2019).

[112]. Trillaud, F., Palanki, H., Trociewitz, U. P., Thompson, S. H., Weijers, H. W., & Schwartz, J. Normal zone propagation experiments on HTS composite conductors. *Cryogenics*, *43*(3-5), 271-279. 2003.

[113]. Bhattarai, K.R., 2019. *Understanding Multi-Physics of Quench in" No-Insulation" Rare Earth Barium Copper Oxide Superconducting Magnets* (Doctoral dissertation, The Florida State University).

[114]. Song, Jung-Bin, et al. "Over-current quench test and self-protecting behavior of a 7 T/78 mm multi-width no-insulation REBCO magnet at 4.2 K." *Superconductor Science and Technology* 28.11 (2015): 114001.

[115]. Kim, Young-Gyun, et al. "Investigation of HTS racetrack coil without turn-to-turn insulation for superconducting rotating machines." *IEEE transactions on applied superconductivity* 22.3 (2011): 5200604-5200604.

[116]. Choi, Y. H., Hahn, S., Song, J. B., Yang, D. G., & Lee, H. G. (2011). Partial insulation of GdBCO single pancake coils for protection-free HTS power applications. *Superconductor Science and Technology*, *24*(12), 125013.

[117]. Lee, Tae Sung, et al. "The effects of co-wound Kapton, stainless steel and copper, in comparison with no insulation, on the time constant and stability of GdBCO pancake coils." *Superconductor Science and Technology* 27.6 (2014): 065018.

[118]. L écrevisse, Thibault, Yukikazu Iwasa. "A (RE) BCO pancake winding with metal-as-insulation." IEEE Transactions on Applied Superconductivity 26.3 (2016): 1-5.

[119]. Chan, Wan Kan, and Justin Schwartz. "Improved stability, magnetic field preservation and recovery speed in (RE) Ba2Cu3O x-based no-insulation magnets via a graded-resistance approach." *Superconductor Science and Technology* 30.7 (2017): 074007.

[120]. Jo, Young-Sik, et al. "2G HTS magnet with smart insulation method." *IEEE Transactions on Applied Superconductivity* 28.3 (2017): 1-4.

[121]. Wilson, Martin N. "Superconducting magnets." (1983).

[122]. M. Igarashi et al., “Persistent current HTS magnet cooled by cryocooler (1) - Project overview,” IEEE Trans. Appl. Supercond., vol. 15, no. 2, pp. 1469–1472, Jun. 2005.

[123]. Oomen, Marijn P., et al. "HTS flux pump for cryogen-free HTS magnets." *IEEE transactions on applied superconductivity* 15.2 (2005): 1465-1468.

[124]. Z. Bai, G. Yan, C. Wu, S. Ding, C. Chen, “A novel high temperature superconducting magnetic flux pump for MRI magnets,” *Cryogenics*, vol. 50, no. 10, pp. 688–692, 2010.

[125]. L. Fu, K. Matsuda, M. Baghdadi, and T. Coombs, “Linear flux pump device applied to high temperature superconducting (HTS) magnets,” *IEEE Trans. Appl. Supercond.*, vol. 25, no. 3, Art. no. 4603804, Jun. 2015.

[126]. C. Hoffmann, D. Pooke, and A. Caplin, “Flux pump for HTS magnets,” *IEEE Trans. Appl. Supercond.*, vol. 21, no. 3, pp. 1628–1631, Jun. 2011.

[127]. Z. Jiang, K. Hamilton, N. Amemiya, R. Badcock, C. Bumby, “Dynamic resistance of a high-Tc superconducting flux pump,” *Appl. Phys. Lett.*, vol. 105, no. 11, Art. no. 112601, 2014.

[128]. C. Bumby, Z. Jiang, J. Storey, A. Pantoja, and R. Badcock, “Anomalous open-circuit voltage from a high-Tc superconducting dynamo,” *Appl. Phys. Lett.*, vol. 108, no. 12, Art. no. 122601, Mar. 2016.

[129]. Hamilton, Kent, et al. "Design and performance of a “squirrel-cage” dynamo-type HTS flux pump." *IEEE Transactions on Applied Superconductivity* 28.4 (2018): 1-5.

[130]. S. Lee et al., “Persistent current mode operation of a 2G HTS coil with a flux pump,” *IEEE Trans. Appl. Supercond.*, vol. 26, no. 4, Art. no. 0606104, Jun. 2016.

[131]. J. Geng and T. Coombs, “Mechanism of a high-Tc superconducting flux pump: Using alternating magnetic field to trigger flux flow*,” Appl. Phys. Lett.*, vol. 107, no. 14, Art. no. 142601, 2015.

[132]. J. Geng et al, “Operational research on a high-Tc rectifier-type superconducting flux pump,” *Supercond. Sci. Tech.*, vol. 29, no. 3, Art. no. 035015, 2016.

[133]. J. Geng and T. Coombs, “An HTS flux pump operated by directly driving a superconductor into flux flow region in the *E-J* curve,” *Supercond. Sci. Tech.*, vol. 29, no. 9, Art. no. 095004, 2016.

[134]. L. J. M. van de Klundert and H. H. J. ten Kate, “Fully superconducting rectifiers and flux pumps Part 1: Realized methods for pumping flux,” Cryogenics, vol. 21, no. 4, pp.195–206, 1981.

[135]. L. J. M. van de Klundert and H. H. J. ten Kate, “On fully superconducting rectifiers and flux pumps. A review. Part 2: Commutation modes, characteristics and switches,” Cryogenics, vol. 21, no. 5, pp. 267–277, May 1981.

[136]. James Gawith, “Development of HTS Transformer-Rectifier Flux Pumps” PhD dissertation, University of Cambridge, 2019.

[137]. G. B. J. Mulder, H. H. J. ten Kate, H. J. G. Krooshoop, and L. J. M. van de Klundert, “Development of a thermally switched superconducting rectifier for 100 kA,” *IEEE Trans. Magn.*, vol. 27, no. 2, pp. 2333–2336, Mar. 1991, doi: 10.1109/20.133685.

[138]. L. M. Barkov *et al.*, “Superconducting rectifier flux pump for magnet system of the CMD-2 detector,” *IEEE Trans. Appl. Supercond.*, vol. 9, no. 3, pp. 4585–4590, Sep. 1999, doi: 10.1109/77.791914.

[139]. H. L. Laquer, K. J. Carroll, and E. F. Hammel, “An automatic superconducting flux pump,” *Phys. Lett.*, vol. 21, no. 4, pp. 397–398, Jun. 1966, doi: 10.1016/0031-9163(66)90501-4.

[140]. J. Geng *et al.*, “Origin of dc voltage in type II superconducting flux pumps: field, field rate of change, and current density dependence of resistivity,” Feb. 2016, doi: 10.17863/CAM.419.

[141]. R. C. Mataira, M. D. Ainslie, R. A. Badcock, and C. W. Bumby, “Origin of the DC output voltage from a high-Tc superconducting dynamo,” *Appl. Phys. Lett.*, vol. 114, no. 16, p. 162601, Apr. 2019, doi: 10.1063/1.5085226.

[142]. Jun Ma, Jianzhao Geng, Wan Kan Chan, Justin Schwartz, Tim Coombs, “A temperature-dependent multilayer model for direct current carrying HTS coated-conductors under perpendicular AC magnetic fields”, *Superconductor Science and Technology*, vol. *33, no.* 4, Art. ID 045007, 2020.

[143]. Jun Ma, *et al*, “Impact of Stabilizer Layers on the Thermal-Electromagnetic Characteristics of Direct Current Carrying HTS Coated Conductors under Perpendicular AC Magnetic Fields”, *IEEE Transactions on Applied Superconductivity,* vol. 30, no. 4, Art. ID 6600906, 2020.

[144]. Jianzhao Geng, Chao Li, and Tim A. Coombs. "A fast AC field controlled impedance in HTS coated conductors: Response speed and electric field value." *IEEE Transactions on Applied Superconductivity* 27.6 (2017): 1-5.

[145]. Jun Ma, Jianzhao Geng, Tim Coombs, “Flux pumping for non-insulated and metal-insulated HTS coils”. *Superconductor Science and Technology*, vol. 31, no. 1, Art. ID 015018, 2017.

[146]. Ma, Jun, et al. "High-temperature superconducting (HTS) transformer-rectifier flux pump for powering no-insulation superconducting magnet with low characteristic resistance." *Physica C: Superconductivity and its Applications* 560 (2019): 1-6.

[147]. Hong, Z., A. M. Campbell, and T. A. Coombs. "Numerical solution of critical state in superconductivity by finite element software." Superconductor Science and Technology 19.12 (2006): 1246.

[148]. Geng J, Coombs T A. Modeling methodology for a HTS flux pump using a 2D H-formulation[J]. Superconductor Science and Technology, 2018, 31(12): 125015.